The complex spin-orbit interaction (SOI) of two-dimensional hole gas (2DHG) systems - the relativistic coupling of the hole spin degree of freedom to their movement in an electric field - is of fundamental interest in spin physics due to its key role for spin manipulation in spintronic devices. In this work, we were able to evaluate the tunability of Rashba-SOI-related parameters in the 2DHG system of InAlAs/InGaAs/InAs:Mn quantum well heterostructures experimentally by analyzing the hole density evolution of quantum interference effects at low magnetic fields. We achieved to cover a significant range of hole densities by the joint action of the variation of the manganese modulation doping concentration during molecular beam epitaxy and external field-effect-mediated manipulation of the 2D carrier density in Hall bar devices by a metallic topgate.

Within these magnetotransport experiments, a reproducible phenomenon of remarkable robustness emerged in the transverse Hall magnetoresistivity of the indium 2DHG systems which are grown on a special InAlAs step-graded metamorphic buffer layer structure to compensate crystal lattice mismatch. As a consequence of the strain relaxation process, these material systems are characterized by anisotropic properties along different crystallographic directions. We identify a puzzling offset phenomenon in the zero-field Hall magnetoresistance and demonstrate it to be a universal effect in systems with spatially anisotropic transport properties.

Universitätsverlag Regensburg

ISBN 978-3-86845-137-5

gefördert von:

Alumni der physikalischen Fakultät der Universität Regensburg e.V.

Universität Regensburg

Dissertationsreihe Physik - Band 51

Josef Loher

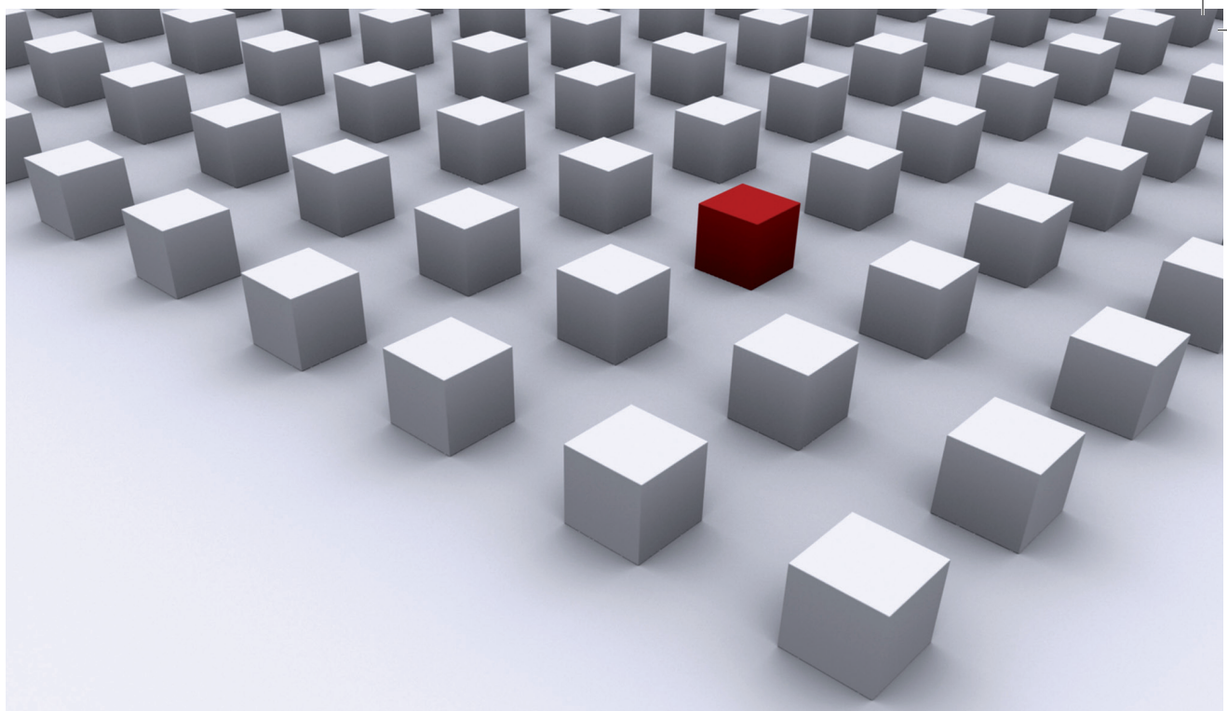

Josef Loher

Two-dimensional hole systems in indium-based quantum well heterostructures

Universitätsverlag Regensburg

51

Dissertationsreihe Physik

Josef Loher

Two-dimensional hole systems in indium-based quantum well heterostructures

Two-dimensional hole systems in indium-based quantum well heterostructures

Dissertation zur Erlangung des Doktorgrades der Naturwissenschaften (Dr. rer. nat.)
der Fakultät für Physik der Universität Regensburg
vorgelegt von

Josef Loher

aus Deggendorf
im Dezember 2015

Die Arbeit wurde von Prof. Dr. Dominique Bougeard angeleitet.
Das Promotionsgesuch wurde am 25.09.2015 eingereicht.

Prüfungsausschuss:	Vorsitzender:	Prof. Dr. Vladimir Braun
	1. Gutachter:	Prof. Dr. Dominique Bougeard
	2. Gutachter:	Prof. Dr. Christian Schüller
	weiterer Prüfer:	Prof. Dr. Karsten Rincke

Dissertationsreihe der Fakultät für Physik der Universität Regensburg, Band 51

Herausgegeben vom Präsidium des Alumnivereins der Physikalischen Fakultät:
Klaus Richter, Andreas Schäfer, Werner Wegscheider

Josef Loher

Two-dimensional hole systems in indium-based quantum well heterostructures

Universitätsverlag Regensburg

Bibliografische Informationen der Deutschen Bibliothek.
Die Deutsche Bibliothek verzeichnet diese Publikation
in der Deutschen Nationalbibliografie. Detailierte bibliografische Daten
sind im Internet über http://dnb.ddb.de abrufbar.

1. Auflage 2016

Leibnizstraße 13, 93055 Regensburg

Konzeption: Thomas Geiger
Umschlagentwurf: Franz Stadler, Designcooperative Nittenau eG
Layout: Josef Loher
Druck: Docupoint, Magdeburg
ISBN: 978-3-86845-137-5

Weitere Informationen zum Verlagsprogramm erhalten Sie unter:
www.univerlag-regensburg.de

Contents

1 Introduction

1.1 Indium-based spintronics

For decades, spin-orbit interaction (SOI), the relativistic coupling of the spin degree of freedom to the movement of carriers in an electric field, has sparked a rich variety both of fundamental research in spin physics and of new spin-based technological applications. In 1984, Bychkov and Rashba [1] formulated the concept of a SOI that arises from the spatial inversion asymmetry of the confining potential of low-dimensional carrier systems: the Rashba spin-orbit coupling (SOC). The possibility to tailor and actively influence this potential and hence to manipulate the spin magnetic moment has been driving new developments in material science ever since, ultimately leading to the crystallization of the highly active field of spintronics [2, 3, 4]. Semiconductor spintronics, spin-based electronics where it is the moving carriers' spin degree of freedom rather than a charged carrier state that is addressed by SOI to encode and process information, may allow spin-based logic, communication and storage operations in the quest for future solid-state computational concepts going beyond the physical restrictions of today's charge-based silicon electronics [5]. With its central role also for novel states of matter, e.g. topological insulators, Majorana fermions or two-dimensional (2D) Dirac materials, the Rashba-type of SOI is still adding exciting new facets to the reel of spintronic research fields [6].
As a catalyst to many scientific developments in this field, a key part in spintronical device prospects is ascribed to the all-electrical spin field-effect transistor (FET) famously proposed by Datta and Das in 1990 [7]. Their concept requires the creation of a polarized density of spins injected from magnetized contacts into a semiconducting 2D channel, the electrical SOC-induced manipulation of these spins during their ballistic time of flight provided a low spin relaxation rate, and the subsequent detec-

tion of the new spin state. As an essential ingredient for spin FET functionality, the ability to provoke spin precession by external metallic-gate-controlled electric fields is given by the presence of the intrinsic Rashba spin-orbit interaction of the semiconductor material. The Rashba field induced by a broken structural inversion symmetry of the confining potential in quantum well (QW) heterostructures relativistically transforms into an effective momentum-dependent magnetic field that lifts the degeneracy of spin states. Despite the conceptual clarity and the great progress already having been achieved in electrical spin injection and detection, e.g. [8, 9], outstanding technical and physical challenges have been impeding a technologically relevant demonstration of a spin FET in a semiconductor material system.

Exceptionally large Rashba spin splitting is found in narrow-direct-gap semiconductor compounds with strongly non-parabolic subband dispersions, such as InAs and InSb [10, 11]. Indeed, the calculated characteristic Rashba coefficients of the topmost conduction and valence subbands of indium arsenide (InAs), $r_{41}^{6c6c} = 117.1$ eÅ^2 and $r_{41}^{7v7v} = -43.35$ eÅ^2, respectively, greatly exceed e.g. the gallium arsenide (GaAs) ones, $r_{41}^{6c6c} = 5.206$ eÅ^2 and $r_{41}^{7v7v} = -9.720$ eÅ^2, or that of other common materials [11]. III-V heterosystem alloys based on the high-SOC material indium (In) have consequently been among the first to enable the demonstration of gate-induced spin manipulation via Rashba SOI by Nitta, Koga and co-workers [12, 13, 14] as well as of the fabrication of a spin-injected Datta-Das-type of device by Koo *et al.* [15] modulating a non-local high-mobility channel conductance. Early this year, Chuang *et al.* [16] then succeeded in the striking realization of a functional all-electrical and all-semiconductor spin FET device from an $In_{0.75}Al_{0.25}As/In_{0.75}Ga_{0.25}As/InAs$ two-dimensional electron gas (2DEG) system where the spin orientation is manipulated in direct ballistic source-drain conductance. Here the authors engaged asymmetrically biased pairs of quantum point contacts (QPCs), also prepared from indium-based ternaries, replacing common ferromagnetic contacts to create a spin-orbit-induced non-equilibrium spin distribution for an efficient spin generation and detection [17, 18]. These novel all-semiconductor designs should ease the integration of these nanostructures into current semiconductor circuit architectures.

With the great experimental progress having been achieved in pursuing the prospects of spintronics in electronic systems, research on emerging high-mobility 2D hole systems has been intensified as well given their advantageous properties: The Rashba SOI strength in hole systems should be more significant owing to the p-like character of the valence band (VB) wave function with respect to the s-like conduction band (CB). Also the effective masses of carriers are in principle higher for holes than for electrons [11]. However, a strong SOI represents a double-edged condition: While the ability of an effective Rashba spin manipulation is enhanced, also the degree of spin relaxation increases, detrimental for the coherent modulation of a spin signal. Still, long spin dephasing times are reported from 2D hole spin dynamics in low-doped p-type AlGaAs/GaAs QW samples at low temperatures by

Korn *et al.* originating from details within the complexity of the valence band structure [19, 20]. Enhanced 2D hole spin conservation is also found in the persistent state of the spin helix symmetry that arises when the Rashba SOI parameter α is tuned to match the strength of the Dresselhaus parameter β, which marks the fixed SOI from the inversion asymmetry in non-centrosymmetric crystals [21, 22, 23, 24, 25, 26]. A tunability of the Rashba coefficient α, parametrizing the strength of the interaction, is hence highly important.

This work intends to contribute to the understanding of the spin-orbit coupling within the two-dimensional hole gas (2DHG) systems of InAs-based quantum well heterostructures. We particularly explore the tunability of the Rashba parameter α in manganese-doped $In_{0.75}Al_{0.25}As/In_{0.75}Ga_{0.25}As/InAs$ QW heterostructures by both the variation of the concentration of the p-type doping and external electric gating, hence varying an effective internal Rashba magnetic field. In these studies, the strength of the SOI is probed by its distinct influence on 2D transport phenomena of quantum interference that manifest in low-field corrections to the longitudinal Drude magnetoresistivity. From the emerging rich hole density spectrum of these quantum corrections in low-temperature magnetotransport experiments on Hall bar devices, the characteristic spin- and phase-relaxation times of the 2DHG system are extracted and information on the valence subband spin splitting as well as on the tuning of the Rashba parameter is presented. As the doping concentration and 2D hole density are significantly reduced, localizing effects of disorder start to dominate the diffusive 2D transport replacing signatures of pronounced hole-hole interaction.

In the course of these transport experiments, a reproducible phenomenon of remarkable robustness emerged in the transverse Hall magnetoresistivity of these indium 2DHG systems: High-In compound heterostructures are epitaxially realized on GaAs substrates with the use of an $In_xAl_{1-x}As$ step-graded metamorphic buffer layer system to compensate the crystal lattice mismatch. As a consequence of the strain relaxation process, these material systems are characterized by anisotropic properties along different crystallographic directions. We identify an offset phenomenon in the zero-field Hall magnetoresistance in directions other than the distinct orientations of the anisotropic system that is being accompanied by an overshooting signature in the quantum Hall regime. An experimental materials study and theoretical considerations demonstrate these phenomena to be of universal interest in anisotropic systems.

1.2 The structure of this work

The composition of this thesis starts in Chapter 2 with the introduction of the theoretical concepts fundamental to the experiments on 2D hole systems, focussing on the effects of 2D Drude magnetotransport in a magnetic field and on the SOI in 2D hole systems as well as the associated mechanism of spin relaxation.
Chapter 3 then provides the technological background to the molecular beam epitaxial growth process of III-V semiconductor heterocrystals and the methods of their subsequent structural and magnetotransport characterization in the low-temperature experiments of this work. An optimized and reliable growth process of high-In alloys on a GaAs substrate via the incorporation of a step-graded metamorphic buffer layer concept is addressed in Chapter 4 by structural investigations and by magnetotransport measurements on 2DEG systems in undoped QW structures. On the basis of these epitaxial studies, this work's $In_{0.75}Al_{0.25}As/In_{0.75}Ga_{0.25}As/InAs$ QW heterostructures with manganese (Mn) modulation doping are composed and explored in 2D hole magnetotransport in the following.
Anisotropic morphological and magnetotransport characteristics along different crystallographic directions of the high-In 2D carrier system are featured in Chapter 5. We present anomalies that occur in the classical and quantum Hall resistivities regarding crystallographic orientations, which we analyze extensively both experimentally and theoretically.
The main part of this thesis, Chapter 6, then discusses the tunability of the Rashba spin-orbit interaction of 2DHGs in disordered InAs:Mn QW heterostructures by investigating a significant hole density spectrum of quantum interference signatures. From the characteristics of the longitudinal magnetoresistivity in a high-density regime, corrections due to hole-hole interaction are identified and the anisotropic effective hole masses of the system are carefully extracted. Fitting the weak antilocalization feature by theory yields the characteristic dephasing and spin-orbit scattering times that are evaluated on their gate- and temperature-dependences, respectively. As the system is transferred into a low-density regime characterized by insulating effects of localization, a combined hole density evolution of the energy spin splitting and of the Rashba parameter can be given.
Chapter 7 adds aspects of strong localization from exchange coupling in highly diluted magnetic InAs:Mn QW systems where a low concentration of magnetic Mn^{2+}-ions is placed in the vicinity of the 2D hole gas.
Chapter 8 concludes the experimental results achieved and discusses perspectives of the material system.
Supplementary information on the fabrication of samples and their basic experimental characterization is provided in Appendices A and B, respectively.

2 Theoretical concepts

This chapter is designed to be the backbone of theoretical concepts relevant in this study, particularly for 2D hole magnetotransport in low-dimensional III-V semiconductor systems. The First part features an introduction to the basics of diffusive transport in a magnetic field and certain magnetoresistive phenomena therein, while the second half focusses on the nature and properties of the valence band structure of 2D hole systems in the presence of spin-orbit interaction.
Specific theoretical background to the effects discussed is additionally provided in each corresponding experimental section along with brief reviews of associated historic experimental and theoretical preliminary works.

2.1 Magnetotransport in two-dimensional systems

The emerging success of molecular beam epitaxy (MBE) has enabled the atomically precise composition of layered semiconductor heterosystems where the energy band structure can effectively be tailored to create low-dimensional carrier systems. Magnetotransport of carriers in these potential environments has consequently been triggering the discovery and understanding of important quantum phenomena like the quantum Hall effect and the localizing effects of quantum interference that are presented in the following sections.

2.1.1 The two-dimensional carrier gas

A two-dimensional gas of charge carriers, electrons or holes, is created by confining their motional degree of freedom in one direction (z-direction) leaving the carriers

to move freely perpendicular to it in the plane spanned by the other two directions (defined as x- and y-direction). Band engineering of heterostructures forms a confinement potential, usually in growth direction z, either at the interface of two semiconductor materials of different energy band gaps, or by embedding a low-band-gap material into a semiconductor of wider energy gap creating the quantum well formation (e.g. InAs or GaAs compounds in between InAlAs or AlGaAs, respectively). When only the lowest state of quantized energy subbands is occupied at low temperatures, the system is regarded to be effectively two-dimensional.

For the motion in the x-y-plane the dispersion relation in these heterostructures is parabolic, with

$$E_{n,\mathbf{k}} = E_n + \frac{\hbar^2 \mathbf{k}_\parallel^2}{2m^*}, \tag{2.1}$$

where $\mathbf{k}_\parallel = (k_x, k_y)$ denotes the in-plane wave vector and m^* is the constant effective mass of carriers. Each state $(n, \mathbf{k})$ is described by an envelope wave function $\psi_{n,\mathbf{k}}(x, y, z) = \chi_n(z)\, e^{i(k_x x + k_y y)}$ with a function χ_n characterizing the quantization in z-direction and plane Bloch waves of the free in-plane motion of carriers [10]. It follows from a parabolic dispersion that the 2D density of states $\mathcal{D}_{2D}$ for each subband n is constant as a function of the energy,

$$\mathcal{D}_{2D}(E) = \frac{g_s g_v m^*}{2\pi\hbar^2}. \tag{2.2}$$

Here, the degree of spin degeneracy is $g_s = 2$ in both GaAs heterostructures and e.g. Si MOSFETs[1], and g_v represents the valley degeneracy of conduction band minima, which is $g_v = 1$ in GaAs heterosystems. For two-dimensional hole gas systems, however, the dispersion relation is non-parabolic at higher values of $\mathbf{k}_\parallel$ leading to an energy-dependent effective hole mass and a density of states that is constant only in first approximation.
In the quantum limit of one occupied quantized subband at low temperatures, only states at the Fermi energy are contributing to the two-dimensional transport with a sheet density of the carrier gas $n_s = \mathcal{D}_{2D} \cdot E_F$. The Fermi energy E_F is thus given as

$$E_F = \frac{\hbar^2 \pi}{m^*} \cdot n_s, \tag{2.3}$$

with the corresponding states in k space being occupied up to the Fermi wavenumber

$$k_F = \sqrt{\frac{2m^* E_F}{\hbar^2}} = \sqrt{\frac{4\pi n_s}{g_s g_v}}, \tag{2.4}$$

defined via the dispersion relation.

[1] Metal–oxide–semiconductor field-effect transistor

2.1.2 2D Drude transport in a magnetic field

At small magnetic fields where quantum effects are still negligible, two-dimensional transport of carriers is well described in the framework of the Drude theory [27, 10]. Here, the system is treated as a gas of free carriers scattering elastically by lattice atoms or other carriers within a mean transport scattering time τ_{tr}. Accelerated by an electric field $\mathbf{E}$ in between collision events, carriers have gained a mean, so-called drift velocity $\mathbf{v}_D$ in steady state. In a magnetic field $\mathbf{B}$, perpendicular to the 2D motion, carriers of charge $|e|$ are deflected by the Lorentz force, such that in steady state the equation of motion reads

$$\frac{m^*}{\tau_{tr}}\mathbf{v}_D = |e|\left(\mathbf{E} + \mathbf{v}_D \times \mathbf{B}\right). \tag{2.5}$$

At $B = 0\,\mathrm{T}$, the characteristic mobility μ of the system can be derived as the proportionality constant that couples the drift velocity $\mathbf{v}_D$ of carriers and the electric field $\mathbf{E}$ as

$$\mu = \frac{|e|\tau_{tr}}{m^*}, \tag{2.6}$$

determined by the mean transport scattering time τ_{tr} between two collisions. The resulting current density $\mathbf{j}$ is then calculated from the drift velocity by

$$\mathbf{j} = \sigma\mathbf{E} = |e|n_s\mu\mathbf{E} = |e|n_s\mathbf{v}_D, \tag{2.7}$$

with the electrical conductivity σ connecting $\mathbf{j}$ and $\mathbf{E}$.

The Hall effect

Applying a finite magnetic field in z-direction perpendicular to the x-y-plane of the two-dimensional carrier gas, the conductivity σ of Ohm's law (2.7) transforms into a 2×2 tensor, hence

$$\begin{pmatrix} j_x \\ j_y \end{pmatrix} = \begin{pmatrix} \sigma_{xx} & \sigma_{xy} \\ \sigma_{yx} & \sigma_{yy} \end{pmatrix} \cdot \begin{pmatrix} E_x \\ E_y \end{pmatrix}. \tag{2.8}$$

For reasons of the symmetry in isotropic systems, $\sigma_{xx} = \sigma_{yy}$ and $\sigma_{xy} = -\sigma_{yx}$ applies for the components of the conductivity tensor $\boldsymbol{\sigma}$. From tensor inversion the components of the isotropic tensor of the specific resistivity $\boldsymbol{\rho} = \boldsymbol{\sigma}^{-1}$ eventually yield

$$\rho_{xx} = \rho_{yy} = \frac{\sigma_{xx}}{\sigma_{xx}^2 + \sigma_{xy}^2} = \frac{m^*}{n_s e^2 \tau_{tr}}, \tag{2.9}$$

$$\rho_{xy} = -\rho_{yx} = \frac{\sigma_{xy}}{\sigma_{xx}^2 + \sigma_{xy}^2} = \frac{B}{|e|n_s}. \tag{2.10}$$

While the longitudinal resistivity component ρ_{xx} is constant, independent of B, yet determined by the characteristic scattering times limiting the mobility of the system,

the Hall resistivity ρ_{xy} is a linear function of the magnetic field. On the basis of these considerations, the system's essential properties of sheet carrier density n_s and mobility μ can thus be derived from Equations (2.9) and (2.10) by

$$en_s = \left(d\rho_{xy}/dB|_{B=0}\right)^{-1}, \tag{2.11}$$

$$\mu = en_s\rho_{xx}\,(B=0)\,. \tag{2.12}$$

These characteristic indicators for the quality of the 2D carrier system are typically acquired from low-temperature magnetotransport experiments at low **B** on samples patterned in a so-called Hall bar (HB) geometry as depicted in Fig. 2.1. This device layout guarantees the correct measurement of the Hall resistivity, $\rho_{xy} = \frac{U_H}{I} = R_H$, along the y-direction, precisely perpendicular to the direction of the longitudinal resistivity, $\rho_{xx} = \frac{U}{I}\frac{W}{L} = R_{xx}\frac{W}{L}$, along the x-direction of the current flow. The factor W/L of width W and length L accounts for the geometry of the Hall bar. Equipotential lines in Figure 2.1 normal to the electric field vector **E** visualize the

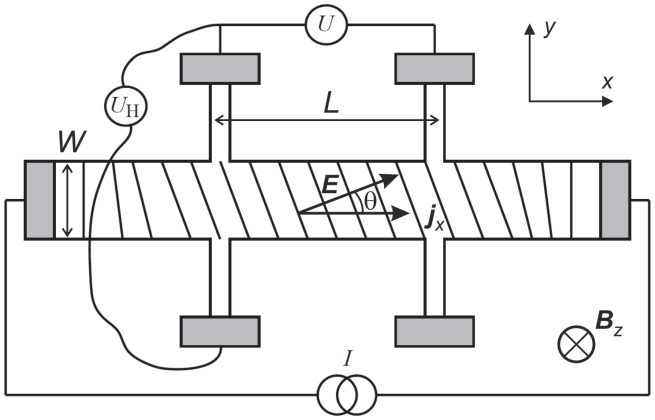

Figure 2.1: *Scheme of a standard Hall bar geometry of width W and length L used for transport measurements in a magnetic field, featuring the equipotential lines normal to the direction of* **E** *that visualize the origin of the classical Hall voltage U_H, adapted from* [10].

generation of the Hall voltage U_H, with the directions of the current density vector **j** and of **E** enclosing the Hall angle θ, which becomes zero as $B \to 0$ T obeying $\tan\theta = \mu B$.

The two-dimensional carrier system is validly described by the classical Drude model of conductivity only for weak magnetic fields where $\omega_c\tau_{tr} \ll 1$, with the time scale of the cyclotron frequency $\omega_c = eB/m^*$ competing with τ_{tr}, the transport scattering time.

2.1.3 Quantum Hall effect

For higher magnetic fields $\mu B = \omega_c\tau_{tr} > 1$, the constant density of states at zero magnetic field, Eq. (2.2), condenses into a series of Landau levels (LL), δ-peaks equally separated in energy by $\hbar\omega_c$, as a result of the Bohr-Sommerfeld quantization of self-interfering carriers. In real systems, these peak levels experience a Lorentzian-type of broadening into bands due to scattering by impurities. Landau levels are

highly degenerate with the number of states per unit area $N_L = eBg_s/h$ depending on the magnetic field: as the field increases, the separation of LLs grows, leading to a reduction of the number of increasingly degenerate LLs below the Fermi energy, which is expressed by the filling factor

$$\nu = \frac{n_s}{N_L} = \frac{n_s h}{eBg_s}. \tag{2.13}$$

Here, the two spin levels of states spin-up and spin-down, are regarded as separated energy levels. At high magnetic fields, the spin degeneracy of each Landau level is lifted by the Zeeman energy $g^*\mu_B B$, where g^* is the effective g-factor and μ_B is the Bohr magneton, such that the degree of spin degeneracy is $g_s = 1$.

In magnetotransport experiments on 2D carrier systems, Landau quantization manifests in the magnetoresistive phenomena of Shubnikov-de Haas (SdH) oscillations in the trace of ρ_{xx} (see Sec. 2.1.4) and the integer quantum Hall effect (QHE) in ρ_{xy}. Figure 2.2 demonstrates exemplarily that the transverse Hall resistance is

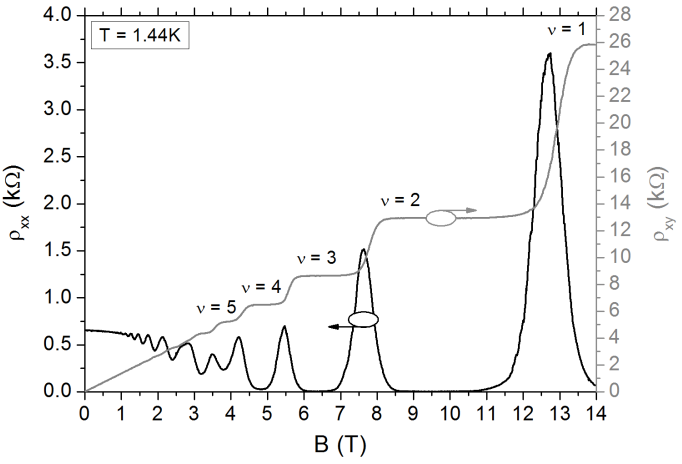

Figure 2.2: *Exemplary magnetotransport measurement of a 2DHG at low temperature, which, as a consequence of Landau level formation, exhibits Shubnikov-de Haas oscillations in the longitudinal resistivity $\rho_{xx}(B)$ as well as quantum Hall plateaus at integer filling factors in the transverse resistivity $\rho_{xy}(B)$ at higher magnetic fields.*

characterized by sharp plateaus in $\rho_{xy}(B)$ at higher magnetic fields, independent of the material or sample geometry, that appear precisely at resistance values

$$\rho_{xy} = \frac{1}{\nu}\frac{h}{e^2} = \frac{1}{\nu} \cdot R_K, \qquad \nu \in \mathbb{N}, \tag{2.14}$$

with $R_K = h/e^2 = 25812.807\ \Omega$, the von-Klitzing constant [28], while $\rho_{xx}(B)$ experiences a minimum in magnitude.

The QHE can be explained in the framework of the Landauer-Büttiker formalism by the existence of states on the edges of a finitely sized sample. When the Fermi energy lies exactly in between two LLs via localized states within the sample, transport is carried solely along these one-dimensional edge channels, dissipationless and ballistically, in opposite directions along opposite edges of the structure. By this macroscopic separation of counterpropagating edge states, scattering from edge to

edge and backscattering of carriers is reduced, hence causing quantized plateaus in $\rho_{xy}(B)$ and a minimal or even zero $\rho_{xx}(B)$ at stronger magnetic fields.

More detailed reviews on the QHE are presented in e.g. [27] or [10]. In the following, the effect of SdH oscillations is discussed in order to provide the basic analytical tools to experimentally deduce important material parameters of this study.

2.1.4 Shubnikov-de Haas effect

In an increasing magnetic field, Shubnikov-de Haas oscillations in $\rho_{xx}(B)$ arise from the tuning of the increasingly quantized density of states of broadened Landau levels oscillating at the Fermi level. The minima and maxima of SdH oscillations are $1/B$-periodic with

$$\Delta\left(\frac{1}{B}\right) = \frac{g_s e}{n_s h}, \tag{2.15}$$

which can be employed in the experimental acquisition of the sheet carrier density.

If only one electric subband is occupied, the oscillating part of the magnetoresistance $\rho_{xx}(B)$ is described by Ando [29, 30] and Coleridge [31] *et al.* by

$$\frac{\Delta\rho_{xx}}{\rho_0} = 4\frac{\chi}{\sinh\chi}\exp\left(\frac{-\pi}{\omega_c\tau_q}\right)\cos\left(\frac{2\pi\epsilon}{\hbar\omega_c} - \pi\right), \tag{2.16}$$

with the temperature-dependent Dingle factor $\chi/\sinh\chi$, where $\chi = 2\pi^2 k_B T/(\hbar\omega_c)$, with the cyclotron frequency $\omega_c = eB/m^*$, the amplitude of the relative magnetoresistivity $\Delta\rho_{xx}(B) = (\rho_{xx}(B) - \rho_0)$, where ρ_0 is the resistivity at magnetic field $B = 0$ T, and $\epsilon = E_F - E_1$ representing the energy difference between the energies of the Fermi level and the first occupied subband.
Following Elhamri *et al.* [32] by approximating $\sinh\chi$ by $\exp\chi/2$, and considering that at the extrema of the SdH oscillations the cosine term is ± 1, yields a simplified Ando relation

$$\ln\left(\frac{A}{T}\right) \approx C_1 - \frac{2\pi^2 k_B m^*}{e\hbar B}T, \tag{2.17}$$

with the T-dependent SdH amplitude $A = \Delta\rho_{xx}/\rho_0$ and a T-independent term C_1. Fitting this modified Ando formula to a plot of $\ln(A/T)$ versus T, gives a linear slope from which the effective mass $m^*(B)$ for a fixed magnetic field B can be extracted. This procedure has been applied for the evaluation of the effective masses of 2DHGs in the InAs heterostructures of this thesis, see Section 6.2.2.
The B-dependent, exponential decay of the envelope function of the SdH oscillations is governed by the quantum scattering time τ_q in Eq. 2.16. This single particle lifetime τ_q differs from the classical Drude transport scattering time τ_{tr} in a way that in Boltzmann theory the scattering rate $1/\tau_{tr} = \int P(\theta)\, d\Omega$, with the quantum mechanic transition probability P from one particular momentum eigenstate to

another and the scattering angle θ, emphasizes the importance of large-angle scattering over small-angle scattering, whilst $1/\tau_q = \int P(\theta)(1-\cos\theta)\,d\Omega$ includes the total scattering events of the system [31]. The quantum scattering time therefore is a measure for the Lorentzian collision broadening of Landau levels with the FWHM[2] $\Gamma = \hbar/2\tau_q$ [10]. At a fixed temperature, τ_q can be derived from Eq. 2.16 from the linear slope of a Dingle plot [33, 32]

$$\ln\left(\frac{1}{4}\frac{\Delta\rho}{\rho_0}\frac{\sinh\chi}{\chi}\right) = C_2 - \left(\frac{\pi m^*}{e\tau_q}\right)\frac{1}{B}, \tag{2.18}$$

where C_2 is a non-oscillating term. Knowing the value of the effective mass, τ_q has been calculated from Eq. 2.18 to determine the Dingle ratio τ_{tr}/τ_q of scattering processes in InAs heterostructures, also to be found in Section 6.2.2.

The Drude theory considers quantum mechanical scattering by individual impurities. In the 1980s, however, scattering theories were developed that systematically incorporated the phase-coherent motion between multiple scattering events, describing the effects of quantum interference in diffusive systems, where scattering occurs on length scales that are small compared to the sample size [10].

2.1.5 Quantum interference in diffusive transport

In disordered metal and semiconductor systems, conduction charge carriers are scattered by defects or impurities. As illustrated in Fig. 2.3, multiple phase-coherent scattering events lead to constructive interference of two time-reversed partial waves travelling along the same closed trajectory but in opposite directions. This quantum mechanical effect of *weak localization* (WL) effectively enhances the backscattering probability of carriers leading to a quantum reduction of the conductance and an increase of the resistivity. A prerequisite for this interference effect is that the phase coherence length exceeds the elastic mean free path of the diffusive transport. In an external magnetic field B, the time-reversal symmetry is broken as the waves propagating along the two paths acquire a phase difference that suppresses constructive interference. Thus, a restoration of the original conductance without the quantum interference correction can be observed as a positive magnetoconductivity or a negative magnetoresistivity (NMR), respectively, forming a peak signature around $B = 0$ [34]. A more detailed view on the suppression of the WL by a magnetic field will be given in Section 6.4. In the presence of strong spin-orbit interaction (see Section 2.2), however, the phase-coherent backscattering probability is reduced. Spin dephasing of the two time-reversed partial waves leads to destructive spin interference which gives rise to an enhanced conductance. An external magnetic field again destroys the phase-coherent time-reversal symmetry, which appears as a positive magnetoresistive effect in form of a dip at low magnetic fields around $B = 0$.

[2]Full width at half maximum

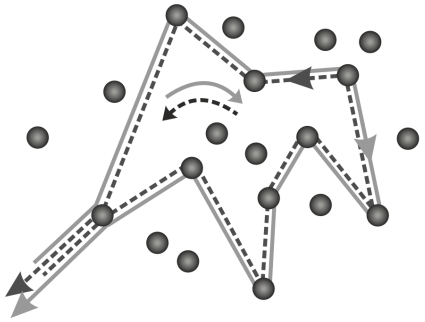

Figure 2.3: *Interfering partial waves experiencing multiple scattering events in a diffusive system as they propagate in opposite directions on a time-reversed trajectory.*

A qualitative approach to the understanding of this *weak antilocalization* (WAL) effect will be given following the reasoning of Bergmann [35] in [10]. A consequence of SOI is that spins are rotated by an effective magnetic field in between or during scattering events in a diffusive system (see Section 2.2.3). This way, a particular initial spin state $|s\rangle$ of a partial wave is transferred into a state $|s'\rangle = \mathcal{R}|s\rangle$ on the Bloch sphere where the rotation operator $\mathcal{R}$ is the product of subsequent infinitesimal rotations. The counterpropagating, time-reversed partial wave experiences the same subsequent rotations, but in reverse order and with inverted angles of the individual rotations. At the end of the trajectory the spin arrives at a final state $|s''\rangle = \tilde{\mathcal{R}}|s\rangle$ having performed a finite rotation $\tilde{\mathcal{R}} = \mathcal{R}^{-1}$. The contribution to the return probability of the interfering spin states of the two time-reversed paths is then given by the matrix element $\langle s''|s'\rangle = \langle s''|\mathcal{R}^2|s'\rangle$. In the case of negligible SOI essentially no spin rotation takes place and the expectation value of $\langle s''|s'\rangle$ is 1, thus resembling the enhanced backscattering probability of the weak localization. If, however, spin-orbit coupling is strong, the initial spin polarization gets completely randomized while scattering along the trajectory. Still, the complementary spin on the time-reversed path performs the exact opposite rotation and so the expectation value of the matrix element $\langle s''|s'\rangle$ yields an average interference contribution of $-1/2$ on averaging over many pairs of interfering time-reversed paths [35]. This concludes that strong SOI reduces the backscattering probability leading to weak antilocalization dominated by destructive interference.

The appearance of WAL therefore unambiguously marks the influence of spin-orbit coupling in a system, making this effect a suitable experimental tool for evaluating the strength of the interaction. In this work, this access to characteristic parameters of SOC is employed extensively in the investigation of quantum interference phenomena of 2DHGs in indium-based QW heterostructures in Section 6.2.3.

2.2 Spin-orbit coupling in two-dimensional systems

The spin and the orbital motion of a carrier interact via spin-orbit coupling. Due to relativistic Lorentz transformation, an electron that moves in the strong Coulomb

potential of an atom or crystal lattice at rest will experience the effective electric field $\mathbf{E} = -(1/q)\nabla V_0$ as an effective magnetic field in its own rest frame. In lowest order of v/c, the magnetic field $\mathbf{B}' = -(1/c^2)\,\mathbf{v}\times\mathbf{E}$ couples to the carrier's magnetic moment, the spin, via a Zeeman-type interaction[3]. The non-relativistic approximation to the relativistic Dirac equation then gives rise to the Pauli spin-orbit (SO) correction term to the Hamiltonian

$$\mathcal{H}_{SO} = -\frac{\hbar}{4m_0^2c^2}\,\boldsymbol{\sigma}\cdot\boldsymbol{p}\times(\nabla V_0)\,, \tag{2.19}$$

as the microscopic driving force for spin-orbit coupling effects [11]. Here $\hbar$ is the Planck's constant, m_0 is the free electron mass, $\boldsymbol{\sigma} = (\sigma_x, \sigma_y, \sigma_z)$ is the vector of the Pauli spin matrices, $\boldsymbol{p}$ is the momentum operator and V_0 represents the Coulomb potential.

The strength of the atomic SOI thus depends on the gradient of the potential, which is also true for the periodic potential in crystals. The potential gradient, in turn, is larger the higher the nuclear charge of the element, making SO effects more important with elements of higher atomic number. III-V semiconductors like gallium arsenide and in particular indium arsenide, as well as the elementary semiconductor germanium (Ge), therefore show stronger SO effects than e.g. silicon (Si) [10].
The effective electric field in the lattice-periodic potential of a three-dimensional crystalline solid on the other hand, will only be non-zero if the crystal lattice lacks a certain inversion symmetry. In binary III-V semiconductors manifesting in the zinc blende crystal structure, a fcc-type of lattice with a basis consisting of two different species of atoms, the so-called bulk inversion asymmetry (BIA) thus adds another contribution to the SOI as it originates from the ionic nature of these bulk compound materials, where microscopic electric fields are inverted when switching the anionic and cationic sites.

Spin-orbit interaction has a profound influence on the energy band structure, and, in addition, new SOC phenomena will appear in low-dimensional systems due to size quantization.

2.2.1 Energy band structure of III-V semiconductor compounds

The motion of carriers in crystalline solids is determined by energy bands $E_n(\mathbf{k})$ of band index n and the wave vector $\mathbf{k}$. The calculation of such band structures using pseudopotential methods is presented in Fig. 2.4 for III-V semiconductor compounds GaAs (a) and InAs (b). In both cases, in GaAs as in InAs, the valence band maximum (Γ_8^v) and the conduction band minimum (Γ_6^c) are at the Γ point, separated by a direct band gap energy of 1.52 eV in GaAs and only small 0.42 eV in InAs at low temperatures [37]. Due to the similarities in band and crystal parameters of binary

[3] c denotes the velocity of light in vacuum and primed variables refer to the electron rest frame.

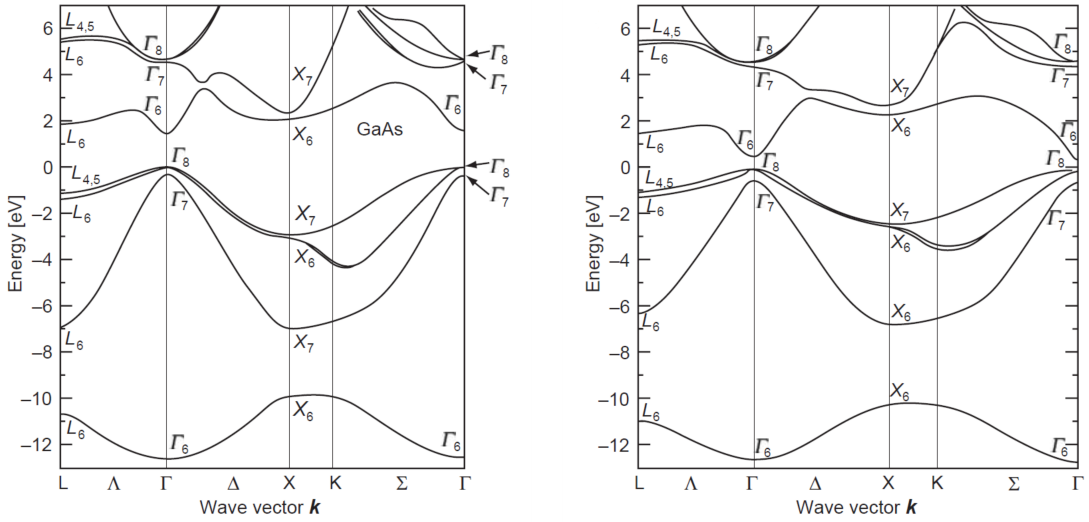

Figure 2.4: *Calculated band structures of the direct-band-gap III-V semiconductor compound materials* **(a)** *GaAs and* **(b)** *InAs applying pseudopotential methods including spin-orbit effects,* [36, 10].

compound III-V semiconductors, like GaAs, AlAs, InAs and GaSb, all crystallizing in the zinc blende structure, the theoretical aspects in the following apply for both systems.

Figure 2.5 (left) qualitatively illustrates the band structure of bulk GaAs around the Γ point. In a tight-binding picture the conduction band electronic states are described by s-like atomic orbitals with orbital angular momentum $l = 0$, whereas the states of the valence band have p-like symmetry with $l = 1$ [11, 38]. When taking into account the spin $s = 1/2$ (Fig. 2.5, middle), conduction band electron states have a total angular momentum $j = l + s = 1/2$, while atomic spin-orbit coupling splits the sixfold degeneracy of the p-type VB into a fourfold degenerate state of $j = 3/2$ and a twofold spin degenerate split-off band of $j = 1/2$. Here, this gap energy Δ_0 separating $j = 3/2$ and $j = 1/2$ VB states can serve as a measure of the strength of the Pauli SOI affecting the system. With $\Delta_0 = 341$ meV in GaAs and even 390 meV in InAs [37], compared to 44 meV in Si [10], it is another indication of the importance of SO effects in III-V hole systems. At an in-plane wave vector $\mathbf{k}_\parallel \neq 0$, the fourfold degenerate topmost VB state of effective spin $j = 3/2$ further splits into the so-called heavy hole (HH) and light hole (LH) degenerate pairs of states, characterized by z components of angular momenta $m_j = \pm 3/2$ and $m_j = \pm 1/2$, respectively. New phenomena of SOC effects arise in low-dimensional systems as depicted on the right of Fig. 2.5. Here, confinement along the axis z induces a size quantization that lifts the fourfold degeneracy of the HH and LH subbands even at $\mathbf{k}_\parallel = 0$. It should be noted that an additional source of subband

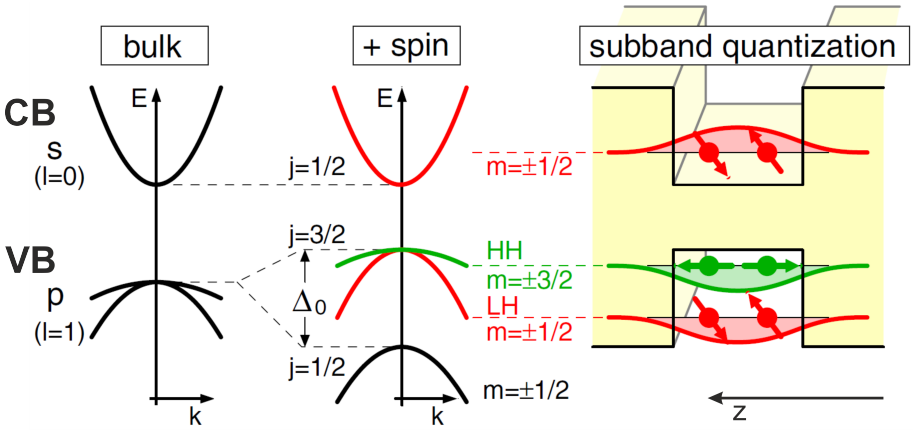

Figure 2.5: *Qualitative sketch of the band structure of bulk GaAs in the vicinity of the Γ point at* $\mathbf{k}_{\|} = 0$. *(Left) An energy gap separates the s-like conduction band (CB) from the p-like valence band (VB). (Middle) Spin-orbit interaction lifts the sixfold degeneracy of the VB separating* $j = 3/2$ *and* $j = 1/2$ *states by the split-off gap* Δ_0. *(Right) In 2D systems size quantization lifts the fourfold degenerate* $j = 3/2$ *VB subband states generating a HH-LH splitting even at* $\mathbf{k}_{\|} = 0$ *with a spin quantization axis perpendicular to the 2D plane,* [38].

quantization may arise by strain applied to the bulk crystal.
As designated, 'heavy' and 'light' hole states have large and small effective hole masses, respectively, regarding the bound motion perpendicular to the plane of the 2D system. For the in-plane motion, however, the so-called mass inversion occurs where the HH subband is characterized by a smaller in-plane effective mass than the LH subband. This leads to an anticrossing of the strongly bound HH states' steep dispersion relation and of the flat dispersion of the weakly bound LH subband states at finite $\mathbf{k}_{\|}$ as a result of HH-LH mixing (Fig. 2.6).

In 2DHG systems of typical hole densities of $p \approx 10^{11}$ cm^{-2}, the Fermi energy level lies between the topmost LH and HH subbands, which is why in the quantum limit at

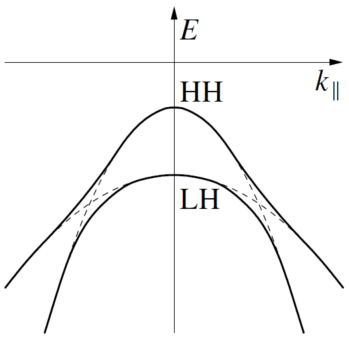

Figure 2.6: *Split HH and LH dispersion relations* $E(\mathbf{k}_{\|})$ *avoiding crossing at* $\mathbf{k}_{\|} \neq 0$, [11].

low temperatures generally only the HH subband is occupied [39, 10]. The effective masses of heavy holes in GaAs are listed as $m^*_{hh} = 0.51\,m_0$ and as $m^*_{hh} = 0.39\,m_0$ in InAs (for [001] growth direction), with m_0 being the free electron mass, thus by far exceeding the CB effective electron masses of $m^*_e = 0.067\,m_0$ (GaAs) and $0.0239\,m_0$ (InAs) [40, 37, 41]. Winkler argues in [11] that, since a remarkable symmetry in the analytical expressions for SO coupling terms of electrons and holes is found, SO coupling effects for both particle states are, in principle, also of the same order of magnitude. SO coupling energies of electrons and holes then are to be compared in relation to their kinetic energies, which therefore suggests that hole systems, having the greater effective mass, are more subject to the influence of SOI than electron systems.

In addition, it needs to be considered that, while electrons in the CB of bulk semiconductors and 2D systems have an almost isotropic and parabolic dispersion $E(\mathbf{k})$, the energy dispersions of HH and LH hole states are highly anisotropic and non-parabolic depending on the direction of the wave vector $\mathbf{k}$ and its magnitude. As illustrated in Fig. 2.7 (a) these 'warped spheres' of the Fermi surface characterize the effective hole mass to be an anisotropic parameter, and the values above only to be regarded as estimates [42].

Figure 2.7 (b) exemplarily shows the numerical result of the calculation of the hole

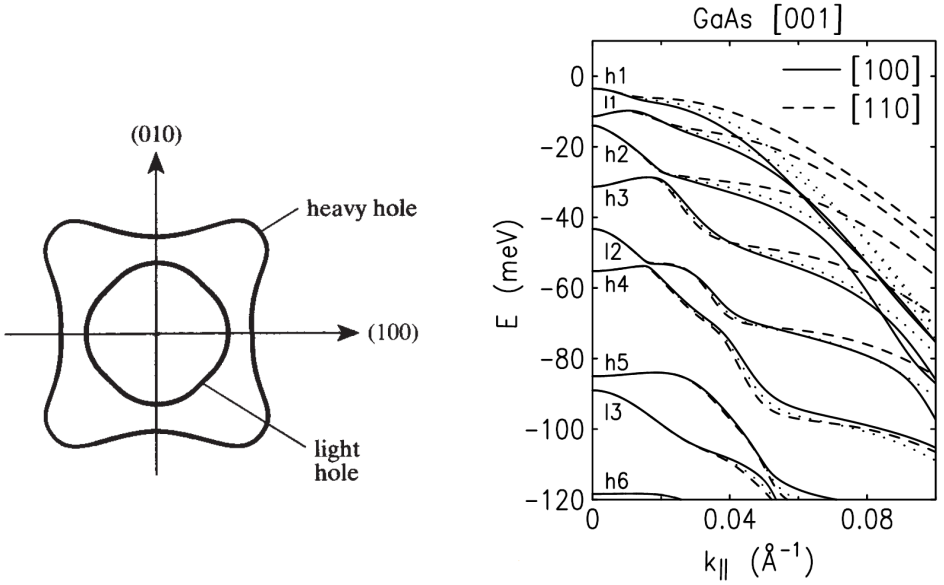

(a) **(b)**

Figure 2.7: (a) *The anisotropic Fermi contours of the spin-split 2D hole subband dispersion,* [42]*, and* **(b)** *the calculated anisotropic hole subband dispersion* $E(\mathbf{k}_{\|})$ *in* [100] *and* [110] *crystallographic directions of a* 150 *Å wide* $GaAs/Al_{0.3}Ga_{0.7}As$ *QW in* [001] *growth direction,* [11]*. Dotted lines represent the axial approximation.*

subband dispersion $E(\mathbf{k}_\parallel)$ for a GaAs QW in [001] growth direction based on a 8×8 $\boldsymbol{k}\cdot\boldsymbol{p}$ Hamiltonian from reference [11], where also further information on the calculation can be found. It should be noted that for the high-symmetry crystallographic growth directions [001] and [111] the hole subband states at $\mathbf{k}_\parallel = 0$ are pure HH and LH states (if small k-linear terms coupling HH and LH states are neglected), other than for low-symmetry directions [113] and [110] where weak mixing of HH-LH eigenstates occurs [43, 38].

Having established the influence of SOI and confinement on the band structure, in particular on the VB structure, other important SO coupling phenomena can be distinguished in a two-dimensional system, particularly a 2D hole system, also within a given subband. The next section will introduce these so-called Dresselhaus and Rashba SO phenomena, with the focus on the latter.

2.2.2 Spin splitting of 2D hole systems

Spin degeneracy of the carrier energies, $E_\uparrow(\mathbf{k}) = E_\downarrow(\mathbf{k})$, in a periodic solid-state system at $B = 0$ is a combined effect of space inversion symmetry, $E_\uparrow(\mathbf{k}) = E_\uparrow(-\mathbf{k})$, and time inversion symmetry, $E_\uparrow(\mathbf{k}) = E_\downarrow(-\mathbf{k})$, according to the Kramers degeneracy theorem. Here, $\mathbf{k}$ is the wave vector and arrows $\uparrow,\downarrow$ represent the projection of spin-up and spin-down states, respectively. Space inversion asymmetry, however, lifts this degeneracy even in the absence of an external magnetic field and splits the energy dispersion into two branches, $E_\uparrow(\mathbf{k})$ and $E_\downarrow(\mathbf{k})$. In a 2D system, this breaking of the spatial symmetry can be caused either by bulk inversion asymmetry of the underlying crystal structure or by structure inversion asymmetry (SIA) of a confining potential. Additionally, low atomic symmetry of heterointerfaces can contribute to the zero-field spin splitting [11].

In the non-centrosymmetric zinc blende lattice structure of III-V binary compounds, like GaAs, InAs and InSb, the well known BIA contribution to the spin splitting, often referred to as the Dresselhaus term in the Hamiltonian [44], is essentially a fixed materials property. While the BIA spin splitting of the conduction band is characterized by a bulk Dresselhaus term with cubic symmetry of the wave vector $\mathbf{k}$, the Dresselhaus term of 2D electron gases exhibits a linear dependence in the lowest order of $\mathbf{k}$ [10].

The SIA-induced spin splitting in quantum structures, on the other hand, can be tuned by the confining potential $V(\mathbf{r})$ causing a spatial inversion asymmetry that is characterized by an effective electric field $\boldsymbol{\mathcal{E}}$. This potential may consist of a built-in potential or an external potential. Since both options can be addressed experimentally by the tailored epitaxy of heterostructures or by external gating, respectively, the SIA SO coupling is in the heart of interest with respect to the application in future spintronic devices (see the Introduction 1.1). Honoring the fundamental theoretical works of Bychkov and Rashba [1], the spin splitting due to SIA is commonly referred to as the Bychkov-Rashba or simply Rashba SO splitting. In lowest order of $\mathbf{k}$, the Rashba term of the SIA spin splitting of CB electron states

induced by the effective electric field $\boldsymbol{\mathcal{E}} = (0, 0, \mathcal{E}_z)$ is expressed as

$$\mathcal{H}_R^e = \alpha \mathcal{E}_z \mathrm{i} \left(k_- \sigma_+ - k_+ \sigma_- \right), \tag{2.20}$$

where $\sigma_\pm = \frac{1}{2}(\sigma_x \pm \mathrm{i}\sigma_y)$ are the Pauli spin matrices and $k_\pm = \frac{1}{2}(k_x \pm \mathrm{i}k_y)$, with k_x, k_y denoting the components of the in-plane wave vector $\mathbf{k}_\parallel$. The Rashba coefficient α is a prefactor that depends on the material [38].

In case of the Rashba model for the valence band, however, the situation is rather different. Following symmetry hierarchy arguments in [11], the quantization axis due to size quantization (as the usually dominant effect) of hole states of orbital quantum number $l = 1$ and effective spin $j = 3/2$ is enforced along the direction of growth, perpendicular to the 2D plane. As already discussed, size quantization separates the HH states with a z component of the angular momentum $m_j = \pm 3/2$ from the LH states along this quantization axis in energy. Generally, the effective Hamiltonian of the SOI tends to orient the spin vector in the plane of the 2D system. Yet, since there can only be one quantization axis in the system, this effect has to compete with the energy quantization of the HH-LH splitting along the growth direction. This constitutes that for HH subband states of $m_j = \pm 3/2$ Rashba SO splitting at $B = 0$ is a higher order correction, unlike for LH subband states of $m_j = \pm 1/2$ or CB electrons of $l = 1/2$ which are not affected by subband quantization [11]. Therefore, the spin splitting of HH subbands due to Rashba SIA is considered to be cubic in k and, in contrast, k-linear in case of LH subbands [45], similar to CB electrons described by Eq. (2.20). It was shown that k-linear splitting of the HH states is dominated by BIA, however, it is negligible for typical hole densities [43].
The Hamiltonian of the cubic Rashba SO splitting of a HH subband is then described by

$$\mathcal{H}_R^{HH} = \alpha^h \mathcal{E}_z \mathrm{i} \left(k_+^3 \sigma_- - k_-^3 \sigma_+ \right), \tag{2.21}$$

where the effective electric field $\mathcal{E}_z = ep/(2\epsilon\epsilon_0)$ is proportional to the density p [38, 11], with ϵ and ϵ_0 denoting the dielectric permittivity and the vacuum permittivity, respectively. This relation implies that modulation of $\mathcal{E}_z$, and thus of the Rashba SOI, is accessible via the hole density p. The density, in turn, can be tuned externally by a metallic gate or *in-situ* by variation of the concentration or spacer width of an asymmetric modulation doping.

In contrast to electron systems where the Rashba coefficient is material-specific and independent of the geometry of the 2D system, third order perturbation theory yields a Rashba coefficient of

$$\alpha^h = \frac{e\hbar^4}{m_0^2} a \gamma_3 \left(\gamma_2 + \gamma_3 \right) \left[\frac{1}{\Delta_{11}^{hl}} \left(\frac{1}{\Delta_{12}^{hl}} - \frac{1}{\Delta_{12}^{hh}} \right) + \frac{1}{\Delta_{12}^{hl} \Delta_{12}^{hh}} \right], \tag{2.22}$$

for the first HH subband, with e.g. $a = 64/(9\pi^2)$ for an infinitely deep, rectangular QW grown in [001] [38, 11]. In this expression, γ_2 and γ_3 are the material-dependent

Luttinger parameters and the splitting $\Delta^{\nu\nu'}_{\lambda\lambda'} = E^{\nu}_{\lambda} - E^{\nu'}_{\lambda'}$ with E^{h}_{λ} and E^{l}_{λ} being the energies of the λth HH and LH subbands, respectively. It is apparent from Eq. (2.22) that the Rashba spin splitting of a HH system not only depends on the effective electric field $\mathcal{E}_z$ but also on the separation of the HH and LH subband states thus illustrating the fact that in 2DHG systems SO coupling effects are always competing with HH-LH splitting [11].
As it is convenient, numerical results of the Rashba SOI are often represented by the effective Rashba coefficient $\alpha^h\mathcal{E}_z$ [39]. With a cubic spin-split HH subband dispersion of $E_{\pm}\left(\mathbf{k}_{\parallel}\right) = \langle\mu_h\rangle\,\mathbf{k}_{\parallel}^2 \pm \left\langle\alpha^h\mathcal{E}_z\right\rangle\mathbf{k}_{\parallel}^3$[4] in the lowest order of $\mathbf{k}_{\parallel}$, where μ_h (times $2/\hbar^2$) describes the reciprocal effective hole mass, the effective cubic Rashba coefficient is

$$\left\langle\alpha^h\mathcal{E}_z\right\rangle = \sqrt{\frac{2}{\pi}}\,\langle\mu_h\rangle\,\frac{p\,(\tilde{p}_+ - \tilde{p}_-) + \Delta p\,(\tilde{p}_+ + \tilde{p}_-)}{6p^2 + 2\Delta p^2}, \tag{2.23}$$

with $\tilde{p}_{\pm} = \sqrt{p \pm \Delta p}$. This illustrates that, since the branches of the dispersion relations differ, a spin-split HH subband could effectively be regarded as a two subband system having different subband densities $p_{\pm}$ with opposite spin orientations $\pm 3/2$.

An exemplary self-consistent numerical calculation of the energy dispersion $E\left(\mathbf{k}_{\parallel}\right)$ of the HH subband by Winkler [43, 11] is demonstrated in the lower part of Fig. 2.8 for a [001] grown $GaAs/Al_{0.40}Ga_{0.5}As$ heterostructure with a total density of $p = 2 \times 10^{11}$ cm^{-2}. Here, the calculation was performed fully taking into account both SIA *and* BIA terms. As a result, lines of different style demonstrate that

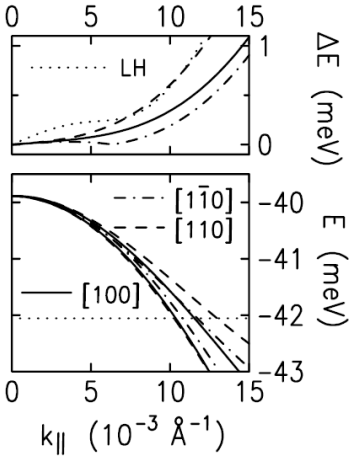

Figure 2.8: *Self-consistent calculation based on a* 14×14 *extended Kane model of (lower part) the anisotropic energy dispersion* $E_{\pm}\left(\mathbf{k}_{\parallel}\right)$ *and (upper part) the spin splitting* $\Delta E = E_{+}\left(\mathbf{k}_{\parallel}\right) - E_{-}\left(\mathbf{k}_{\parallel}\right)$ *of the topmost HH subband of a* $GaAs/Al_{0.40}Ga_{0.5}As$ *heterostructure grown in* [001] *direction with a total density of* $p = 2 \times 10^{11}$ cm^{-2}. *Lines of different style refer to different directions of the wave vector* $\mathbf{k}_{\parallel}$ *and the dotted line in* $E_{\pm}\left(\mathbf{k}_{\parallel}\right)$ *indicates the position of the Fermi level, whereas the dotted line in* $\Delta E\left(\mathbf{k}_{\parallel}\right)$ *traces the LH subband splitting,* [43].

the dispersion $E\left(\mathbf{k}_{\parallel}\right)$ reveals a distinct anisotropy of $\Delta\mathbf{k}_{\parallel}$ for different directions of $\mathbf{k}_{\parallel}$ at the Fermi level (dotted line). The corresponding HH spin splitting $\Delta E\left(\mathbf{k}_{\parallel}\right)$ in the upper part of Fig. 2.8 reflects this anisotropy. It is found that the splitting is highest along [110] and lowest along [1$\bar{1}$0] with the [100] direction following an

[4] Angular brackets indicate averaging over position-dependent quantities in the calculation [39].

intermediate level. Note, however, that the sign of the electric field $\mathcal{E}_z$ is not defined unambiguously in [43]. In general, the HH energy splitting, being only small in magnitude at low $\mathbf{k}_\parallel$, is basically dominated by the $\mathbf{k}_\parallel^3$ proportionality at larger $\mathbf{k}_\parallel$. Unlike that, the splitting of the LH subband is linear for low $\mathbf{k}_\parallel$ and of higher order only for larger $\mathbf{k}_\parallel$ because of HH-LH mixing and an increasing non-parabolicity of bands in the latter case.

Figure 2.9 presents the spin-split Fermi contours of a 2DHG considering again both SIA and BIA (of unequal strength) as well as the combined effective magnetic SO field $\boldsymbol{\mathcal{B}}_{SO}\left(\mathbf{k}_\parallel\right)$, as calculated by Dollinger in [46]. Combining BIA and SIA

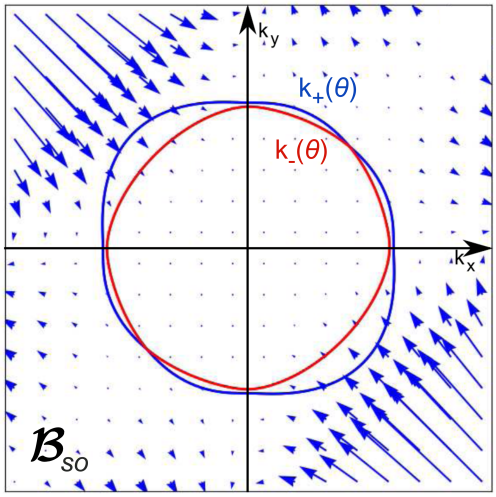

Figure 2.9: *Fermi contours for different spin directions and corresponding effective SO field of a spin-split 2DHG according to the model of Dollinger taking into account unequal BIA and SIA. Blue and red contours $k_\pm(\theta)$ indicate the angular anisotropy of the two subband spin species. Blue arrows illustrate the momentum-dependent orientation and strength of the SO field $\boldsymbol{\mathcal{B}}_{SO}\left(\mathbf{k}_\parallel\right)$,* [46].

terms, considering both cubic in $\mathbf{k}_\parallel$ contributions being dominant, yields an angular spin splitting for the HH subband of

$$E_+\left(\mathbf{k}_\parallel\right) - E_-\left(\mathbf{k}_\parallel\right) = 2k_\parallel^3\sqrt{\alpha^2+\beta^2-2\alpha\beta\sin\left(2\theta\right)}, \tag{2.24}$$

where $\alpha = \left\langle \alpha^h \mathcal{E}_z \right\rangle$ denotes the effective Rashba and β the Dresselhaus coefficient [47, 11]. The interplay of Rashba and Dresselhaus effects reduces the fourfold symmetry pattern of the HH contours of constant energy in the plane of $\mathbf{k}_\parallel = (k_x, k_y) = \left(k_\parallel\cos\theta, k_\parallel\sin\theta\right)$ (see also Fig. 2.7 (a)) to a twofold symmetry with the main axes in [110] and [1$\bar{1}$0] direction. In turn, the symmetry axis of this twofold symmetry and, as a consequence, the angular anisotropy of the splitting, depends on the sign of the product $\alpha\beta$ in Eq. (2.24) [48]. This implies, since the Dresselhaus parameter β is a fixed material constant, that the symmetry of the SOI anisotropy may be inverted via a tuning of the effective Rashba potential. Experimentally, this has been demonstrated for the interfering Rashba and Dresselhaus SOI of GaAs 2DEGs in [49] or at the interfaces of Fe/GaAs/Au heterojunctions in [50]. Here, in Fig. 2.9, $\Delta k_\parallel = k_+ - k_-$, with the subscripts $+/-$ assigned to the upper and lower energy branch of the spin-split dispersion, respectively, is highest along [$\bar{1}$10], intermediate along [100] and minimal in [110] direction. Since $\Delta k_\parallel$ can be expressed in terms of

the Rashba parameter α as the characteristic energy length scale $(2m^*\alpha)/\hbar^2$ (for parabolic dispersions) [7, 51, 11], it can be regarded as a reflection of the anisotropy of the energy splitting.
Spin-orbit interaction of a spin in a certain state $\mathbf{k}_\parallel$ is induced by an effective $\mathbf{k}_\parallel$-dependent magnetic field $\boldsymbol{\mathcal{B}}_{SO}(\mathbf{k}_\parallel)$ which is aligned parallel with the orientation of the spin expectation value $\langle\mathbf{S}\rangle$ in the k_x-k_y-plane. In Fig. 2.9 the strength of this effective magnetic SO field $\boldsymbol{\mathcal{B}}_{SO} = \langle\mathbf{S}\rangle\Delta k_\parallel$ is represented through the dimensions of its arrows. Thus, in some $k_\parallel$ regions of $\boldsymbol{\mathcal{B}}_{SO}$ the vectorial interference of BIA and SIA contributions is additive while in others it can lead to a decrease of the spin splitting [11].

Figures 2.8 and 2.9 have shown that the subtle, anisotropic effects of SOI on the spin splitting of the energy subband structure of 2D hole systems arising from inversion asymmetry can be quantified either by ΔE at a fixed wave vector $\mathbf{k}_\parallel$ or by $\Delta k_\parallel$ at a given energy E. The latter quantity $\Delta k_\parallel$ will particularly be of importance in spin-dependent scattering processes leading to spin relaxation, which will be highlighted briefly in the next section.

In the end, it should be noted that strain may also have a significant impact on the energy band structure. For 2DHGs in strained QWs for instance, the order of the topmost HH and LH subbands can be reversed generating a spin splitting linear in $\mathbf{k}_\parallel$ [52]. For more information on the effects of strain on the SO coupling of 2D electron and hole systems the reader is referred to the detailed descriptions in [53] and [54].

2.2.3 Spin relaxation

In a system which is characterized by energy spin splitting due to a strong SO coupling, spin relaxation is affected by the effective magnetic SO field $\boldsymbol{\mathcal{B}}_{SO}$ that depends on the wave vector $\mathbf{k}$. In a more intuitive picture, this relativistic field may be viewed as a close resemblance to a Zeeman field. Breaking of the time inversion symmetry by an external magnetic field $\mathbf{B}$ causes a finite energy spin splitting $\Delta E = g^*\mu_B\mathbf{B}$ that is referred to as the Zeeman spin splitting, with the effective g-factor g^* and the Bohr magneton μ_B [11]. In close analogy to the Zeeman Hamiltonian $\mathcal{H}^z_{6c} = \frac{1}{2}g^*\mu_B\mathbf{B}\cdot\boldsymbol{\sigma}$ for a spin-1/2 electron of the Γ^c_6 conduction band, the Rashba SO Hamiltonian of a 2D electron system (2.20) can be rewritten in the form

$$\mathcal{H}^e_R = \frac{1}{2}\boldsymbol{\mathcal{B}}_{SO}(\mathbf{k})\cdot\boldsymbol{\sigma}, \tag{2.25}$$

with the internal effective magnetic field $\boldsymbol{\mathcal{B}}_{SO} = 2\alpha\mathcal{E}_z(k_y, -k_x, 0)$ [38].
The spin of a carrier in a certain momentum state $\mathbf{k}$ is subject to this $\mathbf{k}$-dependent effective SO magnetic field $\boldsymbol{\mathcal{B}}_{SO}$ and will precess about its axis with an average frequency $\langle\boldsymbol{\Omega}_{SO}\rangle$, given by $\boldsymbol{\Omega}_{SO} \equiv \boldsymbol{\mathcal{B}}_{SO}/\hbar$ [38]. Upon scattering into another momentum state $\mathbf{k}'$ on the Fermi surface, the spin precession will be characterized by a different rotation axis defined by an effective field $\boldsymbol{\mathcal{B}}_{SO}(\mathbf{k}')$ of different orienta-

tion and magnitude. In between two scattering events, the effective magnetic field $\boldsymbol{\mathcal{B}}_{SO}$ is regarded to be constant and the spin will precess about an angle $\langle \boldsymbol{\Omega}_{SO} \rangle \cdot \tau_p$ for the effective elastic momentum scattering time τ_p. In the diffusive limit, when the momentum scattering time is shorter than the time for a full precession cycle, i.e. $\langle \boldsymbol{\Omega}_{SO} \rangle \cdot \tau_p \ll 1$, the spin orientation performs a random walk of successive small fractional cycles on the Bloch sphere and will eventually have lost its initial direction after a large number of random scattering events. By this important spin relaxation mechanism, the *D'yakonov-Perel'* mechanism (DP) [55], the spin polarization decays with a rate that is proportional to the momentum scattering time, namely

$$\tau_{SO}^{-1} \propto \langle \boldsymbol{\Omega}_{SO}^2 \rangle \cdot \tau_p, \tag{2.26}$$

where the characteristic time τ_{SO} scales the randomization of the spin direction due to SOI.
The DP mechanism is considered to be the major spin-dependent scattering mechanism in inversion asymmetric III-V semiconductor compounds and their corresponding low-dimensional heterostructures[5] [10, 3]. Relation (2.26) illustrates the counterintuitive fact that in disordered systems, where $\langle \boldsymbol{\Omega}_{SO} \rangle \cdot \tau_p \ll 1$, the larger scattering rate results in a decrease of the spin relaxation, hence a longer spin lifetime τ_{SO}, analogous to the effect of motional narrowing. With the scattering rate being high in the diffusive regime, the angle of precession remains small before the next momentum scattering so that the initial spin orientation is conserved over numerous scattering events. As the spin splitting $\Delta k_{\|}$ has been found to differ in systems characterized by both BIA and SIA in the previous section, spin relaxation due to the DP mechanism may also be anisotropic in different crystallographic directions.

The analogy to a Zeeman field which was used to describe the effective magnetic SO field of the electronic spin splitting more instructively, however, does not hold for hole systems. Winkler has shown that, strictly speaking, SOI for hole systems of angular momentum $j = 3/2$ cannot be written in terms of an effective Zeeman field and that spin precession for hole systems qualitatively differs as being understood as a non-trivial periodic motion in spin space [38]. In general, SO coupling is more important in the energy spectrum of the valence band, and spin orientation is lost faster, often disappearing with τ_{SO} on the scale of τ_p. The relation $\langle \boldsymbol{\Omega}_{SO} \rangle \cdot \tau_p \ll 1$ so holds less frequently than for electrons in experimentally accessible systems. Still, it was discussed that in the strong momentum scattering regime ($\langle \boldsymbol{\Omega}_{SO} \rangle \cdot \tau_p \ll 1$) the overall situation is similar to electron spin relaxation and the same random walk model of the DP mechanism can be adapted [56].

It should be noted that the elastic collisions, determining the total effective momentum relaxation time τ_p which governs the motional narrowing effect of the DP mechanism, may be a result of carrier transport scattering by impurities and phonons ($\tau_{tr} = \mu m^*/e$) as well as of electron-electron (e-e) or hole-hole (h-h) scattering not

[5] With exception of narrow-gap materials exhibiting a huge separation of the topmost VB and the SO split-off band, as in InSb, where EY mechanism dominates (see below).

affecting the mobility [57], hence, $\tau_p^{-1} = \tau_{tr}^{-1} + \tau_{e-e,h-h}^{-1}$, respectively. The latter e-e scattering in particular has been shown to dominate the DP mechanism in n-type zinc blende semiconductors of high density and high mobility 2DEGs at elevated temperatures, $T \gg T_F$, with τ_{tr} being the dominant time scale below the Fermi temperature T_F [58].

While the DP mechanism does not alter the spin orientation during an elastic scattering event, the *Elliott-Yafet* mechanism (EY) [59, 60] exactly describes the occurrence of spin-flip during momentum scattering by impurities or phonons due to the coupling of spin eigenstates. Complementary to the DP effect, the spin orientation is then preserved in between scattering events instead. Thus, the spin-orbit scattering rate increases with an increasing momentum scattering rate, and hence, the linear proportionality here is $\tau_{SO}^{-1} \propto \tau_p^{-1}$, unlike for the DP mechanism.

At last, two other spin-dependent scattering mechanisms of minor importance in zinc blende semiconductors shall be named briefly: The *Bir-Aronov-Pikus* mechanism is relevant in p-doped semiconductors where electron-hole exchange interaction creates fluctuating local magnetic fields that lead to spin relaxation. And, for completeness, *hyperfine interaction* causes spin relaxation of carriers in semiconductor crystal lattices whose atomic nuclei possess a non-zero magnetic moment that induces spin randomization upon scattering. A detailed review of all discussed spin-dependent scattering mechanisms is provided by [3].

3 Experimental methods

The novel indium-based III-V heteromaterials of this project have been created by molecular beam epitaxial crystal growth. This chapter is designed to introduce the technical features of the growth process as well as the experimental methods of structural and physical characterization of III-V semiconductor material samples for low-temperature magnetotransport experiments.

3.1 Molecular beam epitaxy

In semiconductor research, crystalline heterostructures of high quality are realized by molecular beam epitaxy, since this process technique provides sharp interfaces of atomic monolayer-precision as well as exact doping profiles. High-purity materials are evaporated or sublimated from heated Knudsen-type effusion cells into an UHV[1] environment that contains a manipulator stage mounting the heated wafer substrate. Impinging molecular beams interact with this heated crystalline substrate material as the adsorbed atoms diffuse on the flat substrate surface, form two-dimensional clusters or re-evaporate. Incorporation of atoms on energetically favorable lattice sites then takes place at lattice steps or after migration along these steps at a kink in Frank-van der Merwe step growth mode forming semiconductor films monolayer by monolayer. In this regime, the growth kinetics of III-V semiconductors are determined by the three temperatures of the substrate temperature lying in between the evaporation temperatures of the group-III and group-V materials. III-V crystal growth at the characteristically small growth rates of MBE is typically performed

[1] Ultra-high vacuum at a typical base pressure below 10^{-11} mbar to ensure low concentrations of residual background impurities in the growth chamber

at a beam flux ratio V/III $\gg 1$, effectively being controlled by the flux of group-III atoms and hence the temperature of the source-III material at an abundance of arsenic. Pneumatically triggered tantalum shutters at the openings of the effusion cells provide the abrupt regulation of molecular beam fluxes, with the simultaneous opening of two group-III cells enabling the epitaxy of ternary III-V semiconductor materials.

The spintronic MBE system

The molecular beam epitaxy of all III-V heterostructure systems of this project was realized in a modified Veeco GEN II solid-source MBE system, the so-called spintronic chamber C. The spintronic MBE system is part of the Regensburg MBE

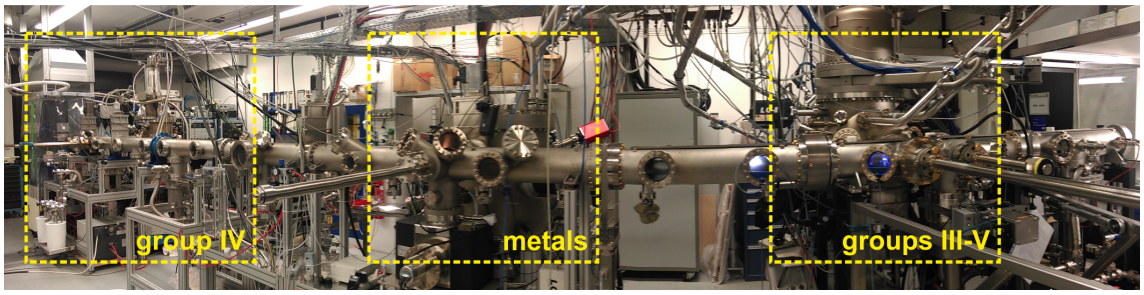

Figure 3.1: *Panoramic view of the Regensburg MBE cluster currently featuring, from right to left, the III-V spintronic chamber, the metals chamber and the group-IV SiGe chamber, all connected by an UHV transfer channel.*

cluster facility of the Bougeard Group, see Fig. 3.1, which currently consists of the III-V spintronic chamber, the metals chamber managed by the Back Group and the group-IV SiGe chamber. All three chambers are connected via an UHV transfer channel at their integrated buffering and loading chambers to enable wafer substrate exchange in between growth chambers without breaking the vacuum for high-purity hybrid metal/semiconductor heterostructures. For the growth of III-V semiconductor compound heterostructures, the spintronic chamber is equipped with a number of solid-source effusion cells that store the high-purity materials in conical pyrolytic boron nitride crucibles. In addition to the group-III indium cell, two gallium cells and an aluminium cell, as well as the group-V arsenic valved cracker cell, also subliming manganese effusion and silicon or carbon filament cells are integrated for p- and n-type doping. Details on filament and effusion cell architectures are presented in e.g. [61, 62, 63]. Providing uniformly good thermal contact, liquid gallium fixes the 2-inch GaAs substrate wafers (here, GaAs crystals grown in (100) orientation) on tantalum holders which are mounted on a manipulator heater inside the chamber after several degassing steps. During growth, continuous azimuthal rotation of the substrate manipulator at a standard speed of 7 rpm maximizes the homogeneity of epitaxial films and minimizes material gradients across the wafer that originate

from the asymmetric spatial arrangement of the effusion cell ports in the system. A so-called beam flux ionization gauge is installed on the back side of the manipulator to determine the beam equivalent pressures (BEP) of material flux ratios when rotated to face the effusion cells, yielding e.g. a maximum $\mathrm{BEP_{As}} \approx 1 \times 10^{-5}$ Torr for arsenic. The manipulator is housed inside liquid-nitrogen-cooled cryopanels that line the main chamber walls absorbing the arsenic pressure during growth and, together with a cryogenic pump, providing a background pressure below 10^{-11} mbar. An auxiliary titanium sublimation pump supports an optimum UHV by the pumping of hydrogen gas. The substrate temperature T_S is measured via the intensity of infrared radiation by engaging an Ircon-2000 pyrometer for $T_S \gtrsim 400$ °C or an Impac IP120 pyrometer sensitive for $T_S \approx 300 - 400$ °C. Below $T_S \approx 300$ °C, the commercial Bandit system may be used to perform pyrometry via band edge spectroscopy as established in [63].
As an important instrument for *in-situ* monitoring and characterization of the growth status of crystalline films, a RHEED[2] gun together with a photoluminescent detector screen are implemented in the MBE chamber. RHEED is a highly surface-sensitive method due to the very small angle of grazing incidence of the high-energy electron beam (accelerated at 15 kV) interfering at the sample surface. A comprehensive survey of the diffraction patterns characteristic for various stages of growth surfaces is listed in [63]. By digitally recording and analyzing the periodic intensity oscillations of the specular beam reflection, which occur during the completion of monolayer by monolayer growth, the growth rates are deduced. The calibration of GaAs and AlAs growth rates $\mathcal{R}_{\mathrm{GaAs}}$ and $\mathcal{R}_{\mathrm{AlAs}}$, respectively, is conducted prior to each sample growth session using a dedicated RHEED sample[3] to accommodate small day-to-day fluctuations of the beam fluxes at constant cell temperatures.

In this work, high-quality crystalline layers of GaAs-based compound heterosystems have been realized at a growth rate of $\mathcal{R}_{\mathrm{GaAs}} \approx 2.83$ Å/s, substrate temperatures of $T_S \approx 620$ °C and arsenic-rich conditions of a $\mathrm{BEP_{As}} \approx 0.6 - 1 \times 10^{-5}$ Torr. For In-containing ternary alloys the substrate temperature needs to be lowered to $T_S < 500$ °C to enhance the incorporation of indium atoms and avoid clustering or island formation. Further information on the growth process of In heterostructures will be provided in the next Chapter 4.

Indium cell calibration

In the fabrication of the main high-In ternary alloys of this project, which are based on a step-graded $\mathrm{In}_x\mathrm{Al}_{1-x}\mathrm{As}$ buffer system of increasing In content x (see Chapter 4), a calibration of the InAs growth rate $\mathcal{R}_{\mathrm{InAs}}$ is essential. Here, the In flux was calibrated by monitoring RHEED oscillations from again the standard GaAs RHEED sample, since monolayer-smooth InAs substrates are demanding in surface

[2]Reflection high-energy electron diffraction
[3]An approximately $4 \times 4\ \mathrm{mm}^2$ piece of smooth GaAs wafer material

preparation for RHEED observation and rather costly. The determination of the InAs growth rate is achieved by comparing the AlAs growth rate and an $In_xAl_{1-x}As$ growth rate with a small In fraction x at a certain temperature of the In effusion cell, hence $\mathcal{R}_{\mathrm{InAs}} = \mathcal{R}_{\mathrm{InAlAs}} - \mathcal{R}_{\mathrm{AlAs}}$. At $T_S = 430\,^{\circ}\mathrm{C}$, first the AlAs growth rate is deduced from RHEED oscillations before the InAlAs growth rate is recorded when opening the In cell. Despite the occurring lattice mismatch from the incorporation of indium, the growth of thin $In_xAl_{1-x}As$ compound layers proceeds pseudomorphically as the In fraction remains small. In between the RHEED calibration steps of $\mathcal{R}_{\mathrm{InAs}}$, the sample surface is smoothed by growing AlGaAs/GaAs superlattice layers at $T_S \gtrsim 620\,^{\circ}\mathrm{C}$. As this procedure is rather time consuming, the flux calibration of the In cell is performed in regular extended time intervals or after major maintenance operations at the MBE system. Figure 3.2 documents two sets of $\mathcal{R}_{\mathrm{InAs}}$ calibrations at various In cell temperatures in the time period relevant for the growth of the In heterostructures of this thesis. The relative concurrence of the data points illustrates the stability of $\mathcal{R}_{\mathrm{InAs}}$ in time.

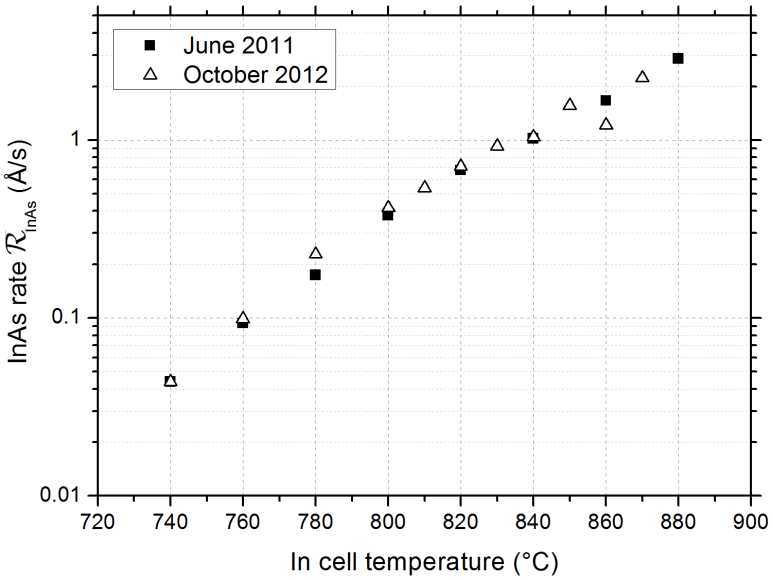

Figure 3.2: *Calibrations of the InAs growth rate $\mathcal{R}_{\mathrm{InAs}}$ in the growth period relevant for the In-containing heterosystems of this thesis demonstrating the stability of the performance of the indium cell.*

In general, very small growth rates $\mathcal{R}_{\mathrm{InAs}}$ could also be calibrated by observing the formation of strain-induced InAs quantum dots on (001) GaAs at a critical thickness of 1.65 - 1.85 monolayers of InAs provoking a significant transition in the RHEED pattern [64, 65].
A confirmation of the accuracy of the established method of $\mathcal{R}_{\mathrm{InAs}}$ determination is given by *ex-situ* structural characterization: The In concentration of the heterosystem achieved can either be controlled by X-ray diffraction (XRD) or by Secondary ion mass spectroscopy (SIMS) analysis, which is also able to confirm grown layer

thicknesses, as it will be introduced briefly amongst other methods in the next section.

3.2 Characterizing the crystal

To ensure the specifications and quality of III-V epitaxial crystal growth, the following listed methods of structural characterization were engaged in the optimization of InAs-based heterosystems.

Secondary ion mass spectroscopy

At the beginning of this work, secondary ion mass spectroscopy performed at Probion[4] labs yielded valuable information on the specific elemental composition and the intended layer thicknesses of the In heterostructure growth process. With this technique, a focussed primary ion beam of an energy ranging from 500 eV to 15 keV destructively sputters the surface of the specimen and ejects a fraction of ionized atoms from the sample. These secondary ions are collected by an extraction electrode and analyzed by mass spectrometry at the ion detector. A profilometer simultaneously provides a depth-resolved calibration of the system as the sputtering of the sample progresses. Quantification of the mass spectrometry results is possible by processing a variety of standards of known composition in the same run under identical experimental conditions. Depending on the required analysis, Cs^+-ions or O_2^+-ions are frequently used as primary ion species. In the given process, sputtering by primary Cs^+-ions and detection of secondary MCs^+-ions was engaged in the so-called MCs^+ mode to quantify the atomic concentration of the elements of interest M, namely In, Ga and Al, with the simultaneous monitoring of As. This method is supposed to show only small influence of the ternary matrix composition on the ionization rate producing a SIMS signal directly proportional to the depth-resolved concentration of single elements in the sample.

Transmission electron microscopy

Transmission electron microscopy (TEM) exploits the wave nature of high-energy electrons to image and analyze the crystal structure of semiconductor systems on a sub-Å atomic resolution. Electron plane waves with a small de Broglie wavelength interact with the atoms of the crystal lattice as they pass through ultra-thin sample specimens (around 100 nm in thickness). Complex processes of scattering and diffraction by the periodic atomic Coulomb potentials modulate the electron wave amplitude and phase generating a contrast information that is detected after

[4]Maurice Quillec, www.probion.fr, Bagneux, France

a system of objective apertures and lenses. In this thesis, TEM[5] imaging of heterostructure cross-sections provides information on the nature of dislocations in a step-graded metamorphic buffer system established for strain relaxation in high-In compounds, see Sec. 4.1. Details on TEM functionality and the applied methods of contrast generation are presented in [66].

Atomic force microscopy

The topography of the surface of the indium-based heterosystems of this thesis is screened by atomic force microscopy (AFM) in order to quantify characteristic morphological parameters like the surface roughness or possible dislocation defect densities.
The scanning movement of an oscillating cantilever's Si probe tip in close distance to the sample surface (tapping mode) is being mapped by a laser beam reflected from the back side of the cantilever tip. As the amplitude of the oscillation of the cantilever changes with the sample surface morphology, information on the topography is recorded by monitoring these deviations and hence keeping the mean relative distance of the oscillating tip to the surface constant by closing a feedback loop that maintains a constant oscillation amplitude. For our studies, a Veeco Dimension Icon atomic force microscope[6] with ScanAsyst was used for high-resolution imaging of 10×10 µm^2- or 20×20 µm^2-sized sample details with a common Si tip.

3.3 Low-temperature magnetotransport

Low-temperature electrical characterization and magnetotransport experiments on the grown heterosystems were conducted in cryogenic setups applying high external magnetic fields on different types of 2D transport devices.

Magnetotransport device design

A fast and convenient way to acquire information on the quality of established two-dimensional carrier systems is provided by samples in the van der Pauw (vdP) geometry as these require only little effort in preparation [67, 10]. Illustrated in Fig. 3.3 (a), up to eight alloyed InZn ohmic contacts[7] are placed in the corners and on the flats of typically 5×5 mm^2 quadratic wafer pieces. The sheet resistivity is deduced from the cyclic permutation of contacts according to the vdP method by automated four-terminal measurements at low temperatures. A more detailed description of the van

[5] FEI Tecnai F30 operating at 300 kV, Group of Prof. Dr. Zweck, University of Regensburg. All imaging of this thesis was realized by Florian Aumeier [66].
[6] Courtesy of the Chair of Prof. Dr. Weiss, University of Regensburg. All imaging was performed by Imke Gronwald.
[7] Recipes for alloyed n- and p-type InZn ohmic contacts are listed in Appendix A

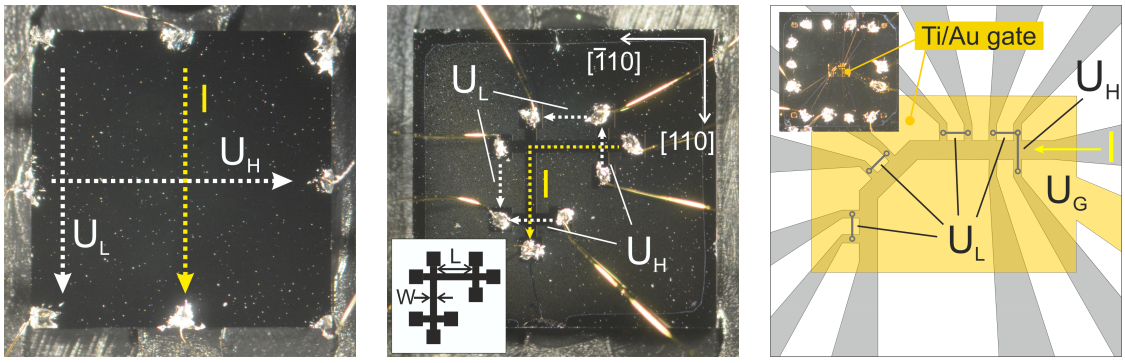

(a) (b) (c)

Figure 3.3: *Illustrations of samples fabricated in* **(a)** *the van der Pauw geometry and in form of* **(b)** *a regular L-shaped and of* **(c)** *the modified L-shaped Hall bar, featuring a Ti/Au gate electrode, with I denoting the applied current, U_H and U_L the measured Hall and longitudinal voltage, respectively, and U_G the gate potential.*

der Pauw procedure is given in Appendix B. In a Hall measurement configuration, as it is indicated in Fig. 3.3 (a), the sheet carrier density is then derived from the low-field slope of the Hall magnetoresistance by Eq. (2.11), with the sheet carrier mobility being acquired by Eq. (2.12) from the zero-field longitudinal resistance. Also, basic first 2D magnetoresistance characterizations in the quantum Hall regime have been performed in vdP geometry, see Appendix B, where typically no information on the crystallographic orientation of magnetotransport properties is recorded. For precise low-temperature magnetotransport measurements on well-defined structural premises along certain crystallographic orientations hence various mesoscopic Hall bar concepts were realized: Besides a regular straight Hall bar design (not shown), variations of L-shaped Hall bars were patterned by standard optical lithography and wet chemical etching (cf. Fig. 3.3 (b)) with their legs along distinguished orthogonal crystallographic directions, here [$\bar{1}$10] and [110]. For a detailed listing of the parameters of each processing step required, the reader is referred to the recipes in Appendix A. In order to determine magnetotransport properties along three different distinguished crystallographic directions simultaneously, e.g. [$\bar{1}$10], [100] and [110], also the modified L-shaped design illustrated in Fig. 3.3 (c) was frequently engaged. Here, the exemplary device in the inset of Figure 3.3 (c) features a golden metallic topgate electrode allowing the gate-induced variation of the sheet carrier density by the electric field effect. Details on the fabrication of Ti/Au gate electrodes above insulating layers of Al_2O_3 are found in Appendix A as well.
The dimensions of the Hall bars in width and length, W/L, are set to be either 200 µm/1000 µm for regular straight and L-shaped Hall bars (cf. Fig. 3.3 (b)) or 50 µm/50 µm for modified L-shaped devices (cf. Fig. 3.3 (c)). During the evaluation of magnetotransport properties, the corresponding geometrical factors W/L are considered whenever needed.

Cryogenic measurement setups

Low-temperature magnetotransport experiments on these devices were carried out in cryogenic measurement environments of variable temperature range and magnetic field strengths chosen according to the experimental requirements. A standard low-frequency lock-in technique at a reference frequency of 17 Hz was engaged with constant bias currents ranging from 10 nA up to 1 µA. Every sample provided with a topgate electrode was tested for current leakage across the insulating layers. Illumination by a red light emitting diode (LED) generating a persistent photoconductivity effect is possible in each setup.

^{4}He dewar

The majority of magnetotransport experiments of this study was conducted in a ^{4}He dewar cryostat setup, which allows a quick characterization of magnetotransport properties at $T = 4.2$ K and $T = 1.44$ K under external magnetic fields up to $B = 6$ T applied perpendicularly to the sample plane. As it is illustrated in Figure 3.4, a vacuum isolated magnetic rod mounting a superconducting magnet coil is lowered into the dewar vessel filled with liquid ^{4}He. Within the magnet rod, the sample rod is inserted, cooling the sample mount (see the right of Fig. 3.4 for a detailed view) inside the coil to a temperature of $T = 4.2$ K. By pumping on the interior ^{4}He volume of the magnet rod with a closed needle valve, connecting the sample volume inside the magnet rod to the ^{4}He reservoir, temperatures as low as $T = 1.44$ K can be reached. The temperature of the system is controlled by a diode temperature sensor in close vicinity to the sample.

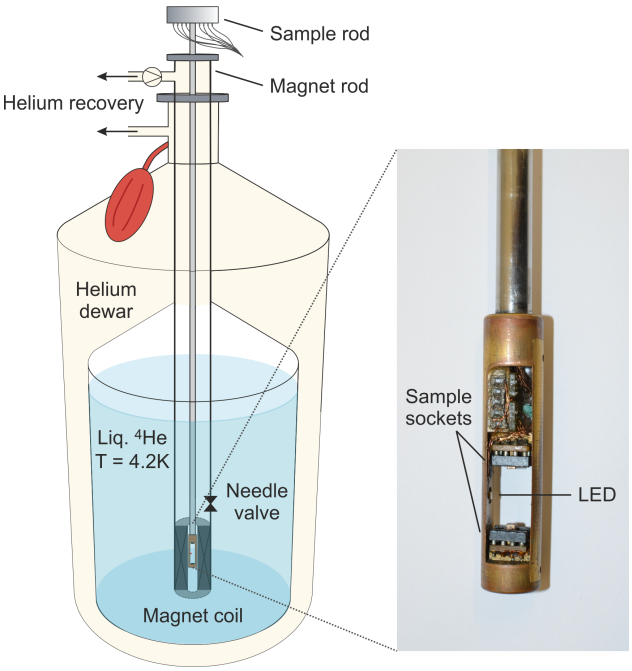

Figure 3.4: *Sketch of the ^{4}He dewar cryostat employed for magnetotransport experiments at temperatures of* 4.2 K *and* 1.44 K *featuring a detail view of the tip of the sample rod that mounts two sample sockets and the LED. The sample rod is inserted in a magnet rod which has been lowered into the liquid helium reservoir.*

^{3}He/^{4}He dilution refrigeration

Cryogenic temperatures in the mK-range are achieved in a dilution refrigeration system[8] that harnesses the unique properties of a mixture of liquid ^{4}He and ^{3}He. In a mixing chamber, the ^{3}He/^{4}He mixture separates into two phases below a temperature of 0.87 K: A lighter, concentrated ^{3}He phase and a heavier, diluted ^{4}He-rich mixed phase. The diluted phase contains 6.6% ^{3}He as the maximum soluble concentration of ^{3}He in ^{4}He, while above this concentration, two separate phases are energetically favorable. A cooling effect is generated by pumping ^{3}He via the still from the diluted phase at the bottom of the mixing chamber[9], leading ^{3}He to 'evaporate' from the concentrated phase into the diluted phase to maintain a constant concentration of diluted ^{3}He in the mixture. The energy of the change in enthalpy of ^{3}He required for this phase transition is retrieved thermally from the surroundings, effectively cooling the mixing system to a base temperature of about 15 mK. Figure 3.5 displays the principle of operation of a ^{3}He/^{4}He dilution refrigerator schematically. The insert of the ^{3}He/^{4}He circulation system housed in the inner vacuum chamber is itself placed in a ^{4}He reservoir inside the outer vacuum chamber where superconducting magnet coils enable magnetic fields up to 19 T, see the left of Fig. 3.5.

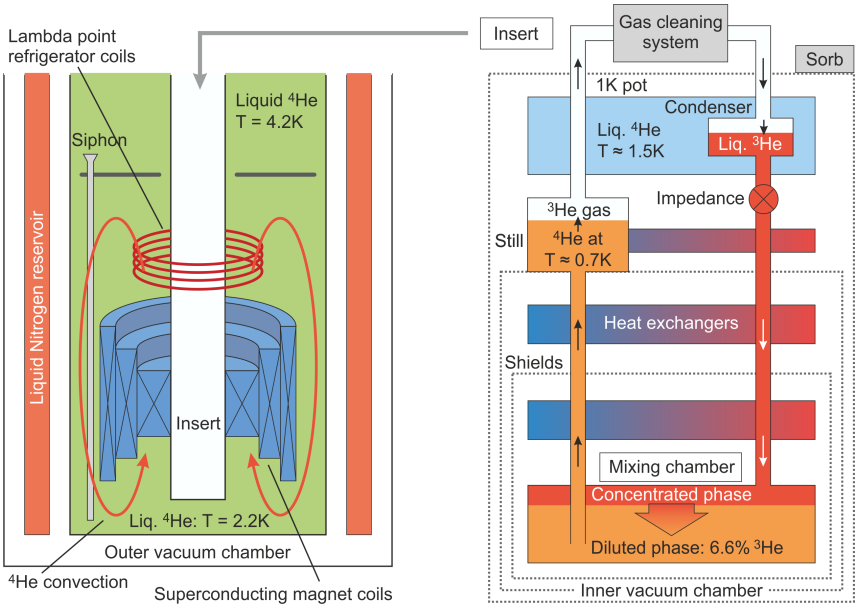

Figure 3.5: *Simplified scheme of the setup and operation mode of a toploading ^{3}He/^{4}He dilution refrigeration system realizing temperatures between* 1 K *and* 15 mK *as well as magnetic fields up to* 19 T.

[8] Toploading OXFORD KelvinoxTLM dilution refrigerator, Chair of Prof. Dr. Weiss, University of Regensburg

[9] Evaporation of ^{3}He in the still is enhanced due to a latent heat of ^{3}He three orders of magnitude smaller than of ^{4}He at $T \approx 0.7$ K.

4

Designing InAlAs/InGaAs/InAs QW heterostructures for 2D magnetotransport

Two-dimensional electron gas systems based on $In_xAl_{1-x}As/In_xGa_{1-x}As$ quantum wells, with or without an incorporated InAs channel well, have intensely been studied as these potentially offer superior properties for spin-dependent device application over the $Al_xGa_{1-x}As/GaAs$ material compound system: A strong intrinsic spin-orbit interaction, small effective electron masses and a particularly large bare g-factor (cf. Introduction 1.1). The majority of experiments on high-mobility 2DEGs in these indium heterosystems yet has been performed on the basis of the $In_{0.52}Al_{0.48}As/In_{0.53}Ga_{0.47}As$ system of fixed material alloy composition, since it can readily be grown epitaxially lattice-matched on the commercially available binary substrate InP [13, 68, 69, 15]. As this substrate, however, presets the final indium concentration in the active layers, it would be desirable to gain a higher flexibility in heterostructure alloy composition and thus a potential tunability of material parameters. It was found that an arbitrary final indium content x can be achieved in ternary alloys by employing a step-graded buffer layer system: The indium concentration is increased gradually in order to adapt the final high-In layers to a highly lattice-mismatched standard GaAs substrate [70, 71]. With the occurring strain being released during metamorphic buffer layer growth via the formation of dislocations buried deep beneath the active layers, the mobilities of 2D carrier systems are not degraded. Very high indium concentrations are ultimately enabled by this necessary buffer layer system, which also hold the benefits of minimizing alloy disorder scattering, highest for $x \lesssim 0.50$ [72], as well as of providing highly transmissive

metal-semiconductor interfaces in devices for $x \gtrsim 0.75$ [73].

4.1 Strain engineering by step-graded $In_xAl_{1-x}As$ buffer layer growth

With the lattice constant of InAs $a_{\mathrm{InAs}} = 6.0583$ Å distinctively exceeding $a_{\mathrm{GaAs}} = 5.65325$ Å of GaAs (at $T = 300$ K, [37]), high-In compositions on conventional GaAs substrates suffer from the strong lattice mismatch of a maximum $\Delta a \approx 6.7\%$. During growth, the in-plane lattice constants of a thin InAs film would so pseudomorphically adapt the lattice constant of the GaAs substrate, while its out-of-plane lattice constant expands in accommodation to the compressive strain. At a critical thickness, the epitaxial build-up of strain-induced elastic energy in the thin pseudomorphic film may relax by the formation of energetically more favorable crystal lattice defects. Typically, so-called misfit dislocations manifest in missing lattice (half-)planes confined in a plane parallel to the heterointerfaces. Depending on interactions within this distribution of misfit dislocations, so-called threading dislocations may arise along crystal lattice planes different from the plane of growth. Threading dislocations are thus particularly to be minimized as they degrade the mobility when penetrating the active epilayers where they act as scattering centers for free carriers in 2D systems.

To overcome the lattice mismatch of the given GaAs substrates to the aspired $In_{0.75}Al_{0.25}As/In_{0.75}Ga_{0.25}As$ QW heterosystems of this thesis, a step-graded buffer layer design of suitable indium gradient is employed, which acts to confine the dislocations from strain relaxation and so to provide the defect-free, lattice-matched new virtual substrate for an active QW region of high 2D carrier mobility. Our experiments on strain engineering are based on the buffer layer concepts established by Capotondi [74] and Ercolani [75] and colleagues.

Sketched schematically in the left of Fig. 4.1, the common composition of all buffered high-In heterostructures is as follows: The undoped semi-insulating GaAs (001) substrate wafer is covered by short-period $Al_{0.50}Ga_{0.50}As/GaAs$ superlattice (SL) layers of 5 nm each, repeated 10 times. The incorporation of this additional superlattice layer was demonstrated to be crucial to decrease the density of threading dislocations in the system, as it screens impurities located at the surface of the wafer substrate. These impurities prevent a gliding of nucleating dislocation threads during growth. The further threading dislocations are able to propagate unimpaired at the front of monolayer step flow growth towards the edges of the sample, the longer is the resulting extension of misfit dislocation segments and hence the degree of relaxation [76, 77].

Subsequent to the superlattice layers, strain and lateral lattice constants are gradually adapted during the metamorphic growth of 50 nm thick (above the critical thickness) $In_xAl_{1-x}As$ buffer layers with a slowly increasing indium content x. For

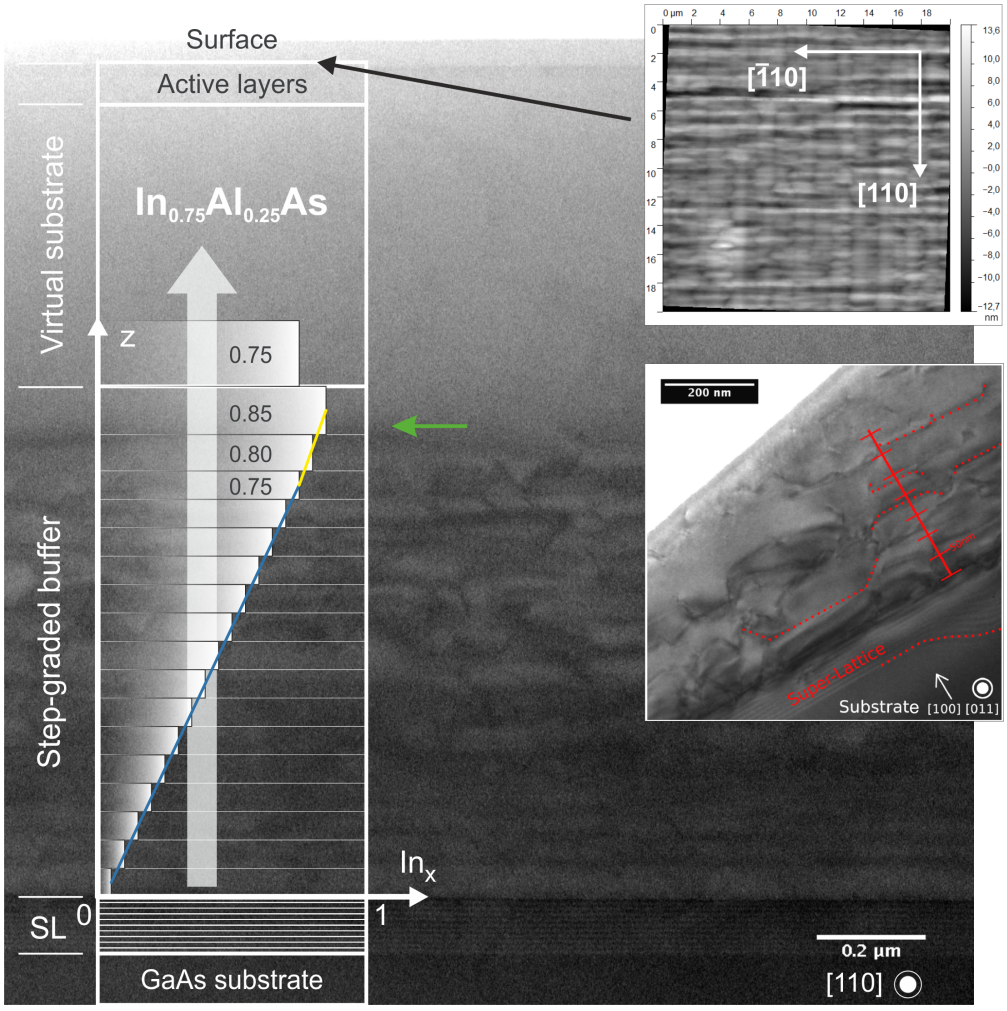

Figure 4.1: *Sketch of the metamorphic step-graded buffer layer design applied for lattice-matched growth of fully relaxed $In_{0.75}Al_{0.25}As/In_{0.75}Ga_{0.25}As/InAs$ heterosystems on a standard GaAs substrate. The indium fraction x is increased gradually from $x \approx 0.05$ to an overshooting $x = 0.85$ to accommodate to a lattice-matched $In_{0.75}Al_{0.25}As$ virtual substrate. A cross-sectional TEM image along the [110] crystallographic direction illustrates strain relaxation by the formation of in-plane misfit dislocations up to the last overshooting layers of the buffer sequence (green arrow). Red dotted lines in the center right figure mark the predominantly curved shape of the dislocation segments from contributions of 60° threading dislocations at their ends, from [66]. Within the cross-sectional detail of the main figure, the virtual substrate layers of constant composition and the active QW layers above are found to be completely defect-free. Still, the upper right AFM image of the surface of this In heterostructure reveals the asymmetric cross-hatching topography of undulations along the ⟨110⟩ directions, characteristic for these step-graded buffered systems.*

the growth of the In-containing buffer layer, the temperature was reduced from $T_S = 620\,°C$ during SL growth to $T_S = 360\,°C$ (330 °C at an earlier stage of our studies) to avoid the formation of three-dimensional islands [78]. With the Al rate being kept constant in the continuous growth of the $In_xAl_{1-x}As$ layers, the process is controlled by ramping the indium cell temperature stepwise. Therein, the indium concentration x is increased by $\Delta x = 0.05$ from a starting $x \approx 0.07$ up to the final indium content $x = 0.75$. In an advancement compared to a strictly linear step-graded design towards $x = 0.75$, additional control of a residual strain in the QW region is gained from a buffer layout incorporating extra, so-called overshooting steps of indium concentrations exceeding the nominally desired final indium fraction of $x = 0.75$ [79]. Residual strain is present in the last buffer layers, since the formation of plastic defects requires elastic energy, thus generating shorter lateral lattice constants than in the case of a fully unstrained system of the same desired nominal composition. Following the thorough quantitative studies on strain relaxation through generation of misfit dislocations by Capotondi *et al.* [80, 81], we adopt a step-graded $In_xAl_{1-x}As$ buffer layer sequence where the In content is increased linearly to a maximum indium concentration of $x = 0.85$. The gradient of 1%/10 nm below $x = 0.75$, blue line in Fig. 4.1, changes to a smaller gradient above $x = 0.75$, as indicated by the yellow line. Above the $x = 0.75$ step, the overshooting layers are slightly wider to take account of the finite time the indium cell needs to reach the thermal equilibrium required for the specific high-In compositions of the overshooting. The correctness of the In concentrations achieved within each compositional step and the thicknesses of individual steps of the buffer system were controlled by SIMS analysis. A $400 - 500$ nm thick $In_{0.75}Al_{0.25}As$ layer of constant composition of again $x = 0.75$ then provides the strain-relaxed virtual substrate for the various electrically active $In_{0.75}Al_{0.25}As/In_{0.75}Ga_{0.25}As/InAs$ QW layouts which host the two-dimensional carrier systems as introduced in the following sections.
In a series of samples with different maximum indium concentrations of the overshooting, we could consistently confirm good magnetotransport properties for a final overshooting of $x = 0.85$ (see also the next Section 4.2). This suggests a high degree of strain relaxation by the compensation of residual strain within this buffered system.

For an in-depth investigation on the structural process of strain relaxation through the incorporation of intentional defects, detailed transmission electron microscopy studies on the presented step-graded $In_xAl_{1-x}As$ buffer layout including an overshooting region were conducted by Aumeier[1] [66]. A representative cross-sectional bright field TEM image of the heterosystem along the [110] crystallographic direction is depicted as the background of the main Fig. 4.1 and also in the inset center right micrograph. As intended, strain induced by lattice mismatch is released via the formation of misfit dislocations which are mostly confined within the plane of

[1]Group of Prof. Dr. Zweck, University of Regensburg. Specifically imaging samples from wafers C120314B, C120314C and C120322A, cf. Appendix B.

growth, concentrated on the brink of the graded In concentration steps. The overall density of dislocations declines slightly in the upper overshooting layers of smaller gradient, hence reducing the interactions between misfit dislocations that generate threading nucleation. Applying the so-called weak beam dark field imaging technique, Aumeier was able to identify the nature of the threading dislocations, which are visible in between successive layers of misfit dislocation segments, as mostly 60°-dislocations [66]. Indicated by red dotted lines in the inset figure at the center right of Fig. 4.1, these 60°-dislocations add to the formation of overall curved shapes of dislocation segments [66]. Judging from the statistical TEM cross-section detail of the main Figure 4.1 in the [110] direction, misfit dislocations seize to appear within the overshooting layers (green arrow), leaving the constant $In_{0.75}Al_{0.25}As$ composition layer and the well separated active QW layers above free of defects and, on average, unstrained [73]. Additional TEM investigations along the [100] crystallographic direction (not shown) indicated defects extending about 20 nm wider up into the overshooting layers than in the [110] direction of Fig. 4.1 [66]. Differences in the extension of the defect-free region may originate from the known preferential elongation of misfit dislocations parallel to the $[\bar{1}10]$ direction. This may cause a small asymmetry in strain relaxation along the orthogonal $\langle 110 \rangle$ directions due to the anisotropic conditions for nucleation and propagation of dislocations [80].

In another structural characteristic common to all In-heterostructures based on the described step-graded buffer system, their surface reveals a striking anisotropic topography: A representative plan-view AFM image in the upper right of Fig. 4.1 illustrates that the surface is corrugated by $10 - 20$ nm deep trenches accurately aligned along the $\langle 110 \rangle$ crystallographic directions in a sort of *cross-hatching* pattern. The periodicity of undulations of this surface morphology along these directions is highly anisotropic: A periodicity of around $1 - 1.5$ µm along the $[\bar{1}10]$ crystallographic direction consistently exceeds a periodicity of $0.5 - 1$ µm along [110].
The dynamics of this phenomenon are still under discussion. It is suggested that lateral mass transport in the surface step flow during growth causes these undulations in order to eliminate steps from dislocations forming and gliding on {111} planes [82]. Most commonly, however, although the last layers of misfit dislocations are buried deep beneath the surface, the roots of this cross-hatching pattern are being attributed to an orthogonal network of misfit dislocations which forms along the $\langle 110 \rangle$ directions within the $In_xAl_{1-x}As$ step-graded buffer during strain relaxation [83, 76]. Spatial changes in the strain fields of these networks of dislocations may then lead to a locally modulated growth rate [84, 85]. The coexistence of a characteristic network of dislocations in the buffer and its imprint as a pattern of undulations on the surface then suggests that this asymmetric morphology also impacts the properties of the active QW layers in between.
A quantitative analysis of this anisotropic structural phenomenon and its profound influence on 2D magnetotransport are subject to detailed discussion in the next Chapter 5 of this thesis.

Having created a strain-relaxed and defect-free $In_{0.75}Al_{0.25}As$ substrate of high indium concentration, different designs of active QW heterosystems can now be realized for experiments on 2D carrier systems. In the following two sections, we introduce two sets of active layers: The first hosting 2DEGs in undoped InAs QW heterostructures, and the second generating 2DHGs from different manganese modulation doping concepts.

4.2 Heterostructure optimization by 2DEGs in undoped InAs QW systems

The process of establishing the optimal growth parameters for high-quality strain-relaxed buffer systems was evaluated, aside from methods of structural characterization, by measuring the low-temperature transport mobility of a two-dimensional electron gas readily emerging in completely undoped InAs QW heterostructures. The experimental parameter of a high 2DEG mobility lets us infer on the quality of unstrained active high-In-layers.

For the generation of these 2D electron systems without any intentional n-type doping, a special property of the $In_{0.75}Al_{0.25}As/In_{0.75}Ga_{0.25}As$ heterosystem is utilized: the ionization of deep-level donor states within the energy band offset of the $In_{0.75}Al_{0.25}As/In_{0.75}Ga_{0.25}As$ heterojunction [78]. By deep-level photo-induced current transient spectroscopy on an unintentionally doped $In_{0.75}Al_{0.25}As$ bulk sample as a reference, Capotondi *et al.* [78] could verify that charge carrier transfer into the $In_{0.75}Ga_{0.25}As$ quantum well takes place from deep donor levels identified as lying within the conduction energy band discontinuity of $In_{0.75}Al_{0.25}As/In_{0.75}Ga_{0.25}As$ at an activation energy of $0.12 - 0.17$ eV below the $In_{0.75}Al_{0.25}As$ conduction band minimum. This mechanism therefore enables 2D electronic magnetotransport and can reproducibly be controlled by the growth conditions serving as a quality criterion for the buffered heterosystem.

Figure 4.2 (a) depicts the detailed QW region of the engaged heterosystem as it is grown lattice-matched upon the strain-relaxed $In_{0.75}Al_{0.25}As$ virtual substrate. An $In_{0.75}Ga_{0.25}As$ quantum well of 30 nm total thickness with a symmetrically embedded InAs channel of 4 nm is formed in between $In_{0.75}Al_{0.25}As$ barrier layers. On top of the upper 120 nm $In_{0.75}Al_{0.25}As$ layer a 10 nm $In_{0.75}Ga_{0.25}As$ layer caps the heterosystem to prevent oxidation, which is optional in case of a high final fraction of indium. No intentional modulation doping layer has been incorporated in the $In_{0.75}Al_{0.25}As$ barrier layers of Fig. 4.2 (a).

The concept of the InAs-channel-insertion in between $In_{0.75}Ga_{0.25}As$ QW layers was introduced by Akazaki *et al.* [86] and adapted by Richter *et al.* [87] for Si-doped $In_{0.75}Al_{0.25}As/In_{0.75}Ga_{0.25}As$ QW heterosystems. Compared to a simple, channel-free $In_{0.75}Ga_{0.25}As$ QW, an additional InAs channel has proven beneficial for the 2D electron mobility, since alloy disorder scattering is reduced significantly for a carrier

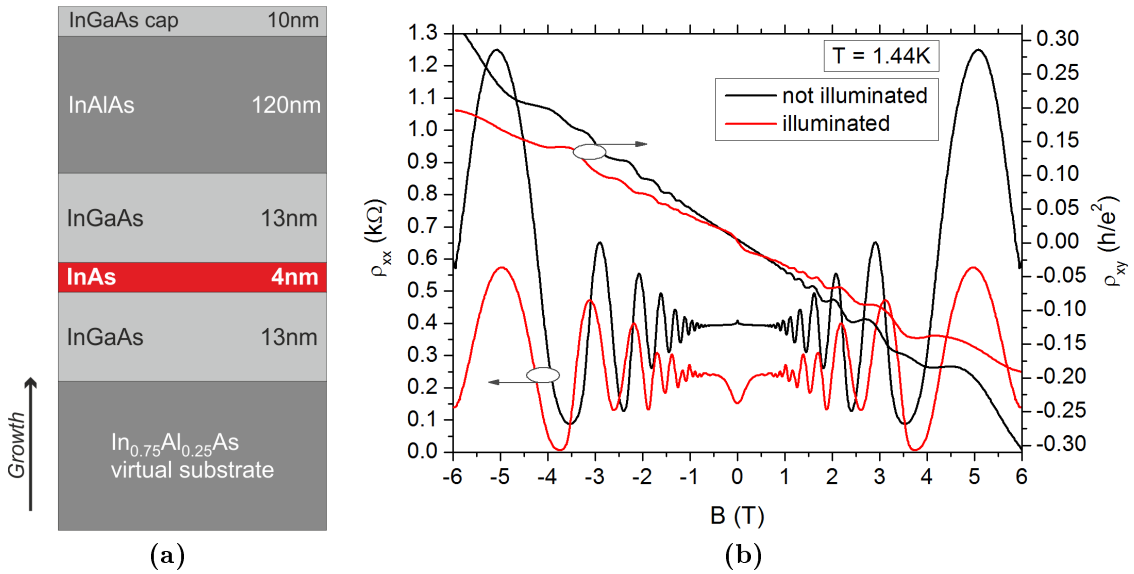

Figure 4.2: (a) *Layer sequence of the active QW region of the unintentionally doped InAs heterostructure concept on the basis of a strain-relaxed* $In_{0.75}Al_{0.25}As$ *virtual substrate. The 2DEG is confined in an* $In_{0.75}Ga_{0.25}As$ *QW featuring a symmetrically embedded InAs channel.* **(b)** *Representative magnetoresistive traces demonstrate the formation of a pronounced quantum Hall system featuring SdH oscillations in the longitudinal magnetoresistivity* $\rho_{xx}(B)$ *and quantum Hall plateaus in the transverse resistivity* $\rho_{xy}(B)$ *at* $T = 1.44$ K*. Illumination frequently leads to the occupation of a second subband for structures grown at* $T_{\text{active}} = 470\,^{\circ}\text{C}$*, which manifests itself in a classical two-band positive magnetoresistivity* $\rho_{xx}(B)$ *at low magnetic fields (red set of magnetoresistivity traces).*

density profile confined in the binary InAs compound layer. An enhanced mobility has also been confirmed by Capotondi *et al.* [88] and later by Ercolani *et al.* [73], who transferred this method to the given symmetric QW layout of Fig. 4.2 (a). With the lattice mismatch of InAs and $In_{0.75}Al_{0.25}As$ still being about 1.7%[2], the InAs layer is compressively strained. The critical thickness of pseudomorphic growth was determined to be 7 ± 1 nm, while highest 2DEG mobilities were measured for a 4 nm channel width [88]. The width of the InAs channel was consequently set to 4 nm for all respective InAs QW heterosystems of this thesis.

In order to optimize device quality and stability, we prepared an extensive epitaxial series of heterostructures on the basis of this 2DEG system varying the growth temperature parameters under a consistently high As_4 flux of $\text{BEP}_{\text{As}} \approx 8\times10^{-6}$ Torr. Low-temperature magnetotransport measurements as a function of a perpendicular magnetic field were performed in van der Pauw geometry (cf. Sec. 3.3 and Appendix B) not explicitly considering the transport anisotropies of the cross-hatched

[2]Lattice constants $a_{\text{In}_x\text{Ga}_{1-x}\text{As}} = 6.058 - 0.405(1 - \text{x})$ Å and $a_{\text{InAs}} = 6.0583$ Å [40, 37]

system.
We found that keeping the growth temperatures of both the buffered substrate and the active QW layers equally fixed at $T_S \approx 330 - 360$ °C typically yields 2D systems of poor electron mobility $\mu_e \ll 1 \times 10^3$ cm^2/Vs that are subject to strong magnetoresistive characteristics of localization. A record $\mu_e = 6.0 \times 10^4$ cm^2/Vs was still achieved in one particular sample (wafer ID: C110705A) of low electron density $n_s = 2.6 \times 10^{11}$ cm^{-2} at $T = 1.44$ K, yet only after the activation of deep level donor states by the illumination from a red LED with a photon energy above the energy gap. However, structures of similar performance could not be re-grown reproducibly, demonstrating the lack of stability applying these growth temperatures. We achieved improved device stability at a high electron mobility, without the need for illumination, by ramping the growth temperature from $T_{\text{buffer}} \approx 360$ °C for the step-graded buffer towards $T_{\text{active}} = 470$ °C during the epitaxy of high-In active layers, as it is also reported in [78].
Figure 4.2 (b) exemplarily documents the magnetoresistivities of such a 2DEG at $T = 1.44$ K confined in completely undoped QW epilayers grown at $T_{\text{active}} = 470$ °C. The black set of traces indicates the 2D nature of a quantum Hall system manifesting in the formation of Shubnikov-de Haas oscillations in the longitudinal magnetoresistivity $\rho_{xx}(B)$ and quantum Hall plateaus in the transverse Hall resistivity $\rho_{xy}(B)$ at higher magnetic fields. The negative Hall coefficient of $\rho_{xy}(B)$ demonstrates electron transport, with a mobility of $\mu_e = 9.5 \times 10^3$ cm^2/Vs at an electron sheet density of $n_s = 3.6 \times 10^{11}$ cm^{-2}. A small peak in ρ_{xx} at zero magnetic field may be attributed to the weak localization correction (see Sec. 2.1.5). In general, the systems grown at $T_{\text{active}} = 470$ °C are found to exhibit a mobility ranging from $\mu_e = 8 - 10 \times 10^3$ cm^2/Vs at a density of $n_s = 3.5 - 5 \times 10^{11}$ cm^{-2}.
With this, a set of growth parameters for stable buffered and strain-relaxed InAs material heterosystems with a high-In content has been determined in the optimization of unintentionally doped 2DEG systems.

After illumination, however, these systems were found to show an increased tendency to form a parabolic drop of the $\rho_{xx}(B)$ signature near zero magnetic field. The red traces of Fig. 4.2 (b) of then $\mu_e = 1.5 \times 10^4$ cm^2/Vs at a density of $n_s = 5 - 6 \times 10^{11}$ cm^{-2} illustrate this positive magnetoresistivity correction to ρ_{xx}, which saturates at higher fields and is accompanied by a small non-linear anomaly in the trace of ρ_{xy} around $B = 0$ T. Such characteristics of the longitudinal and transverse magnetoresistivities can be associated with classical two-band electron magnetotransport due to the population of a second quantized energy subband [89, 90]. The two types of charge carriers of different densities and mobilities, contributing to the longitudinal magnetotransport on two subband energy channels, also manifest in a beating modulation of the $\rho_{xx}(B)$ oscillations in Fig. 4.2 (b). With the minima of $\rho_{xx}(B)$ approaching zero resistivity at higher magnetic fields, a parallel conducting channel of the QW heterostructure can be excluded [91].

The foundation of a growth process established so far by means of structural and transport characterization can now be adapted in the fabrication of 2D hole gas

InAs QW heterosystems with a p-type modulation doping aiming to the investigation of spin-orbit-related effects.

4.3 2DHG systems from p-type Mn modulation doping

Two-dimensional hole systems are of particular interest for spintronic device application, since spin manipulation via the Rashba SO interaction should potentially be more significant owing to the higher effective masses of holes as compared to the lower effective electron masses of the high-mobility 2DEGs discussed before.
While Hirmer *et al.* [92] have demonstrated 2D hole conductivity in InAs heterostructures using non-magnetic carbon (C) in a special p-type doping scheme, we employ the transition metal manganese as a diluted magnetic acceptor material in the InAlAs barriers of the $In_{0.75}Al_{0.25}As/In_{0.75}Ga_{0.25}As/InAs$ QW heterosystem, following the works of Wurstbauer [93]. During molecular beam epitaxy, Mn dopants are substituting lattice sites of group-III elements In, Al or Ga in the III-V host matrix, providing a localized spin magnetic moment of $S = 5/2$, as well as a free hole charge carrier [94]. For the incorporation of the Mn modulation doping layer, the MBE growth temperature is reduced slightly from $T_S = 360$ °C to about $T_S < 330$ °C to avoid a three-dimensional clustering of manganese atoms.

In the following two paragraphs, two concepts of Mn modulation doping are introduced in more detail that fundamentally differ in their effects on low-temperature magnetotransport experiments of 2DHGs in InAs QW heterosystems: A regular doping scheme, where the Mn doping is performed after the QW growth, and an inverted doping layout, where the Mn-doped layer is deposited before the QW leading to an asymmetric broadening of the Mn doping profile into the vicinity of the 2DHG.

Non-magnetic 2DHG systems

Figure 4.3 (a) presents the layer scheme of the single-sided regular Mn modulation doping employed for the formation of the non-magnetic 2DHG systems in the InAs QW heterostructures of our studies. Based on a strain-relaxed and defect-free $In_{0.75}Al_{0.25}As$ virtual substrate, a 2DHG system is hosted in a 20 nm wide $In_{0.75}Ga_{0.25}As$ QW region featuring an InAs channel of 4 nm that is asymmetrically embedded within the $In_{0.75}Ga_{0.25}As$ barrier layers providing hole states above the Fermi level. A 5 nm $In_{0.75}Al_{0.25}As$ spacer separates this compressively strained InAs channel of the 2DHG and the 7 nm wide $In_{0.75}Al_{0.25}As$ layer of diluted Mn doping. As the doping layer is grown after the QW, the presence of magnetic Mn^{2+}-ions in the vicinity of the free 2D carriers due to backdiffusion is not readily expected and the system therefore regarded as non-magnetic. A final $In_{0.75}Al_{0.25}As$ layer of 36 nm then caps the heterosystem.

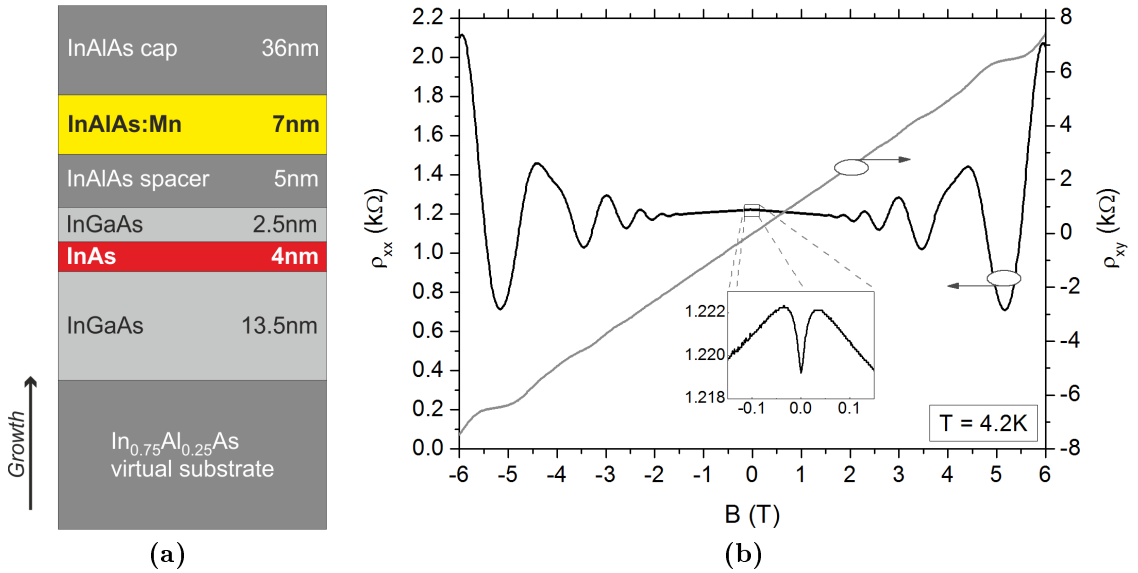

Figure 4.3: (a) *Layer sequence of the active QW region of the non-inverted, regular doping layout. An InAlAs:Mn layer of diluted manganese doping, separated by an InAlAs spacer layer from the QW, provides the 2D hole carriers confined in the InAs channel well which is asymmetrically embedded within the InGaAs QW layers.* **(b)** *Representative magnetotransport measurements of a Hall bar sample at* $T = 4.2$ K *(wafer C120314B,* $T_{\mathrm{Mn}} = 787$ °C*, cf. Appendix B) document a 2DHG quantum Hall system featuring SdH oscillations in the longitudinal magnetoresistivity* $\rho_{xx}(B)$ *and quantum Hall plateaus in the transverse resistivity* $\rho_{xy}(B)$*. The inset highlights a distinct weak antilocalization signature of* $\rho_{xx}(B)$ *at* $B = 0$ T*.*

Successful generation of a two-dimensional hole gas system is indicated in the magnetotransport Figure 4.3 (b) by a positive coefficient of the Hall resistivity $\rho_{xy}(B)$ featuring quantum Hall plateaus at higher magnetic fields, while pronounced Shubnikov-de Haas oscillations shape the longitudinal magnetoresistivity $\rho_{xx}(B)$. No influence of the magnetic Mn impurities in the proximity of the 2DHG is observed, which indicates sufficiently low Mn doping concentrations for an unimpaired 2DHG of a hole density $p = 5.0 \times 10^{11}$ cm^{-2} and a mobility $\mu_h = 1.0 \times 10^4$ cm^2/Vs at $T = 4.2$ K. The model magnetotransport curves of Fig. 4.3 (b) also feature a distinct WAL dip in $\rho_{xx}(B)$ at $B = 0$ T, a quantum correction to the longitudinal magnetoresistivity which will be subject to detailed discussion in Chapter 6, as its presence offers a gateway to the spin-orbit-related parameters of the high-In system (see Sec. 2.1.5).

In general, the non-magnetic 2D hole system of regular doping is the primary system of investigation in this thesis, since aside from the main SO-interaction-related discussions in Chapter 6 also anisotropic anomalies in the magnetotransport properties of InAs systems will be presented on the basis of this heterostructure in

the next Chapter 5.

Diluted magnetic 2DHG systems

In contrast to the regular doping layout introduced in the previous paragraph, in the inverted concept adapted from Richter *et al.* [87] and Heyn *et al.* [77], the doping layer is grown before the active $In_{0.75}Ga_{0.25}As/InAs$ QW layers, see the layer sequence of Fig. 4.4 (a). With a fraction of manganese atoms segregating along with the active zone of epitaxial growth, a significant amount of magnetic Mn^{2+}-ions also resides in the vicinity of the InAs channel of the QW region, as illustrated. This asymmetric broadening of the Mn doping profile has been confirmed qualitatively by SIMS analysis in [93].

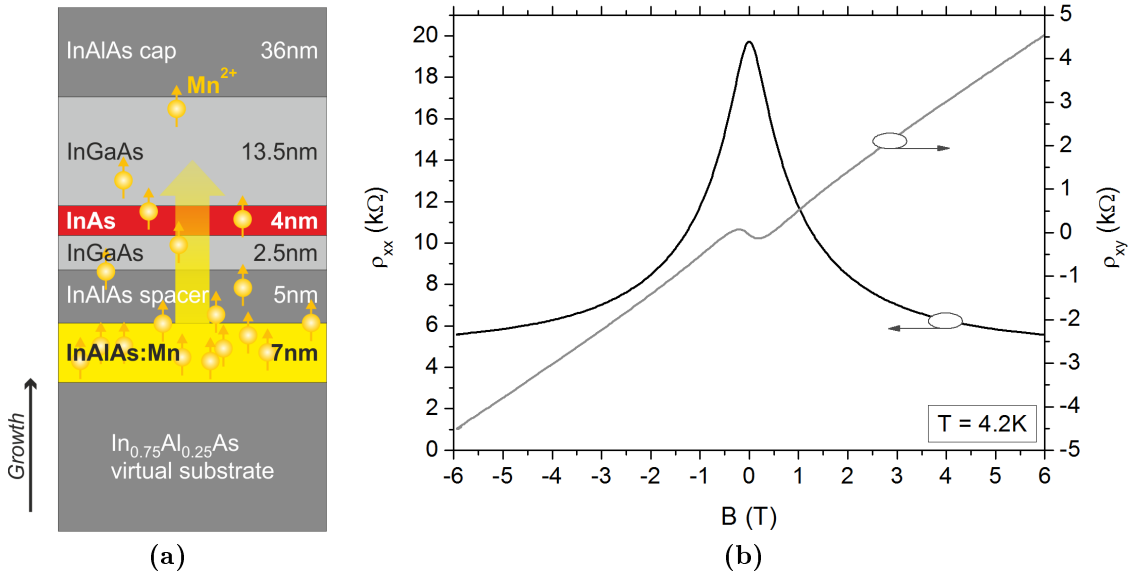

Figure 4.4: (a) *Layer sequence of the active QW region of the inverted doping concept. Contrary to the regular scheme in Fig. 4.3 (a), the carrier supplying InAlAs:Mn doping layer is grown prior to the InGaAs/InAs QW layers leading to a significant concentration of manganese ions in the vicinity of the 2DHG in the InAs channel due to segregation.* **(b)** *As a consequence, the longitudinal magnetoresistivity $\rho_{xx}(B)$ is dominated by a strong localization correction peak around $B = 0$ T due to exchange coupling of the spins of itinerant holes and localized Mn^{2+}-ions, which also manifests in an AHE feature of the transverse resistivity at $\rho_{xy}(0)$ (representative curves from wafer C120224B, $T_{\mathrm{Mn}} = 798$ °C, at $T = 1.44$ K).*

Exact quantification of the Mn doping concentration has remained a difficult task. Calculations from flux calibration of the Mn effusion cell by Wurstbauer *et al.* [93] claim to yield an absolute Mn acceptor concentration $< 1 - 2 \times 10^{20}$ cm^{-3} in the doped layers of an inverted InAs:Mn structure, where, according to SIMS,

roughly more than 1% of that maximum doping concentration is estimated to have segregated into the InAs channel. We could likely regard these values as rough upper limits of the Mn concentration in the investigated InAs:Mn samples of this thesis, as we consistently engaged lower temperatures of the Mn effusion cell. However, these attempts of quantification are questionable, as, due to the small probing volume of the doping layer and the very low concentrations of the diffusing Mn atoms, SIMS analysis has reached its detection limit. Therefore, we use the temperature of the manganese effusion cell as the parameter of relative classification of the Mn doping concentrations of all InAs:Mn QW heterostructures, see Appendix B, given that these were grown within a short period of time.

As a consequence of manganese segregation, drastic differences in magnetotransport are observed with respect to the non-inverted doping layout. Figure 4.4 (b) exemplarily documents the strong reduction of the longitudinal resistivity under the application of a perpendicular magnetic field forming a pronounced peak of $\rho_{xx}(B)$ at $B = 0$ T. This negative magnetoresistivity correction is ascribed to an effect of strong localization due to the coupling of itinerant free holes and localized magnetic moments of the Mn^{2+}-ions in the vicinity of the InAs channel. Effects of magnetic coupling further manifest themselves in the distinct non-linear signature of the anomalous Hall effect (AHE) in the transverse Hall magnetoresistivity around zero field.
Since these interesting properties of magnetoresistive phenomena of the inverted doping scheme have been investigated thoroughly by Wurstbauer *et al.* [95, 96] regarding the effects of a significant concentration of Mn^{2+}-ions $x_{Mn^{2+}}$ in the plane of the 2DHG system, we will focus on the regime of highly diluted Mn concentrations in the channel and particularly comment on the effects on the low-field metal-to-insulator transition in Chapter 7.

In a systematic approach to explore the regimes of the occurring magnetoresistive effects at a changing ratio of $p/x_{Mn^{2+}}$ in the inverted structures, and at a changing hole density p in non-inverted structures, we have extensively varied the Mn doping concentration in both presented InAs:Mn heterostructure schemes by predominantly lowering the Mn cell temperature, see Appendix B.

It shall be noted that, besides the regular and the inverted modulation-doped InAs heterosystems introduced above, also a series of structures in the so-called double-sided Mn doping design was prepared. These combine both doping concepts in joint upper and lower Mn modulation doping layers spatially separated from an $In_{0.75}Ga_{0.25}As$ QW well, where the InAs channel now is symmetrically embedded. This way, an additional lever is offered to manipulate the ratio of manganese ions and the hole density, with, for instance, the amount of manganese ions in the channel being comparable to an inverted sample doped at the same Mn cell temperature. Although these samples did not contribute significantly to the studies of this thesis, their low-temperature magnetotransport characterization in van der Pauw geometry is still featured in Appendix B for completeness.

5 Magnetotransport in anisotropic 2D carrier systems

With the origin of the pronounced cross-hatching surface topography of indium-based heterosystems lying in the growth process of the buffer, as introduced in Sec. 4.1, this characteristic texture should also be reflected in the morphology of the active QW layers in between and hence affect the two-dimensional magnetotransport properties: Indeed, Hall bar experiments along different crystallographic directions reveal anisotropies of the longitudinal magnetoresistivities and also anomalies in the transverse Hall resistivity occur, defining the anisotropic magnetotransport in these 2D carrier systems. A knowledge of these anisotropies is vital for the comprehensive and correct analysis of any transport property of 2D hole gases in the InAs heterostructure systems of interest in this thesis.

Isotropically, the low-temperature mobility of 2D hole gas systems is limited by ionized impurity scattering due to background impurities or remote acceptors, as well as by alloy disorder scattering in ternary compounds from local compositional potential fluctuations in the crystal [30, 97, 10]. Other, anisotropic scattering mechanisms are therefore to be discussed for the cause of the observed asymmetries in the 2D magnetotransport of cross-hatched indium systems.

5.1 Anisotropic scattering of 2DHGs in high-In systems

Depending on the crystallographic direction of the current flow, all Hall bar magnetotransport experiments on 2D hole gas systems in non-inversely doped InAs:Mn

QW heterostructures reveal significantly differing longitudinal magnetoresistivities. Figure 5.1 (a) illustrates the characteristics of $\rho_{xx}(B)$ for current densities $\mathbf{j}$ aligned parallel to the crystallographic directions $[\bar{1}10]$ and $[110]$ and for the so-called diagonal alignment along $[010]$ and $[100]$ at $T = 4.2$ K, exemplarily from samples of wafer C120314B ($T_{\mathrm{Mn}} = 787$ °C, see Appendix B). Experimentally, these configura-

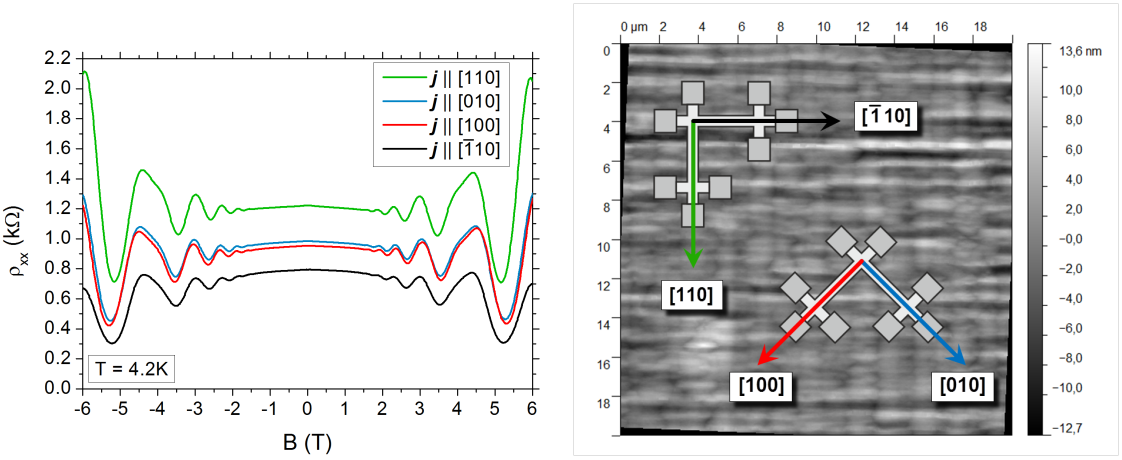

(a) (b)

Figure 5.1: (a) *The longitudinal magnetoresistivity curves $\rho_{xx}(B)$ of the 2DHG InAs:Mn QW heterosystem in L-shaped Hall bars of wafer C120314B, which are oriented as sketched in scheme* **(b)** *with respect to the cross-hatched system: either parallel to the distinguished cross-hatching directions along $[\bar{1}10]$ and $[110]$, or in diagonal orientation along $[010]$ and $[100]$ crystallographic directions (Hall bars are not in scale to the AFM image). The zero-field resistivities in (a) at $T = 4.2$ K clearly illustrate the hole mobility anisotropy $\mu_{[\bar{1}10]} > \mu_{[010],[100]} > \mu_{[110]}$ of the InAs system.*

tions are realized by patterning L-shaped Hall bars with orientations parallel to the cross-hatching as well as diagonally oriented to the distinguished orthogonal $\langle 110 \rangle$ directions, as it is illustrated in Fig. 5.1 (b) on the background of the AFM image of the investigated wafer. The zero-field longitudinal resistivity $\rho_{xx}(0)$ is systematically found to be lowest along the $[\bar{1}10]$ direction, highest along the $[110]$ direction and intermediate in directions $[010]$ and $[100]$. Judging from the B-positions of the SdH minima, the 2D hole sheet densities do hardly vary for the different crystallographic directions and can thus be regarded as constant across the Hall bar samples (cf. Table 5.1). By that, the zero-field resistivity anisotropy is directly translated via Eq. (2.12) into a hole mobility anisotropy $\mu_{[\bar{1}10]} > \mu_{[010],[100]} > \mu_{[110]}$ in these systems. Identically asymmetric behavior has also been reported for the 2D hole mobilities of Mn-doped [95, 98] and C-doped [92] InAs QW heterostructures, as well as for 2DEGs in indium QW heterosystems based on a similar metamorphic buffer layer design, e.g. [99, 87, 100, 73].

For quantification and comparability, we define the mobility anisotropy as $\Delta\mu = \left(\mu_{[\bar{1}10]} - \mu_{[110]}\right)/\mu_{[\bar{1}10]}$. Any other proposed anisotropy quantification of parameters in this chapter will be calculated accordingly. With this, we find the maximum hole mobility of $\mu_{[\bar{1}10]} = 1.560 \times 10^4$ cm^2/Vs exceeding the lowest mobility of $\mu_{[110]} = 1.027 \times 10^4$ cm^2/Vs by $\Delta\mu = 34.2\%$.
Table 5.1 correlates the established magnetotransport properties with parameters of the cross-hatching formation deduced from a quantitative analysis of line scans of the corresponding AFM image (see Fig. 5.1 (b)) by Gwyddion data visualization and analysis software. For the morphologically relevant parameters of the cross-

Crystal direction	Hole density p [$\times 10^{11}$ cm^{-2}]	Hole mobility μ [$\times 10^4$ cm^2/Vs]	RMS roughness [nm]	Periodicity [μm]
[110]	4.98	1.027	2.89 ± 0.30	≈ 0.896
[010]	5.06	1.252	2.54 ± 0.32	-
[100]	5.09	1.287	2.39 ± 0.35	-
[$\bar{1}$10]	5.04	1.560	2.01 ± 0.36	≈ 1.334
Anisotropy	-	34.2%	30.4%	32.8%

Table 5.1: *Characteristic magnetotransport properties in the respective crystallographic directions deduced from Fig. 5.1 (a), as well as the surface morphology parameters, RMS roughness and periodicity, extracted from the corresponding AFM image analysis of Fig. 5.1 (b). The Anisotropies of the cross-hatching morphology parameters in the* $\langle 110 \rangle$ *directions are found to be in the range of the mobility anisotropy.*

hatching, the RMS[1] roughness and the periodicity of the periodic undulations from FFT[2] analysis, we consistently identify the lowest (strongest) RMS roughness to be in the [$\bar{1}$10] ([110]) direction, which is the direction of longest (shortest) periodicity. This suggests smooth topographical variation of the InAs QW channel plane hosting the 2DHG in the [$\bar{1}$10] direction, whereas scattering should be enhanced along the [110] direction. While the RMS roughness in diagonal directions [010] and [100] is intermediate in value, no information on the periodicity can confidently be extracted from the FFT analysis along these crystallographic directions. Being aware of small possible statistical deviations between the cross-hatching formations of the mapped AFM sample and the actual Hall bar samples of magnetotransport measurements, we find good agreement between $\Delta\mu = 34.2\%$ and the acquired cross-hatching anisotropies of 30.4% and 32.8% for both the statistical RMS roughness and the periodicity, respectively, see Tab. 5.1.
However, although the actual amplitude of the surface roughness can reach more than 20 nm (cf. Fig. 5.1 (b)), it still is modulated on a long µm-scaled periodicity. Indeed, detailed TEM cross-sections of the QW region have shown not to indicate

[1]Root mean square
[2]Fast Fourier transform

any pronounced interface roughness on length scales in the range of the elastic mean free paths (cf. $l_{e,[\bar{1}10]} \approx 183$ nm and $l_{e,[110]} \approx 120$ nm) but rather suggest atomically smooth interfaces. Therefore, a direct correlation of the roughness and periodicity of the cross-hatching with an anisotropic scattering potential due to a structural non-planarity of the heterointerfaces of the 4 nm InAs channel seems improbable.

In general, literature favors anisotropic spatial variations in residual in-plane strain correlated with the cross-hatched morphology of metamorphic buffer layer growth as the explanation for anisotropic carrier mobilities [101, 102, 103, 76, 100]. Other than that, again interface roughness [87, 104, 97] and piezoelectric effects of sheer non-zero uniaxial strain [102] or roughness-induced piezoelectric charges in lattice-mismatched systems [105] are proposed to play a role in the asymmetric scattering mechanism limiting carrier mobilities.

According to calculations by Capotondi *et al.* [88] and Ercolani *et al.* [73], interface roughness is indeed identified only as a minor contribution to the anisotropic scattering in buffered high-In QW heterostructures. By means of spatially resolved photoemission electron microscopy, Ercolani and co-workers [73] could instead demonstrate that the indium concentration within a ternary $In_{0.75}Ga_{0.25}As$ QW alloy is modulated locally according to the periodicity and roughness of the respective AFM topography, highly asymmetrically in the distinguished $\langle 110 \rangle$ crystallographic directions of the cross-hatching. It was then calculated that these variations of the indium concentration modulate the conduction band energy profile in association with the given transport anisotropy of the 2DEG system in the InGaAs QW heterostructure of that study [73, 106]. Hirmer [107] performed energy band simulations of the valence band edge during her investigations on carbon-doped InAs:QW 2DHG heterostructures on identical buffered substrates, where the indium target fraction x in the active layers was varied from $x = 0.40$ to $x = 0.75$ and InAs channels of 4 nm, 2 nm and 0 nm width were inserted. For one occupied subband, the hole density profile always showed to penetrate the interfaces of the InAs channel, asymmetrically embedded in InGaAs QW layers [107]. With a significant portion of the hole wave function leaking into the surrounding ternary $In_{0.75}Ga_{0.25}As$ compound layers of the InAs-channel-inserted 2DHG QW system, a similar modulation of the indium concentration in correlation with the cross-hatching morphology as in the study of Ercolani [73] could be regarded in our system. A proposed associated modulation of the valence band energy profile could then be assumed to cause anisotropic hole transport properties. The influence of compositional fluctuations of the indium concentration in the ternary QW layers is further supported by the findings of Ercolani *et al.* [73] and Hirmer [107] upon the insertion of the binary InAs channel in the InGaAs QW: Apart from an overall increase of the hole mobility due to the reduction of alloy disorder scattering, also the mobility anisotropy is reduced, all the more, the greater the width of the binary InAs channel region where no compositional fluctuations are expected.

Aside from this introduced asymmetric energy band modulation due to the compositional In fluctuations in the ternary compound layers, Hirmer further claims

that variations of residual strain contribute to the anisotropic scattering in the cross-hatched 2D system [107]. X-ray diffraction measurements confirm an anisotropic strain relaxation in the active layers with the lattice constant being almost fully relaxed along the $[\bar{1}10]$ crystallographic direction, while a residual compressive strain was identified for the lattice constant along the low-mobility [110] direction [107].

In conclusion, the inherent asymmetric residual strain of the system from the network of dislocations in the step-graded buffer layers, see Sec. 4.1, and the hence preferential incorporation of indium in low-strain-regions during the growth of ternary alloys may lead to both the accumulating roughness of the cross-hatching morphology and a local modulation of the In concentration, which affects the energy band modulation then directly and by effects of strain. The particular interplay of these mechanisms in the anisotropic longitudinal magnetotransport properties of buffered high-In QW systems is still an open question.

5.2 Hall effect anomalies in anisotropic systems

Unlike the anisotropic zero-field levels of $\rho_{xx}(0)$ and related hole mobilities observed in the previous section due to anisotropic scattering, no deviation should be found in the transverse resistivity $\rho_{xy}(B)$ as the trace of the Hall resistance in a perpendicular magnetic field is expected to be independent of scattering details, since it is determined by the carrier density (cf. Sec. 2.1.2, Eq. (2.10)). While this is true for ρ_{xy} at $B = 0$ T in the situation of $\mathbf{j} \parallel [\bar{1}10]$ and $\mathbf{j} \parallel [110]$, a reproducible anomaly of $\rho_{xy}(0)$ is witnessed for magnetotransport experiments on 2DHGs in InAs-based heterosystems when the current density is aligned along the diagonal directions [010] and [100].

5.2.1 Phenomenology

Figure 5.2 introduces the transverse Hall resistivity curves $\rho_{xy}(B)$ directly associated with the anisotropic longitudinal resistivities $\rho_{xx}(B)$ and corresponding magnetotransport properties presented in Fig. 5.1 and Tab. 5.1, respectively. Like earlier in Sec. 5.1, experiments on the 2DHG system were conducted on L-shaped HB devices of the non-inversely doped InAs:Mn QW heterostructure (wafer C120314B, $T_{\mathrm{Mn}} = 787\,^{\circ}\mathrm{C}$) at $T = 4.2$ K, either aligned along the parallel crystallographic directions $[\bar{1}10]$ and [110] or the diagonal directions [010] and [100].
As expected from textbook Hall effect theory (see Sec. 2.1.3), the traces of $\rho_{xy}(B)$ in the $\langle 110 \rangle$ directions of extreme cross-hatching periodicity and roughness, and hence of extreme mobilities, coincide, following a typical Hall characteristic including quantum Hall plateaus of $\rho_{xy}(B)$ in between higher quantizing magnetic fields. However, in the case of a current applied along a Hall bar in the diagonal directions of intermediate mobilities, a rather unexpected phenomenon emerges: As the detail

view of the zero-field region in the inset of Fig. 5.2 highlights, $\rho_{xy}(B)$ is shifted from zero resistivity towards negative values of $\rho_{xy}(0)$ for $\mathbf{j} \parallel [010]$ and towards positive values for $\mathbf{j} \parallel [100]$, even at $B = 0$ T. Reading a significant $\Delta\rho_{xy,[010]}(0) = 219\ \Omega$

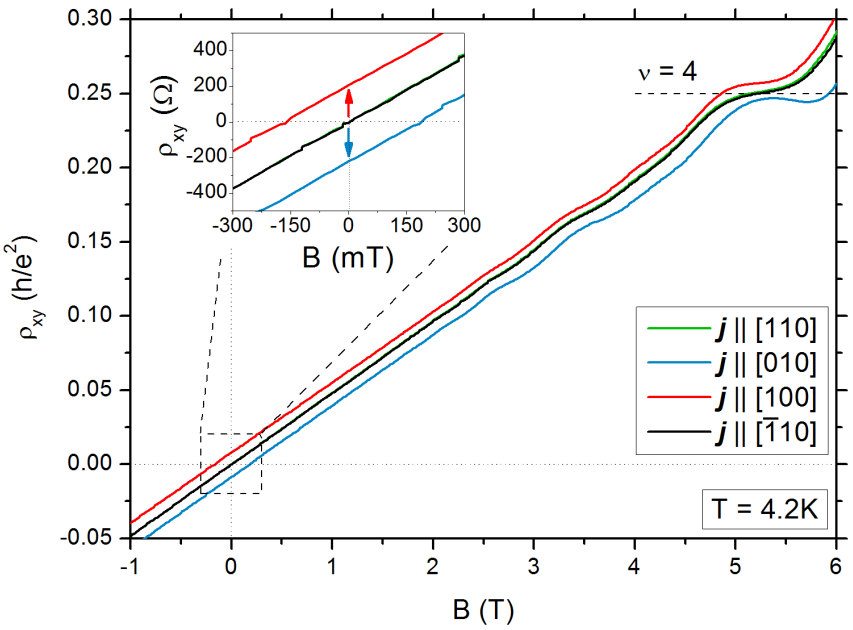

Figure 5.2: *Transverse Hall resistivity curves $\rho_{xy}(B)$ from the magnetotransport experiments of the cross-hatched InAlAs/InGaAs/InAs:Mn heterosystem in Fig. 5.1 at $T = 4.2$ K under different crystallographic alignments of the current density* $\mathbf{j}$*. The inset reveals the unusual offset phenomenon of $\rho_{xy}(B)$: For the diagonal directions* [010] *and* [100] *only, the Hall traces are shifted in opposite directions even at $B = 0$ T. As a consequence of this finite offset in $\rho_{xy}(B)$, a non-monotonic overshoot-like anomaly is visible at quantized Hall plateaus, here most pronounced for $\nu = 4$ (dashed level).*

along [010] and $\Delta\rho_{xy,[100]}(0) = 210\ \Omega$ along [100], the traces of the Hall resistivities are shifted symmetrically in opposite directions. We have found the orientation of this finite, non-zero *offset* of the zero-field Hall resistivity to be reproducible for each crystallographic direction in every diagonal Hall bar sample made from the InAs system. Variation of the temperature in a range from $T = 30$ mK up to 4.2 K brought no notable change to this phenomenology at $B = 0$ T (not shown).
As a second peculiar feature of the Hall magnetoresistivity, an apparent anomaly of $\rho_{xy}(B)$ at quantizing fields arises from this offset of $\rho_{xy}(0)$ along diagonal crystallographic directions: Indicated exemplarily for $\nu = 4$ in Fig. 5.2, the resistivity traces do not seem to reach the plateau of the universal resistivity value associated with the respective filling factor (cf. Eq. 2.14, dashed line as a guide to the eye in Fig. 5.2). Additionally, they exhibit an unusual *overshooting* characteristic in their shape, a property that will be revisited in Sec. 5.2.3 of this chapter.

Most commonly, a finite value of the transversal Hall resistivity ρ_{xy} in the absence of a magnetic field is thought to be a manifestation of ohmic contacts not being aligned exactly opposing each other, hence giving rise to a longitudinal contribution to the transverse resistivity. Since, however, it is the nature and purpose of the Hall bar structure to provide a precisely defined measurement geometry minimizing this mixing of different contributions in the resistivities, this argument should be regarded as a rather speculative approach. Even though it may still be a fairly accepted explanation for single devices, the discovery that these robust offsets in $\rho_{xy}(0)$ are found for every Hall bar in the diagonal configuration in a reproducible manner clearly speaks for a more general principle at the root of this observation. In order to further investigate the nature of this offset phenomenon and to simultaneously exclude any influence of the L-shaped geometry, we patterned straight Hall bars along various angles relative to the cross-hatching, also in between the diagonal and parallel crystallographic directions. Figure 5.3 (a) sketches these Hall bar

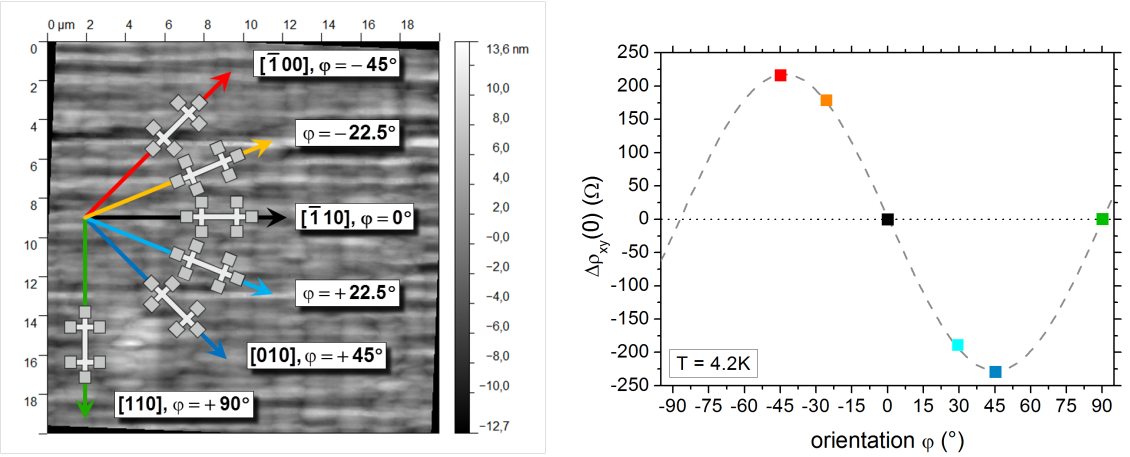

(a) (b)

Figure 5.3: (a) *Scheme of Hall bars patterned along various crystallographic directions of the cross-hatched InAs system and their angles of orientation φ with respect to the direction* $[\bar{1}10]$. *Plotting the zero-field transversal magnetoresistivity* $\Delta\rho_{xy}(0)$ *from magnetotransport experiments at* $T = 4.2\,\mathrm{K}$ *according to these orientations in* **(b)**, *a clear overall sinusoidal trend of offsets* $\Delta\rho_{xy}(0)$ *is revealed by the dashed sine function fitted to the color-referenced data points.*

orientations on the background of an exemplary AFM image of the wafer's cross-hatched surface morphology. Figure 5.3 (b) then indicates that, while there are again finite offsets $\Delta\rho_{xy}(0)$ to be witnessed in the diagonal $\langle 100\rangle$ orientations at angles $\varphi = \pm 45°$ with respect to the $[\bar{1}10]$ direction ($\varphi = 0°$), there is also a significant, yet smaller offset in the orientations of about $\varphi = +22.5°$ and $-22.5°$. Combining the data of all orientations, one recognizes the amplitudes of the offset to follow a clear sinusoidal trend illustrated by the dashed line fitted to a sine function. This

observation further underlines the importance of the geometrical aspect of this effect with respect to the distinguished in-plane crystallographic directions along the cross-hatching where $\Delta\rho_{xy}(0) = 0$.

A further indication of the universality of the effect in cross-hatched InAs-heterostructures is given by the fact that this offset phenomenon has been documented before in comparable InAs-based 2D hole gas QW systems doped with carbon in the magnetotransport studies conducted by Hirmer [107]. Here, the effect was mainly attributed to a possible direction-dependent scattering process manifesting in the diagonal directions of the cross-hatched morphology due to effects of the orthogonal $\langle 110 \rangle$ directions' broken mirror symmetry of the periodic surface grating. This is then believed to result in a non-zero Hall voltage by holes scattered towards the opposite edges of the HB, already at $B = 0$ T.
A piezoelectric offset voltage in Hall effect devices in the absence of a magnetic field was also reported as sensitive to mechanical strain in [108]. However, no reasonable configuration of any intrinsic residual strain from the metamorphic buffer layer growth (see Sec. 4.1) nor of the compressively strained InAs channel can be thought of that would produce offset voltages of such mirror symmetry in the diagonal crystallographic directions only.

These approaches to the explanation of the offset effect are therefore not entirely conclusive for the given situation. In an effort to narrow down possible options of its exact physical origin, we have thus tracked the effect in a systematic study of various semiconductor materials. Engaging the resources of MBE-grown III-V compound heterostructures at hand, we will investigate both 2D hole and electron gases in systems with and without a distinct cross-hatching morphology in the following section. Within this pool of material systems, different strengths of the spin-orbit interaction are also to be expected.

5.2.2 Materials study

For orientation, Figure 5.4 displays the simplified layer schemes of all III-V semiconductor systems of this section's material study beneath the corresponding AFM images of their respective heterostructure surfaces. All systems under investigation host a two-dimensional carrier system confined in a quantum well, Fig. 5.4 (a), (b) and (d), or in the triangular potential of a single interface, Fig. 5.4 (c). They, however, differ in the presence of a type of cross-hatching formation, which exists in (a) and (b), while there is only the diffuse texture of a smooth surface in (c) and (d).

The corresponding magnetotransport figures discussed in this section all highlight magnetoresistance traces in the regime of $B \to 0$ T, if possible, on similar scales for comparability. Therein, traces of the transverse Hall magnetoresistivities are displayed by their positive absolute values calculated from again the absolute values of recorded Hall voltages over the applied electric current.
Depending on the heterosystem, the curves of $\rho_{xx}(B)$ will exhibit various corrections

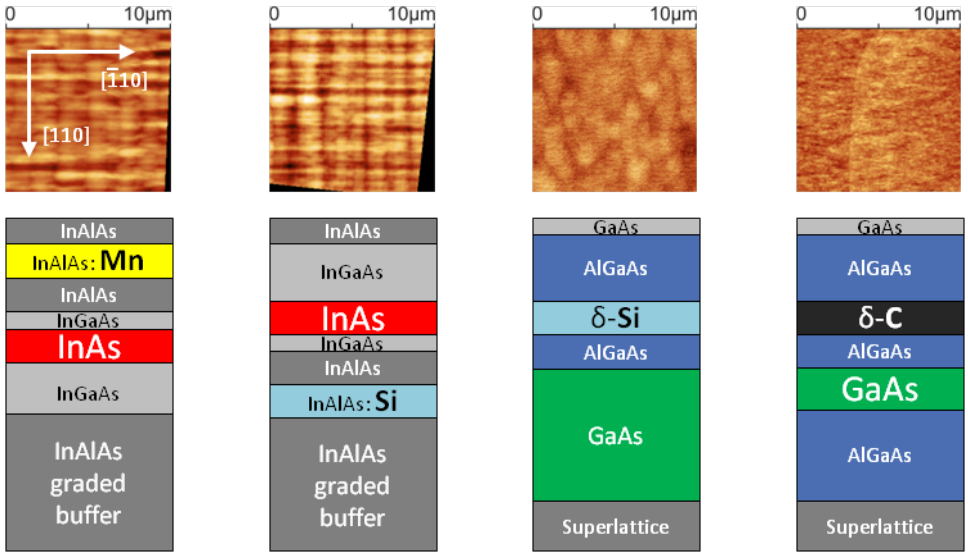

Figure 5.4: *For orientation, the simplified schemes of the layered semiconductor 2D heterosystems under study beneath the corresponding AFM images of the heterostructure surfaces:* **(a)** *InAlAs/InGaAs/InAs:Mn (wafer ID: C120314B),* **(b)** *InAlAs/InGaAs/InAs:Si (C061122A),* **(c)** *AlGaAs/GaAs:Si (C120531B) and* **(d)** *AlGaAs/GaAs:C (D090723A).*

to the magnetoresistivity, whose nature will be identified here yet not discussed in great detail, as the underlying physical effects are addressed elsewhere in this thesis and will not have any crucial influence on the outcome of this study.

The offset to the transverse magnetoresistivity of interest has clearly been documented in the diagonal directions [010] and [100] of InAs:Mn, see Fig. 5.2, and InAs:C [107] QW heterostructures. Both 2D hole gas systems are characterized by distinct crystallographic anisotropies in magnetotransport due to their pronounced cross-hatching morphology. So, in order to further support the likely morphological origin of the phenomenon and to exclude any major influence of the hole nature of the carrier system, we commence our study with a 2DEG in a similar InAlAs/InGaAs/InAs heterosystem doped with silicon, see Fig. 5.4 (b), also exhibiting a comparable cross-hatching formation. Figure 5.5 depicts these magnetoresistive experiments on again L-shaped Hall bars at $T = 1.44$ K with the electric current being aligned along directions [$\bar{1}$10] and [110] in (a), while Fig. 5.5 (b) demonstrates the measurements in diagonal configuration of $\mathbf{j} \parallel [010]$ and $\mathbf{j} \parallel [100]$ (see also the inset illustrations of both L-shaped HB configurations in Fig. 5.5 for orientation). Both sets of traces of $\rho_{xx}(B)$ are dominated by effects of quantum interference in the vicinity of $B = 0$ T (cf. Sec. 2.1.5). Again, we find the known mobility anisotropy of the cross-hatched

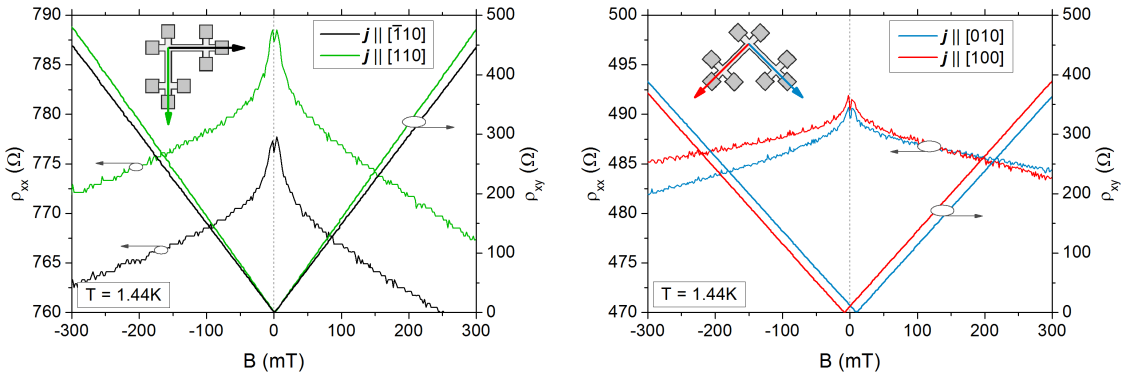

Figure 5.5: *Magnetotransport of a 2DEG system in an* ***InAlAs/InGaAs/-InAs:Si*** *heterostructure, cf. Fig. 5.4 (b), at* $T = 1.44$ K*, with the current aligned along* **(a)** *the* $[\bar{1}10]$ *(black) and the* $[110]$ *(green) crystallographic direction, as well as along (b) the* $[010]$ *(blue) and the* $[100]$ *(red) direction (see the inset illustrations of the L-shaped Hall bars). A clear offset in* $\rho_{xy}(0)$ *of* **(b)** *is observed in this cross-hatched system of anisotropic mobilities.*

InAs system manifesting in $\rho_{xx,[\bar{1}10]}(0) < \rho_{xx,[110]}(0)$ in Fig. 5.5 (a), while $\rho_{xx}(0)$ in (b) is virtually identical for [010] and [100], although smaller in magnitude than in (a). Mobilities are $\mu_{[\bar{1}10]} = 2.28 \times 10^4$ cm^2/Vs and $\mu_{[110]} = 2.21 \times 10^4$ cm^2/Vs in Fig. 5.5 (a), yielding only a small anisotropy $\Delta\mu = 3.1$ %, and a surprisingly higher diagonal mobility of $\mu_{[010],[100]} = 2.67 \times 10^4$ cm^2/Vs in (b).
Apparently from $\rho_{xy}(0)$ in (b), a clear, but small offset exists in this system with $\Delta\rho_{xy}(0) = 11\ \Omega$. Its occurrence stresses that the offset phenomenon of InAs 2D heterosystems may indeed be regarded as some form of yet another direct implication of the cross-hatching morphology on zero-field anisotropic scattering as it has been speculated earlier by Hirmer [107]. Additionally, the relatively small value of $\Delta\rho_{xy}(0)$ in the 2D electron system with respect to the InAs hole system before in Sec. 5.2.1 may indicate that the higher effective mass of holes could play a role in the magnitude of the effect.

Next, to put this reasoning to the test, we switch within III-V semiconductor compounds from InAs-based to GaAs-based 2D heterosystems. These are not known to exhibit any form of a distinctive cross-hatching formation of their heterostructures, which has been confirmed by AFM imaging in Fig. 5.4 (c) and (d). In particular, we continue our study of crystallographically resolved magnetotransport experiments in Fig. 5.6 with a high-mobility 2DEG in the modulation-doped, single interface system AlGaAs/GaAs:Si, see Fig. 5.4 (c).

Indeed, no offset effect of $\rho_{xy}(B)$ can be distinguished in the diagonal configuration in Fig. 5.6 (b), as $\rho_{xy}(0)$ is exactly zero for both these directions. This, once again, strengthens a cross-hatching-based hypothesis for the explanation of the

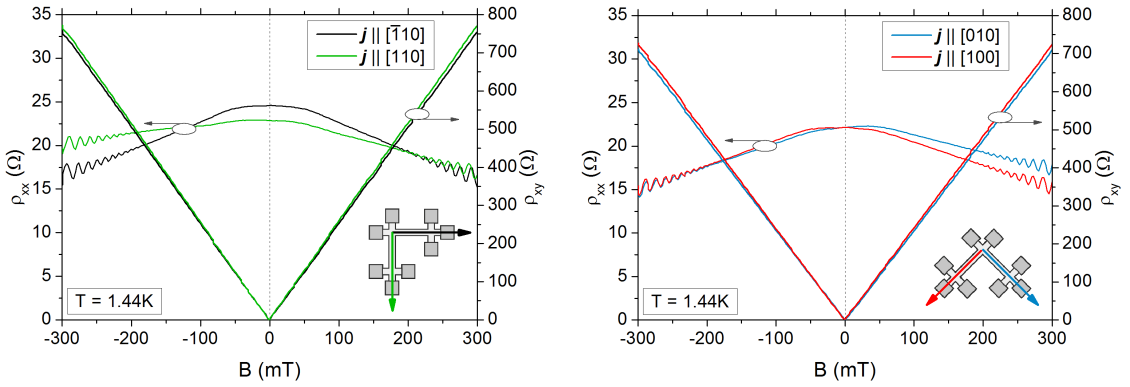

Figure 5.6: *Magnetotransport of a 2DEG system in an **AlGaAs/GaAs:Si** heterostructure, cf. Fig. 5.4 (c), at $T = 1.44$ K, with the current aligned along* **(a)** *the* $[\bar{1}10]$ *(black) and the* $[110]$ *(green) crystallographic direction, as well as along* **(b)** *the* $[010]$ *(blue) and the* $[100]$ *(red) direction (see the inset illustrations of the L-shaped Hall bars). There is no traceable offset in* $\rho_{xy}(0)$ *of (b) in this high-mobility system.*

phenomenon. There exists a rather small anisotropy of the mobilities along $[\bar{1}10]$ and $[110]$ in Fig. 5.6 (a), with $\Delta\mu = 8.8\,\%$ from $\mu_{[\bar{1}10]} = 1.04 \times 10^6$ cm^2/Vs and $\mu_{[110]} = 1.14 \times 10^6$ cm^2/Vs, and also $\mu_{[010],[100]} = 1.13 \times 10^6$ cm^2/Vs in Fig. 5.6 (b) is quite similar. SdH oscillations of the high-mobility system dominate $\rho_{xx}(B)$ already at low field strengths of about $B = 200$ mT, while the negative magnetoresistive background of $\rho_{xx}(B)$ around $B = 0$ T in these high-mobility 2DEG systems is commonly attributed to electron interaction effects with long-range potential fluctuations in the ballistic transport regime [109]. Apart from a slight asymmetry of $\rho_{xx}(B)$ with respect to $B = 0$ T, there, however, seems to be a greater degree of overall concurrence of both sets of $\rho_{xx}(B)$ traces in the examined magnetic field range than in Fig 5.5. In general, this high-mobility system therefore does not seem to be affected from any crystallographically anisotropic scattering conditions.

To our surprise, as we were studying a 2D hole gas system of an AlGaAs/GaAs:C QW heterostructure (see Fig. 5.4 (d)) next, in Fig. 5.7 at $T = 1.44$ K, a very pronounced offset effect of $\Delta\rho_{xy}(0) = 36\ \Omega$ unexpectedly reappeared for the diagonal directions in Fig. 5.7 (b). Since the AlGaAs/GaAs system has no morphologic texture that would be comparable to the cross-hatching topography, see the AFM images of Fig. 5.4 (c) and (d), this would then contradict any peculiarities of scattering by morphological anisotropy potentials to be the sole origin of this distinct offset effect. Also, the prominently strong anisotropy of mobilities $\mu_{[\bar{1}10]} = 6.79 \times 10^4$ cm^2/Vs and $\mu_{[110]} = 4.18 \times 10^4$ cm^2/Vs in Fig. 5.7 (a) is striking and not readily clear.

For high-mobility electron systems in modulation-doped AlGaAs/GaAs structures, interface roughness is usually identified as the cause of anisotropic mobilities along the $\langle 110 \rangle$ directions [110, 111, 112, 113], since the else important mobility-

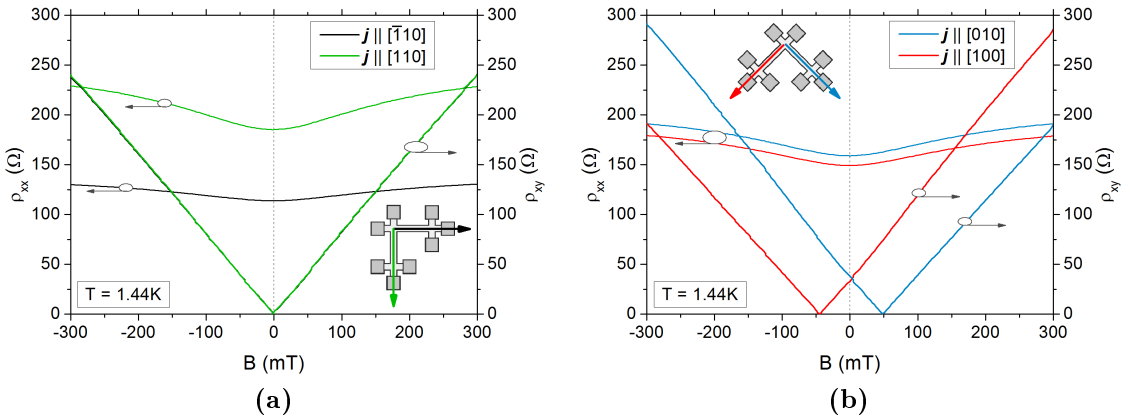

Figure 5.7: *Magnetotransport of a 2DHG system in an* ***AlGaAs/GaAs:C*** *heterostructure, cf. Fig. 5.4 (d), at* $T = 1.44$ K*, with the current aligned along* **(a)** *the* $[\bar{1}10]$ *(black) and the* $[110]$ *(green) crystallographic direction, as well as along* **(b)** *the* $[010]$ *(blue) and the* $[100]$ *(red) direction. A pronounced offset occurs in* $\rho_{xy}(0)$ *of (b). Although the system lacks of any cross-hatching morphology, it still exhibits a strong anisotropy of* $\rho_{xx}(0)$ *in (a) indicating an anisotropic scattering process.*

limiting processes of background impurity scattering and scattering by remote impurities, as well as of alloy disorder scattering are of isotropic nature. Roughness at the heterointerfaces of AlGaAs/GaAs arises from the kinetics during growth of GaAs-based compounds: With the capture rate for migrating Ga atoms on a (001) growth surface being higher at atomic steps in the $[\bar{1}10]$ than in the $[110]$ direction, randomly formed terraces or monolayer-thick islands are shaped, which are preferentially elongated in the $[\bar{1}10]$ crystallographic direction [114, 111, 112, 113]. If such atomic-scaled steps are conserved at the interfaces of the AlGaAs/GaAs heterostructure, scattering is then reduced for carriers near the interface along the $[\bar{1}10]$ direction, while it is enhanced for transport along the $[110]$ direction. By that, depending on the growth conditions of the samples, electron mobility anisotropies as high as $\Delta\mu = 40\,\%$ are reported, increasing with the carrier density [114, 110, 111, 112], while $\Delta\mu$ is stated as low as $5 - 10\,\%$ for ultra-high-mobility 2DEG structures of comparably low carrier density, $\mu > 10^7$ cm^2/Vs and $n = 2.4 \times 10^{11}$ cm^{-2}, respectively, [112].

Indeed, in the high-mobility AlGaAs/GaAs 2D hole gas system of Fig. 5.7 (a), we find a strong mobility anisotropy of $\Delta\mu = 38.4\,\%$ and apparently also $\mu_{[\bar{1}10]} > \mu_{[110]}$, which is thus to be ascribed as due to interface roughness scattering. The absence of a distinct anisotropy in the high-mobility 2DEG of the AlGaAs/GaAs sample in Fig. 5.6 ($\Delta\mu = 8.8\,\%$) on the other hand, may then be regarded as an indication of only a small contribution of interface roughness in this high-mobility and low-electron-density system, or of another process, like e-e interaction, dominating, since moreover $\mu_{[110]} > \mu_{[\bar{1}10]}$.

By now, it seems that the offset phenomenon of $\rho_{xy}(B)$ along the diagonal crystallographic directions $\langle 100 \rangle$ is no more restricted to cross-hatched morphologic systems only, but is, more universally, directly related to an existing general mobility anisotropy in the orthogonal directions $\langle 110 \rangle$.

In a final test, we also transferred this hypothesis from III-V to group-IV heterosystems, in particular to a Si/SiGe:P QW system hosting a 2DEG, which was grown in the SiGe chamber of the MBE cluster facility. As a consequence of SiGe graded buffer layer growth, the system is also characterized by a distinct cross-hatching formation. Indications of an existing offset in $\rho_{xy}(0)$ in diagonal configuration to the anisotropic system were indeed witnessed, yet could not be featured in this final study due to reoccurring technical difficulties with single ohmic contacts.

Concluding this comparative study, Table 5.2 offers a survey of the investigated semiconductor heterosystems next to the criteria relevant for approaching a possible explanation of the offset in $\rho_{xy}(B)$ along diagonal crystallographic directions.

Semiconductor heterosystem	Cross-hatching	System	$\Delta\mu$	$\Delta\rho_{xy}(0)$
InAlAs/InGaAs/InAs:Mn	✓	2DHG	35.4 %	✓
InAlAs/InGaAs/InAs:C [107]	✓	2DHG	$\approx$ 20 %	✓
InAlAs/InGaAs/InAs:Si	✓	2DEG	3.1 %	✓
AlGaAs/GaAs:Si	–	2DEG	8.8 %	–
AlGaAs/GaAs:C	–	2DHG	38.4 %	✓

Table 5.2: *Comparative survey of the III-V heterosystems of this materials study together with the characteristics relevant to the discussion of the origin of the offset phenomenon $\Delta\rho_{xy}(0)$. Only the high-mobility AlGaAs/GaAs 2DEG system of relatively small mobility anisotropy and without a cross-hatching at its surface misses the offset phenomenon.*

The common denominator for the occurrence of this universal phenomenon in the Hall resistivity across all studied semiconductor carrier systems seems to be the general existence of a twofold anisotropic scattering mechanism causing anisotropic mobilities, independent of the material-specific reasons for said anisotropic scattering. The resulting situation of different $\rho_{xx}(0)$ levels along distinguished orthogonal crystallographic directions is then accompanied by altered ρ_{xy} traces of Hall systems that are misaligned by an in-plane angle to the anisotropic reference system. Overall, a sinusoidal trend is generated in the emerging $\Delta\rho_{xy}(0)$ offset values of different angular orientations, as seen in Fig. 5.3 of Sec. 5.2.1.

Next, we will therefore solve the given situation of randomly oriented Hall bars in the framework of the standard Drude model in a magnetic field explicitly considering anisotropic scattering times, a problem that has, to the best of our knowledge, not been demonstrated in literature.

5.2.3 Drude model of magnetotransport in an anisotropic system

Following the reasoning of the previous section, we will first derive the tensorial representation of the classical Hall effect in an anisotropic system within an expanded textbook framework of the Drude model in a magnetic field and afterwards view the situation for arbitrary orientations with respect to the anisotropic reference frame. In contrast to the considerations made in Sec. 2.1.3, isotropic symmetry approximations for the components of the conductivity tensor do not hold any longer in the anisotropic case.

According to Section 2.1.2, the equation of motion of carrier drift in a magnetic field $\mathbf{B} = (0, 0, B_z)$ perpendicular to the x-y-plane is

$$m^* \left(\frac{\mathrm{d}\mathbf{v}}{\mathrm{d}t} + \sum_i \frac{v_i}{\tau_i} \vec{e}_i \right) = q \left(\mathbf{E} + \mathbf{v} \times \mathbf{B} \right), \tag{5.1}$$

with $i \in \{x, y\}$ and $\mathbf{E} = (E_x, E_y, 0)$. We now accommodate the anisotropy of the system by defining anisotropic scattering times τ_x and τ_y in the x- and y-direction of the coordinate system, respectively, setting

$$\tau \equiv \tau_x = \alpha \cdot \tau_y, \tag{5.2}$$

where α is the factor parametrizing the anisotropic ratio of τ_x and τ_y. In the steady state of the system, with $\frac{\mathrm{d}\mathbf{v}}{\mathrm{d}t} = 0$, the components of Eq. (5.1) read as

$$m^* \frac{v_x}{\tau} = qE_x + qv_y B = qE_x + v_y m^* \omega_c \tag{5.3}$$

$$\alpha \cdot m^* \frac{v_y}{\tau} = qE_y + qv_x B = qE_y - v_x m^* \omega_c, \tag{5.4}$$

with the cyclotron frequency $\omega_c = eB/m^*$. By setting the electric charge $q = -e$ and using $\mathbf{j} = -n_s e \binom{v_x}{v_y}$ in Eq. (5.3) and (5.4), we find for the components of the electric current density $\mathbf{j}$:

$$j_x = \lambda \left(\alpha E_x + \omega_c \tau E_y \right) \tag{5.5}$$

$$j_y = \lambda \left(-\omega_c \tau E_x + E_y \right), \tag{5.6}$$

where

$$\lambda = \frac{n_s e^2 \tau}{m^* \left[\alpha + (\omega_c \tau)^2 \right]}. \tag{5.7}$$

The tensorial representation of $\mathbf{j}$ can thus be written as

$$\mathbf{j} = \lambda \begin{pmatrix} \alpha & \omega_c \tau \\ -\omega_c \tau & 1 \end{pmatrix} \mathbf{E} = \sigma \mathbf{E}. \tag{5.8}$$

Tensor inversion of the conductivity σ in Eq. (5.8) then gives the general tensor of the specific resistivity ρ in an anisotropic system

$$\rho = \frac{1}{\lambda\left[\alpha + (\omega_c\tau)^2\right]} \begin{pmatrix} 1 & -\omega_c\tau \\ \omega_c\tau & \alpha \end{pmatrix} = \frac{m^*}{n_s e^2 \tau} \begin{pmatrix} 1 & -\omega_c\tau \\ \omega_c\tau & \alpha \end{pmatrix}. \tag{5.9}$$

Now, we rotate the coordinate system of the current density $\mathbf{j}$ and electric field $\mathbf{E}$ with respect to the original anisotropic reference system by an angle φ engaging the rotational operator $\mathcal{R}_\varphi = \left(\begin{smallmatrix} \cos\varphi & -\sin\varphi \\ \sin\varphi & \cos\varphi \end{smallmatrix}\right)$, such that $\mathbf{j}' = \mathcal{R}_\varphi \mathbf{j} = \mathcal{R}_\varphi \sigma \mathcal{R}_\varphi^{-1} \mathcal{R}_\varphi \mathbf{E} = \tilde{\sigma}\mathbf{E}'$. The rotated conductivity tensor $\tilde{\sigma}$ thus yields

$$\tilde{\sigma} = \lambda \begin{pmatrix} \alpha\cos^2\varphi + \sin^2\varphi & \omega_c\tau + (\alpha-1)\cos\varphi\sin\varphi \\ -\omega_c\tau + (\alpha-1)\cos\varphi\sin\varphi & \cos^2\varphi + \alpha\sin^2\varphi, \end{pmatrix}. \tag{5.10}$$

This way, the general resistivity tensor $\tilde{\rho} = \tilde{\sigma}^{-1}$ with respect to an anisotropic 2D system is then given by

$$\tilde{\rho} = \frac{1}{\lambda\left[\alpha + (\omega_c\tau)^2\right]} \begin{pmatrix} \frac{1}{2}\left[1+\alpha+(1-\alpha)\cos 2\varphi\right] & -\omega_c\tau + (1-\alpha)\cos\varphi\sin\varphi \\ \omega_c\tau + (1-\alpha)\cos\varphi\sin\varphi & \frac{1}{2}\left[1+\alpha-(1-\alpha)\cos 2\varphi\right] \end{pmatrix}. \tag{5.11}$$

Considering the situation at zero magnetic field $B = 0$ and $\mathbf{j}' = \left(\begin{smallmatrix} j'_{x'} \\ 0 \end{smallmatrix}\right)$, with $j'_{y'} = 0$ and $j'_{x'}$ along the main axis of a rotated Hall bar, the components of $\mathbf{E}' = \tilde{\rho}\mathbf{j}'$ are

$$\begin{pmatrix} E'_{x'} \\ E'_{y'} \end{pmatrix} = \frac{1}{n_s e\mu} \begin{pmatrix} \frac{1}{2}\left[1+\alpha+(1-\alpha)\cos 2\varphi\right] \\ \frac{1}{2}(1-\alpha)\sin 2\varphi \end{pmatrix} j'_{x'}. \tag{5.12}$$

By this, we have deduced an expression for the Hall resistivity component

$$\tilde{\rho}_{x'y'} = \frac{1}{n_s e\mu}\frac{(1-\alpha)}{2}\sin 2\varphi, \tag{5.13}$$

which is non-zero, even at $B = 0$ T, for a rotation with respect to an anisotropic system, meaning $\varphi \neq 0°$ or $90°$ and $\alpha \neq 1$. Additionally, Eq. (5.13) reveals the characteristic sine-dependence of the offset phenomenology we searched for, being maximal for $\varphi = \pm 45°$ in diagonal configuration to the anisotropic system.

The newly established Eq. (5.13) is now applied in fitting the experimental data of offsets $\Delta\tilde{\rho}_{x'y'}(0)$ of various angular orientations φ with respect to the anisotropic system, first for the set of InAs:Mn HB samples of Sec. 5.2.1 (wafer C120314B) which was used to introduce the empirical sinusoidal trend of the phenomenon in Fig. 5.3 in the first place. The notation of the assigned angles of crystallographic directions is slightly changed in the manner of the scheme Fig. 5.8 (a), again sketched on the background of an AFM image of the cross-hatched surface of the indium system. Precise angles were deduced from measuring light-optical microscope images of the

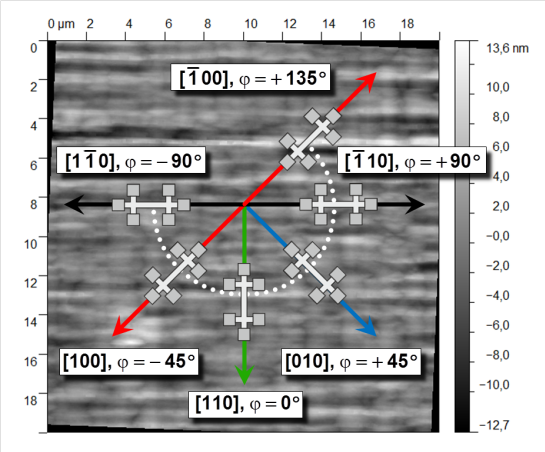

(a)

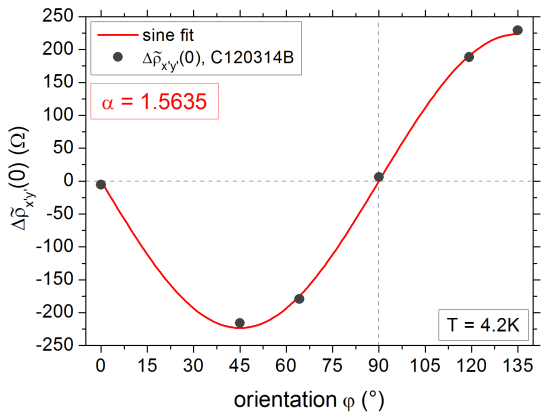

(b)

Figure 5.8: **(a)** *Scheme of the range of angular Hall bar orientations φ with respect to the* [110] *direction of $\varphi = 0°$ in the spectrum of studied crystallographic directions of the cross-hatched InAs system.* **(b)** *The acquired experimental offsets $\Delta\tilde{\rho}_{x'y'}(0)$ of the InAs:Mn system (wafer C120314B), already introduced in Fig. 5.3 of Sec. 5.2.1, for different orientations φ in the notation of (a) at $T = 4.2$ K. The sinusoidal trend of $\Delta\tilde{\rho}_{x'y'}(0)(\varphi)$ is excellently fitted by Eq. (5.13) (red curve) suggesting an anisotropy of 36.1 % from the anisotropy factor $\alpha = 1.5635$.*

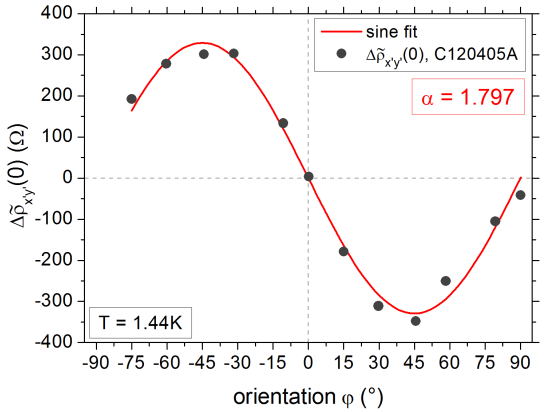

(a)

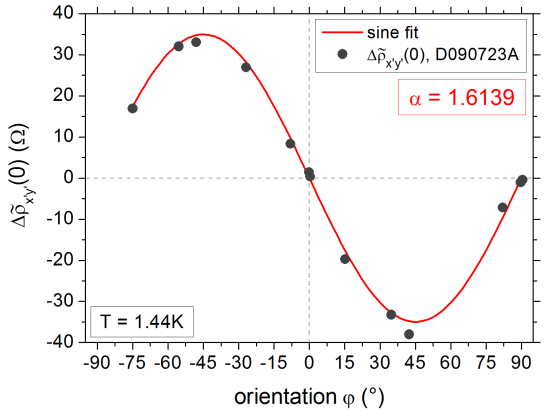

(b)

Figure 5.9: *Experimental offset data $\Delta\tilde{\rho}_{x'y'}(0)$ of various rotated Hall bar samples of orientations φ according to the scheme Fig. 5.8 (a) at $T = 1.44$ K of another InAs:Mn (wafer C120405A)* **(a)** *and the AlGaAs:C QW heterosystem (wafer D090723A)* **(b)**. *Applying Eq. (5.13) in fitting a sine function to the experimental offsets (red traces) yields anisotropy factors α that correspond well with the particular experimental mobility anisotropies.*

devices with respect to the cross-hatching or the sharp breaking edges of the samples along the $\langle 110 \rangle$ directions.

We find that the data in Fig. 5.8 (b) can be fitted precisely by Eq. (5.13) using the experimentally acquired hole density and maximum hole mobility $\mu \equiv \mu_{[\bar{1}10]}$, with the anisotropy factor α being the sole fitting parameter. Thereby, we yield a factor of $\alpha = 1.564$ or, in other terms, an anisotropy of 36.1 %. This is in good agreement with the mobility anisotropy of this particular set of Hall bars of about $\Delta\mu = 35.4$ % (cf. Tab. 5.2). Hence, this suggests that the offset phenomenology of a system rotated in-plane really is the direct consequence of existing anisotropic mobilities in the reference system.

In order to put this finding on a firm experimental basis, we also performed angular scans of another identical InAs:Mn QW heterosystem (wafer C120405A, $T_{\mathrm{Mn}} = 690$ °C), as well as of again the AlGaAs:C QW system (wafer D090723A) already presented in Fig. 5.7 of Sec. 5.2.2, by Hall bars patterned along different orientations φ. Once again, excellent correlation of the experimental offset data $\Delta\tilde{\rho}_{x'y'}(0)$ and the sine fitting curve from Eq. (5.13) is achieved for both the InAs:Mn system in Fig 5.9 (a) and the AlGaAs:C system in Fig. 5.9 (b). For the InAs:Mn system, 2D hole mobilities of $\mu_{[\bar{1}10]} = 1.91 \times 10^4$ cm^2/Vs and $\mu_{[110]} = 1.05 \times 10^4$ cm^2/Vs yield a mobility anisotropy of $\Delta\mu = 45.0$ % that reflects well the system's anisotropy of about 44.4 % suggested by the fit parameter $\alpha = 1.797$ in Fig. 5.9 (a). Anisotropic interface roughness in the AlGaAs:C system was identified to cause a $\Delta\mu \approx 38.4$ % in the previous Section 5.2.2 (cf. Tab. 5.2). This is also very well represented by the anisotropy factor $\alpha = 1.6139$ in Fig. 5.9 (b), giving an anisotropy of about 38.0 %.

Employing an extended framework of the Drude magnetotransport model in a magnetic field including distinguished anisotropic scattering times, we have thus comprehensively described the offset phenomenon of the classical Hall effect as a direct consequence of the deviating alignment of a Hall system with respect to a given system of twofold anisotropic mobility axes.

5.2.4 Overshooting of $\rho_{xy}(B)$ at quantizing fields

As it was already indicated in the offset traces of the transverse magnetoresistivities of Hall bars in diagonal crystallographic configuration at $T = 4.2$ K in Fig. 5.2 of Sec. 5.2.1, anomalies in the quantized plateaus of $\rho_{xy}(B)$ are emerging as the system enters the integer quantum Hall regime at higher magnetic fields, $\mu B = \omega_c \tau_{tr} > 1$. These anomalies shape up to become a clear, well pronounced overshooting of $\rho_{xy}(B)$ at the low-magnetic field ends of quantized Hall plateaus when the temperature of the system is reduced. Figure 5.10 depicts these prominent non-monotonic overshootings of $\rho_{xy}(B)$ in the magnetotransport curves of a HB sample A (red traces) that is aligned along the [100] direction at $T = 30$ mK, fabricated from the known InAs:Mn wafer C120314B of previous sections. A second $\rho_{xy}(B)$ curve of another HB device B (black trace) from the same InAs wafer, yet aligned in $[\bar{1}10]$ orien-

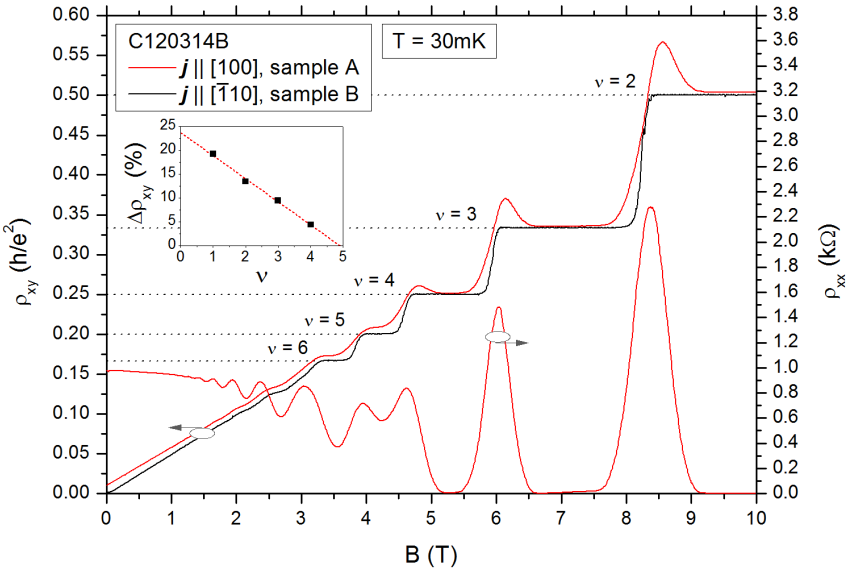

Figure 5.10: *Characteristic low-temperature 2DHG magnetotransport measurements at* $T = 30$ mK *of two Hall bar devices of wafer C120314B known from previous sections:* $\rho_{xy}(B)$ *and* $\rho_{xx}(B)$ *of a sample A, where the current is aligned along the diagonal crystallographic direction* $\mathbf{j} \parallel [100]$ *(red curves), are shown, and, for comparison,* $\rho_{xy}(B)$ *of another sample B with* $\mathbf{j} \parallel [\bar{1}10]$ *(black curve). A clear overshooting is observed at the beginning of the expected quantum Hall plateaus in* $\rho_{xy}(B)$ *of sample A at both even and odd filling factors, while there is nothing alike in the* ρ_{xy} *trace of sample B. As seen from the inset, the relative magnitude of the overshoot* $\Delta\rho_{xy}$ *increases linearly (red dashed line) with decreasing filling factor* ν*.*

tation, is included as a reference system of the regular quantum Hall effect. The overshooting occurs for sample A only, at both even and odd filling factors, being most pronounced below $\nu = 5$. It is found that the relative magnitude of the resistivity overshooting, $\Delta\rho_{xy} = \left(\rho_{xy,max} - \frac{R_K}{\nu}\right) / \frac{R_K}{\nu}$, decreases linearly with respect to the dimensionless filling factor ν. This is indicated in the inset of Fig. 5.10 by the red dashed line as a guide to the eye, including $\Delta\rho_{xy}$ at $\nu = 1$, not shown in the main plot. Despite the offset of $\rho_{xy}(B)$ along the [100] direction, the expected resistance value of the respective quantum Hall plateau is still restored at higher magnetic fields beyond the overshooting at the low-magnetic-field beginning of the plateau.

The formation of this robust phenomenon is obviously again related to the crystallographic orientation of the Hall bar, since a pronounced overshooting in $\rho_{xy}(B)$ only arises in offset directions to the distinguished anisotropic directions $[\bar{1}10]$ and $[110]$.

In the explanation of this phenomenon, therefore, a number of models found in literature for similar overshooting behaviors of $\rho_{xy}(B)$ are likely to be disregarded, as they are typically based on more isotropic approaches, regardless of any causal

relation to anisotropies.

Overshoots in the Hall magnetoresistance of AlGaAs/GaAs heterosystems have been documented by Komiyama *et al.* [115] and Richter *et al.* [116] in the early 1990s, yet only for odd integer filling factors arising from the Zeeman splitting of quantized energy levels according to their interpretation. Richter *et al.* [116] claimed exchange enhancement of the effective g-factor to cause a rapid decoupling of the highest filled and lowest empty bulk energy levels of opposite spin, thus resolving a previously unresolved, strongly coupled spin-split Landau level at certain magnetic fields. The overshooting therefore emerges at the onset of the expected spin-resolved quantized plateau where the two spin-split levels are not yet separated.
Alternatively, Komiyama *et al.* [115] stated that spin-orbit interaction plays a dominant role in the cause of this effect at odd filling factors by the scattering occurring from the mixing of opposite spin states in a LL, which are strongly coupled at the edges of the sample while being decoupled in the bulk. Later, Ramvall *et al.* [117] followed these considerations of coupling effects in between such resolving spin-split energy levels in the interpretation of overshootings in the magnetotransport of an $In_{0.75}Ga_{0.25}As$/InP QW heterosystem at again exclusively odd integer filling factors.

Recently, Kendirlik *et al.* [118] demonstrated the anomalous resistance overshoot in quantum Hall plateaus of a 2DEG in AlGaAs/GaAs heterosystems. The effect occurred for both odd and even integer filling factors making a spin-dependent approach less promising. While the previous discussions were based on the Landauer-Büttiker formalism of one-dimensional edge channels (cf. Sec. 2.1.3), here, the authors employed the idea of scattering between coexisting edge or bulk so-called evanescent incompressible strips in the framework of the self-consistent screening theory of the integer quantum Hall effect (see also [10]). The particular comprehensive model used was first introduced by Sailer and Wild *et al.* [119] for the overshooting in Si/SiGe QW heterostructures, where they crucially considered the direct Coulomb interaction in the 2D carrier system. In the framework of the screening theory, quantized Hall plateaus directly emerge from the confinement of current to incompressible regions, so-called strips, within the 2D carrier system. Under certain conditions, these incompressible strips are to become evanescent below the low-magnetic field edge of a quantum Hall plateau at the edges of the sample, meaning carriers leak into surrounding so-called compressible regions, before fading completely. Depending on the experimental conditions, more than one of these evanescent incompressible strips of different filling factors are supposed to coexist at the edges of the sample for certain magnetic fields. If these strips are then narrower than the Fermi wavelength but exceed the magnetic length, carriers can scatter in between these adjacent evanescent incompressible regions. This leads to the formation of the overshoot, as such leaking incompressible strips are characterized by dissipative current transport [118]. A detailed complete picture of this concept can be found in [119] and [120].

In their experimental investigations of the resistance overshoot, Sailer *et al.* re-

ported on a temperature-(current-)dependence of the magnitude of the effect that is decreasing with increasing temperature (current) [119, 120]. The same experimental behavior is found for the overshoots in $\rho_{xy}(B)$ of our exemplary InAs:Mn sample A of Fig. 5.10 along the [100] crystallographic orientation. The reduction of the magnitude of the effect by heating the carrier gas from $T = 30$ mK up to $T = 800$ mK is demonstrated in the Figure 5.11 (a) detail view of $\rho_{xy}(B)$ at the resistivity level corresponding to $\nu = 3$ for a constant excitation current of $I = 200$ nA. A linear

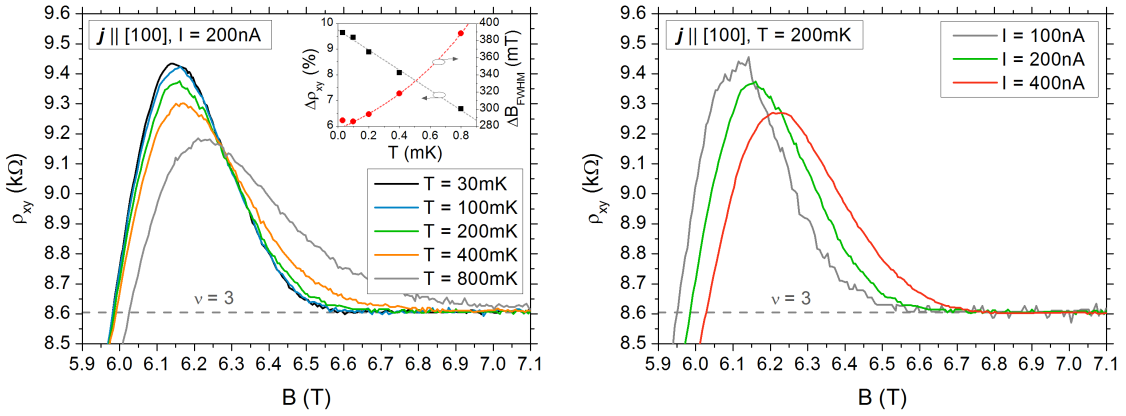

Figure 5.11: (a) *Detail view of the temperature-dependence of the overshooting of* $\rho_{xy}(B)$ *for* $\mathbf{j} \parallel [100]$ *at the onset of the quantum Hall plateau associated with* $\nu = 3$ *in Fig. 5.10. The shape of the overshoot clearly varies with increasing temperature for a constant current of* $I = 200$ nA*: The inset reveals the relative magnitude of the effect* $\Delta\rho_{xy}$ *to be reduced linearly with increasing temperature, while the width of the overshoot* ΔB_{FWHM} *increases exponentially (dashed lines are guides to the eye).* **(b)** *The dependence of the same overshoot formation on varying the current strength at a constant temperature of* $T = 200$ mK*. With the magnitude of the effect again being reduced and the width being increased with enhanced strength of the current, both dependences are of similar character.*

decrease of the relative magnitudes $\Delta\rho_{xy}$ of the overshooting with the temperature is documented in the inset of Fig. 5.11 (a). Simultaneously, the width of the overshoot ΔB_{FWHM} is broadened exponentially above $T = 100$ mK[3] (also see the inset of Fig. 5.11 (a)), while the peak position of the overshooting is being shifted towards higher magnetic fields within the plateau. A similar dependence of $\rho_{xy}(B)$ is observed for varying the strength of the current at a constant temperature of $T = 200$ mK in Fig. 5.11 (b). Since current transport is dissipative in the overshooting regime, Joule heating has a comparable effect on the overshooting formation as increasing the temperature of the system before.

[3]Below $T = 100$ mK, ΔB_{FWHM} saturates.

While there is a resemblance to be found in these dependences to the observations made by e.g. Sailer *et al.*, none of the experiments from literature presented above seem to experience the offset phenomenon at $\rho_{xy}(0)$ that is inseparably correlated with the occurrence of the observed type of overshooting in both odd and even quantized Hall plateaus of the anisotropic systems of this chapter. In fact, no specifications are typically given regarding the exact crystallographic orientation of sample structures.
Instead, the discussed approaches seem to share a common theme of the overshooting effect being correlated with the coupling of closely spaced energy levels. In Sections 5.2.2 through 5.2.4, we have identified and established differing orientations of anisotropic mobilities with respect to a reference system to provoke both the offset and the simultaneously occurring overshoot phenomenon. Qualitatively, the two distinguished anisotropic mobilities might resemble a sort of two-level system closely spaced in energy. The reason for the overshooting along the off-directions may then lie within a dissipative coupling or mixing of these energy levels overlapping, which could be resolved at higher magnetic fields. A thermal broadening of such levels would then shift the restoration of an expected plateau towards higher magnetic fields as it is indicated in the exponential temperature-dependence of ΔB_{FWHM} in the inset of Fig. 5.11 (a).
In the picture of evanescent incompressible strips, their coexistence seems to be more pronounced in diagonal directions for reasons still to be investigated.

Further experimental and theoretical studies are required to back these first qualitative considerations. Angular-resolved HB magnetotransport measurements of $\rho_{xy}(B)$ in the overshooting regime of the magnetic field for instance, could further support this two-mobility-mixing hypothesis.

5.3 Conclusion

In this chapter, we have illustrated that the magnetotransport properties of InAs heterostructures are highly anisotropic. The cross-hatching morphology, which originates from peculiarities of metamorphic buffer layer growth for strain relaxed layers of high indium content, crucially influences scattering and hence the mobilities along the distinguished $\langle 110 \rangle$ crystallographic directions. Corresponding to the characteristic periodicities of the cross-hatching undulations, the hole mobility is highest in $[\bar{1}10]$, lowest in [110] and intermediate in the [100] and [010] directions. Particularly, both the asymmetric valence energy band modulation due to periodic fluctuations of the indium concentration in the ternary $In_{0.75}Ga_{0.25}As$ layers as well as spatial variations of residual strain seem to contribute to the anisotropic scattering of hole transport in the cross-hatched 2D system.

The anisotropic nature of the system is also key to the occurrence of magnetotransport anomalies in the transverse Hall resistivity curves of the two-dimensional carrier system. In the so-called diagonal Hall bar configuration aligned along the

⟨100⟩ crystallographic directions of the InAs system, $\rho_{xy}(B)$ is characterized by overshootings at the beginning of quantum Hall plateaus and by a robust, symmetric offset even at $B = 0$ T. Although first prominently identified in the cross-hatched InAs 2D hole gas system, a comparative study of a variety of semiconductor heterosystems revealed that this offset effect is in fact a more universally relevant phenomenon scaling with the occurrence of a periodic perturbation: Within an extended framework of the magnetic Drude model explicitly considering a general twofold anisotropy of the system, we were able to demonstrate that any 2D system experiencing anisotropic scattering is bound to show this effect in the classical Hall regime along any orientation differing from the ⟨110⟩ directions of the distinguished anisotropies.
We believe that this non-zero Hall resistance at zero magnetic field is an important issue to be addressed, as this universal aspect of magnetotransport experiments in anisotropic systems is not well known and thus commonly lacks interpretation or may even be misinterpreted.
As for the correlated overshooting phenomenon in the quantum Hall regime of anisotropic systems, further investigations are needed to prove a similar causal relation to the existence and possible effective mixing of anisotropic scattering.

Having established a profound impression of fundamental anisotropic magnetotransport features arising from the peculiarities of the cross-hatching morphology of the InAs system, we can now focus on the magnetoresistive subtleties of the InAs:Mn QW 2D hole gas system. In the next, main chapter of this thesis, a thorough analysis of the corrections to the longitudinal magnetoresistivity in particular will provide more information on the nature of the hole gas transport of the system and on key objectives of our study, like the investigation of the tunability of the spin-orbit interaction.

6

Spin-orbit interaction and quantum interference of 2DHGs in disordered InAs:Mn QW heterostructures

6.1 Introduction

Research in the field of spintronics has been fuelled by the idea to electrically generate, modulate and detect a spin-polarized current in semiconductor heterostructures. In this effort, many approaches make use of the materials' intrinsic property of spin-orbit interaction. With the Dresselhaus SO term from bulk inversion asymmetry basically being a fixed property of the semiconductor material, it is the Rashba SO field generated by the structure inversion asymmetry of the potential confining a 2D carrier system (cf. Sec. 2.2.2) that offers a way to tune the SO splitting experimentally. In this chapter, we evaluate the possibilities the $In_{0.75}Al_{0.25}As$/-$In_{0.75}Ga_{0.25}As$/InAs:Mn 2DHG QW system offers in the field of 'spin-orbitronics' [121], as we characterize the nature and strength of the SO interaction by its manifestation in magnetoresistive phenomena of quantum interference.

Spin-orbit coupling in indium-based heterosystems

Historically, amongst several methods allowing for the experimental characterization of the spin-orbit-induced subband spin splitting of 2D carrier systems, the observation of the so-called beating signature in SdH oscillations of the high-field lon-

gitudinal magnetoresistance has proven to be the most conveniently accessible one [122]. Analyzing this characteristic pattern of two subbands with slightly differing densities, thus Störmer *et al.* [123] provided the first demonstration of an inversion asymmetry-induced spin splitting for a 2D hole gas in the valence subbands of an AlGaAs/GaAs heterojunction, which was backed by cyclotron resonance experiments. Eisenstein *et al.* [124] subsequently confirmed the structurally asymmetric origin of the lifting of the spin degeneracy in the lowest AlGaAs/GaAS QW valence subband, until it were Luo *et al.* [125] and Das *et al.* [126] who independently reported spin splitting of 2DEGs by beatings in the conduction band magnetotransport of GaSb/InAs and InGaAs/InAlAs heterostructures, respectively. A more indirect and subtle approach on the quantification of the spin-orbit interaction was then led by Dresselhaus *et al.* [127] by evaluating the precession of spins from the weak antilocalization effect of quantum interference at low magnetic fields of a 2DEG in AlGaAs/GaAs inversion layers (see Sec. 2.1.5). In an innovative work, Jusserand and colleagues [128] were also able to engage Raman scattering experiments in providing comprehensive data on the spin splitting of 2DEGs in AlGaAs/GaAs QWs. Additionally, by measuring the spin-galvanic photocurrent on n-type InAs QWs, Ganichev *et al.* [129] have found a direct way to extract information on the ratio of Rashba and Dresselhaus SO terms.

A variation of the Rashba SOI in indium-based systems by the field effect of a metallic gate electrode has particularly remained an interesting challenge, since it closely resembled the original proposal of the electronic analogue of the electro-optic modulator by Datta and Das [7], where current modulation arises from the SOC-induced spin precession in a narrow-gap semiconductor [11]. In 1997, Nitta *et al.* [12] and Engels *et al.* [130] were the first to succeed in demonstrating the tuning of the Rashba SOI parameter α and of the spin splitting energy by an external gate bias in n-type InGaAs/InAlAs and InGaAs/InP QW heterostructures, respectively. Also using indium-based III-V compound systems, Grundler [131] then showed in an InAlAs/InGaAs QW with inserted InAs channel that the SIA Rashba coefficient of the 2D electron system really is tuned by an external topgate voltage, as the total density was being kept fixed by a second backgate. This was attributed to the fact that the wave function asymmetrically penetrating the interface barriers provided the main contribution to the Rashba term.

Being now able to fabricate strain relaxed QW heterostructures with a high fraction of the high-SOC material indium, the $In_{0.75}Al_{0.25}As/In_{0.75}Ga_{0.25}As/InAs$ system presented in Section 4.3 hosting a 2D hole gas of high effective masses is suited to study a pronounced Rashba SO interaction. Here, we present an extensive investigation of the tunability of the Rashba SOI in this 2DHG system in terms of a continuous tuning of the hole density p. A significant change in p could be achieved by the joint efforts of the variation of the Mn doping concentration during epitaxy and an additional external electric gating of magnetotransport devices. An external electric field induced by the metallic gate electrodes and the internal potential of an asymmetric doping profile should affect both the density and the structural

asymmetry of the well, and hence its internal effective electric field, making p a viable parameter to indicate the field modulation (cf. Eq. (2.21) in Sec. 2.2.2). The existence of a pronounced SOI, however, is also a double-edged condition: On the one hand, spin manipulation is enabled, yet on the other hand, it also represents a source of spin relaxation with spins precessing around the effective Rashba field (see Sec. 2.2.3). In order to address these aspects of the SO system, we focus our studies of this field variation particularly in correlation to a hole density reduction, to quantify the nature of the interaction and to follow its influence on spin relaxation. In the framework of the DP mechanism (see Sec. 2.2.3), enhanced spin coherence might be possible in a low-density regime of the InAs 2DHG QW system due to an increased scattering by disorder.

Defining regimes of longitudinal magnetoresistive phenomena by variation of the hole density

All insights from this study are based on a set of four different MBE-grown wafers whose initial concentration of manganese doping was systematically decreased by a reduction of the temperature of the Mn effusion cell T_{Mn}: starting from $T_{\mathrm{Mn}} = 787\,^{\circ}\mathrm{C}$ for the wafer of ID C120314B, by $T_{\mathrm{Mn}} = 690\,^{\circ}\mathrm{C}$ for C120405A, to $T_{\mathrm{Mn}} = 663\,^{\circ}\mathrm{C}$ for C120404B and $T_{\mathrm{Mn}} = 656\,^{\circ}\mathrm{C}$ for C120530A (cf. Appendix B). By reducing the total density of holes in gated Hall bar devices within this variety of non-magnetic InAs:Mn QW heterostructures, the 2DHG systems are found to probe different regimes of magnetoresistive phenomena in the low-temperature longitudinal magnetoresistance. A survey, Fig. 6.1, is thought to provide a general first orientation in this complex spectrum of magnetoresistive phenomena in the traces of $\rho_{xx}(B)$ and to give an impression of the need to disentangle their individual contributions in order to extract reasonable SO-related parameters. The complete accessible density regime ranging from about $p = 6 \times 10^{11}\ \mathrm{cm}^{-2}$ down to $p = 2 \times 10^{11}\ \mathrm{cm}^{-2}$, as indicated by the p-scale in Fig. 6.1, can be divided into a high- and a low-density part of the spectrum with the borderline being set at about $p = 4 \times 10^{11}\ \mathrm{cm}^{-2}$. For orientation, wafers showing magnetoresistive features associated with the high-density regime, wafers C120314B and C120405A, or with the low-density regime, C120404B and C120530A, are placed along the p-scale according to their intrinsic sheet carrier densities. Two characteristic longitudinal magnetotransport traces $\rho_{xx}(B)$ at $T = 30$ mK from representative measurements of the high-density (right diagram in Fig. 6.1) and the low-density regime (left diagram) illustrate this differentiation. Distinctively different magnetoresistive phenomena are found in the high-, mid- and low-field-regimes of applied magnetic fields B (indicated by white and grey shaded areas): For the low-field region, the inset detail views of $\rho_{xx}(B \to 0)$ above both main plots of Fig. 6.1 reveal effects of quantum interference shaping the trace of ρ_{xx} around $B = 0$ T. In the high-density regime, weak antilocalization dominates, while a dominant weak localization signature emerges when the system descends into

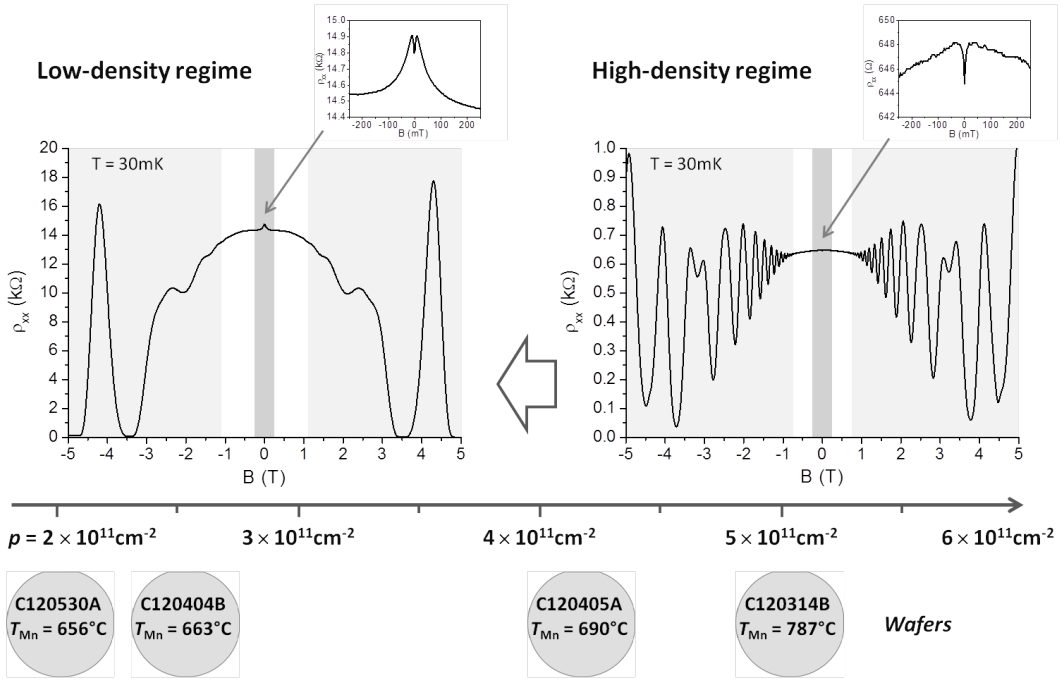

Figure 6.1: *A survey sketch for the classification of the characteristic high-, mid- and low-B-field phenomena of the longitudinal magnetoresistivities $\rho_{xx}(B)$ of 2D hole gases in this work's non-inversely doped InAs:Mn QW heterostructures, as they are expected and discussed in this chapter in terms of hole density variation. The density p is continuously tuned from a high-density (associated with wafers C120314B and C120405A) to a low-density regime (C120404B and C120530A) via a combination of reducing the Mn doping concentration by lowering the temperature of the Mn effusion cell (T_{Mn} of the depicted wafers) and additional external electric gating. Special interest is paid to the evolution of the low-field quantum interference effects of weak antilocalization and weak localization (see the detailed view of ρ_{xx} around $B = 0$ T above the main plots) as the they offer a gateway to the spin-orbit interaction of this system.*

the low-density regime. In the so-called mid-field region (white segments in Fig. 6.1) beyond these quantum interference effects and before the SdH oscillations dominate the high-field quantum Hall region in the light grey area, a pronounced negative parabolic background characterizing the trace of $\rho_{xx}(B)$ is most clearly visible in both carrier density regimes. The presence of the sharp weak antilocalization SO feature in the vicinity of $B = 0$ T enables the analysis of an apparently strong SO coupling in the 2DHG InAs QW systems of this work.

Given the introduced classification of magnetoresistive regimes, this chapter is composed as follows: From HB measurements of wafers C120314B and C120405A, Section 6.2 first considers the individual analysis of the characteristic high-, mid- and low-field features of the longitudinal magnetoresistances in the high-density part

of the p-spectrum of the right side in Fig. 6.1. Therein, in Sec. 6.2.1, the nature of the prominent mid-field parabolic NMR background of the white region in the right panel is identified, which then allows the approximation of the anisotropic effective hole mass from the T-dependence of the SdH oscillations in the high-field regime in Section 6.2.2, a property essential to the further discussion. Indicated in the inset of the right panel, the low-field behavior of the magnetoresistance is dominated by a pronounced WAL dip signature of SO quantum interference, whose analysis in terms of crystallographic directions as well as gate- and temperature-dependence in Sec. 6.2.3 allows to characterize the phase- and spin-coherent transport of the anisotropic diffusive SO system.
With the density of the InAs 2DHG system being lowered, we find in Section 6.3 that the WAL undergoes a transition towards a WL-dominated magnetoresistance in the low-density regime (Sec. 6.3.1, see the insets of the right and left panel in Fig. 6.1, respectively). This implies a possible manipulation of the Rashba SOI and hence the splitting of hole spin subbands (Sec. 6.3.2). By eventually addressing the localization-induced enhancement of the low- and mid-field magnetoresistive behavior in the low-density limit of this study in Sec. 6.4 from measurements of wafers C120404B and C120530A, a comprehensive picture of the evolution of quantum interference phenomena in the disordered InAs:Mn hole gas QW system has been compiled in this range of hole densities.

6.2 Diffusive magnetotransport of high-density 2DHGs

The experiments of this chapter were performed in a ^{3}He/^{4}He dilution refrigeration system with a base temperature of 15 mK for measurements up to 1000 mK in a perpendicularly applied magnetic field up to 19 T, while a ^{4}He dewar cryostat enabled temperatures of 4.2 K and 1.44 K at $B = 6$ T (see Sec. 3.3). For the electric characterization, standard lock-in techniques at a frequency of 17 Hz were applied with constant excitation currents of normally 10 nA or 300 nA in the dilution system and up to 1 μA in the dewar refrigerator. Samples were modelled in Hall bar geometries of different crystallographic orientations, as introduced in Sec. 3.3, and equipped with a metallic Ti/Au-topgate above insulating layers of Al_2O_3 (see Appendix A for fabrication details). The density of the 2D hole gas is determined from the $1/B$-periodicity of the minima of the SdH oscillations in $\rho_{xx}(B)$ and confirmed by the slope of the Hall resistivity $\rho_{xy}(B)$, with the average 2D carrier mobilities then being calculated from the zero-field magnetoresistivity $\rho_{xx}(0)$ by Eq. (2.12).

Both the density and the mobility change systematically with the gate bias V_G. Figure 6.2 displays a typical $p(V_G)$-characteristic of a gated HB sample, here from wafer C120314B, which reveals an apparently strong hysteretic behavior between an initial accumulating sweep of V_G from about +30 V down to −30 V (black branch)

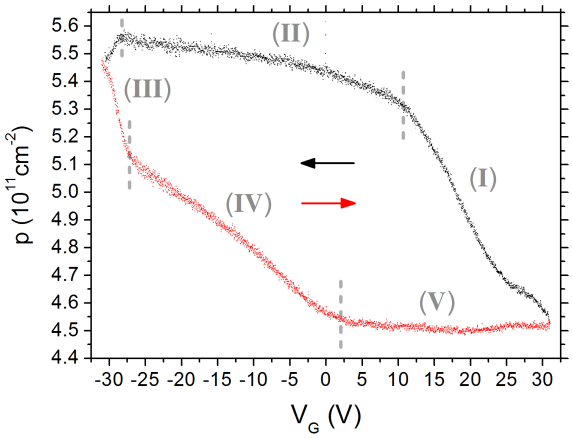

Figure 6.2: *An exemplary continuous variation of the hole density p by a gate bias voltage V_G reveals a pronounced hysteresis between an accumulating sweep of V_G (black) and a back sweep of V_G depleting (red) the 2DHG. Details of different stages of this evolution of $p(V_G)$ at corresponding Roman numerals are provided in the text.*

and an immediate subsequent back sweep of the gate bias depleting the 2DHG (red branch). Starting in a state of lowest hole density at $V_G = +30$ V, we observe a linear increase in density (**I**) as a decreasing gate electrode bias capacitively accumulates holes in the QW plane by the field effect, as it is expected for gated structures from theory [10]. With further reduction of the gate bias, however, the system enters a regime of saturation (**II**). This behavior was already discussed in other works for comparable doping schemes [132, 133, 134]: The doping layer of the heterosystem is situated between the topgate and the QW (cf. Fig. 4.3 in Sec. 4.3). Inducing an energy band bending by reducing the gate bias, carriers start to occupy either non-ionized remote acceptor states in the interjacent doping layer or charge 'traps' at the semiconductor-insulator interface, when the energy levels of these sites meet the Fermi energy level in the QW. A charge transfer via then energetically allowed tunnelling of carriers from the QW into these sites above the valence band edge sets in. By further reduction of the gate voltage, also the VB maximum of the doping layer reaches E_F enabling charge reconfiguration from the 2DHG into the doping layer with subsequent relaxation into higher localized states. By these processes, further increase of the 2D carrier density in the QW by the gate electric field is getting compensated due to an electrostatic potential build-up in the doping layer and saturation of $p(V_G)$ is observed. Reversing the gate bias at $V_G = -30$ V, the state of maximum hole density accumulation is rapidly decreasing linearly by the immediate capacitative depletion of the QW in (**III**) at a similar rate as in (**I**) with tunnelling from the 2DHG into the doping layer still being possible. As the impurity energy states fall below the Fermi energy with increasing V_G in (**IV**), the slope of $p(V_G)$ decreases, since the reverse charge transfer from the doping layer to the 2D hole system is too slow to cause a pronounced change of p [133]. The different regimes of the two segments (**II**) and (**IV**) thus illustrate asymmetric charge reconfiguration rates from the 2DHG to the doping layer and vice versa [133]. Finally, the system descends into a saturated level of the initial hole density in (**V**) as the doping layer is fully ionized.

In general, the absence of leakage currents in this range of comparably high gate

voltages indicates that excellent insulating quality of the dielectricum was achieved. Yet, the high voltages required to gain a significant change in the hole density also demonstrate that the capacitive coupling of the gate and the 2DHG in the QW is rather weak.

The gate-density-dependent measurements of this chapter have all been conducted starting from a hole gas system in a fully accumulated state. Following the red branch of $p\,(V_G)$ in Fig. 6.2, lower levels of carrier densities are then successively adjusted by gate-depleting the hole system. All magnetoresistive experiments of this Section 6.2 were performed on Hall bar samples of the high-density range of Fig. 6.1 with hole sheet densities above $p = 4 \times 10^{11}$ cm^{-2} and corresponding hole mobilities between about $\mu_h = 1.0 \times 10^4$ cm^2/Vs and 2.5×10^4 cm^2/Vs. In all plots of longitudinal resistivities ρ_{xx} of this chapter, the measured Hall bar magnetoresistances have been scaled according to their corresponding geometrical factor W/L (cf. Sec. 3.3).

6.2.1 Negative correction to the longitudinal magnetoresistivity

Apparent from Survey 6.1, aside from high-field SdH oscillations, all longitudinal magnetoresistivity traces $\rho_{xx}\,(B)$ of this study's regularly doped InAs:Mn QW heterostructures most prominently share a distinct parabolic negative background as a common feature in the magnetoresistance range of medium perpendicularly applied magnetic fields. A characteristic example of this negative correction to $\rho_{xx}\,(B)$ is on display in Fig. 6.3 for a HB sample of $T_{\mathrm{Mn}} = 690$ °C with a corresponding high hole density of $p = 4.58 \times 10^{11}$ cm^{-2} and a mobility of $\mu = 1.37 \times 10^4$ cm^2/Vs, aligned along the [010] crystallographic direction at $T = 1$ K. The magnetoresistive background (red dashed line in Fig. 6.3) is most clearly visible in the ρ_{xx} data below $B \approx 0.8$ T, before the onset of the SdH oscillations.
Generally, the field-dependent correction to the Drude magnetoresistance is most pronounced in $\rho_{xx}\,(B)$ along the low-mobility crystallographic direction and is en-

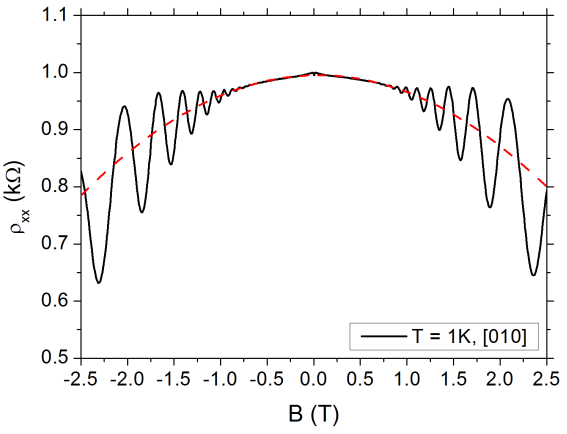

Figure 6.3: *Display of a typical curve of $\rho_{xx}\,(B)$ in the [010] direction of a HB sample ($T_{\mathrm{Mn}} = 690$ °C) at $T = 1$ K that is dominated by a distinct parabolic NMR background most clearly visible at magnetic fields below $B \approx 0.8$ T, as indicated by the red dashed line.*

hanced by reducing both the carrier density or the temperature. It is reported that a strong quasiclassical low-temperature NMR effect from the combined scattering by smooth long-range disorder and rare strong scatterers would manifest itself in a parabolic signature that is independent of temperature [135]. In contrast, here, the origin of this highly temperature-responsive correction may rather be attributed to the process of carrier-carrier interaction in the following.

It was Al'tshuler and Aronov [136] who led the theoretical interpretation of the carrier-carrier-interaction-induced correction to the classical Drude conductivity, which has its origin in the Coulomb interaction between carriers enhanced by their diffusive motion ($k_B T\tau/\hbar \ll 1$). Gornyi together with Mirlin [137] extended the theory to the ballistic transport regime ($k_B T\tau/\hbar \gg 1$). In the last decades, the effect has then widely been identified in e.g. high-quality AlGaAs/GaAs heterostructures for both high-mobility 2DEGs [138, 139, 109, 140] and high-mobility 2DHGs [141, 142].

From perturbation theory, a parabolic correction to the longitudinal component of the magnetoresistivity is described by [139, 143]

$$\rho_{xx}(B) = \rho_0^2 \left(\omega_c^2 \tau^2 - 1\right) \delta\sigma_{hh}, \tag{6.1}$$

where $\delta\sigma_{hh}$ denotes the correction to the Drude conductivity $\sigma_0 = 1/\rho_0$ induced by carrier-carrier interaction, henceforth hole-hole interaction, in the diffusive, so-called 'metallic' regime of $E_F\tau_{hh}/\hbar \gg 1$. When $k_B T\tau_{hh}/\hbar < 1$, the correction $\delta\sigma_{hh}$ in two-dimensional carrier systems is then given as [139, 143]

$$\delta\sigma_{hh} = -\left[4 - 3\frac{2+F}{F}\ln\left(1+\frac{F}{2}\right)\right]\left(\frac{e^2}{2\pi^2\hbar}\right)\ln\left(\frac{\hbar}{k_B T\tau_{hh}}\right), \tag{6.2}$$

with $F = \int \frac{d\theta}{2\pi}\left[1 + \frac{2k_F}{\kappa}\sin\left(\frac{\theta}{2}\right)\right]^{-1}$, the Hartree interaction factor, being the angular average over the statistically screened Coulomb interaction, the Fermi wave vector k_F and the inverse screening length κ.

The h-h interaction is characterized by the time scale of impurity scattering, τ_{hh}. It is expected that short-range scattering by magnetic impurities in the given modulation-doped InAs:Mn QW heterostructures is reduced, since the ionized impurities are well separated from the 2DHG by an undoped InAlAs spacer (cf. Sec. 4.3) and evidence of back diffusion of Mn dopants from the InAlAs:Mn layer into the QW and the spacer region beneath is missing. However, scattering by the long-range potential of remote Mn impurities with a correlation length depending on the thickness of the spacer layer still prevails.

In the following, the details of the interaction correction to $\rho_{xx}(B)$ are investigated by adopting the method established by Choi *et al.* [139]. In order to verify its parabolic nature, the correction $[\rho_{xx}(B) - \rho_{xx}(0)]/\rho_{xx}(0)$ to the Drude magnetoresistivity is thus plotted versus B^2 in Figure 6.4 for temperatures ranging from $T = 1000$ mK down to $T = 30$ mK, exemplarily for two gated Hall bar structures of wafers with (a) $T_{\mathrm{Mn}} = 690$ °C and (b) $T_{\mathrm{Mn}} = 656$ °C (cf. Fig. 6.1), both oriented

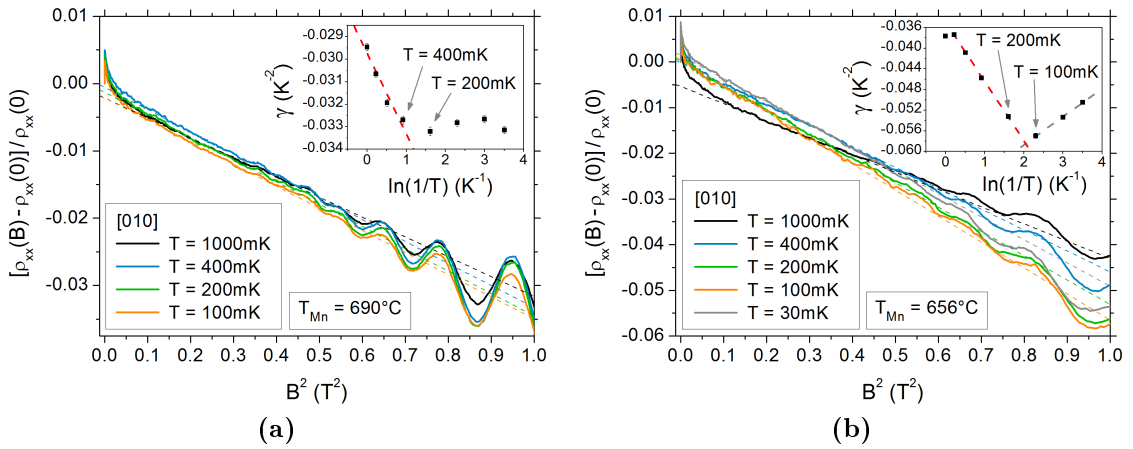

Figure 6.4: *Plotting negative corrections to the longitudinal Drude magnetoresistivity* $[\rho_{xx}(B) - \rho_{xx}(0)]/\rho_{xx}(0)$ *versus* B^2 *for various temperatures from* $T = 30$ mK *up to* $T = 1$ K *reveals the parabolic nature of the corrections in the mid-field range of gated Hall bar samples of* **(a)** $T_{\mathrm{Mn}} = 690\,^{\circ}\mathrm{C}$ *and* **(b)** $T_{\mathrm{Mn}} = 656\,^{\circ}\mathrm{C}$ *aligned along the* [010] *crystallographic direction, with corresponding hole densities* $p = 4.58 \times 10^{11}\ \mathrm{cm}^{-2}$ *and* $p = 3.88 \times 10^{11}\ \mathrm{cm}^{-2}$*, respectively (For clarity, only selected temperature traces are shown in both main plots). Dashed lines in the main plots represent the linear fits to the interaction corrections of slopes* γ*, while the insets show these* T*-dependent, linear slopes* γ *as a function of* $\ln(1/T)$*. Here, again linear fits to the data applying combined Equations (6.1) and (6.2) (red dashed lines) provide the h-h interaction times* τ_{hh} *of the systems.*

along the [010] crystallographic direction. While a second negative magnetoresistivity feature around zero magnetic field is associated with the suppression of the weak localization effect (see Sec. 2.1.5 and our later discussion in Sec. 6.4) and SdH oscillations start to dominate the traces above $B \approx 0.3$ T, both sets of data exhibit T-dependent, linear slopes γ at medium magnetic fields. Dashed lines in the main plots of Fig. 6.4 indicating the corresponding linear fits (cf. Eq. (6.1)) demonstrate that the magnitude of the slopes increases with reduced temperature. Plotting γ versus $\ln(1/T)$, as seen in the inset of Fig. 6.4, the h-h scattering times can then be extracted from linear fits combining Equations (6.1) and (6.2) under usage of the corresponding experimentally determined hole densities of $p = 4.58 \times 10^{11}\ \mathrm{cm}^{-2}$, Fig. 6.4 (a), and $p = 3.88 \times 10^{11}\ \mathrm{cm}^{-2}$, Fig. 6.4 (b). Here, τ_{hh} and the Hartree factor F are engaged as fitting parameters. This way, linear fits (red dashes in the insets of Fig. 6.4) suggest $\tau_{hh} \approx 0.37$ ps for the sample of $T_{\mathrm{Mn}} = 690\,^{\circ}\mathrm{C}$ (a) and a significantly longer $\tau_{hh} \approx 1.8$ ps in case of $T_{\mathrm{Mn}} = 656\,^{\circ}\mathrm{C}$ (b). The factor F yields approximately 1.665 in both cases (cf. $F = 1.5 - 1.7$ in [107]).
Unexpectedly, there is a distinct deviation from the linear temperature-dependence of γ that occurs between temperatures $T = 400$ mK and 200 mK in the inset of

Figure 6.4 (a) and between $T = 200$ mK and 100 mK in the inset of (b). In fact, this behavior was found in all HB structures of various crystallographic alignments that were evaluated during this study, with the temperature range of its appearance varying. A rather similar phenomenon was reported by Wurstbauer *et al.* [144] for identical InAs:Mn QW heterostructures of a significantly higher Mn doping concentration at comparable temperatures between $T = 610$ mK and 600 mK. The authors linked the occurrence of two different slopes in γ versus $\ln(1/T)$ in each of the crystallographic directions $[\bar{1}10]$ and $[110]$ to a simultaneously observed T-dependent transition from a weak-antilocalization-dominated signature around zero magnetic field to a signature of $\rho_{xx}(B)$ which was associated with an anisotropic magnetoresistance (AMR). The origin of the emerging AMR was suggested to be due to a phase transition from paramagnetic towards spontaneous ferromagnetic ordering of magnetic Mn^{2+}-ions in the InAlAs:Mn layer close to the 2DHG. It was argued that the resulting change in the properties of the impurity interaction times at the transition temperatures was hence related to exchange coupling of magnetically ordered moments and the free 2D holes' magnetic moments, as their wave functions are believed to penetrate into the doping layer region. In our work, however, a transition towards an AMR-like feature was observed only once: in the intermediate [010] direction of one particular HB structure ($T_{\mathrm{Mn}} = 690\,^{\circ}\mathrm{C}$, $p = 6.0 \times 10^{11}\ \mathrm{cm}^{-2}$) at a transition temperature between 4.2 K to 1.44 K, hence at higher T than in [144]. This transition is depicted in Figure 6.5 (a) where a distinctly increasing magnetoresistance feature at low magnetic fields emerges from a ρ_{xx} curve characterized by a small WAL signature at $B = 0$ T when cooling the sample from $T = 4.2$ K down to $T = 1.44$ K. While the WAL minimum in $\rho_{xx}(B)$ still superimposing the effect at $T = 1.44$ K remains located at $B = 0$ T upon inverting the sweep direction of the magnetic field in Fig. 6.5 (b), a small hysteresis of the magnetoresistive changes in the vicinity of $B = 0$ T illustrates the magnetic origin of the effect. This phenomenon was else absent in every other HB sample of this study and in particular in the other crystallographic HB orientations of this sample. The uniqueness of this finding thus indicates that this single observation most likely was due to local fluctuations of highest manganese doping concentrations. More importantly, our study demonstrates the occurrence of a deviation from a continuous linear dependence of γ at low temperatures in Fig. 6.4 in the clear absence of the AMR effect. We conclude that both phenomena are not necessarily linked as suggested in [144]. Still, in this context it should be noted that the evaluation of the h-h interaction time in identical InAs QW heterostructures, yet doped with non-magnetic carbon, by Hirmer revealed only a single linear slope in $\gamma(\ln 1/T)$ [107]. Also, the insets of Fig. 6.4 suggest a transition temperature scaling with the system's Mn doping concentration, as it is slightly lower for a significantly lower T_{Mn}. Consequently, both these arguments could support the reasoning for the origin of the low-temperature deviation in magnetic exchange coupling.

Apart from that, however, we have deduced an increased value of τ_{hh} at reduced concentrations of Mn from Fig. 6.4 which implies a reduced h-h interaction. The im-

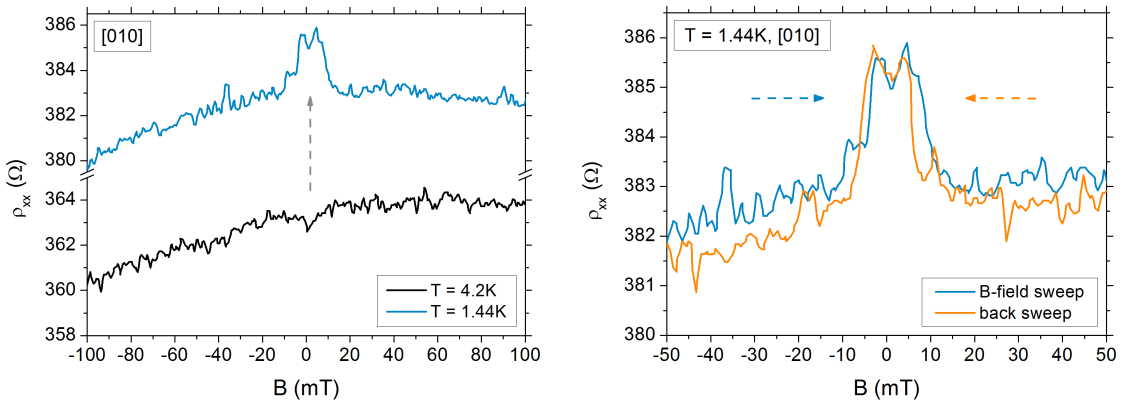

Figure 6.5: (a) *Single experimental observation of the magnetoresistive transition from a WAL- to an AMR-dominated* $\rho_{xx}(B)$ *trace in the vicinity of* $B = 0$ T *for the* [010] *direction of a HB sample (*$T_{\mathrm{Mn}} = 690$ °C, $p = 6.0 \times 10^{11}$ cm^{-2}*) upon reducing the temperature from* 4.2 K *down to* 1.44 K. **(b)** *Changing the sweep direction of the magnetic field (dashed arrows) reveals a hysteretic behavior of* $\rho_{xx}(B)$ *at low B-fields that demonstrates the magnetic origin of the effect.*

portance of carrier-carrier interactions in 2D systems is often parametrized by the dimensionless Wigner-Seitz radius $r_s = E_C/E_F = (\pi p)^{-1/2}/a_B$ [113, 145, 146, 147], as the average inter-electron separation measured in the effective Bohr radius a_B, defining the ratio of the Coulomb energy E_C to the Fermi energy E_F. Therefore, h-h Coulomb interactions are supposed to become more prominent at lower hole densities p, hence lower Mn doping concentrations. This cannot be confirmed from our findings for τ_{hh} in Fig. 6.4. For that reason, instead of effects of magnetic ordering, we favor emerging localization due to insufficient screening from long-range bare Coulombic disorder of charged impurities as an explanation for the low-temperature deviations in the given regular InAs 2D QW systems. While γ shows a more or less saturating behavior at lowest temperatures in the inset of Fig. 6.4 (a), it follows a dependence $\propto \ln(1/T)$ in Fig. 6.4 (b) (black dashed line). This latter dependence might be connected to a low-temperature, logarithmic increase of the resistance in the insulating phase of low-density disordered systems. We shall revisit and extend this interpretation of a disorder-dominated system in Section 6.2.3 focussing on spin dephasing by inelastic scattering and in Section 6.4 dealing with the effects of increasing disorder due to less screening in systems of further reduced density. Thereby, also the intuitively controversial observation that the magnitude of a h-h-interaction-induced background of the magnetoresistivity gets more pronounced with decreasing hole density or decreasing temperature is tackled. For now, we conclude that a background can be fitted with a parabolic correction to the longitudinal magnetoresistivity in all investigated samples reflecting h-h interaction. We subtract this

background from $\rho_{xx}(B)$ in order to study the dependences of high-field SdH oscillations or low-field effects of quantum interference in the following sections of this chapter.

6.2.2 Temperature damping of SdH oscillations: m_h^* and τ_q

We will determine the effective masses of holes m_h^* and also the quantum scattering time τ_q by an iterative analysis of the temperature- and magnetic-field-dependence, respectively, of the peak amplitudes of Shubnikov-de Haas oscillations. Since the physical interpretation of the longitudinal magnetoresistivity $\rho_{xx}(B)$ at higher magnetic fields is complicated by Zeeman splitting, only the lower-field minima are considered, where the amplitudes can accurately be extracted. Due to the absence of an oscillating beating signature in $\rho_{xx}(B)$ of all 2DHG samples investigated, one can assume that there are no contributions of two different subbands and only the first HH subband is occupied.
If only one subband is occupied, in order to obtain the effective mass, the relative longitudinal magnetoresistivity $\Delta\rho_{xx}(B) = \rho_{xx}(B) - \rho_0$ normalized to the zero-field longitudinal resistivity ρ_0 is commonly fitted to the Dingle factor $\chi/\sinh\chi$ of the Ando formula, Eq. (2.16), where $\chi = 2\pi^2 k_B T/(\hbar\omega_c)$. The procedure is illustrated exemplarily in Fig. 6.6 for the [010] direction of a 2DHG with a high hole density of $p = 5.09 \times 10^{11}$ cm^{-2} ($T_{\mathrm{Mn}} = 787$ °C). Engaging the simplified Ando formalism, Eq. (2.17), as introduced in Section 2.1.4, we can deduce the effective mass $m_h^*(B)$ from the linear slope $[-2\pi^2 k_B m_h^*/(e\hbar B)]$ of the plot $\ln[\Delta\rho_{xx}/(\rho_0 T)]$ versus T for a fixed magnetic field in the main plot of Fig. 6.6 (a). There, the inset of (a) depicts the corresponding normalized $\Delta\rho_{xx}(B)$ for temperatures $T = 30$ mK and 4.2 K. In the given example, the data of minima at different B-fields are evaluated for temperatures only above 100 mK, where each slope in Fig. 6.6 (a) is sufficiently linear for the simplified form to be valid. Deviations from this linearity for $T \leq 100$ mK may be related to the growing influence of insulating behavior as proposed in the previous section. The extracted values of the effective hole masses $m_h^*(B)$ are reported in Fig. 6.6 (b), exhibiting a linear dependence on the magnetic field. The procedure has been conducted in numerous 2DHG heterostructures: $m_h^*(B)$ varies significantly with B in all samples analyzed, a fact that was also observed in other studies of 2DHGs in III-V systems [124, 148, 144] and is yet to be understood. It may arise from non-parabolicity of the HH subband at higher values of $\mathbf{k}_\parallel$ [95]. Here, linear extrapolation of $m_h^*(B)$ to $B = 0$ T reveals $m_{h,[010]}^* \approx (0.12 \pm 0.089)\ m_0$[1]. With a relative error of 74%, the accuracy of this result, as of all values of m_h^* gained by this method, is limited. Not only does the subtraction of the parabolic background produce an uncertainty in the resulting amplitudes of $\rho_{xx}(B)$, but also, more crucially, the linearly fitted slope of $\ln[\Delta\rho_{xx}/(\rho_0 T)](T)$, and thus $m_h^*(B)$, is highly sensitive to the chosen range of temperatures.

[1] m_h^* in terms of the free electron mass $m_0 = 9.109 \times 10^{-31}$ kg

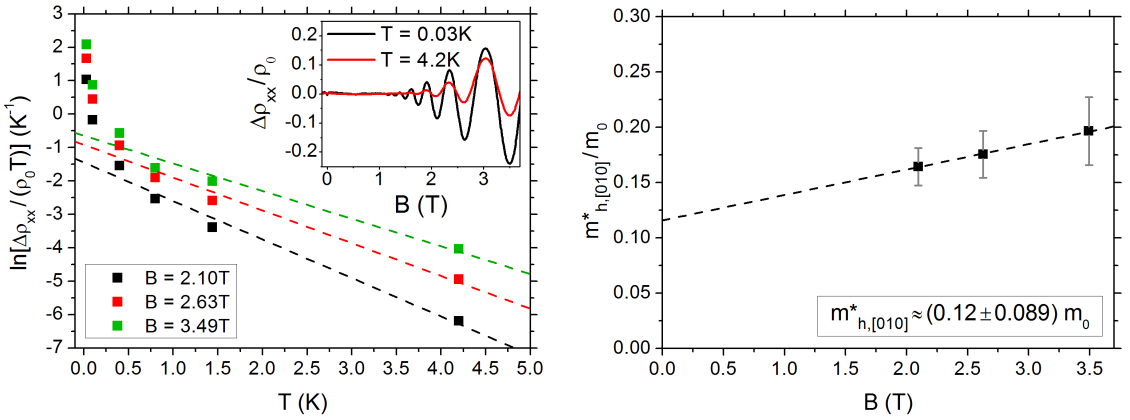

Figure 6.6: *Exemplary evaluation of the effective mass m_h^* of a 2DHG in* [010] *direction with $p = 5.09 \times 10^{11}$ cm^{-2} by fitting the temperature damping of the normalized amplitudes $\Delta\rho_{xx}/\rho_0$ in a range of $T = 30$ mK to 4.2 K (see the inset in (a)). A second order polynomial background due to the h-h-interaction-induced NMR correction to $\rho_{xx}(B)$, which was fitted in the low-field range between ± 1.2 T before the magnetoresistance starts to oscillate, had necessarily been subtracted.* **(a)** *Applying the simplified Ando formula, $m_h^*(B)$ can be deduced from the linear slope of a plot $\ln[\Delta\rho_{xx}/(\rho_0 T)]$ versus T. Extrapolating $m_h^*(B)$ to $B = 0$ T in* **(b)** *then suggests $m^*_{h,[010]} \approx (0.12 \pm 0.089)\, m_0$.*

In the literature, experimental and theoretical values of HH effective masses m^*_{HH} in InAs are also diverging to a great extent as a survey listed in [41], ranging from $0.15\, m_0$ up to even $0.95\, m_0$, suggests. A comparison, however, is difficult given the complexity of hole band structures of different heterosystems. In this thesis, m^*_{HH} has persistently been found to be less than the theoretically proposed high HH value for InAs of $m^*_{HH} = 0.39\, m_0$ [40]. Considering a significant fraction of the hole wave function spreading from the InAs channel into the surrounding InGaAs QW layers, where $m^*_{HH} = 0.465\, m_0$ ($In_{0.53}Ga_{0.47}As$, [40]) is even higher, cannot explain these findings. The deviation could, however, arise from a mixing of the split HH and LH subband states, where the effective light-hole mass reads as $m^*_{LH} = 0.026\, m_0$, at higher $\mathbf{k}_\parallel$ (cf. Fig. 2.6 of Sec. 2.2.1).
We further note that calculating m_h^* for different crystallographic directions always yields the effective hole mass to be highest in [110], lowest in [$\bar{1}$10] and intermediate in [010]. On the basis of the evaluation of a number of InAs 2DHG heterostructures of different wafers, the anisotropic effective hole masses are observed to be $m^*_{h,[\bar{1}10]} \equiv 0.10\, m_0$, $m^*_{h,[010]} \equiv 0.12\, m_0$ and $m^*_{h,[110]} \equiv 0.15\, m_0$ in accordance with the findings by Wurstbauer [144] and Hirmer [107] regarding both the absolute values and the direction-dependence of m_h^* for 2DHGs in InAs QW systems of identical design. The effective masses have been determined by the same approach, involving

large error bars, in all three works. Although these values cannot claim to be accurate, with their deviations lying within large error margins, they still consistently reflect the anisotropic character of the effective hole mass in these indium systems qualitatively.

While the non-parabolic energy dispersion of HH subbands typically suggests unequal values of m_h^* in $\mathbf{k}_\parallel$ directions $\langle 100 \rangle$ and $\langle 110 \rangle$ in the (001)-plane (see Fig. 2.7 (a)), the differences in the orthogonal directions [110] and [$\bar{1}$10] may be a consequence of the anisotropic energy dispersion of a combined both cubic BIA and SIA spin splitting as it was presented in Fig. 2.9 in Sec. 2.2.2. The anisotropy of m_h^* could, however, also reflect an anisotropic modulation of the potential landscape originating from the inhomogeneous distribution of indium that has been discussed in Section 5.1 [144].

Keeping the temperature fixed, in a complementary analysis to the calculation of m_h^*, the Ando formalism Eq. (2.16) also provides access to the quantum scattering time τ_q that defines the quantum mechanical corrections to the B-dependent envelope function of low-field SdH oscillations (see Section 2.1.4). Engaging our experimentally determined, anisotropic effective hole masses, one can derive τ_q from the slope of the simplified Dingle plot at a fixed temperature according to Eq. (2.18) by Elhamri *et al.* [32]. Figure 6.7 (a) summarizes the acquired values of the Dingle ratio τ_{tr}/τ_q of the Drude transport scattering time $\tau_{tr} = \mu m_h^*/e$ over the quantum scattering time τ_q for different crystallographic directions at $T = 1.44$ K as a function of the achieved hole density range p of this study. Experimental variation of p

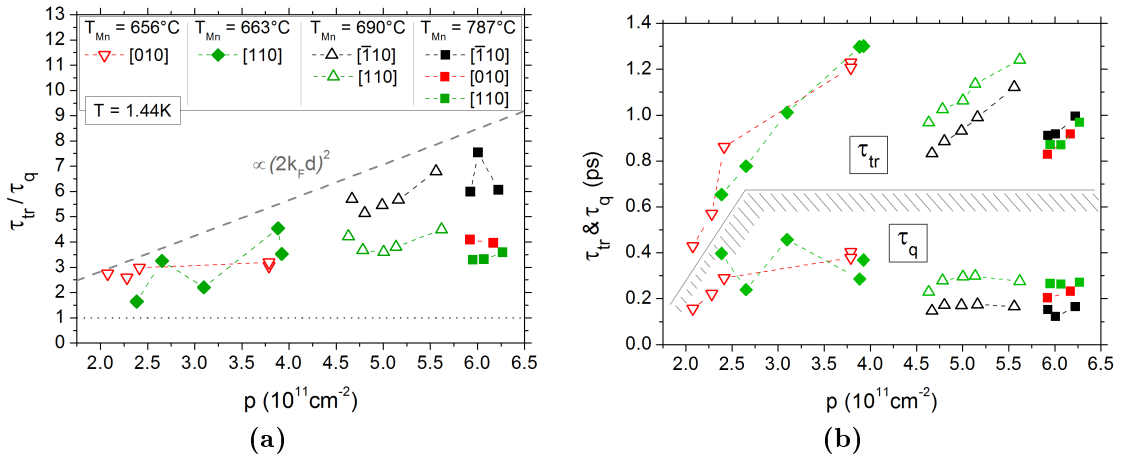

Figure 6.7: (a) *The summarized Dingle ratios of transport scattering and quantum scattering times $\tau_{tr}/\tau_q > 1$ (dotted level) in different crystallographic directions at $T = 1.44$ K indicate the dominance of small-angle scattering by long-range Coulomb potentials throughout the investigated hole density range. Theory predicts $\tau_{tr}/\tau_q = (2k_F d)^2$ for scattering by a smooth disorder, illustrated by the calculated dashed line.* **(b)** *The individual p-trends of τ_{tr} and τ_q associated with the ratios τ_{tr}/τ_q in (a).*

was realized in heterostructures of varied Mn doping concentrations, with each structure additionally offering the possibility of gate-induced modulation of the carrier density.
We find for any crystallographic direction and hole density a ratio $\tau_{tr}/\tau_q > 1$ (values above the dotted line in Fig. 6.7 (a)), suggesting a dominating fraction of small-angle scattering, typically induced by the long-range Coulomb potential of remote impurities [10]. The dominating influence of long-range scattering potentials is also supported by the impression that the distribution of $\tau_{tr}/\tau_q\,(p)$ roughly follows the theoretically predicted relation $\tau_{tr}/\tau_q = (2k_F d)^2$ for scattering by smooth disorder (calculated grey dashed line in Fig. 6.7 (a)) [149], where $d = 7.5$ nm is determined by the average spacing between the 2D hole gas and the remote ionized dopants (cf. Fig. 4.3 in Sec. 4.3). Figure 6.7 (b) provides the individual p-dependences of the time scales τ_{tr} and τ_q, associated with the values of the ratio τ_{tr}/τ_q in Fig. 6.7 (b), with τ_{tr} being found mainly in the upper half and τ_q in the lower half of the diagram. Their p-trends suggest that the overall trend of a decreasing Dingle ratio $\tau_{tr}/\tau_q\,(p)$ seems to be governed by the decline of the transport scattering time $\tau_{tr} \propto p$, as τ_q is rather constant over the whole range of p along each crystallographic direction. The evolution of $\tau_{tr}/\tau_q\,(p)$ is thus to be interpreted as a mere reflection of the mobility and density evolution of the system. In Section 6.4, a reduced screening from disorder is identified as the mobility limiting scattering process when driving the system towards lower hole densities.

6.2.3 Weak antilocalization analysis of SO parameters

On the basis of the earlier considerations regarding the parabolic h-h interaction contribution to the resistivity and with a profound knowledge of the anisotropic effective hole mass of the system, we experimentally address SOI-related quantities, like the spin splitting of the energy spectrum or the spin and also phase relaxation processes, by the analysis of the characteristic weak antilocalization dip in the longitudinal magnetoresistance at zero magnetic field. While the reduced conductance due to weak localization is the result of constructive quantum interference of time-reversed partial waves scattered in a disordered system, weak antilocalization instead enhances the conductance with the partial waves interfering destructively under the influence of spin dephasing due to SOI (see Sec. 2.1.5 on quantum interference in diffusive transport). A perpendicular external magnetic field breaks the spatial phase coherence along the two closed paths and a negatively curved signature of the magnetoconductance is formed.

The rivalling coexistence of WL and WAL at low magnetic fields was first predicted by Hikami *et al.* [150] already in 1980 and soon thereafter observed experimentally by Bergmann [151] in the magnetoconductance of thin metallic films of magnesium covered with layers of the high-SOC-material gold of varied thicknesses. For semiconductor materials, Poole *et al.* [152] then were the first to demonstrate WAL in the 2D inversion layer of an InP MOSFET and, in the following,

e.g. Kawaguchi *et al.* [153] in n-inversion layers of InAs, until in 1992, Dresselhaus [127] and also Chen *et al.* [154] succeeded in quantifying the spin splitting parameters of conduction subbands of GaAs/AlGaAs and AlSb(ZnTe)/InAs/AlSb heterostructures, respectively, from the analysis of the low-field WAL. In subsequent years, the effect was employed to study the spin splitting in numerous n- and also p-type systems, as e.g. for 2DEGs in InGaAs/InAlAs QWs [13], for a hole gas in strained InGaAs/GaAs QW heterostructures [155], or in carbon-doped GaAs/AlGaAs heterostructures [90].
In their pioneering works, Al'tshuler *et al.* [156] and Hikami *et al.* [150] describe the low-field behavior of the magnetoconductance to be determined by the leading spin relaxation mechanism of the system. While the theory of Hikami, Larkin and Nagaoka (HLN) [150], originally developed in the context of metallic systems, assumes Elliott-Yafet skew scattering, Pikus and Pikus [157] and later Knap [34] found that in systems, where the mechanism of D'yakonov and Perel' prevails, an improved quantitative fitting can be achieved by the model of Iordanskii, Lyanda-Geller and Pikus (ILP) [158], which readily includes the DP mechanism of spin relaxation (for both spin relaxation mechanisms, see Sec. 2.2.3). They furthermore extended the theory for the case that both linear and cubic Rashba and Dresselhaus contributions to the spin relaxation rate have to be considered, while the HLN theory regards k^3-terms only (see Sec. 2.2.2). Finally, Golub [159] optimized the ILP theory for WAL in ballistic two-dimensional systems of high mobility.

In 2D semiconductor heterostructure systems with inversion asymmetry, it is commonly accepted that the observation of a weak antilocalization minimum in the magnetoresistance is an unambiguous sign that the DP spin relaxation mechanism dominates [34], see Sections 2.1.5 and 2.2.3. The quantum correction to the magnetoconductance associated with WAL then usually is fitted by either the ILP or also the HLN theory to quantify the SOI strength from extracting the characteristic time scales of spin-orbit scattering and phase coherence. If only k^3-terms are considered and linear terms can reasonably be omitted, the ILP theory provides the same result for SOI-induced corrections to the magnetoconductivity $\sigma(B)$ as the HLN theory, in form of [150, 158, 34]

$$\begin{aligned}\Delta\sigma(B) - \Delta\sigma(0) = \frac{e^2}{\pi h}\Bigg\{&\Psi\left(\frac{1}{2}+\frac{B_\phi + B_{SO}}{B}\right) + \frac{1}{2}\Psi\left(\frac{1}{2}+\frac{B_\phi + 2B_{SO}}{B}\right)\\ &-\frac{1}{2}\Psi\left(\frac{1}{2}+\frac{B_\phi}{B}\right) - ln\frac{B_\phi + B_{SO}}{B} - \frac{1}{2}ln\frac{B_\phi + 2B_{SO}}{B} + \frac{1}{2}ln\frac{B_\phi}{B}\Bigg\},\end{aligned} \tag{6.3}$$

with the digamma function $\Psi(x)$, and, as fitting parameters, the phase coherence field $B_\phi = \hbar/(4De\tau_\phi)$ as well as the spin-orbit scattering field $B_{SO} = \hbar/(4De\tau_{SO})$. For a 2DHG in a disordered system, the dephasing time τ_ϕ and the SO scattering time τ_{SO} can then be calculated from these characteristic fields with the use of the diffusion constant $D = v_F^2\tau_{tr}/d$, where $d = 2$ is the effective dimensionality of the system, $v_F = \hbar k_F/m_h^*$ is the Fermi velocity and $k_F = \sqrt{2\pi p}$ the Fermi wave vector,

by the known elastic carrier mean free time τ_{tr}, the effective hole mass m_h^* and the hole density p.

We have successfully adapted the HLN model in the low-field WAL analysis of all gated InAs heterostructures of this study. It seems reasonable from the theory of spin splitting in 2DHGs in Section 2.2.2 that, in our samples, holes confined in an InAs QW occupying the highest HH subband states are only influenced by dominating k^3 both Dresselhaus and Rashba SOI contributions due to the coupling of HH and LH subbands [39, 11]. Yet, it has to be kept in mind that, since Hikami *et al.* based their considerations on electron systems, individual contributions of mixed cubic BIA and SIA terms to the spin splitting are not separable.

The WAL effect of quantum interference is best observed in systems of mobilities $\mu < 10^5$ cm^2/Vs [10], hence in the diffusive regime where $\tau_{tr} \ll \tau_{SO}$, when the phase coherence length of the carriers l_ϕ exceeds l_e, their elastic mean free path. As a representative of the highest density system of this study with $T_{\mathrm{Mn}} = 787$ °C, traces of $\Delta\rho_{xx} = \rho_{xx}(B) - \rho_{xx}(0)$ of a 2DHG with $p = 5.44 \times 10^{11}$ cm^{-2} in an L-shaped HB aligned along [$\bar{1}$10], [010] and [110] crystallographic directions at $T = 100$ mK are displayed in Fig. 6.8 (a). Every curve of reduced magnetoresistivity is found to exhibit a pronounced WAL signature of positive magnetoresistance. The effect is

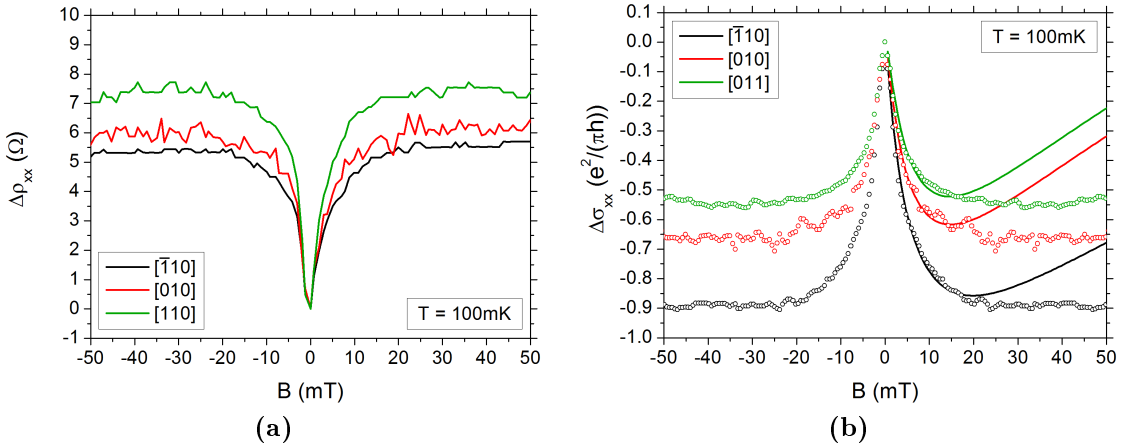

Figure 6.8: (a) *Raw data of reduced magnetoresistivities* $\Delta\rho_{xx}(B)$ *along different crystallographic directions of a high-density 2DHG of* $p = 5.44 \times 10^{11}$ cm^{-2} *(C120314B,* $T_{\mathrm{Mn}} = 787$ °C*) at* $T = 100$ mK *and* **(b)** *the corresponding edited magnetoconductivities* $\Delta\sigma_{xx}(B)$ *(see text) fitted in consistency with the* k^3 *HLN theory (solid lines).*

most distinct in $\Delta\rho_{xx}$ along the low-mobility direction [110]. For the reduced magnetoconductivity correction $\Delta\sigma_{xx} = \sigma_{xx}(B) - \sigma_{xx}(0)$ in Fig. 6.8 (b), with $\sigma_{xx} = 1/\rho_{xx}$, the parabolic h-h background was subtracted from the measured resistivities $\rho_{xx}(B)$ in a physically reasonable magnetic field range prior to the emergence of SdH oscillations, before the data was spline interpolated and symmetrized to improve the

terms and quality of the fit. Since the model of HLN is based on the diffusion approximation, its formal validity is limited by the transport field $B_{tr} = \hbar/(2el_e^2)$. For comparability, the fitting interval was thus chosen to be defined as $B \leq \pm 20$ mT for all WAL signatures of every sample investigated, since B_{tr} was calculated to be at least 20 mT in the whole experimentally accessible density range. Intervals of a wider range of low magnetic fields did not improve the quality of the fits.
The solid lines in Fig 6.8 (b) demonstrate that the experimental $\Delta\sigma_{xx}$ data can be reproduced precisely below the transport field in consistency with the k^3 HLN model (6.3). For higher magnetic fields, the fit deviates significantly from the experiment, since the diffusive condition $B < B_{tr}$ is no longer satisfied. Having adapted the diffusion constant $D\,(m_h^*)$ separately for each conductivity correction, $\tau_{SO,[\bar{1}10]} = 1.72$ ps and $\tau_{\phi,[\bar{1}10]} = 31.1$ ps are extracted in the $[\bar{1}10]$ direction and $\tau_{SO,[110]} = 5.06$ ps and $\tau_{\phi,[110]} = 41.5$ ps in [110], while the time scales in the crystallographic direction [010] are of intermediate values, $\tau_{SO,[010]} = 3.30$ ps and $\tau_{\phi,[010]} = 34.2$ ps (cf. Table 6.1). For $[\bar{1}10]$, τ_{SO} nearly matches the value of $\tau_{tr} = 0.92$ ps, which is a characteristic sign for a system in the regime of strong SOC [90]. This

Crystal direction	$\tau_{SO}\,[ps]$	$l_{SO}\,[nm]$	$\tau_{\phi}\,[ps]$	$l_{\phi}\,[nm]$	$\tau_{tr}\,[ps]$	$l_{e}\,[nm]$
[110]	5.06	218.6	41.5	626.0	0.93	198.3
[010]	3.30	218.3	34.2	702.8	0.91	114.4
$[\bar{1}10]$	1.72	190.3	31.1	809.6	0.92	139.5

Table 6.1: *Summarized anisotropic transport- and SO-parameters for different crystallographic directions retrieved from the WAL analysis of Fig. 6.8 at* $T = 100$ mK.

is reflected by the observation of the pure WAL effect in the magnetoconductivity data of the $[\bar{1}10]$ direction in Fig. 6.8 (b), whereas in [110], where $\tau_{SO} > \tau_{tr}$, a slight positive curvature of $\Delta\sigma_{xx}$ at higher magnetic fields hints at an underlying wider WL effect. Strictly speaking, as SOI is considered only a weak perturbation in the HLN theory ($\tau_{SO} \gg \tau_{tr}$) [150, 158], the model would formally be inadequate in the limit of strong SOI ($\tau_{SO} \leq \tau_{tr}$).
As a side aspect it should be noted that fitting with τ_ϕ and τ_{SO} as the only fitting parameters in Eq. (6.3) via $B = \hbar/\,(4De\tau)$ together with adapted diffusion constants $D\,(m_h^*)$ yields calculated values of the characteristic fields B_ϕ and B_{SO} that are identical with the results in case of B_ϕ and B_{SO} as the direct fitting parameters. This suggests that the influence of the respective $D\,(m_h^*)$, and thus of the uncertain anisotropic effective hole masses of Sec. 6.2.2, on the evaluated SOI parameters is either small or that our experimentally determined effective hole masses are plausible. Also, characteristic lengths derived from the values of direct fit parameters B_{SO} and B_ϕ in Eq. (6.3) do not differ from lengths calculated from the diffusion constant and fitting parameter τ via $l = \sqrt{D \cdot \tau}$, hence supporting the general confidence in the fitting procedure.

It can be seen from Fig. 6.8 that the crystallographic direction of the small-

est reduction of $\Delta\rho_{xx}$, the $[\bar{1}10]$ direction, is also the one of the strongest *relative* enhancement of $\Delta\sigma_{xx}$. With $\tau_{SO,[\bar{1}10]} < \tau_{SO,[110]}$, this suggests that the SOI acts strongest in the high-mobility direction $[\bar{1}10]$ and by that indicates that the nature of the spin relaxation mechanism should be the DP one, as discussed in Section 2.2.3. Hence, the spin-orbit relaxation length $l_{SO} = 218.6$ nm in [110] exceeds $l_{SO} = 190.3$ nm in the $[\bar{1}10]$ direction, as noted in Table 6.1. So, considering that the phase coherence lengths are $l_\phi = 626.0$ nm in [110] and $l_\phi = 809.6$ nm in $[\bar{1}10]$ at $T = 100$ mK, the fabrication of 2D-hole-based nanodevices of dimensions, where spin- and phase-coherent manipulation of holes can be performed, is technologically within reach given the long characteristic length scales of this system.

Having demonstrated the anisotropic nature of SOI parameters in terms of the crystallographic directions of p-type InAs heterostructures, the next paragraph studies the influence of a topgate on these SO parameters. The ability to change the Rashba SO field while the cubic Dresselhaus contribution remains fixed will then be discussed in Sec. 6.3.

Reducing spin relaxation by the DP mechanism

By using metallic topgates on InAs:Mn QW heterostructures, significant hole density variations were achieved during this thesis. In an L-shaped HB specimen of the next lowest Mn doping concentration (C120405A, $T_{\mathrm{Mn}} = 690$ °C) with respect to the samples discussed earlier in this paragraph, hole density reduction by a gate bias voltage was possible from $p = 5.13 \times 10^{11}$ cm^{-2} at $V_G = -25V$ down to $p = 4.06 \times 10^{11}$ cm^{-2} at $V_G = +5V$. This goes along with a decrease of the anisotropic mobilities from 2.45 to 1.80×10^4 cm^2/Vs in $[\bar{1}10]$ and from 1.48 to 1.13×10^4 cm^2/Vs in [110] direction at $T = 30$ mK. The effect of gate bias tuning on the prevailing WAL correction to the magnetoconductivity is presented in Fig. 6.9 (a) exemplarily for the $[\bar{1}10]$ crystallographic direction. The magnitude of the effect $\Delta\sigma_{xx}$ as well as the B-position of the minimum of the characteristic magnetoconductivity, marked by the minima of the individual solid fitting curves, are seen to decrease with reduced density. It is commonly accepted [34] that the position of the minimum of the conductance is largely determined by the spin-orbit field B_{SO}, and hence by the spin relaxation rate, whereas the height of $\Delta\sigma_{xx}$ is predominantly set by B_ϕ, and thus by the phase relaxation rate. As the minimum shifts towards higher magnetic fields with increasing carrier density, an increasing contribution of the dominant B_{SO}-field and therefore a reduced τ_{SO} are implied. Figure 6.9 (b) combines the extracted τ_{SO} values from fitting $\Delta\sigma_{xx}$ again to the k^3 HLN model (6.3), together with the calculated elastic transport scattering time τ_{tr} over the tuned density of holes, each for $T = 30$ mK and directions $[\bar{1}10]$ and [110]. Upon reduction of the hole density, τ_{SO} indeed is found to increase, while at the same time the elastic transport scattering time τ_{tr} shows the inverse behavior. This documents the following two aspects: First, it is clearly confirmed that the DP mechanism is the dominant mechanism of spin relaxation in this system,

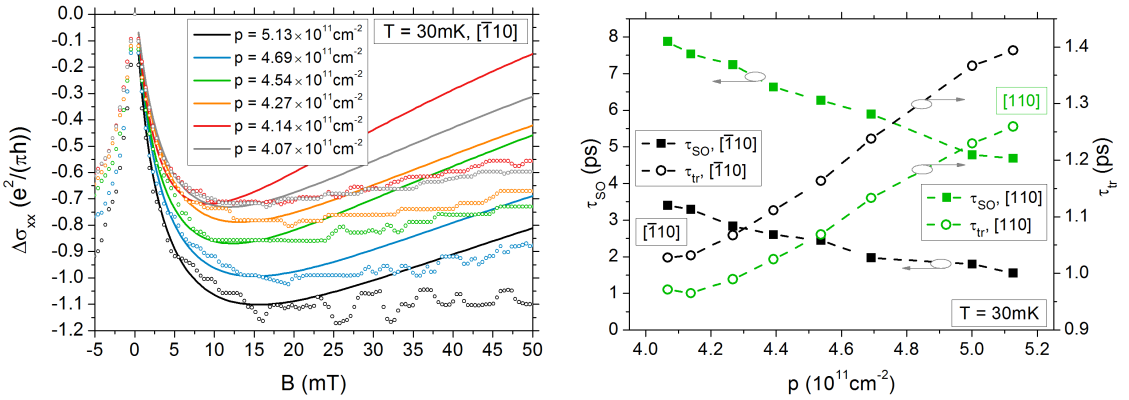

(a) (b)

Figure 6.9: (a) *Exemplary gate-bias-dependence of the reduced magnetoconductivity in* [$\bar{1}$10] *direction at* $T = 30$ mK *in terms of the hole density* p *fitted according to the HLN model (solid lines).* **(b)** *Summary of extracted* τ_{SO} *and* τ_{tr} *times over the tunable density range from directions* [$\bar{1}$10] *and* [110] *at* $T = 30$ mK. *The linear relations of spin-orbit scattering times and inverse transport scattering times,* $\tau_{SO} \propto \tau_{tr}^{-1}$, *in both directions clearly identify the D'yakonov-Perel' spin relaxation mechanism (note the different time scales left and right).*

as $\tau_{SO}(p) \propto \tau_{tr}^{-1}(p)$ (cf. Eq. 2.26). Secondly, it suggests that the scattering process defining the SO correction to the conductivity is the elastic scattering by potential fluctuations from disorder rather than elastic h-h scattering. Since the lowest values of τ_{tr} are in the low-mobility direction [110], this is also the direction of the longest τ_{SO} times. The corresponding maximal spin-orbit length is $l_{SO} \approx 240$ nm at the gate-induced low-density limit. It should also be noted that τ_{SO} as well as τ_{tr} miss a distinct reaction to the variation of the temperature, as the data for various temperatures practically coincide (not shown). This T-dependence is reasonable for scattering by disorder.

From the HLN fittings, the second characteristic SOI time scale τ_ϕ, like τ_{tr}, is found to decrease weakly with reduced hole density, e.g. from 56 ps to 49 ps at $T = 30$ mK in [110] direction (not shown). In contrast to τ_{SO}, the phase breaking time τ_ϕ is determined by inelastic scattering processes and highly sensitive to temperature changes, an issue that will be addressed in the next section.

Dephasing by inelastic scattering

Effects of quantum interference are observed at low temperatures in weakly disordered, diffusive systems, where carriers experience multiple elastic scattering, before the coherence of their wave function is broken by inelastic processes. In low-temperature 2DEG semiconductor systems, the temperature-dependence of these

effects' amplitudes is often described in terms of the dephasing or phase breaking rate given as [136, 160, 161]

$$\frac{1}{\tau_\phi(T)} = \frac{1}{\tau_\phi^0} + \frac{1}{\tau_\phi'(T)}, \text{ where again } \frac{1}{\tau_\phi'(T)} = \frac{1}{\tau_{e-e}} + \frac{1}{\tau_{e-p}}, \tag{6.4}$$

with a contribution independent of temperature τ_ϕ^0 and a temperature-dependent dephasing time $\tau_\phi'(T)$. The rate $1/\tau_\phi'(T)$ in turn is determined by contributions of inelastic electron-electron (τ_{e-e}) and electron-phonon (τ_{e-p}) scattering. With lattice vibrations getting suppressed at low temperatures, e-e interactions dominate the decoherence of electron waves. This mechanism typically is differentiated into interactions with a large energy transfer revealing a temperature-dependence of the dephasing rate $1/\tau_\phi' \propto T^2$ at temperatures above a critical temperature, $T > T_c = \hbar/(k_B\tau_{tr})$, and into interactions with small energy transfer that are characterized by $1/\tau_\phi' \propto T$ at $T < \hbar/(k_B\tau_{tr})$ in two dimensions [162, 163]. The latter, so-called Nyquist mechanism, can be interpreted as the quasielastic interaction of an electron with fluctuations in the electromagnetic background produced by the thermal motion of a sea of electrons [161].
Assuming that these considerations are valid for 2D hole dephasing, we discuss the temperature evolution of the phase breaking rate exemplarily in the $[\bar{1}10]$ and the [010] direction of a 2DHG system ($T_{\mathrm{Mn}} = 690$ °C) of density $p = 5.0 \times 10^{11}$ cm^{-2} and mobilities $\mu_{[\bar{1}10]} = 2.40 \times 10^4$ cm^2/Vs and $\mu_{[010]} = 1.95 \times 10^4$ cm^2/Vs at $T = 1$ K. The dephasing time τ_ϕ was extracted from fitting the WAL correction $\Delta\sigma_{xx}$ to the HLN theory as demonstrated in the upper and lower right part of Fig. 6.10 separately for selected temperatures of the $[\bar{1}10]$ and [010] direction, respectively. The left of Fig. 6.10 then summarizes $1/\tau_\phi(T)$ for temperatures between 20 mK and 4.2 K. Using the known elastic transport scattering times, we obtain the critical temperatures $T_{c,[\bar{1}10]} = 5.7$ K and $T_{c,[010]} = 6.1$ K marking the transition from large to small energy transfer mechanisms. Hence, for the given temperature range, dephasing is dominated by quasielastic small energy h-h scattering [162]. It is found that $1/\tau_{\phi,[\bar{1}10]} > 1/\tau_{\phi,[010]}$, since h-h scattering is enhanced due to the higher mobility in $[\bar{1}10]$ crystallographic direction. In this regime, several authors found for $\sigma \gg e^2/\hbar$ [162, 136, 164, 10]

$$\frac{1}{\tau_\phi} \approx \frac{e^2/\hbar}{\sigma} \ln\left(\frac{\sigma}{e^2/\hbar}\right) \frac{k_B T}{\hbar} = a \cdot T. \tag{6.5}$$

In both crystallographic directions, $1/\tau_\phi(T)$ follows a linear dependence only for temperatures above 600 mK, illustrated by linear dashed traces in the left of Fig. 6.10, with the $[\bar{1}10]$ direction exhibiting a finite, negative intercept at $T = 0$. While in [010] direction the slope $a = 0.03915\,\mathrm{Kps}^{-1}$ of the dashed linear fit is well ascertained by the value $0.03881\,\mathrm{Kps}^{-1}$ calculated with Eq. (6.5), the fitted slope $a = 0.05988\,\mathrm{Kps}^{-1}$ in $[\bar{1}10]$ differs significantly from a calculated $0.03465\,\mathrm{Kps}^{-1}$, even though the dephasing rate perfectly follows a linear T-dependence above 600 mK.

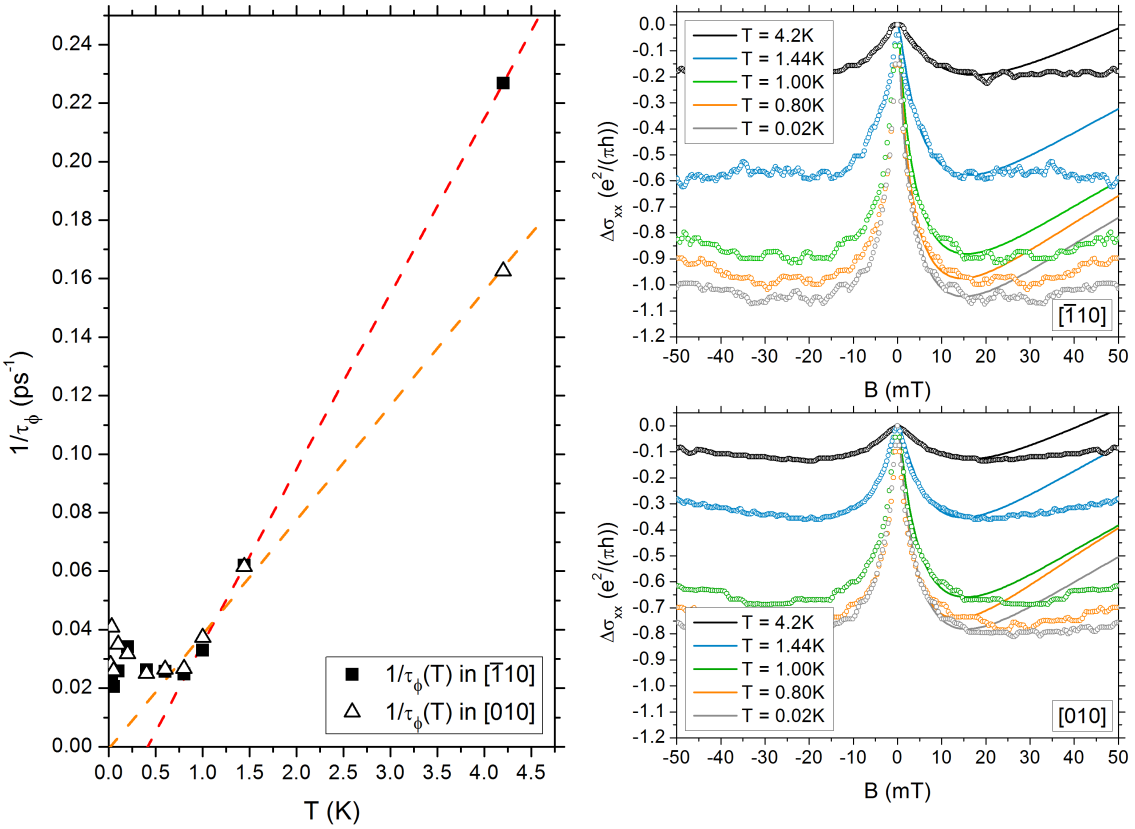

Figure 6.10: *(left) The temperature evolution of the phase decoherence rate* $1/\tau_\phi\,(T)$ *deduced from adapting the HLN model to the conductivity correction* $\Delta\sigma_{xx}$ *in* $[\bar{1}10]$ *(upper right) and* $[010]$ *(lower right) direction at selected temperatures ranging from* 20 mK *to* 4.2 K. *The dashed lines of* $1/\tau_\phi$ *versus* T *in the left represent the linear dependence of the experimental values above* 600 mK. *Below* $T = 600$ mK *a saturating behavior of the dephasing rate is observed for both crystallographic directions.*

This surprising deviation from the theoretical value is also reported in several other works [165, 166]. Knott *et al.* [98] mentioned a similar discrepancy of the dephasing rate in the high-mobility direction $[\bar{1}10]$ in contrast to consistent slopes of $\tau_\phi^{-1}\,(T)$ in the $[110]$ direction of an InAs QW heterostructure identical to the ones investigated in this chapter, yet of slightly higher hole density $p = 5.45 \times 10^{11}$ cm^{-2}. Some authors attributed this deviation to unconsidered details of the subband structure or to the fact that inelastic scattering by alloy disorder and interface roughness, as well as intersubband scattering are not included in Eq. (6.5) [166]. While this might be true, still, since these aspects apply for both orthogonal directions $[\bar{1}10]$ and $[110]$, the cause of the unidirectional deviation for only the $[\bar{1}10]$ direction in the given example of Fig. 6.10 and in [98] is not explained by these arguments and remains an open question.

As a second aspect, unexpected from pure h-h scattering, $1/\tau_\phi\,(T) \equiv 1/\tau_\phi^0$ sa-

turates in both directions below 600 mK at a finite value and diverges as $T \to 0K$. While the divergence below $T = 200$ mK may be related to effects of sample heating, since a current of 300 nA was applied during the low-temperature measurements of Fig. 6.10, there must be an additional temperature-independent dephasing mechanism leading to saturation. Knott *et al.* [98] assumed that the deviation from the expected linear slope of h-h scattering was associated with an AMR feature which they observed in the $[\bar{1}10]$ direction at a transition temperature between 4.2 K and 1.65 K, while it was missing in the [110] direction. This AMR effect, mentioned earlier in Sec. 6.2.1, is supposed to mark a phase transition towards spontaneous ferromagnetic ordering in the (001) plane of the doping layer of magnetic Mn^{2+}-ions in close vicinity to the 2DHG. Such an observation was also clearly reported by Wurstbauer *et al.* [144] in an identical heterostructure of slightly lower Mn concentration, yet in both the $[\bar{1}10]$ and the [110] direction of $\rho_{xx}(B)$ with the transition occurring between 610 and 600 mK for that latter work. With the exception of a single HB sample ($T_{\mathrm{Mn}} = 690$ °C, [010] direction) already presented in Fig. 6.5 of Sec. 6.2.1, in our work no traces of AMR were found at mK-temperatures, even with a higher overall concentration of Mn doping. The samples investigated in this thesis thus are predominantly below the doping limit inducing the AMR effect. Hence, scattering by the intrinsic fields of a spontaneously magnetized or long-ranged-ordered diluted magnetic doping layer in the vicinity of the 2DHG cannot be the cause of the saturation of $1/\tau_\phi^0$ in our structures. Interestingly, this effect is also reported for 2DHGs in identical InAs QW heterostructures doped with non-magnetic carbon [107], ruling out the AMR to be the sole origin of this observation.
Although the saturation is widely reported, seemingly being universal among materials and in dimensionality, its microscopic origin remains unresolved with several possible dephasing processes likely coexisting in a given system [161, 167]. Here, with inelastic h-h scattering being less efficient at low temperatures, a dominating inelastic scattering by potential fluctuations due to disorder could explain the isotropic low-temperature-independent behavior of the phase breaking rate $\tau_\phi^{-1}(T)$ in the investigated heterostructures.

Concluding this section, the dependences of the characteristic spin-orbit times $\tau_{SO}(p)$ and dephasing times $\tau_\phi(T)$ suggest, first, that the DP mechanism preserves spin orientation by enhanced elastic scattering of holes at disordered Coulomb potentials due to a reduced screening effect of low hole densities. Secondly, inelastic scattering due to disorder could contribute to the dephasing at lowest temperatures while else hole-hole scattering with small energy transfer is the dominating process at temperatures from 600 mK up to 4.2 K.
So far, the SO analysis of the WAL quantum interference effect has been conducted in samples from the high-hole-density range of Figure 6.1. Having established that the DP mechanism provides longer spin relaxation lengths when reducing the hole density, the next section first pursues this development by studying samples from the low-density spectrum, and afterwards highlights the combined overall carrier-

density-dependent evolution of quantum interference phenomena parametrized by characteristic length scales. In the second part of the section, the effective tunability of the SIA-induced spin splitting of the system is then discussed.

6.3 Tunability of the spin splitting by SIA-induced Rashba SOI

In their pioneering work, Koga *et al.* [13] were able to experimentally settle the debate whether the Rashba SOI really is caused by structure inversion asymmetry in quantum well systems, as they witnessed a transition from weak antilocalization to weak localization in the low-field magnetoresistance of a 2DEG that could clearly be associated with the degree of symmetry of an InGaAs QW. The variation of the QW symmetry was realized by changing the ratio of two carrier-supplying doping layers in four heterostructures, while keeping the overall impurity concentration constant and the sheet carrier density fixed by a gate electrode. A symmetric QW showed WL, whereas WAL was provoked by asymmetric doping.
A similar, yet gate-induced transitional behavior between these effects of quantum interference has then been reported several times for 2DEGs e.g. in InAlAs/InGaAs QW heterostructures by Kohda *et al.* [168] and Faniel *et al.* [169], as well as for 2DHGs e.g. in GaAs/InGaAs QWs by Minkov *et al.* [155] and also in Ge/SiGe QW structures by Moriya *et al.* [170]. Furthermore, analyzing the WAL-WL crossover has also become a viable tool to study SOI in one-dimensional n-type InGaAs or InAs narrow stripes and nanowires [171, 172, 173, 174], where lateral confinement acts as the main source of Rashba SIA.

In the following, we will present a gate-induced transition of quantum interference effects, which has, to the best of our knowledge, not yet been documented for 2D hole gases in these InAs QW heterostructures. The underlying ability to tune the spin-orbit scattering time to some extent suggests that direct control of a Rashba-type SOI by an external electric field perpendicular to the 2DHG plane is possible. Hence, the variation of a zero-field spin splitting by the strong Rashba SOI of this system could pave the way for spin manipulation in future spintronic devices.

6.3.1 Suppression of weak antilocalization by Rashba SOI

In the previous section, it was found that the magnitude of the weak antilocalization effect depends on the ratio of the phase breaking and spin relaxation rates. A small phase breaking rate and fast spin relaxation increase the magnitude of the WAL, while a long spin relaxation length and decreasing phase coherence led to a reduction of the effect. A display of this behavior is provided by Figure 6.11 (a). It describes a gate-induced suppression of the amplitude of the WAL correction to the longitudinal magnetoconductivity of a HB sample in the [110] direction at $T = 1.44$ K, processed

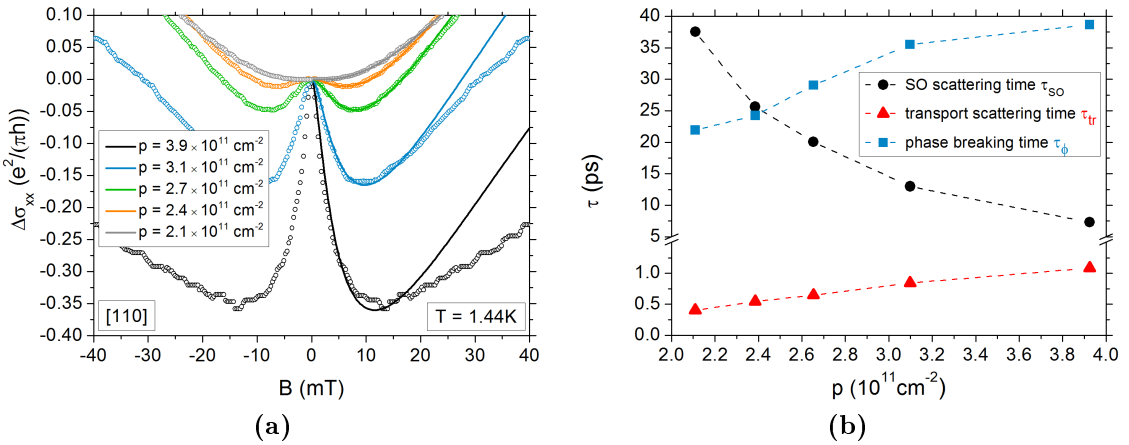

Figure 6.11: *The gate-induced suppression of* **(a)** *the reduced magnetoconductivity correction* $\Delta\sigma_{xx}$ *in the* [110] *direction of a low-density sample* ($T_{\mathrm{Mn}} = 663$ °C, *C120404B) at* $T = 1.44$ K *can be correlated to* **(b)** *the point at* $p = 2.4 \times 10^{11}$ cm^{-2} *where the condition* $\tau_\phi = \tau_{SO} \gg \tau_{tr}$ *of characteristic time scales deduced from the solid HLN fitting curves in (a) is matched (dashed lines are guides to the eye).*

from the low-T_{Mn} wafer C120404B (cf. Fig. 6.1). Here, the transition from WAL to WL upon reducing the hole density can in fact be correlated with crossing trends of the characteristic $\tau_{SO}(p)$ and $\tau_\phi(p)$ times in Figure 6.11 (b), again deduced from the fitting of the low-field magnetoconductivity correction to the HLN theory (6.3) in Fig. 6.11(a). For $\tau_{SO} < \tau_\phi$, the WAL peak is observed at zero magnetic field, and for $\tau_{SO} > \tau_\phi$, there is only the positive magnetoconductivity of the WL effect, since phase-coherent backscattering still exists as $\tau_\phi \gg \tau_{tr}$. The WAL peak vanishes, when the two rates $\tau_\phi^{-1}(p) = \tau_{SO}^{-1}(p)$ are comparable at about $p = 2.4 \times 10^{11}$ cm^{-2}. While τ_{SO} is enhanced by the DP mechanism, the decline of both the dephasing time and the relatively small transport scattering time with hole density reduction is a consequence of a decreasing hole mobility. Since the phase coherence time τ_ϕ, however, strongly depends on the temperature, with the SO scattering time τ_{SO} being T-independent, the occurrence of the transition from WAL to WL at $\tau_\phi = \tau_{SO}$ is a temperature-dependent phenomenon. Higher temperatures favor the suppression of the WAL effect, as they lead to an enhanced dephasing of the hole wave function and hence to shorter phase breaking times making it easier to match the condition $\tau_{SO} = \tau_\phi$.

As an interesting side aspect, contrary to $l_{SO,[110]} > l_{SO,[\bar{1}10]}$ stated in the previous Sec. 6.2.3 on anisotropies in structures from the high-carrier-density limit (cf. Tab. 6.1), the spin relaxation length $l_{SO,[\bar{1}10]} \approx 265$ nm in the low-density limit is slightly higher than $l_{SO,[110]} \approx 244$ nm, even though τ_{SO} was continuously found to exceed the $[\bar{1}10]$-values in the [110] direction throughout the whole p-range. This fact documents that this anisotropy of l_{SO} is a sensitive product, $l_{SO} = \sqrt{D \cdot \tau_{SO}}$,

of the SO scattering time and the relative change of the diffusion coefficient D. The latter D declines with decreasing density and mobility, on average more significantly in $[\bar{1}10]$ than in the $[110]$ direction, thus leading to the change in the relative crystallographic anisotropy of l_{SO} over p.

At this point, a full survey of the p-evolution of the quantum interference phenomena of the InAs:Mn 2DHG system can be presented in Fig. 6.12 for the whole experimentally accessible density range, parametrized by its characteristic length scales l_{SO}, l_ϕ and l_{tr}. As demonstrated, the hole density was consistently tuned by a combination of external electric gating and the variation of the p-type dopant concentration. For simplicity, the data of only the $[\bar{1}10]$ direction, conducted from measurements of just three different HB samples, is shown. All other characterized HB samples of the investigated density range confirmed these trends and values. The inconsistency of $l_\phi\,(p)$ at $T = 800$ mK with respect to the data obtained at

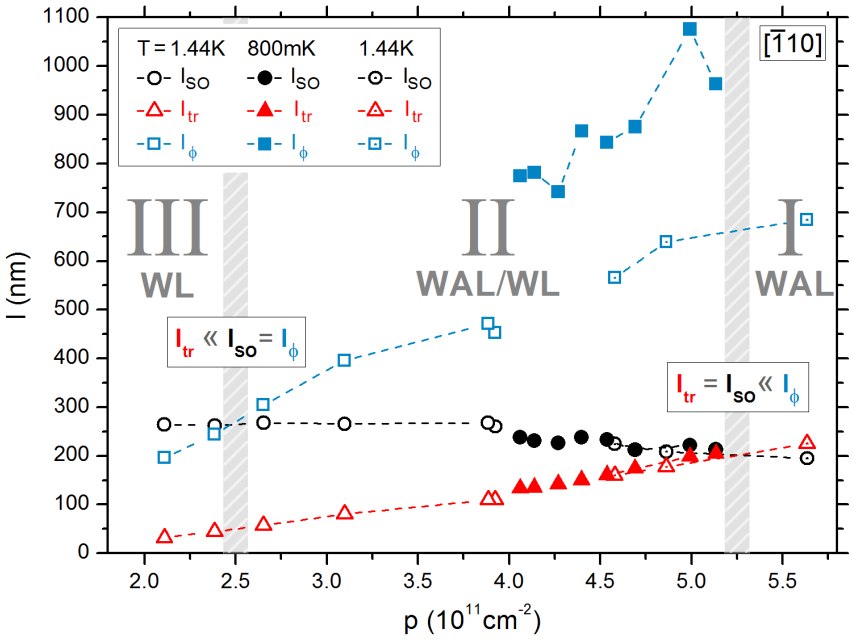

Figure 6.12: *Survey of the combined p-evolution of characteristic length scales of three different gated InAs:Mn QW samples probing the complete 2D hole density spectrum investigated (dashed lines are guides to the eye). Three regimes of varying WAL or WL dominance in the low-field magnetoresistance can be identified that are differentiated by the relative values of the spin relaxation length l_{SO} with respect to the phase coherence length l_ϕ and the elastic mean free path l_{tr}.*

$T = 1.44$ K, else, demonstrates once again the sensitivity of the dephasing processes on the temperature.
In accordance to [10], the whole spectrum of quantum interference effects could be probed, as the system is transferred from a regime of very strong SOI (I) with $l_{SO} \leq$

$l_{tr} \ll l_\phi$, where a pure WAL correction dominates the longitudinal magnetoresistance at $p \gtrsim 5.2 \times 10^{11}$ cm^{-2}, into a wide, most common transition regime (II) with $l_{tr} \ll l_{SO} \ll l_\phi$, where the WAL due to SOI is superimposed on the WL effect. At a transition point $p \approx 2.5 \times 10^{11}$ cm^{-2}, where $l_{tr} \ll l_{SO} = l_\phi$, the system enters the pure WL regime (III) of small SOI with $l_{tr} < l_\phi < l_{SO}$ for a low-density 2DHG. The occurrence of quantum interference phenomena in Fig. 6.12 is governed by the SO scattering length and hence by the Rashba SOI. The enhancement of l_{SO} at low densities, however, is smaller than expected from the tunability of $\tau_{SO}(p)$ (e.g. in Figures 6.9 and 6.11), as it is restricted by a declining diffusion coefficient of the increasingly disordered system.

By adding the carrier density evolution of the Fermi wavelength $\lambda_F = 2\pi/k_F$ in Fig. 6.13 as another length scale with respect to the mean free path $l_{tr}(p)$, it is found that the initially large values of l_{tr} at high densities, fulfilling the *Ioffe-Regel criterion* $k_F l_{tr} \gg 1$ [10], intersect with $\lambda_F(p)$ at the hole density of $p \approx 2.5 \times 10^{11}$ cm^{-2} which characterizes the suppression of the WAL effect in Fig. 6.12. When the energy

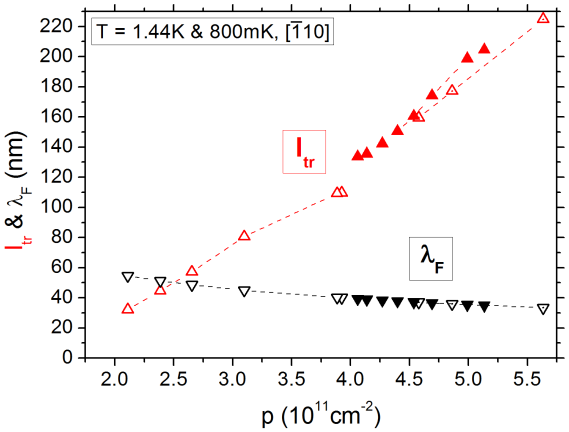

Figure 6.13: *The dependences of the Fermi wavelength $\lambda_F(p)$ and the mean free path $l_{tr}(p)$, corresponding to Fig. 6.12, intersect with decreasing hole densities at $p \approx 2.5 \times 10^{11}$ cm^{-2}, the density value that also marks the suppression of WAL by the WL effect, hence indicating a localization-dominated system.*

criterion approaches $k_F l_e = 1$ ($k_F l_e \approx 4.4$ at $p = 2.1 \times 10^{11}$ cm^{-2} while $k_F l_e \approx 42.3$ at $p = 5.6 \times 10^{11}$ cm^{-2}) and both quantities λ_F and l_{tr} become comparable, the wave functions tend to localize [10]. The WL effect then dominates the WAL phenomenon. The role of localization in these corrections to the longitudinal magnetoresistivity in the low-carrier-density regime will be revisited in Sec. 6.4 at the end of this chapter.

As the entire picture of quantum interference phenomena in the vicinity of zero magnetic field, Fig. 6.1, however, correlates with the evolution of characteristic SO parameters, the next section investigates in detail how the variation of the Rashba SOI affects the spin splitting of this 2D hole system.

6.3.2 Tunability of the Rashba spin splitting

Breaking the spatial inversion symmetry by the BIA of a non-centrosymmetric zinc blende crystal structure and by the SIA of a confining potential leads to a spin

splitting of hole states even at $B = 0$ T. The Dresselhaus term is essentially a fixed material property with its relevance only changing slightly with the geometry of the system, i.e. the QW width, and with the Fermi wave vector [11]. Thus, the experimental access to the variation of the splitting is given by the effective potential gradient $\mathcal{E}_z$ of the dominant Rashba SIA generated through external metallic gating or the internal potential of an asymmetric modulation doping (cf. Section 2.2.2). In a QW heterostructure, a single front gate has the twofold effect of affecting both the asymmetry and the 2D density of the well.

The WAL correction is an unambiguous sign of spin-orbit interaction. Since we have experimentally clearly demonstrated the D'yakonov-Perel' mechanism to dominate the spin relaxation via the effective magnetic SO field in this diffusive 2DHG system, data of the spin splitting energy spectrum ΔE can be generated from the DP relation $\tau_{SO}^{-1} = 2\boldsymbol{\Omega}_{SO}^2 \cdot \tau_{tr}$, as (cf. Section 2.2.3) [155, 38]

$$\Delta E \equiv \boldsymbol{\mathcal{B}}_{SO} = \hbar\boldsymbol{\Omega}_{SO} = \frac{\hbar}{\sqrt{2\tau_{SO}\tau_{tr}}}. \tag{6.6}$$

Figure 6.14 combines the results of the complete $\Delta E\,(p)$ spectrum covering the hole density range achieved in this study. In both anisotropic crystallographic directions $[\bar{1}10]$ and $[110]$, the spin splitting energy drastically increases with in-

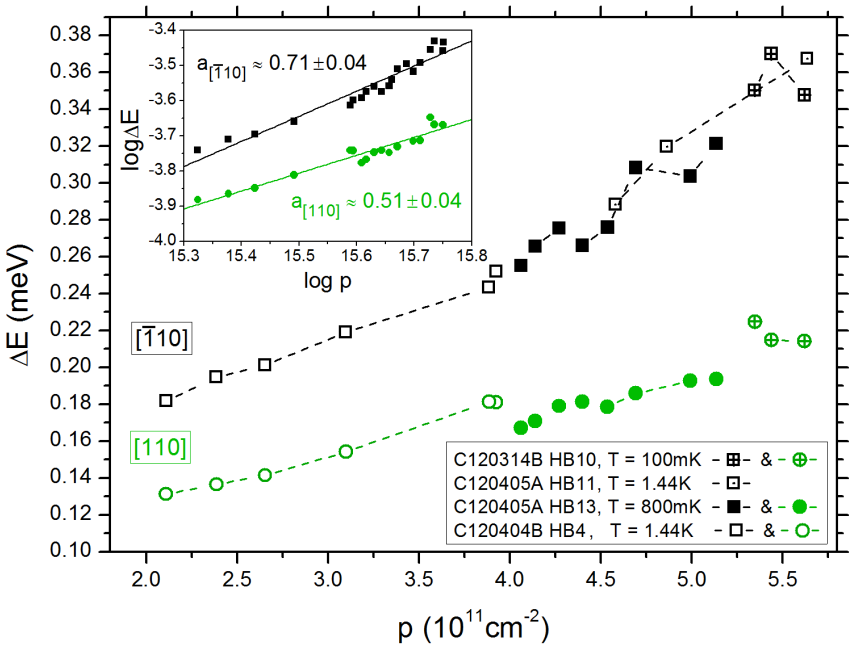

Figure 6.14: *The combined spin splitting energies $\Delta E\,(p)$ from different HB systems vary with the hole density, roughly by a factor* 2, *from* 0.18 meV *to* 0.37 meV *in direction* $[\bar{1}10]$ *and from* 0.13 meV *to* 0.22 meV *in* $[110]$. *Inset: Linear fits to the logarithmic spin splitting energies plotted versus logarithmic densities suggest p^a-dependences with exponents $a_{[\bar{1}10]} \approx 0.71 \pm 0.04$ and $a_{[110]} \approx 0.51 \pm 0.04$.*

creasing hole density. In the $[\bar{1}10]$ direction, a tuning of $\Delta E_{[\bar{1}10]}(p)$ is possible from approximately $\Delta E_{[\bar{1}10]} = 0.18\,\text{meV}$ to $0.37\,\text{meV}$, roughly by a factor of 2, between densities of $p = 2.1 \times 10^{11}\,\text{cm}^{-2}$ and $p = 5.6 \times 10^{11}\,\text{cm}^{-2}$. At the same time, $\Delta E_{[110]}(p)$ was found to be systematically smaller than $\Delta E_{[\bar{1}10]}(p)$, varying from about $\Delta E_{[110]} = 0.13\,\text{meV}$ up to $0.22\,\text{meV}$. This fact basically reflects the dominance of the anisotropy of the long SO scattering times τ_{SO} documented in Fig. 6.9. It so again seemingly confirms that the SOI acts strongest in the $[\bar{1}10]$ direction via the DP mechanism in an anisotropically disordered system. Surprisingly, the absolute magnitudes of the splitting are comparatively small over the whole range of hole densities. When put into relation to their corresponding kinetic energies $E_{kin} = m_h^* v_F^2/2$, the ratio of the anisotropic spin splitting energies ΔE with respect to E_{kin} is ranging from about $\Delta E/E_{kin} = 2.3\%$ in the high-density limit up to 3.9% in the low-density limit, in fact similarly in *both* crystallographic directions. The fraction of ΔE to E_{kin} is less significant than expected from the Fermi energy of holes, which is typically small due to a high effective hole mass supporting the impression of a small spin splitting for reasons unclear. As another aspect, the similarity of ΔE in both crystallographic directions indicates rather an isotropic field of SO interaction although one might expect anisotropic manipulation by an effective SO field of unequal strength in the orthogonal crystallographic directions from the simulation in Fig. 2.9 of Sec. 2.2.2.

In the previous sections, the HLN expression (6.3) has proven to be a suitable model to describe the WAL correction to the low-field longitudinal magnetoresistance of this system. The SOI therefore is regarded to be dominated by k^3-symmetric terms, as it is reasonable in a system of HH-LH separation at $k = 0$, where only the highest HH subband is occupied [43, 11, 38]. Considering exclusively Rashba SOI terms cubic in the in-plane momentum wave vector $k_\parallel$, ΔE can be expressed according to Eq. (2.24) by

$$\Delta E = \alpha^h \mathcal{E}_z k_\parallel^3, \tag{6.7}$$

where the effective electric field perpendicular to the QW plane $\mathcal{E}_z$ is in first order proportional to p (cf. Sec. 2.2.2), and $k_\parallel = k_F$ at the Fermi level, with $k_F \propto p^{1/2}$. An attempt to deduce the experimental p^a-evolution of the spin splitting in Fig. 6.14 by linearly fitting plots of $\log \Delta E$ versus $\log p$ (see the inset) yet yields exponents $a_{[\bar{1}10]} \approx 0.71 \pm 0.04$ and $a_{[110]} \approx 0.51 \pm 0.04$. These a-values are significantly smaller than the expected $p^{3/2}$-characteristic of the k^3-splitting and rather point to a $\Delta E(p)$ that is proportional to about $p^{1/2}$. Hence, the change in carrier density cannot be the driving force in the variation of the spin splitting energy.

To obtain a more profound opinion on the nature of the effective field that induces the spin splitting, it is convenient to display the numerical results in terms of the effective Rashba coefficient $\alpha^h \mathcal{E}_z$ [11] (Figure 6.15). The effective coefficient, calculated from relations (6.6) and (6.7), is then found to decrease with increasing density roughly by $\alpha^h \mathcal{E}_z \propto p^{-1}$, as suggested by linear fits in the inset of Fig. 6.15. Since $\alpha^h \mathcal{E}_z$ is, however, expected to increase, as $\mathcal{E}_z \propto p$ [11], this again nourishes the

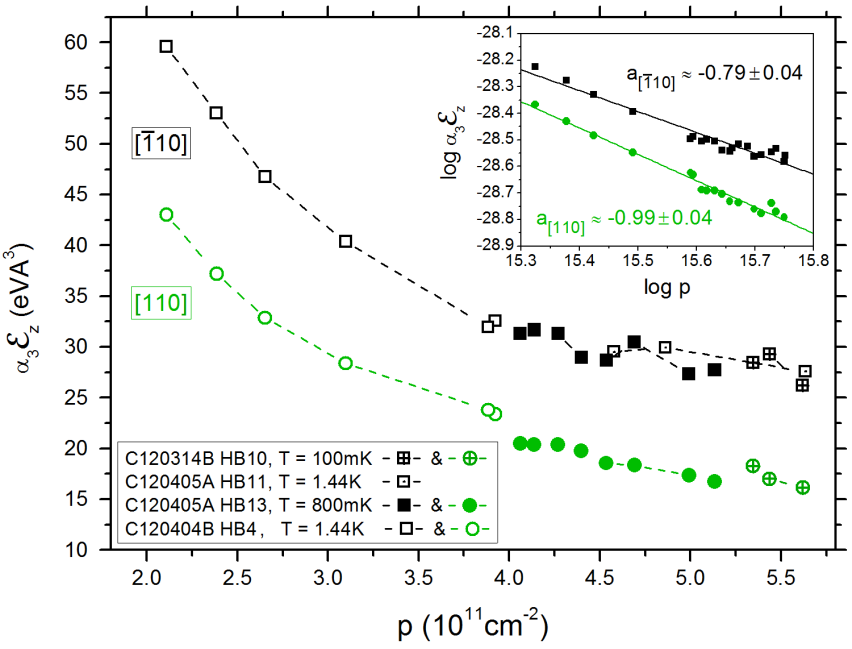

Figure 6.15: *The combined effective Rashba coefficients* $\alpha\mathcal{E}_z(p)$ *of directions* $[\bar{1}10]$ *and* $[110]$*, deduced from the spin splitting energy* $\Delta E(p)$ *in Fig. 6.14, systematically decrease with increasing hole density. Inset: Linear fits to* $\log \alpha\mathcal{E}_z$ *versus* $\log p$ *suggest a proportionality* $\propto p^a$ *of the effective Rashba coefficient characterized by* $a_{[\bar{1}10]} \approx -0.79 \pm 0.04$ *and* $a_{[110]} \approx -0.99 \pm 0.04$.

impression that the Rashba SO splitting is not controlled by p. In Equation (2.22) of Section 2.2.2, the bare Rashba coefficient α^h in 2D HH systems is defined to be inversely proportional to the separation of HH and LH subbands [11]. An increasing separation of HH and LH energies at $k = 0$ is thus bound to reduce the Rashba coefficient. The HH-LH splitting in turn is strongly influenced by the quantum confinement of the QW system and its inherent strain. While in a single heterostructure the subband separation, and hence α^h, is indeed approximately proportional to an electric field E_z [39], the confinement of a strained rectangular QW on the other hand, especially at small carrier densities and with a small asymmetry of the well, means that the system is essentially controlled by the potential steps at the QW interfaces. There, variations of both p or E_z are assigned only a minor role with respect to the large HH-LH splitting. The latter aspect then implies that the Rashba coefficient α^h should only be weakly affected by gate voltage modulation. These considerations lead us to the conclusion that the tunability of the SIA-induced Rashba spin splitting in Fig. 6.14 observed in our InAs:Mn 2DHG QW system is a direct effect of the external gate electric field in the QW rather than provoked by a manipulation of the Rashba coefficient α^h.

We determine the cubic Rashba coefficient α_3^h in our structures, similarly to Eq. (2.22) in Sec. 2.2.2, from the separation of HH and LH energies, E_{HH} and E_{LH},

respectively, measured with respect to the bulk band edge, by

$$\alpha_3^h = \frac{-3e\hbar^4\gamma_3^2}{2m_0^2\left(E_{HH} - E_{LH}\right)^2}, \tag{6.8}$$

following the method of Ohkawa and Uemura [175] in [170]. 8×8-band $\boldsymbol{k} \cdot \boldsymbol{p}$ simulations performed by Hirmer for a comparable C-doped InAs heterostructure in [107] suggest a high HH-LH separation of approximately 60 meV at $k = 0$, which greatly exceeds the spin splitting energies in Fig. 6.14. This high splitting is the consequence of strong quantum confinement in the highly compressively strained pseudomorphic InAs QW channel embedded in between InGaAs layers. Employing the Luttinger parameter $\gamma_3 = 9.2$ for InAs [37] in Eq. (6.8) then suggests a cubic Rashba coefficient of $\alpha_3^h = 2.05 \times 10^6$ eÅ^4, independent of the density and the external gate bias. This is comparable to values of α_3^h obtained for AlGaAs/GaAs single heterostructures [39] and exceeds the Rashba coefficient of a SiGe/Ge QW 2DHG structure [170] by one order of magnitude due to a smaller HH-LH spacing, underlining the general potential of the indium-based 2DHG system for Rashba-type of spin manipulation.

Another implication of a large HH-LH splitting is that these subbands couple at higher values of $k_\parallel$, leading to a nearly isotropic instead of an anisotropically warped VB dispersion at small values of $k_\parallel$ (see Sec. 2.2.1) [107], as already presumed earlier in this section. Hence, the crystallographic anisotropies in Figures 6.14 and 6.15 are no indication of an interplay of SIA and BIA creating an anisotropic spin-orbit field and splitting, like it was introduced in Fig. 2.9 of Sec. 2.2.2, but rather reflect the works of the anisotropic DP scattering.

In conclusion, this 2DHG system of the $In_{0.75}Al_{0.25}As/In_{0.75}Ga_{0.25}As$/InAs:Mn heterostructure offers a high preservation of the spin orientation when driven to lower hole densities, while simultaneously HH subband energy spin splitting exists within the complete range of densities. Although the splitting is small in magnitude, it can be addressed by an external electric field inducing a distinct relative change of ΔE as it is desired for spin manipulation in systems relevant for implementation in spintronic devices.
Still, the Rashba coefficient α^h could not be manipulated by the variation of p, as the coefficient α^h of QW heterostructures is dominated by the HH-LH separation, which is large in our system. A more significant, direct tunability of α^h may be obtained by means of strain engineering or by a variation of the width of the QW [39]. In the InAs:Mn QW heterostructures of this work including a strained InAs channel, however, strain and QW width bare only little room for structural improvement, since these are already highly optimized for the realization of high-quality 2D hole gases in QWs on top of strain relaxed virtual substrates with high In content.

6.4 Quantum corrections to the Drude resistivity in low-density disordered systems

Demonstrated in Sec. 6.3.1, the SO-induced WAL gradually weakens due to the increasingly dominant role of the WL effect as the 2D hole system is driven towards a low-density regime by the joint reduction of the Mn doping concentration and the gate electric field effect. First indications of weak localization in the low-field longitudinal magnetoresistivity $\rho_{xx}(B)$ are found early in this process of decreasing p, in the regime corresponding to $l_{tr} \ll l_{SO} \ll l_{\phi}$, as discussed in Fig. 6.12, with the WL effect completely taking over the WAL when $l_{tr} \ll l_{\phi} \leq l_{SO}$. Associated with the emergence of WL is a pronounced h-h-interaction-induced parabolic correction to $\rho_{xx}(B)$ at medium magnetic fields, introduced in Sec. 6.2.1. It is already observable for the highest carrier densities of this study, in the $l_{SO} \leq l_{tr} \leq l_{\phi}$ regime, where traces of a distinct WL peak around $B = 0$ T are still absent.
Concluding the journey of this chapter from the high- to the low-density regime of 2DHGs in regularly doped InAs:Mn heterostructures, this section highlights these quantum corrections to the Drude resistivity on the low-density side of the p-spectrum. The findings are mainly represented by HB measurements of wafers $T_{\mathrm{Mn}} = 663\,^{\circ}\mathrm{C}$ and $T_{\mathrm{Mn}} = 656\,^{\circ}\mathrm{C}$ (cf. Survey 6.1) which exhibit the most distinct parabolic background to $\rho_{xx}(B)$ of the study and can have negligible WAL due to a pronounced WL at $B = 0$ T.

Both many-body quantum phenomena of the disordered low-density system, the WL and h-h interaction, tend to localize the wave function of carriers through constructive interference. On the one hand, weak localization originates from one-particle self-interference of phase-coherent partial waves multiply scattered on counterpropagating trajectories (cf. Sec. 2.1.5), and on the other hand, multiply scattered holes interfere on h-h interaction amplitudes on their diffusive motion through a disordered system [176, 10].
Figure 6.16 demonstrates this localizing trend in the low-density-dependence of the longitudinal magnetoresistivity $\rho_{xx}(B)$ of a gated HB structure ($T_{\mathrm{Mn}} = 656\,^{\circ}\mathrm{C}$) in [010] direction at $T = 1.44$ K for densities tuned from $p = 3.88 \times 10^{11}\ \mathrm{cm}^{-2}$ down to $p = 1.85 \times 10^{11}\ \mathrm{cm}^{-2}$ with a corresponding reduction of mobilities from $\mu_h = 1.46 \times 10^4\ \mathrm{cm}^2/\mathrm{Vs}$ to $3.7 \times 10^3\ \mathrm{cm}^2/\mathrm{Vs}$. As the QW system is depleted by the field effect, it undergoes a transition towards a regime of increasingly insulating character where both contributions to the zero-field resistivity, the WL peak and the associated parabolic background, are enhanced, as it is illustrated for the latter by the dashed lines of second order polynomial fits to the magnetoresistivity in the medium field range below $B \approx \pm 1.5$ T in Fig. 6.16 (a). Around $B = 0$ T, the WL effect is suppressed by the influence of a small magnetic field on the phase coherence of the orbital part of the partial wave functions of the carriers, with the magnetic field B_c marking the crossover from the WL-dominated regime towards the h-h-interaction-dominated NMR correction at higher fields. The dependence of

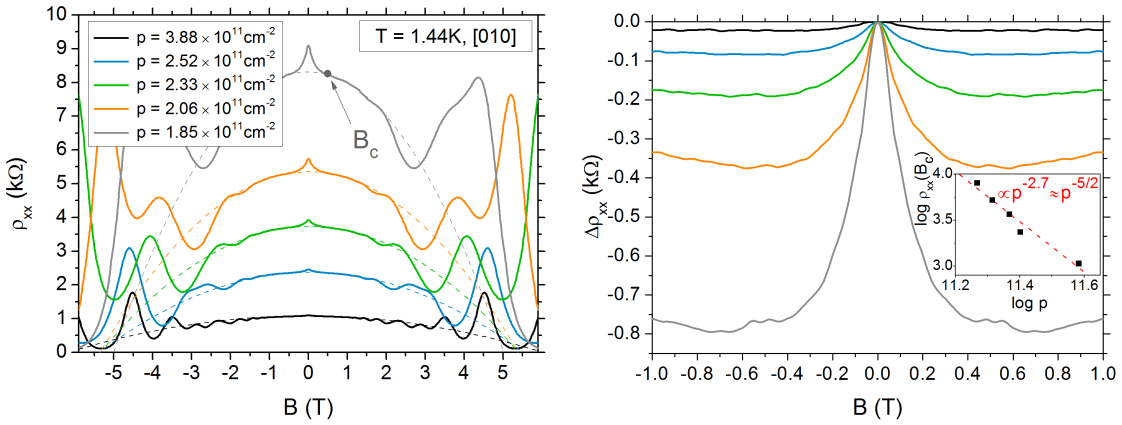

Figure 6.16: *The p-dependence of $\rho_{xx}(B)$ in the* [010] *direction of a low-density HB sample (C120530A, $T_{\mathrm{Mn}} = 656\,^{\circ}\mathrm{C}$) at $T = 1.44$ K is governed by the characteristic corrections to the Drude magnetoresistivity of* **(a)** *the h-h interaction at magnetic fields $B > B_c$ and* **(b)** *the weak localization correction $\Delta\rho_{xx} = \rho_{xx}(B) - \rho_{xx}(0)$ for $B < B_c$ (parabolic background, dashed lines in (a), removed). Both corrections are enhanced with gate-reduced density p. Inset: A log-log plot of $\rho_{xx}(B_c)$ versus p yields a density-dependence that is close to $\propto p^{-5/2}$, an indication for scattering by a smooth random potential.*

the magnitude of the WL resistance peak $\Delta\rho_{xx} = \rho_{xx}(B) - \rho_{xx}(0)$ (parabolic background removed) on the hole density is explicitly depicted in Fig. 6.16 (b). The inset traces the value of $\rho_{xx}(B_c)$ at the crossover field versus p on a log-log scale and reveals $\rho_{xx}(B_c) \propto p^{-5/2}$, which is characteristic for scattering by smooth disorder [149]. Although both correction features slightly vary in magnitude for different crystallographic directions of ρ_{xx} following the overall mobility anisotropy of the cross-hatched system, they qualitatively share the same phenomenologies in every direction. Therefore, remote doping impurities are normally regarded to serve as the isotropic main source of this disorder, before scattering by residual background impurities in the QW or by interface roughness are to become important.
The phenomenon of enhanced scattering at reduced hole density due to an increasing influence of disorder, as it has been proposed a couple of times earlier in this chapter in Sec. 6.2.1 or in Sec. 6.2.3, is best understood in the framework of the non-linear screening from fluctuating potentials [177, 10, 145]. According to this theory, a correlated 2D carrier system of high-density effectively screens the long-range potentials of remote charged impurities. As the density is lowered, the system ceases to be spatially homogeneous since spatial fluctuations of the random impurity distribution cause a local failure of effective screening. Fragmenting into a potential landscape of 'hills' and charge 'puddles' in this non-linear breakdown of the screening, localizing spatial inhomogeneities give rise to a semiclassical percolation

transition into an effectively insulating phase [178, 179, 180].

The situation of a weakly localized system ($k_F l_e > 1$, $r_s < 1$) in an insufficiently screened regime also becomes apparent in the temperature-dependence of the given HB heterostructure at a fixed $p = 3.8 \times 10^{11}$ cm^{-2} in Fig. 6.17. Upon cooling the

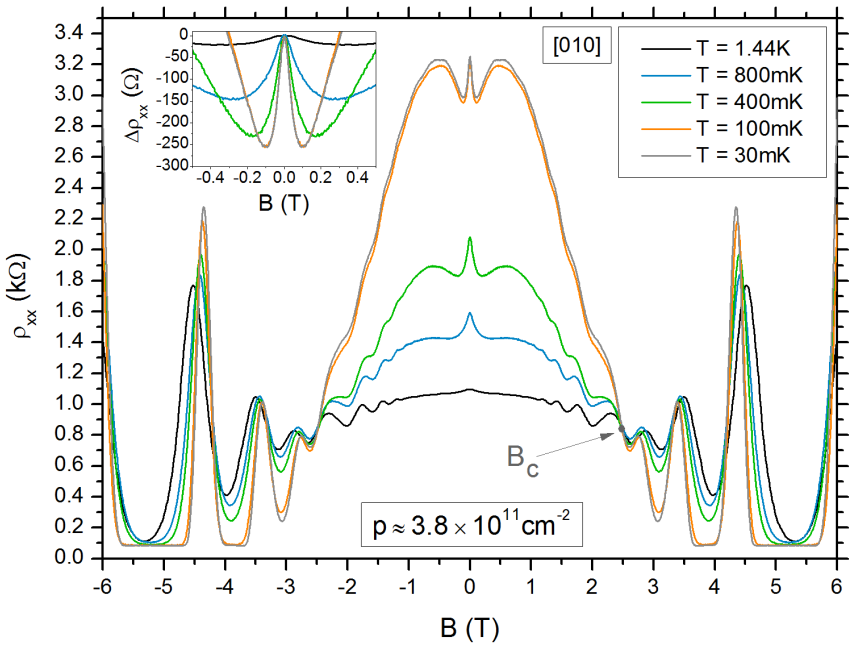

Figure 6.17: *Reducing the temperature of the HB system of Fig. 6.16 from* $T = 1.44$ K *down to* $T = 30$ mK *at* $p = 3.8 \times 10^{11}$ cm^{-2}*, reveals a transition of* $\rho_{xx}(B)$ *from the quantum Hall regime at high magnetic fields towards an insulating phase below a common field* $B_c \approx \pm 2.5$ T*. As the disordered system approaches zero temperature, increasing localization of carriers on insufficiently screened potential sites of remote ionized impurities enhances the sharpness and magnitude of the WL,* $\Delta\rho_{xx}(B)$ *(inset), and the parabolic background. Sample heating masks a further differentiation of* $\rho_{xx}(B)$ *below* $T = 100$ mK*.*

system from $T = 1.44$ K down to $T = 30$ mK, a similarly strong increase in $\rho_{xx}(B)$ is found to emerge at magnetic fields below a critical field of $B_c \approx \pm 2.5$ T, common to all temperatures. At this critical field, the oscillating quantum Hall state undergoes a transition towards insulating properties. Both the parabolic background and the weak localization correction to the Drude resistivity $\Delta\rho_{xx}(B)$ (inset of Fig. 6.17) logarithmically increase with reduced temperature, albeit sample heating masking a further differentiation of the magnetoresistivity for $T \leq 100$ mK. Such a temperature-induced transition of a disordered 2D carrier system towards an effective insulator is predicted by the well established scaling theory [181] of Anderson-Mott localization [182] in the thermodynamic limit of zero temperature. At low temperatures, potential fluctuations tend to localize wave functions to the localization length scale ζ. The strength of the localization in a 2D system can then

be estimated by the exponential relation [10]

$$\zeta \approx l_e \, \mathrm{e}^{k_F l_e/2}, \tag{6.9}$$

assuming $k_F l_e \gg 1$. Deduced from the measurements in Fig. 6.17, Figure 6.18 hence illustrates that the localization length rapidly approaches the scale of the Fermi wavelength λ_F as the temperature is reduced, with $\zeta \approx \lambda_F$ around $T = 400$ mK and even $\zeta \ll \lambda_F$ for temperatures below. The system has reached the regime of strong localization [10]. Carriers are then said to be localized around single impurities

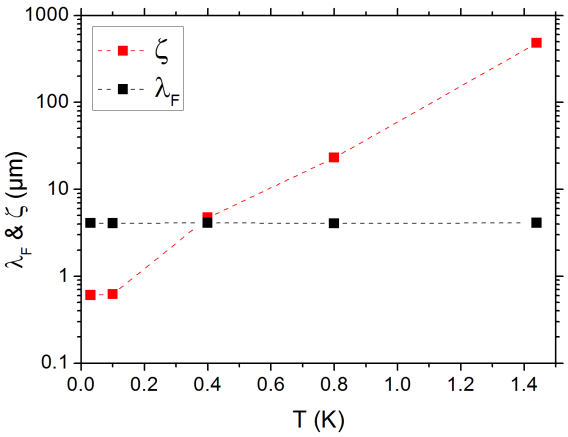

Figure 6.18: *The increasing strength of localization with decreasing temperature in Fig. 6.17 can be parametrized by the localization length ζ of Eq. (6.9) that becomes comparable to the Fermi wavelength at $T = 400$ mK and even smaller than λ_F for temperatures below, hence reflecting the strong localization of this system (note the logarithmic scale - dashed lines are guides to the eye).*

and transport is characterized by hopping in between localization sites either by thermal activation or by quantum tunnelling [10]. As the density would be increased, however, weak potential fluctuations due to an efficient screening lead to delocalized extended states of $\zeta \gg \lambda_F$ at the Fermi level.

For more than two decades, the nature of the transition towards such an extended two-dimensional state, which, contradicting the scaling theory, might exist even at absolute zero temperature in form of a zero or finite resistivity, has been widely discussed as a phenomenon commonly referred to as the 2D metal-insulator transition (MIT) [183]. The MIT is indicated in the density-tuned crossover from a low-density insulating temperature-dependence of the zero magnetic field longitudinal resistivity $\rho_{xx,0}(T)$, characterized by a large negative $\partial\rho_{xx,0}(T)/\partial T < 0$ as $T \to 0$, to a high-density effectively 'metallic' regime of a weak or moderately positive $\partial\rho_{xx,0}(T)/\partial T \gtrsim 0$ at low temperatures [184]. This alleged quantum phase transition of the ground state critically depends on the strength of the fluctuating potential, and therefore on the carrier density. It is characteristically triggered by a sharp critical density p_c separating the low-density insulating phase ($p < p_c$) from the high-density metallic phase ($p > p_c$) at the lowest temperatures accessible [185, 145].

The first report of an unambiguously identified MIT is ascribed to Kravchenko *et al.* in 1994 [186] in the inversion layers of an n-type high-mobility, low-density Si MOSFET. Although challenging the conventional 2D scaling theory of localization

for non-interacting carriers in weakly disordered systems [187], the MIT has subsequently been observed numerously in a variety of materials like n-type [188, 189] and p-type [141, 190, 142] AlGaAs/GaAs heterostructures, as well as p-type Si/SiGe [147, 191] or n-type InAs [192] QW systems.
Figure 6.19 presents a weak effective metallic phase in $\rho_{xx,0}(T)$, a rare occurrence in the range of the p-type InAs:Mn 2DHG QW systems of this study, along the [010] direction of an ungated HB sample ($T_{\mathrm{Mn}} = 690\,^{\circ}\mathrm{C}$) at a 2D hole density of $p = 4.72 \times 10^{11}\ \mathrm{cm}^{-2}$ (red data). Next to that, the typical $\rho_{xx,0}(T)$ traces of strong insulating behavior at $T \to 0$ of a gated sample ($T_{\mathrm{Mn}} = 656\,^{\circ}\mathrm{C}$) at lower hole densities $p = 3.70 \times 10^{11}\ \mathrm{cm}^{-2}$ and $p = 2.75 \times 10^{11}\ \mathrm{cm}^{-2}$ are shown (black data). In the

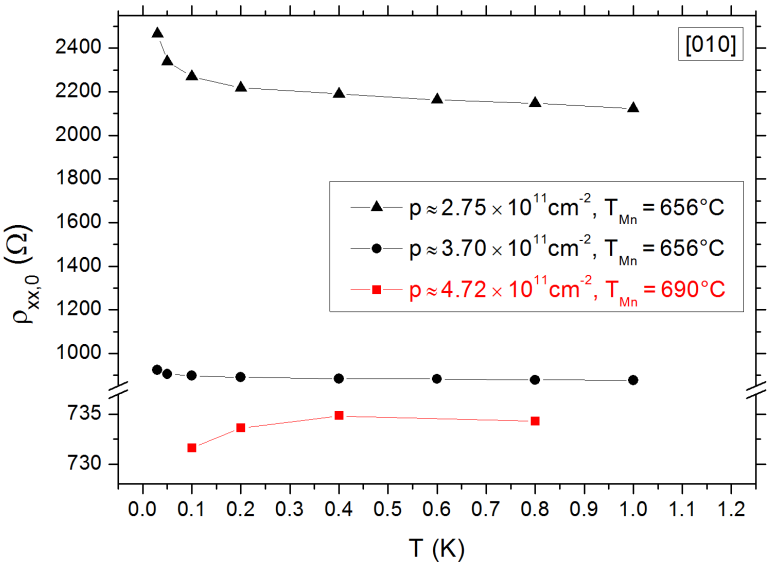

Figure 6.19: *Indications of a possible MIT in the regularly doped InAs:Mn 2DHG system emerge within the variety of samples as an illuminated, ungated HB sample of high density $p = 4.72 \times 10^{11}\ \mathrm{cm}^{-2}$ ($T_{\mathrm{Mn}} = 690\,^{\circ}\mathrm{C}$) demonstrates a weakly positive $\partial\rho_{xx,0}/\partial T \gtrsim 0$ when the system approaches absolute zero temperature (red data, lines are guides to the eye), whereas the black data traces exemplarily illustrate the otherwise common insulating phase of a large negative $\partial\rho_{xx,0}/\partial T < 0$ for an also illuminated, yet additionally gated sample of $T_{\mathrm{Mn}} = 656\,^{\circ}\mathrm{C}$ at lower densities $p = 3.70 \times 10^{11}\ \mathrm{cm}^{-2}$ and $p = 2.75 \times 10^{11}\ \mathrm{cm}^{-2}$. For clarity, note the different scales of $\rho_{xx,0}(T)$.*

insulating phase, we see that the smaller the density, the stronger is the influence of localizing potential fluctuations at low temperatures. It should be noted that both samples of this example have been illuminated, hence the metallic phase was generated by externally enhancing the carrier density and thus the effective screening from partially neutralized impurities.

In the context of this discussion, having a knowledge of the impurity doping density N_d, the threshold density p_c of the MIT is calculated according to Efros

et al. by [177, 193, 10]

$$p_c = \beta \frac{\sqrt{N_d}}{s}, \tag{6.10}$$

where $\beta = 0.11$ is a numerical coefficient and $s = 7.5$ nm denotes the separation of the modulation doping layer (regarded as δ-shaped) from the 2DHG plane. Here, assuming that the relation is valid for 2D hole systems and that the critical density is $p_c \lesssim 4.7 \times 10^{11}$ cm^{-2}, judging from the emergence of the MIT in Fig. 6.19, an attempt to quantify the effective Mn doping concentration in this sample of $T_{\mathrm{Mn}} = 690$ °C would thus yield $N_d \gtrsim 1.47 \times 10^{19}$ cm^{-3}, which represents a lower bound to the doping concentration of the system. In general, a clear observation of the MIT so can provide a method for the quantification of the modulation doping concentration of the system.

Although not explicitly witnessed within the density and temperature variations of $\rho_{xx,0}(T, p)$ of one single sample, the anomalous low-temperature behavior in Fig. 6.19 still suggests that a MIT is probable for some of the highest densities and mobilities of 2DHGs in the given InAs material, in a sense that sufficient screening leads to an effective 2D metallic phase rather than a real quantum phase transition might occur. Yet, the prevailing insulating trend in the absence of the MIT confirms that the 2D hole systems of this study's density range are predominantly in a density-inhomogeneity-driven percolation state of insufficiently screened, smooth long-range Coulombic potentials of disordered ionized impurities [145]. This strongly supports this chapter's established basic assumption of disorder as the main source of scattering in the diffusive transport of this system.

In the considerations above, low-temperature density-induced insulating behavior at $B = 0$ T and enhanced quantum corrections to the Drude magnetoresistivity were shown to be governed by an interplay of carrier-carrier interactions and quantum localization due to strong disorder. In the low-density regime, the framework of the screening theory suits the realistically dominant long-range impurity Coulomb potentials. In the high density regime earlier in Sec. 6.2.1, we discussed experimentally similar behavior of a parabolic background in $\rho_{xx}(B)$ in the spirit of carrier-carrier interaction, formally described under the assumption of h-h constructive interference upon scattering on short-ranged impurity potentials and associated so-called Friedel oscillations [194, 142, 10]. Following Das Sarma *et al.* [145], both these descriptions, the h-h interaction and the screening theory, are to be seen as complementary approaches to the nature of the low-density insulating regime of 2DHGs in regularly doped disordered InAs:Mn QW heterostructures.

6.5 Conclusion

The possibilities of an effective tuning of the Rashba SOI in a two-dimensional hole gas system have been explored by continuously and significantly decreasing the density in Mn-doped QW heterostructure alloys based on the high-SOC material InAs by the joint reduction of the doping concentration and external electric gating for the first time in this system. The emerging rich density spectrum of regimes of interference and interaction quantum corrections to the longitudinal Drude magnetoresistivity could be correlated with the relative carrier-density- and temperature-evolution of spin- and phase-relaxation times of the 2DHG system. These characteristic time scales were deduced from the analysis of the low-field WAL interference phenomenon on the basis of anisotropic transport parameters and effective hole masses. Although small in magnitude, the spin splitting energy of the HH subband was distinctly modified over the whole range of achieved densities. This variation was found to represent the direct effect of the external electric field rather than a manipulation of the Rashba parameter. Indeed, this parameter is determined mainly by the large HH-LH splitting of the strained QW channel than by the externally applied electric field. Spin-dependent scattering by the D'yakonov-Perel' mechanism in the SO field leads to a higher preservation of spin orientation at the low-carrier-density limit of the density spectrum covered.
In general, the principle governing the trends of spin- and phase-dependent transport parameters over the studied range of densities has consistently been identified, most clearly in the low-carrier-density regime, as the enhanced localization and scattering within the diffusive percolating motion of holes in a 2D landscape of insufficiently screened, randomly distributed Coulomb potentials of remote doping impurities.

7

Highly diluted magnetic InAs:Mn QW heterostructures

The image established in the previous chapter of non-magnetic 2D hole gases in diffusive InAs:Mn QW heterosystems governed by quantum localization and quantum interference phenomena changes dramatically when charged magnetic impurities reside in close proximity to the free hole gas in the InAs channel. As introduced and illustrated in Sec. 4.3, a small change of the doping concept in the inverted InAs:Mn heterosystem leads to the direct incorporation of magnetic manganese impurities from segregation into the channel region during growth. There, they act as sources of strong localization of carrier spin magnetic moments via magnetic exchange coupling. Instead of long-range Coulomb potential fluctuations from disordered remote impurities, short-range magnetic exchange interaction now is the prevailing mechanism in inverted InAs:Mn systems. Within the strong interplay of free holes and localized Mn^{2+}-ions, magnetic exchange interaction also affects other properties of the diluted magnetic semiconductor (DMS) system as it may generate a giant energy band spin splitting, the formation of bound magnetic polarons, spin-disorder scattering and carrier-mediated ferromagnetic ordering [176, 195]. The modulation doping profile thereby potentially enables high carrier mobilities in the InAs channel to study the effects of the DMS system in magnetotransport experiments.

Continuing our systematic efforts on the consistent classification of magnetoresistive phenomena within the spectrum of manganese-doped InAs QW heterosystems, we have extended the range of inverted InAs:Mn heterostructures grown at various Mn fluxes predominantly towards low temperatures of the Mn effusion cell, hence low concentrations of Mn^{2+}-ions in the InAs channel. With this, we want to document magnetoresistive effects at the transition into the highly diluted limit of

the inverted InAs:Mn system. A survey of all MBE-grown inverted InAs:Mn QW heterostructures of this study is featured in Appendix B.

Figure 7.1 presents exemplary magnetotransport measurement data of the longitudinal resistivity together with the absolute value of the Hall resistivity of an inverted InAs:Mn Hall bar sample of fixed Mn doping concentration, $T_{\mathrm{Mn}} = 717\,^{\circ}\mathrm{C}$ (wafer C120322A, cf. Appendix B), with the current applied along the diagonal [100] crystallographic direction at various low temperatures.

The traces of the Hall resistivity $\rho_{xy}\,(B)$ are found to be characterized by a num-

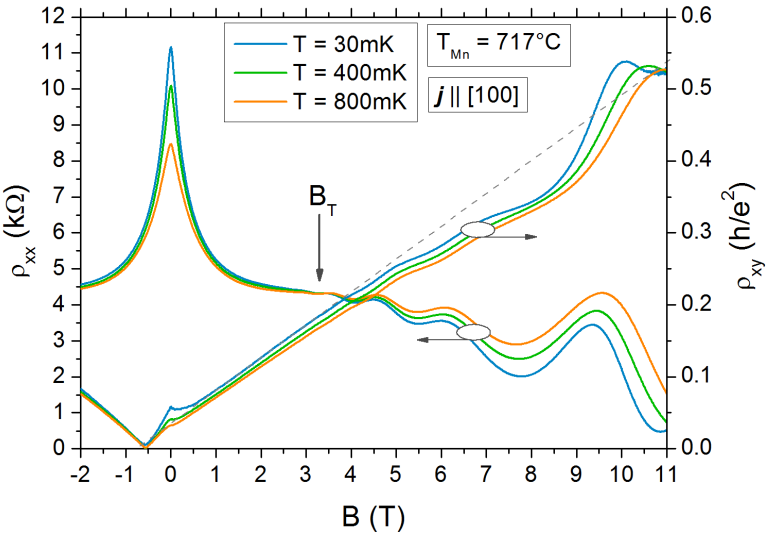

Figure 7.1: *Reducing the temperature from $T = 800$ mK down to $T = 100$ mK enhances the low-field longitudinal NMR signal of strong localization around $B = 0$ T of an inverted InAs:Mn Hall bar structure (C120322A, $T_{\mathrm{Mn}} = 717\,^{\circ}\mathrm{C}$) along the* [100] *crystallographic direction. All traces of $\rho_{xx}\,(B)$ share a common magnetoresistivity value at $B_T = 3.3$ T that marks the transition from the low-field localized regime to the high-field delocalized quantum Hall regime. A negative bending of $\rho_{xy}\,(B)$ from the classical Hall resistivity (indicated by a grey dashed line) is observed for higher magnetic fields.*

ber of anomalous features: Besides the finite offset phenomenon at $B = 0$ T known from Sec. 5.2 for diagonally aligned structures, which is accompanied by overshooting signatures at higher fields around $B \approx 10 - 11$ T, there are signatures of the anomalous Hall contribution around exactly zero magnetic field, regardless of the offsetting. Other than that, a slight negative bending of the Hall magnetoresistivity traces is visible from the expected classically linear Hall resistivity, which would be indicated by a grey dashed line for the trace of $T = 30$ mK. This latter phenomenon has been associated with an additional band of delocalized extended states (see below) [95, 195], as parallel conductance in the InAlAs:Mn doping layer can reasonably

be excluded with the minima of $\rho_{xx}(B)$ approaching zero resistance for high magnetic fields [91].
In the longitudinal magnetoresistivity $\rho_{xx}(B)$, low-field strong localization coexists with the SdH oscillations of the quantum Hall regime at higher magnetic fields.

Exchange coupling of the itinerant hole spins and the localized distribution of magnetic Mn^{2+}-ions residing in the channel region has been introduced in Sec. 4.3 to cause a pronounced reduction of magnetoconductivity at low magnetic fields due to the strong localization of the carriers on Mn acceptor sites. At the absence of an external magnetic field, hole spins are coupled to the parent Mn acceptors in antiparallel alignment of the spin moments by strong *p-d* exchange interaction, forming an energetically favorable spin singlet state [94, 95]. In this strongly localized regime, charge carrier transport may occur by hopping between localized states in the tail region of highly degenerate LLs broadened by magnetic disorder [196, 197, 195]. With the application of a magnetic field perpendicular to the 2D InAs channel plane, hole spins and Mn magnetic moments are then being oriented in parallel to form a triplet-type of state, significantly increasing the radius of localization and consequently decreasing the coupling of holes to the Mn^{2+}-ions due to the Pauli principle. With the potential landscape effectively being flattened as the magnetic moments are aligned in parallel, delocalized extended hole spin states are emerging. This leads to an enhanced conductance in either a spin-up or a spin-down spin channel depending on the polarization of the external magnetic field. The common value of $\rho_{xx}(B_T)$ at a magnetic field $B_T \approx 3.3$ T in Fig. 7.1 thus marks the transition from the regime of strong localization to the delocalized 2D quantum Hall regime with SdH oscillations developing at higher magnetic fields. This observation of a transition field is reminiscent of the temperature-induced increase of $\rho_{xx}(0)$ in the insulating regime of the Anderson-Mott MIT [182] below a critical carrier density, which was introduced in Sec. 6.4 for non-inverted InAs:Mn systems. A temperature-dependent reduction of the scaling of the localization in Fig. 7.1 below B_T may also be associated with an enhancement of hopping transport processes by thermal activation increasing the amount of free holes.

In general, the characteristic magnetoresistive properties of the inverted diluted magnetic 2DHG systems in the regime of strong localization crucially depend on the ratio of the 2D hole density to the manganese ions in the vicinity of the InAs channel, $p/x_{Mn^{2+}}$, rather than mainly on the absolute hole density itself, as it was the case for the non-inverted system in Sec. 6.3.
We can demonstrate this issue in Figure 7.2 (a) by the evolution of the magnetoresistive traces $\rho_{xx}(B)$ with the reduction of the Mn doping concentration temperature from $T_{Mn} = 825$ °C to $T_{Mn} = 700$ °C in various vdP-type of samples at $T = 1.44$ K, cf. Appendix B. For concentrations above $T_{Mn} = 825$ °C, samples were found to be insulating in the whole magnetic field range. In Fig. 7.2 (a), the zero-field resistivity peak $\rho_{xx}(0)$ of strong localization dominating the longitudinal magnetoresistance is reduced greatly with decreasing Mn doping concentration on a logarithmic scale.

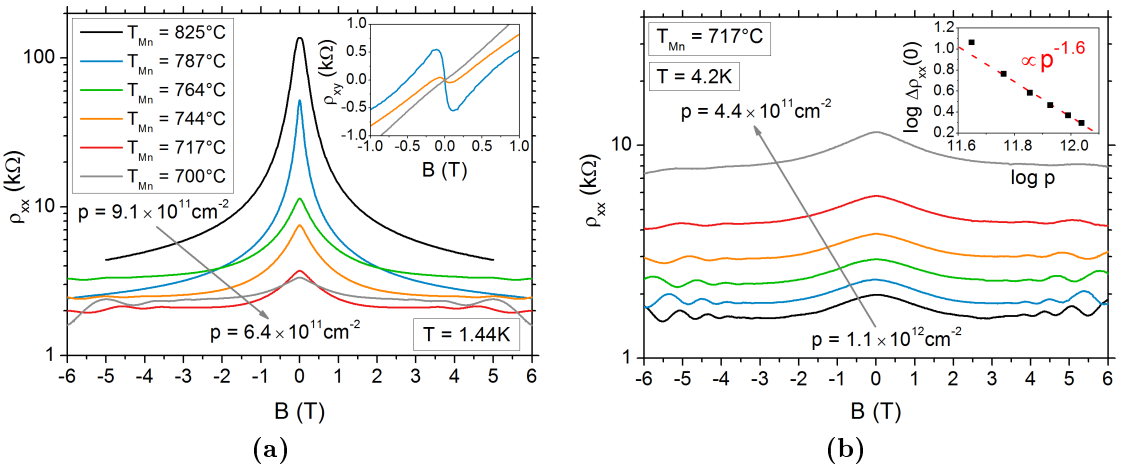

Figure 7.2: (a) *Longitudinal magnetoresistivities* $\rho_{xx}(B)$ *of vdP samples in dependence of different selected Mn doping temperatures* T_{Mn} *on a logarithmic scale at* $T = 1.44$ K. *The dominating NMR signature of strong localization in* ρ_{xx} *around* $B = 0$ T *decreases with decreasing Mn doping concentration,* T_{Mn}, *simultaneously reducing the hole density p. Inset: Associated non-linear corrections to selected* $\rho_{xy}(B)$ *at low magnetic fields due to the contributions of the AHE. The signature vanishes with a decreasing concentration of magnetic* Mn^{2+}*-ions in the InAs channel.* **(b)** *Instead, the gate-induced density variation of* $\rho_{xx}(B)$ *for a fixed Mn concentration (HB structure of wafer C120322A,* $T_{\mathrm{Mn}} = 717$ °C*) at* $T = 4.2$ K *demonstrates an enhancement of strong localization with reduced hole density (note the logarithmic scale of* ρ_{xx}*). Inset: A log-log plot of the overall* $\Delta\rho_{xx}(0)$ *versus p then suggests a density-dependence* $\propto p^{-3/2}$.

Reducing T_{Mn}, decreases both, the amount of segregated Mn^{2+}-ions in the channel as well as the 2D hole density, the latter here from about $p = 9.1 \times 10^{11}$ cm^{-2} down to $p = 6.4 \times 10^{11}$ cm^{-2}. Since SdH oscillations are suppressed in a wide range of magnetic fields due to the dominating strong localization correction for high $x_{\mathrm{Mn}^{2+}}$, hole densities were retrieved from the slope of the classical part of the Hall resistivity. It should also be noted that the 2D hole mobility is not a well defined quantity of the DMS system at low magnetic fields when the zero-field value of ρ_{xx} is determined by the localization signature. By this predominance, also zero-field corrections of quantum interference are irrelevant in the regime of strong localization.
A clear trend of the NMR peak of strong localization becoming less and less dominant in $\rho_{xx}(B)$ is found in Fig. 7.2 (a) as the ratio $p/x_{\mathrm{Mn}^{2+}}$ of free holes decoupled from less and less Mn^{2+}-ions increases. The same phenomenon is witnessed in the low-field Hall characteristics of the anomalous Hall effect, as depicted for selected T_{Mn} in the inset of Fig. 7.2 (a): A decreasing non-linear signal of the AHE indicates a ceasing relevance of the magnetic exchange coupling with reduced Mn concentration. Similar findings are presented and analyzed in more detail regarding the intrinsic

and extrinsic SO-dependent mechanisms contributing to the AHE in these DMS systems by Wensauer and Vogel in [198] and [199], respectively. Nagaosa *et al.* give an extensive general review of the anomalous Hall effect in [197].

A second possibility to manipulate the ratio $p/x_{\mathrm{Mn}^{2+}}$ is provided by the gate-induced variation of p while keeping the Mn concentration fixed. This is demonstrated in Fig. 7.2 (b) at $T = 4.2$ K for a gated Hall bar sample of again $T_{\mathrm{Mn}} = 717$ °C from the lower spectrum of Mn doping concentrations. In the InAs:Mn heterosystems of the inverted doping concept, p-tunability via the gate electric field effect is more efficient due to the absence of an upper screening InAlAs:Mn layer that is present in the case of the regular doping scheme (see Sec. 6.2). Again, from the Hall slope in the classical part of $\rho_{xy}(B)$ (not shown), we find that the 2DHG system can be depleted from $p = 1.1 \times 10^{12}$ cm^{-2} to $p = 4.4 \times 10^{11}$ cm^{-2} by gate, which leads to a strong increase of the zero-field sheet resistivity $\Delta\rho_{xx}(0)$ and the degree of the localization signal (note the logarithmic scale in Fig. 7.2 (b)). A log-log plot of $\Delta\rho_{xx}(0)$ as a function of the hole density p suggests a dependence $\propto p^{-1.6}$ (red dashed line). Decreasing the ratio of $p/x_{\mathrm{Mn}^{2+}}$ in the 2DHG system, leads to a gate-induced loss of many-body screening from magnetic impurity sites in the channel and therefore to an enhanced localization of hole spins.

In conclusion, the experiments of Fig. 7.2 have demonstrated that the opposing trends of an increasing strong localization effect with (a) increasing both p and $x_{\mathrm{Mn}^{2+}}$ and with (b) a decreasing p at a fixed $x_{\mathrm{Mn}^{2+}}$ clearly suggest the ratio $p/x_{\mathrm{Mn}^{2+}}$ to be the key property of the inverted DMS system, confirming the current understanding of the system as established in e.g. [200, 96].

In our experiments, we did not witness the prominent colossal and hysteretic, temperature-dependent and magnetic-field-induced quantum-Hall-to-insulator jumps over several orders of magnitude in the zero-field range of the longitudinal NMR that were reported by Wurstbauer for the InAs:Mn DMS system [201, 93, 202, 96]. The model presented in [96] considers the resistance jumps to be a result of hole overheating effects, while the hysteresis is to be due to a magnetic anisotropy energy barrier of the heavy holes bound to the Mn acceptors by the strong p-d exchange interaction. While temperatures below $T = 1.44$ K are likely to be required for an observation at $T_{\mathrm{Mn}} \geq 700$ °C in Fig. 7.2 (a), the absence of this clear phase transition even at mk-temperatures in Fig. 7.1 here suggests a ratio of $p/x_{\mathrm{Mn}^{2+}}$ sufficiently high enough to prevent the extremely insulating low-field regime under the presented conditions. Moreover, no evidence of long-range ferromagnetic correlation of diluted Mn^{2+}-ions in the vicinity of the 2DHG has been found.

At this point, we want to extend our studies within the spectrum of inverted diluted InAs:Mn QW heterostructures towards further reduced Mn doping concentrations, as we proceed with the characterization of samples containing InAlAs:Mn layers grown at even lower temperatures of the Mn effusion cell (cf. Appendix B). Starting from $T_{\mathrm{Mn}} = 700$ °C, we can track a distinct change in the nature of the longitudinal magnetoresistivity in Fig. 7.3 (a): While the zero-field resistivity $\Delta\rho_{xx}(0)$

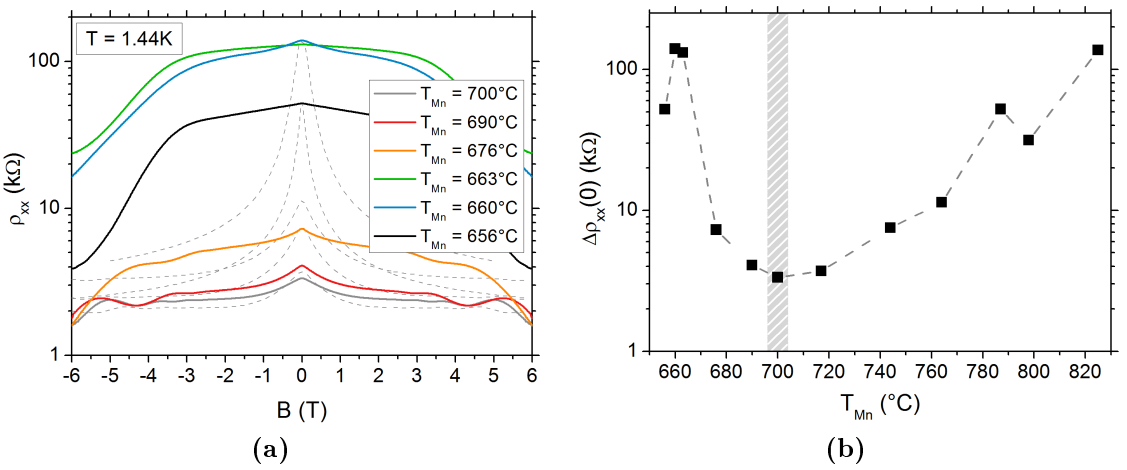

Figure 7.3: (a) *Combined longitudinal magnetoresistivities at* $T = 1.44$ K *from the continued reduction of the Mn doping concentration in the range of* $T_{\mathrm{Mn}} = 700$ °C *to* $T_{\mathrm{Mn}} = 656$ °C *on the background of the indicated dashed* ρ_{xx} *traces of higher* T_{Mn} *from Fig. 7.2 (a).* **(b)** *Summarized zero-field resistivities* $\Delta\rho_{xx}(0)$ *as a function of the temperature of the Mn effusion cell* T_{Mn}. *The dashed line is a guide to the eye.*

was found to decrease continuously with reduced T_{Mn} in Fig. 7.2 (a), we now observe a strong increase of $\Delta\rho_{xx}(0)$ below $T_{\mathrm{Mn}} = 700$ °C, reaching a maximum for about $T_{\mathrm{Mn}} = 660$ °C. Figure 7.3 (b) illustrates this development by combining the values of $\Delta\rho_{xx}(0)$ from the complete spectrum of inverted systems as a function of T_{Mn}[1] on a logarithmic scale.

Interestingly, in this regime of highly diluted Mn concentrations below $T_{\mathrm{Mn}} = 700$ °C, the traces of the longitudinal magnetoresistivity in Fig. 7.3 (a) reveal a close resemblance to the characteristic enhancement of $\rho_{xx}(B)$ in non-inverted InAs:Mn QW systems for low Mn concentrations investigated in the previous Section 6.4 (also see the Survey 6.1). Decreasing the Mn doping concentration in the inverted InAs QW system of course leads to a reduced amount of Mn^{2+}-ions in the channel and a reduced 2D hole density. It seems that at about $T_{\mathrm{Mn}} = 700$ °C a critical ratio $p/x_{\mathrm{Mn}^{2+}}$ is reached where the system in the regime of strong localization via exchange coupling of Mn^{2+}-ions is transferred into an increasing effectively insulating regime of localization by long-range potential fluctuations of remote disordered Mn acceptors, independent of the external magnetic field. The hole density has become too low to form delocalized extended states and transport in a density-disorder-driven percolation state prevails.

It should be noted that enhancing the hole density by illumination (see Appendix B) generates longitudinal magnetoresistivity signatures of high-mobility quantum Hall systems without the pronounced strong localization or insulating features, instead

[1] The determination of hole densities from the low-T_{Mn} magnetoresistivities lacks of sufficient accuracy for p to serve as the scaling.

rather showing the characteristic small peak signature of weak localization correction to ρ_{xx} at $B = 0$ T. This clearly demonstrates an absence or overcompensation of robustly screened, highly diluted Mn^{2+}-sites in the channel region.

We conclude that 2D hole magnetotransport characteristics of inverted highly diluted magnetic InAs:Mn systems join the Anderson-Mott insulating regime of low-density non-magnetic InAs:Mn systems below a certain threshold ratio of $p/x_{Mn^{2+}}$ at $T_{Mn} \approx 700$ °C as the influence of exchange coupling by magnetic Mn^{2+}-ions on a low-density 2DHG ceases.

8
Conclusions and perspective

The present work aimed at the investigation of the complex Rashba spin-orbit interaction of 2D hole systems in Mn-modulation-doped $In_{0.75}Al_{0.25}As/In_{0.75}Ga_{0.25}As/$-InAs quantum well heterostructures as due to its key role for spin manipulation in spintronic functionality. For the first time, we were able to evaluate the tunability of Rashba-SOC-related parameters in these 2DHG structures experimentally from an extensive analysis of the hole density evolution of quantum interference effects at low magnetic fields. We achieved to cover a significant range of hole density variation by the joint action of the variation of the doping concentration during epitaxy and external field-effect-mediated manipulation in transport devices by a metallic topgate.

Molecular beam epitaxy of indium-based ternary alloys of variably high In content was performed on GaAs substrates employing a special metamorphic step-graded buffer concept of $In_xAl_{1-x}As$ layers with gradually increasing In concentration x, in order to compensate for the mismatch of lattice constants. Strain is released by the intentional formation of misfit dislocations within the buffer system, which is composed of two In gradients including final overshooting layers of $x = 0.85$. Detailed high-resolution TEM cross-sectional studies of the heterostructure crystal documented the distribution of dislocations from strain relaxation in the buffer and the consequent realization of defect-free, high-quality crystal layers of constant composition below the QW region.
The optimized set of growth parameters was also established from magnetotransport experiments on 2D electron systems in undoped InAs QW heterostructures, where the carriers originate from ionized deep level donor states.

Strain relaxation in buffered high-In heterosystems via the formation of networks of dislocations is crystallographically inhomogeneous. This leads to a preferential incorporation of indium in low-strain-regions during the growth of the ternary alloyed system as it is reflected in a morphologically anisotropic cross-hatching pattern of periodic undulations of the surface. AFM investigations of cross-hatched InAs:Mn QW heterostructures could link these topographies to the characteristic anisotropic 2DHG magnetotransport behavior of the system, where the highest carrier mobilities are observed in the $[\bar{1}10]$ direction of longest periodicity of the crosshatching undulations. Periodic compositional fluctuations of the In concentration in the ternary compound layers affecting the valence energy band modulation and inherent variations of residual strain are supposed to contribute to the anisotropic scattering potentials of the cross-hatched system limiting the 2D hole mobilities along the distinguished $\langle 110 \rangle$ directions.
In the course of crystal-direction-resolved low-temperature 2D magnetotransport experiments on this anisotropic system, persistent anomalies of the transverse magnetoresistivity were identified along Hall bar orientations other than the distinct cross-hatching directions. In this diagonal alignment, Hall magnetoresistivities were discovered to be non-zero at zero magnetic field and to show overshooting signatures in the quantum Hall regime. Carrying out an extensive comparative study of 2D hole and electron systems in various semiconductor compound heterostructures with or without a cross-hatching formation, we identified the offset in $\rho_{xy}(0)$ along any orientation differing from the directions of the distinguished anisotropies to be an inherent consequence of a 2D carrier system experiencing a twofold anisotropic perturbation. Empirical sinusoidal characteristics of $\Delta\rho_{xy}(0)$ for arbitrary Hall bar orientations with respect to the asymmetric reference system could consistently be fitted within an extended framework of the magnetic Drude model explicitly considering a twofold anisotropic scattering potential. The deduced anisotropy factors of this offset phenomenon in the classical Hall regime were found to be in consistency with the anisotropy of the corresponding 2D carrier mobilities, supporting the universal relevance of this effect in 2D systems defined by anisotropic scattering conditions.
In the quantum Hall regime, future studies on the overshooting signatures, which are possibly connected to the shear existence respectively effective mixing of an anisotropic two-level system, not to issues of misaligned contact fabrication, need to be conducted for further clarification.

The fundamental anisotropic character of the InAs:Mn 2DHG system was also found to be reflected in the effective hole masses, $m^*_{h,[\bar{1}10]} = 0.10\,m_0$, $m^*_{h,[010]} = 0.12\,m_0$ and $m^*_{h,[110]} = 0.15\,m_0$, carefully deduced experimentally from the temperature damping of the SdH oscillations of the high-field longitudinal magnetoresistivity $\rho_{xx}(B)$. Again, from the temperature-dependence of $\rho_{xx}(B)$, we established hole-hole interaction to induce a negative parabolic correction to the mid-field longitudinal magnetoresistivity where deviations in the T-dependence at lowest system temperatures are likely to be caused by emerging localization due to insufficient

screening of the long-range Coulomb potentials of disordered charged doping impurities.

Taking into account this background of magnetotransport properties of the InAs:Mn QW 2DHG system, we performed a thorough analysis of the low-field positive magnetoresistive correction to $\rho_{xx}(B)$, the dip signature of the weak antilocalization, as an unambiguous sign of high spin-orbit interaction. As the WAL magnetoconductivity data could excellently be fitted by the Hikami-Larkin-Nagaoka model considering cubic in k SOI terms for HH subband occupation only, we obtained the characteristic phase coherence and spin-orbit scattering times of the system, τ_ϕ and τ_{SO}, respectively. Again, these were of anisotropic character in terms of crystallographic directions, like all parameters of the system.
In gate-dependent experiments, an increasing τ_{SO} with a decreasing elastic transport scattering time τ_{tr} at reduced hole density p then clearly revealed the works of the DP mechanism as the dominant mechanism of spin relaxation in this system. Spin relaxation lengths up to $l_{SO,[\bar{1}10]} \approx 265$ nm in the low-density limit have shown that the spin orientation is preserved via the DP mechanism through enhanced elastic scattering of holes in disordered Coulomb potentials due to a reduced screening effect at low hole densities. A saturation of the low-temperature-dependence of dephasing times $\tau_\phi(T)$ at $T \to 0$ K suggested that inelastic scattering by potential fluctuations induced by disorder could also contribute to the dephasing at lowest temperatures, while else hole-hole scattering with small energy transfer is the dominant process at temperatures above $T \approx 600$ mK.

As the doping concentration of the InAs:Mn QW system was lowered, we were able to witness gate-induced transitions from weak antilocalization to weak localization in 2DHG magnetotransport that could be linked to crossing trends of the characteristic $\tau_{SO}(p)$ and $\tau_\phi(p)$ times. In fact, a survey of the evolution of quantum interference phenomena was presented in correlation with the relative magnitudes of characteristic time and length scales across the complete experimentally accessible density regime. Combining external electric gating and variation of the p-type doping concentration, a maximum density range from $p = 6 \times 10^{11}$ cm^{-2} down to $p = 2 \times 10^{11}$ cm^{-2} could be probed. Therein, a high-density regime of pure WAL, where $l_{SO} \leq l_{tr} \ll l_\phi$, descends into a regime of mixed WAL and WL signatures, where $l_{tr} \ll l_{SO} \ll l_\phi$, and into a final regime of pure WL of $l_{tr} < l_\phi < l_{SO}$ at lowest hole densities.
With these transitions being governed by the relative strength of SO-related parameters, we were able to vary the HH subband energy spin splitting by a factor of 2 across the complete range of densities, its absolute value yet being unexpectedly small in magnitude. The evaluated dependences of the spin splitting $\Delta E(p)$ and of the effective Rashba coefficient $\alpha^h \mathcal{E}_z$, however, suggest that these are not addressed by the Rashba SOI via a variation of p but rather influenced by the external electric field itself. As the cubic Rashba coefficient α_3^h is dominated by the large HH-LH separation of the 2DHG system due to the compressive strain within the InAs channel, it cannot be manipulated significantly in these indium-based 2DHG

QW heterostructures, limiting a direct tunability.

Concluding our study on low-density 2DHGs, we investigated the insulating nature of strongly localizing effects due to the non-linear breakdown of an effective screening from impurity potentials. We found similar phenomenology in both the regularly and inversely doped InAs:Mn QW heterostructures: In regularly doped structures, we see the universally dominating influence of insufficiently screened smooth disorder confirmed by the occurrence of a MIT towards effectively screened delocalized extended states at highest carrier densities. In inverted structures of highly diluted magnetic Mn doping in the vicinity of the low-density 2DHG channel, we observe that below a threshold ratio $p/x_{\mathrm{Mn}^{2+}}$ at $T_{\mathrm{Mn}} \approx 700\,^{\circ}\mathrm{C}$ the influence of strongly localizing magnetic exchange coupling at higher concentrations of magnetic Mn^{2+}-ions is replaced by localizing long-range impurity potentials.

In summary, while we found the spin relaxation to be reduced in the low-density 2D hole gas system of the anisotropic $\mathrm{In_{0.75}Al_{0.25}As/In_{0.75}Ga_{0.25}As/InAs}$:Mn QW heterostructure by the D'yakonov-Perel' mechanism and the hole energy spin splitting to be varied, a manipulation of the Rashba parameter is yet suppressed. Within the complexity of the valence band hole states, there is a potentiality in tuning the strain-induced HH-LH splitting to influence the Rashba SO parameter. By that, a significant spin manipulation via strong Rashba SOI could be balanced at the given sufficient spin conservation at low 2D hole carrier densities, in order to advance in the investigation of spintronic 2D hole gas devices based on indium arsenide.

A

Processing gated Hall bar structures

1. **Optical lithography and wet chemical etching**
   - Scribe the wafer by a tungsten carbide needle and break pieces of required size - usually 5 mm × 5 mm. Mark each piece for unambiguous determinability of the crystal orientation.

     Cleanroom ambience:
   - Perform standard cleaning procedure of successive acetone baths assisted by ultrasound. Rinse and store the piece in isopropanol until further use.
   - Dry piece with nitrogen and coat with positive photoresist Shipley 1813 in spin coater at 4500 U/min for 30 s. Perform soft bake to remove remaining water on a hotplate at 90 °C for 4 min.
   - Expose masked resist to UV light (274 W) in mask aligner for ca. 54 s (Hall bar structures used are located on masks 43/44b & 58 - mask 52 for gate structures).
   - Develop exposed resist using NaOH-based ARP 300-26 : $H_2O = 1 : 3$ for ca. 42 s. Rinse in a cascade of clear water, dry with N_2 and control the resulting resist pattern under microscope.
   - Perform wet chemical etching of III-V alloys with stirred acetic acid : H_2O_2 : $H_2O = 5 : 1 : 5$ for ca. 50 s (corresponding to ca. 170 - 190 nm etch depth). Rinse in a cascade of clear water, perform standard cleaning and dry with N_2 before confirming the achieved Hall bar height via Dektak surface profilometer.

2. **Ohmic contacts**

   - Scratch the contact pads of the Hall bar by a tungsten carbide needle from the center region of the pads across the edges to surely contact conducting edge channels.

   ***n*-type contacts**

   - Solder droplets of pure indium (In 6N) upon the scratches.
   - Alloy the In contacts at 460 °C for 300 s at a ramp of 300 s in forming gas atmosphere.

   ***p*-type contacts**

   - Solder droplets of indium-zinc mixture (4-6% Zn, In 6N) upon the scratches.
   - Alloy the InZn contacts at 350 °C for 60 s at a ramp of 60 s in forming gas atmosphere.

3. **Insulating layers**

   PECVD

   - Heat cleaned samples on the table of the conditioned plasma reaction chamber to 150 °C.
   - Cover the sample with ca. 14 nm SiO_2 from a 2×10 s plasma of reacting gases SiH_4 (170 sccm) and N_2O (710 sccm) at 20 W and 650 mTorr. Pause by briefly venting the chamber to vary the distribution of pinholes and thus to improve the overall impermeability of SiO_2.
   - If possible: Leave the sample exposed to atmosphere over night to improve oxidization of SiO_2.

   ALD

   - Adjust a gas flow of 20 sccm N_2.
   - Deposit 50 nm of Al_2O_3 in a two-step process of
     - 100 cycles at 80 °C of 0.015 s pulse H_2O/60 s purge and 0.015 s pulse TMA/60 s purge
     - 400 cycles at 150 °C of 0.015 s pulse H_2O/20-60 s purge and 0.015 s pulse TMA/20-60 s purge

4. **Metallic gate electrode**

   - Perform optical lithography of gate structures.
   - Evacuate the chamber of UNIVEX 450 to a base pressure $< 5 \times 10^{-6}$ mbar.
   - Deposit 10 nm of titanium at max. 0.9 Å/s.
   - Deposit 200 nm of gold at ca. 1.8 Å/s.

- Perform lift-off by dissolving the resist in an acetone bath at 60 °C, rinse in isopropanol, control the quality of the lift-off under microscope and blow dry with N_2.

5. **Completing the sample**
   - Solder In droplets for ohmic contact to the metallic gate if existing.
   - Solder gold wires to all contacts used and fix the device to the sample carrier using vacuum grease.
   - Connect the sample with the measurement environment by soldering the gold wires to the carrier's electrode pins.
   - Characterize the contacts by their resistance quality.

B

Van der Pauw characterization of InAs:Mn QW systems

The van der Pauw method [67] offers a quick way to extract the charge carrier density and the mobility of samples in order to gain first impressions of new wafers' characteristics on a daily basis without the need to pattern a Hall bar geometry. It is valid for finite samples of arbitrary, yet completely filled planar shape, where the contacts are small and located along the sample edge. Figure B.1 shows a scheme of the van der Pauw geometry used for the pre-characterization of the wafers of this study, along with the typical configuration for magnetotransport measurements on these vdP samples, with eight small contacts on the corners and in the middle of the flats of a $5 \times 5\,\mathrm{mm}^2$ squared sample. The sheet resistivity is determined in four-terminal measurements by perturbatively switching contacts. The resistance to

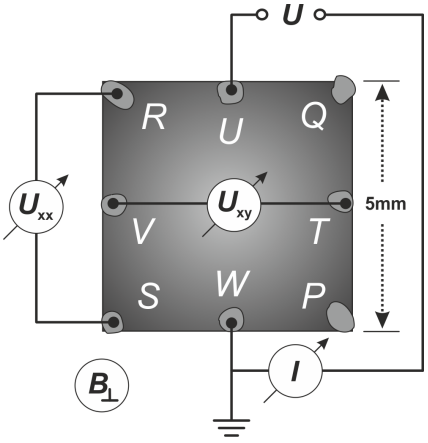

Figure B.1: *Sample geometry and exemplary electrical configuration for measuring the sheet resistivity, as well as $\rho_{xx}(B)$ and $\rho_{xy}(B)$ in magnetotransport experiments based on the van der Pauw method.*

be measured is defined as e.g.

$$R_{\mathrm{PQ,RS}} = \frac{U_{\mathrm{PQ}}}{I_{\mathrm{RS}}}, \tag{B.1}$$

and ρ_{xx} can then be calculated from e.g. $R_{\mathrm{PQ,RS}}$ and $R_{\mathrm{QR,SP}}$ by [67],

$$\rho_{xx} = \frac{\pi}{\ln 2} \frac{R_{\mathrm{PQ,RS}} + R_{\mathrm{QR,SP}}}{2} f\left(\frac{R_{\mathrm{PQ,RS}}}{R_{\mathrm{QR,SP}}}\right), \tag{B.2}$$

with f being the numerical geometry correction factor for the vdP method [10]. Detailed information on these calculations can be found in [67] and [10]. Accordingly, in a magnetic field $B_{\perp}$ normal to the sample plane, the Hall resistivity can be acquired from [10]

$$\rho_{xy}(B) = \frac{R_{\mathrm{PR,QS}}(B) - R_{\mathrm{PR,QS}}(0) + R_{\mathrm{QS,RP}}(B) - R_{\mathrm{QS,RP}}(0)}{2}. \tag{B.3}$$

The following pages are regarded as a catalogue of the InAs:Mn QW heterostructures of this study for orientation and future use, as they feature a collection of vdP magnetotransport curves of every Mn doping series of 2DHG heterostructures grown during this work, sorted by their type of doping profile. With the Mn concentration having been systematically reduced for each doping scheme down to levels of doping concentration where no 2D hole system could be generated any longer, the following diagrams, recorded at $T = 1.44\,\mathrm{K}$ for $B = -6\,\mathrm{T} \rightarrow +6\,\mathrm{T}$ with and without illumination, can also serve as a rough survey of the regimes of magnetoresistive phenomena discussed in this thesis.

The reliability of the van der Pauw geometry in Hall magnetotransport measurements is, however, restricted, since handmade contacts do not precisely oppose each other causing asymmetric resistance curves. The data traces have therefore been symmetrized (anti-symmetrized) to display $R_{xx}(B)$ ($R_{xy}(B)$). Observed sporadic jumps in the resistance traces may have their origin in contacts that are not penetrating the 2D system safely at the edges of the sample. Also, anisotropic mobilities are not considered explicitly, since crystallographic directions have not been tracked in the routine of van der Pauw sample preparation and measurement.

Single-sided Mn doping

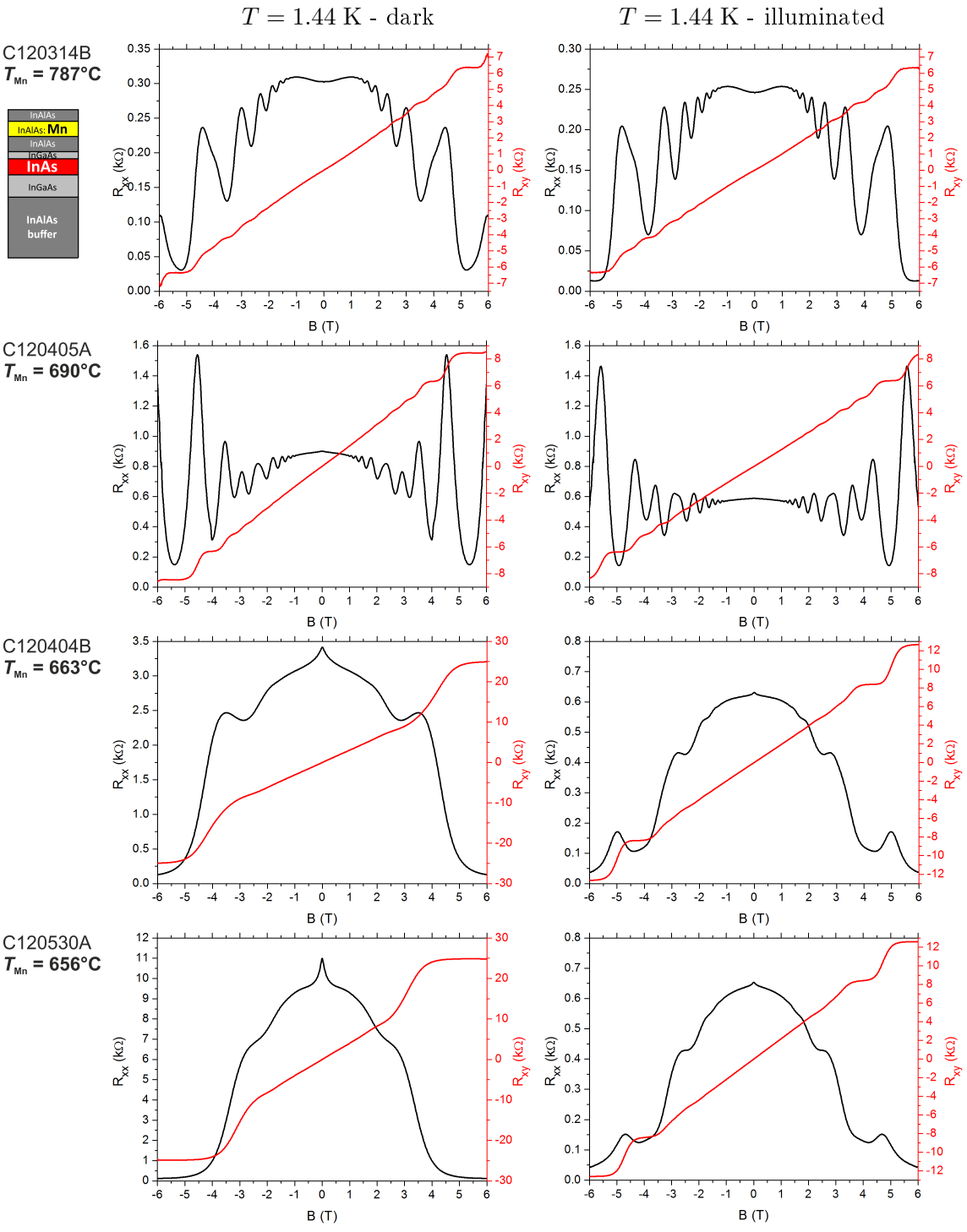

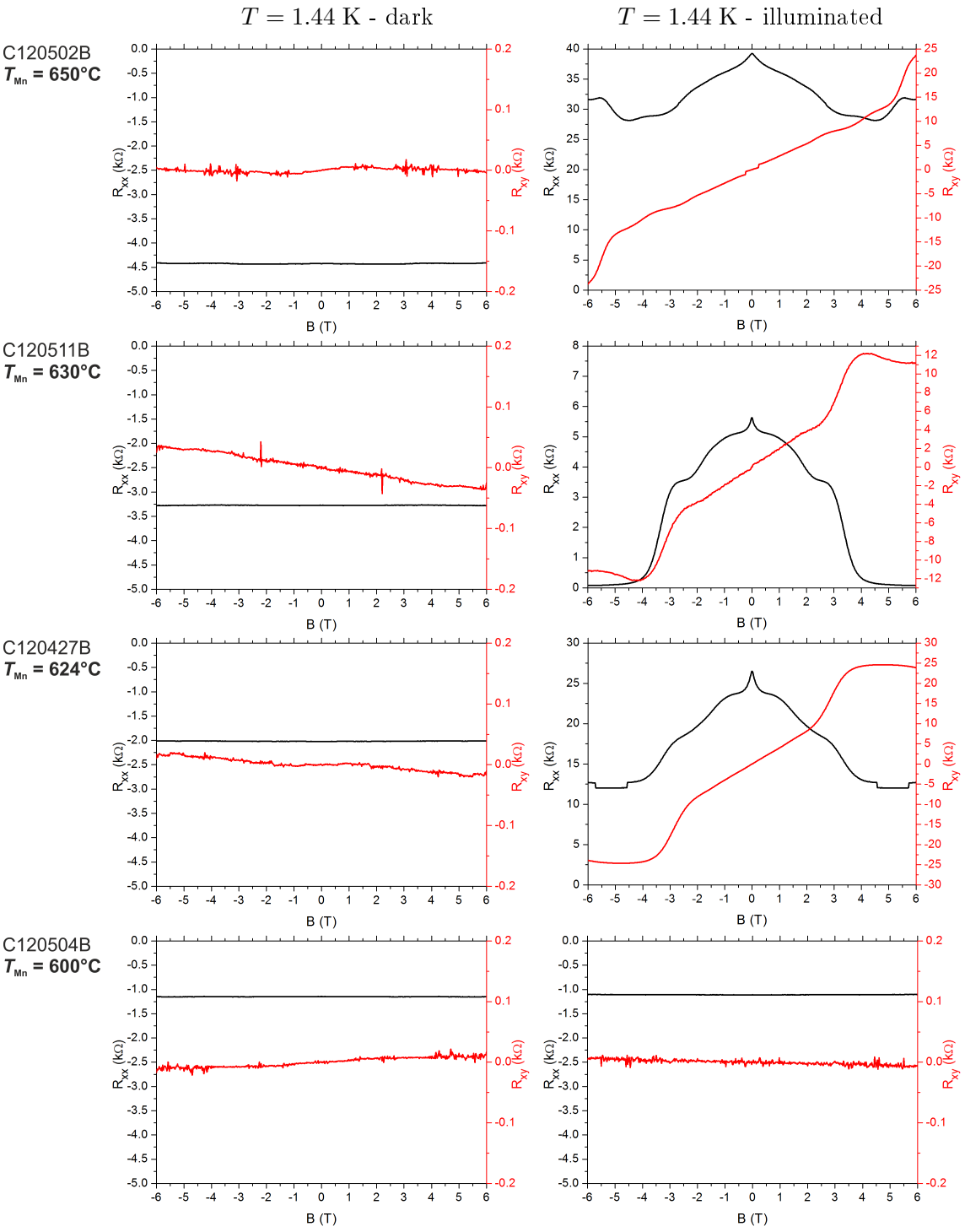

Figure B.2: ***Single-sided Mn doping.*** *Variation of the Mn concentration by the temperature of the Mn effusion cell* T_{Mn}.

Inverted single-sided Mn doping

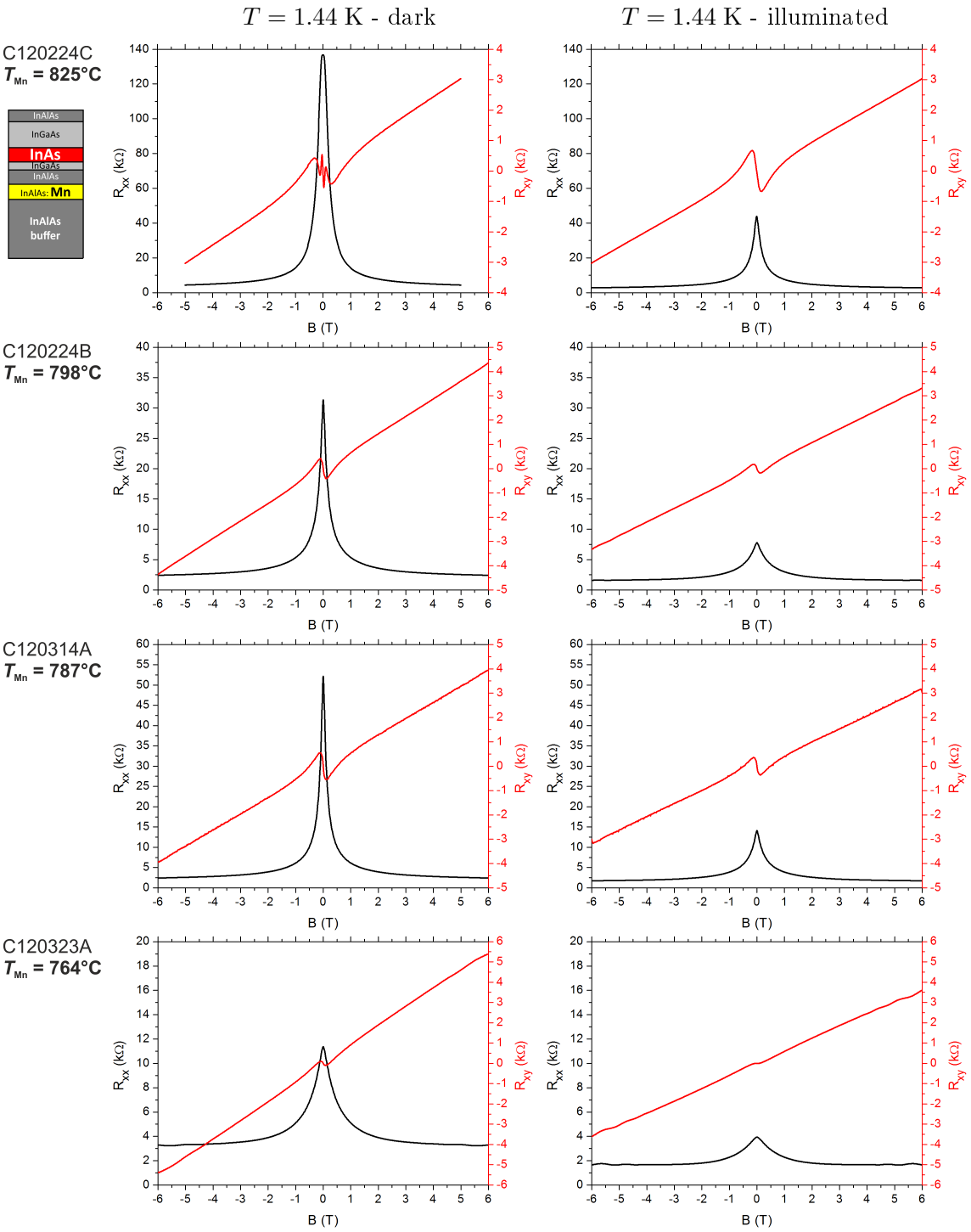

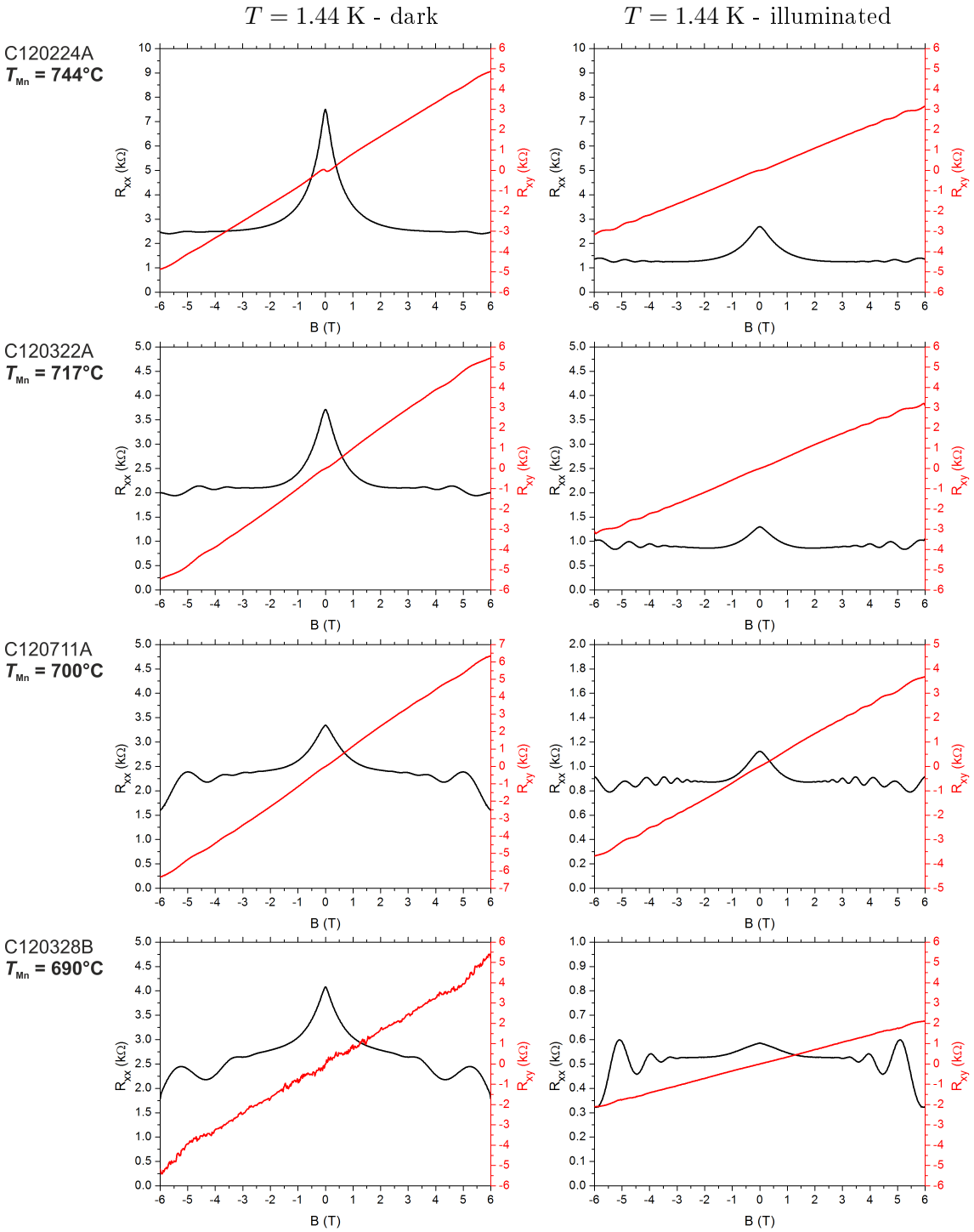
T = 1.44 K - dark
T = 1.44 K - illuminated
C120224A
T_Mn = 744°C
C120322A
T_Mn = 717°C
C120711A
T_Mn = 700°C
C120328B
T_Mn = 690°C
R_XX (kΩ)
R_XY (kΩ)
B (T)

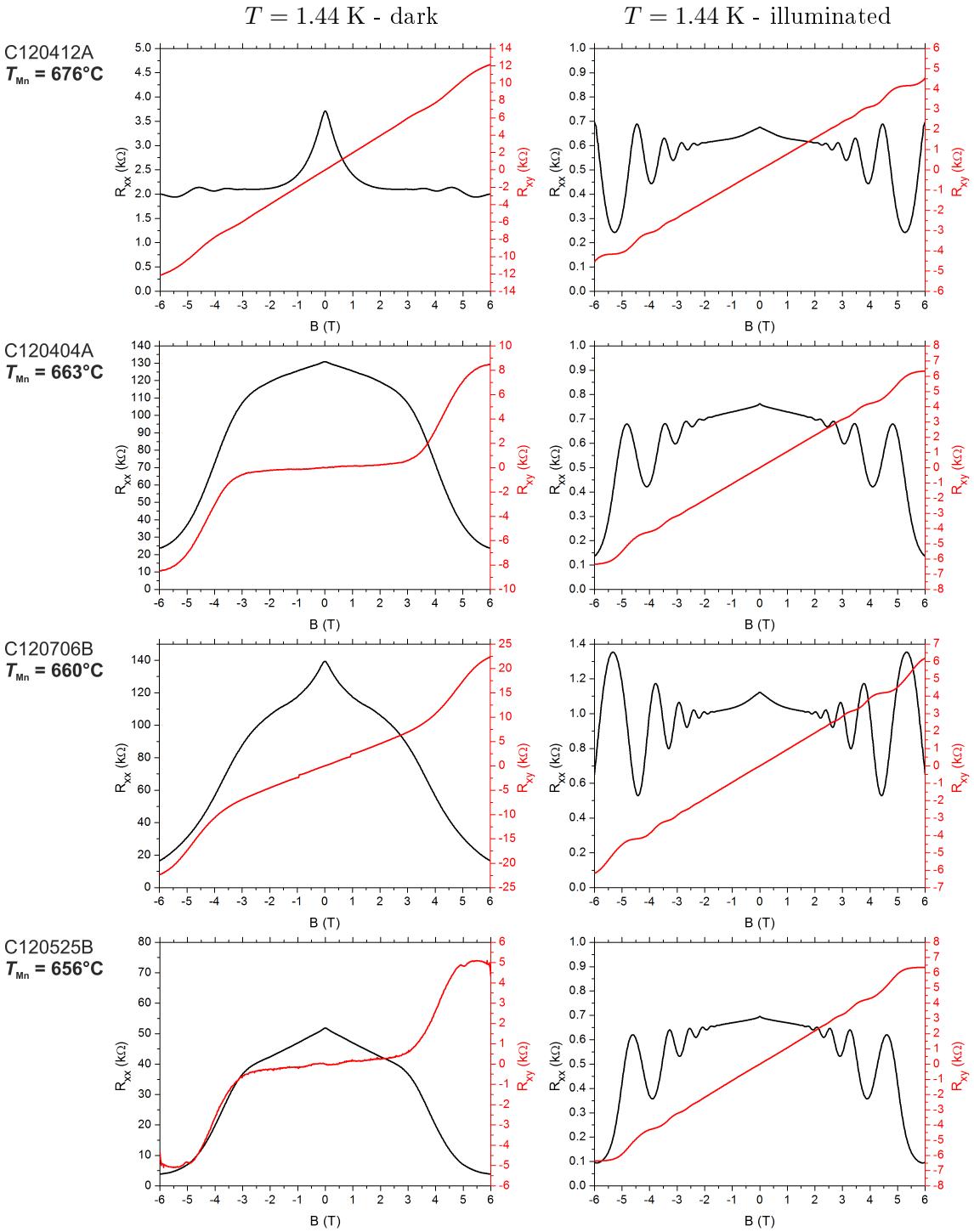
$T = 1.44$ K - dark
$T = 1.44$ K - illuminated
C120412A
T_{Mn} = 676°C
C120404A
T_{Mn} = 663°C
C120706B
T_{Mn} = 660°C
C120525B
T_{Mn} = 656°C
R_{xx} (kΩ)
R_{xy} (kΩ)
B (T)

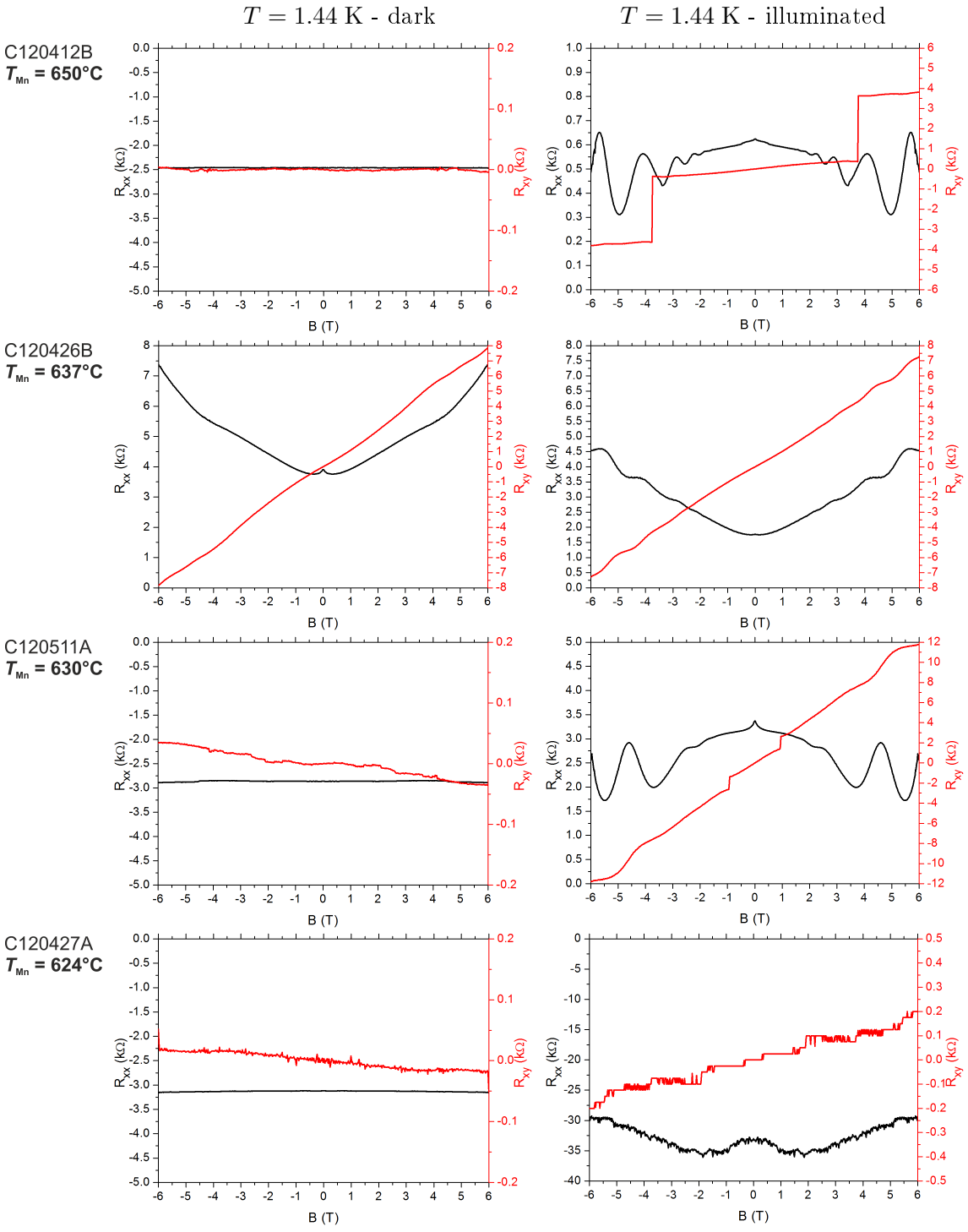

Figure B.3: ***Inverted single-sided Mn doping***. *Variation of the Mn concentration by the temperature of the Mn effusion cell* T_{Mn}.

Double-sided Mn doping

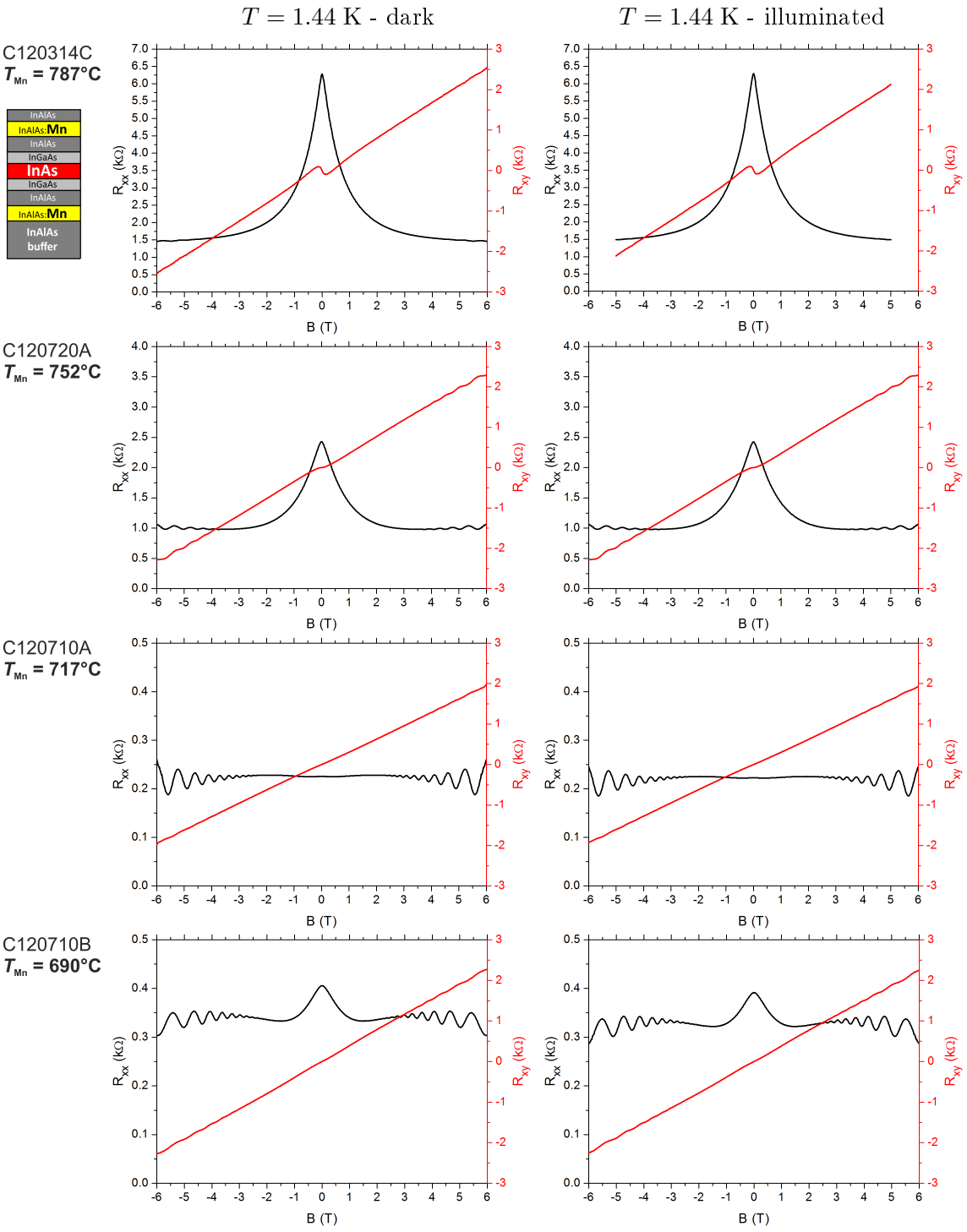

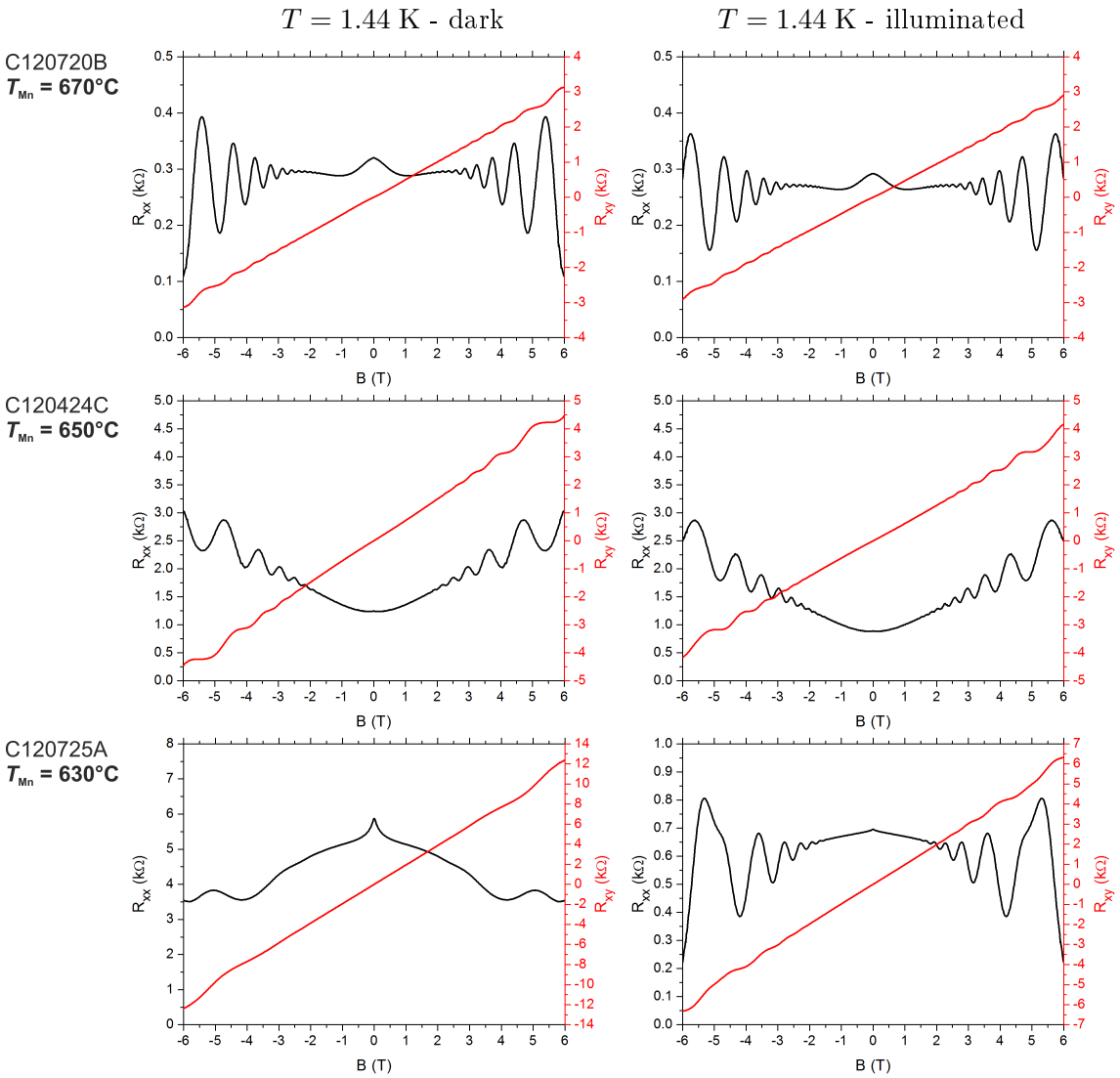

Figure B.4: ***Double-sided Mn doping***. *Variation of the Mn concentration by the temperature of the Mn effusion cell* T_{Mn}.

C

Abbreviations and constants

Constant	Value	Meaning
c	2.99792458×10^{8} m $\cdot$ s^{-1}	speed of light in vacuum
e	$1.602176565 \times 10^{-19}$ C	electron charge
$m_{e/0}$	$9.10938291 \times 10^{-31}$ kg	free electron mass
h	$6.62606957 \times 10^{-34}$ J $\cdot$ s	Planck's constant
	$4.135667516 \times 10^{-15}$ eV $\cdot$ s	
$\hbar$	$1.054571726 \times 10^{-34}$ J $\cdot$ s	reduced Planck's constant
	$6.58211928 \times 10^{-16}$ eV $\cdot$ s	
k_B	$1.3806488 \times 10^{-23}$ J $\cdot$ K^{-1}	Boltzmann constant
μ_B	$9.27400968 \times 10^{-24}$ J $\cdot$ T^{-1}	Bohr magneton
R_K	25812.807 Ω	von-Klitzing constant

Table C.1: *Physical constants and their meaning*

Abbreviation	Meaning
2D	two-dimensional
2DEG	two-dimensional electron gas
2DHG	two-dimensional hole gas
AHE	anomalous Hall effect
AFM	atomic force microscopy
AMR	anisotropic magnetoresistance
BEP	beam equivalent pressure
BIA	bulk inversion asymmetry
CB	conduction band
DMS	diluted magnetic semiconductor
DP	D'yakonov-Perel'
e-e	electron-electron
EY	Elliott-Yafet
FET	field-effect transistor
FFT	fast Fourier transformation
h-h	hole-hole
HB	Hall bar
HH	heavy hole
HLN	Hikami-Larkin-Nagaoka
ILP	Iordanskii, Lyanda-Geller and Pikus
IR	infrared
LED	light emitting diode
LH	light hole
LL	Landau level
MBE	molecular beam epitaxy
MIT	metal-insulator transition
MOSFET	metal-oxide-semiconductor field-effect transistor
NMR	negative magnetoresistance
RHEED	reflection high energy electron diffraction
SIA	structure inversion asymmetry
SdH	Shubnikov-de Haas
SIMS	secondary ion mass spectroscopy
SL	superlattice
SO	spin-orbit
SOC	spin-orbit coupling
SOI	spin-orbit interaction
TEM	transmission electron microscopy
QHE	quantum Hall effect
QPC	quantum point contact
QW	quantum well
UHV	ultra-high vacuum
VB	valence band
vdP	van der Pauw
WAL	weak antilocalization
WL	weak localization
XRD	X-ray diffraction

Table C.2: *Abbreviations and their meaning*

Symbol	Meaning
L, W	length/width of system size
T	temperature
$\mathbf{B}$	(external) magnetic field
$\mathbf{E}$	electric field
V, U	voltage
V_G	gate voltage
I	current
$\mathbf{j}$	current density
R	resistance
ρ	resistivity
σ	conductivity
μ	mobility
$\mathcal{D}$	density of states
$\mathbf{k}_{\parallel}$	in-plane wave vector
N_d	doping density
n_s	sheet carrier density
$n_{e,h}$	electron/hole density
p	hole density
ν	filling factor
ω_c	cyclotron frequency
$m^*_{e,h}$	effective electron/hole mass
g^*	effective Landé-g-factor
D	diffusion constant
T_F	Fermi temperature
E_F	Fermi energy
v_F	Fermi velocity
k_F	Fermi wave vector
λ_F	Fermi wavelength
r_s	Wigner-Seitz radius
Δ_{SO}, ΔE	spin splitting energy
$\beta_{1,3}$	linear/cubic Dresselhaus coefficient
$\alpha_{1,3}$	linear/cubic Rashba coefficient
$l_{e,tr}$	elastic mean free path
l_{SO}	spin-orbit scattering length
l_ϕ	phase coherence length
τ_p	momentum scattering time
$\tau_{e,tr}$	elastic/transport scattering time
τ_q	quantum life time
$\tau_{h-h,hh}$	hole-hole interaction time
τ_{SO}	spin-orbit scattering time
τ_ϕ	dephasing/phase coherence time
$\boldsymbol{\mathcal{B}}_{SO}$	spin-orbit effective magnetic field
$\boldsymbol{\Omega}_{SO}$	spin-orbit precession frequency
$\mathcal{R}$	rotational operator/growth rate

Table C.3: *Physical symbols and their meaning*

Bibliography

[1] Bychkov, Y. A. & Rashba, E. I. Oscillatory effects and the magnetic susceptibility of carriers in inversion layers. *J. Phys. C: Solid State Phys.* **17**, 6039–6045 (1984).

[2] Wolf, S. A., Awschalom, D. D., Buhrman, R. A., Daughton, J. M., von Molnár, S., Roukes, M. L., Chtchelkanova, A. Y. & Treger, D. M. Spintronics: A spin-based electronics vision for the future. *Science* **294**, 1488–1495 (2001).

[3] Žutić, I., Fabian, J. & Das Sarma, S. Spintronics: Fundamentals and applications. *Rev. Mod. Phys.* **76**, 323–410 (2004).

[4] Awschalom, D. D. & Flatté, M. E. Challenges for semiconductor spintronics. *Nature Phys.* **3**, 153–159 (2007).

[5] Feynman, R. P. Simulating physics with computers. *Int. J. Theor. Phys.* **21**, 467–488 (1982).

[6] Manchon, A., Koo, H. C., Nitta, J., Frolov, S. M. & Duine, R. A. New perspectives for Rashba spin-orbit coupling. *Nat. Mater.* **14**, 871–882 (2015).

[7] Datta, S. & Das, B. Electronic analog of the electro-optic modulator. *Appl. Phys. Lett.* **56**, 665–667 (1990).

[8] Ciorga, M., Einwanger, A., Wurstbauer, U., Schuh, D., Wegscheider, W. & Weiss, D. Electrical spin injection and detection in lateral all-semiconductor devices. *Phys. Rev. B* **79**, 165321 (2009).

[9] Oltscher, M., Ciorga, M., Utz, M., Schuh, D., Bougeard, D. & Weiss, D. Electrical spin injection into high mobility 2D systems. *Phys. Rev. Lett.* **113**, 236602 (2014).

[10] Ihn, T. *Semiconductor Nanostructures - Quantum States and Electronic Transport* (Oxford University Press, Oxford, 2010).

[11] Winkler, R. *Spin-Orbit Coupling Effects in Two-Dimensional Electron and Hole Systems* (Springer-Verlag, Berlin, 2003).

[12] Nitta, J., Akazaki, T., Takayanagi, H. & Enoki, T. Gate control of spin-orbit interaction in an inverted $In_{0.53}Ga_{0.47}As/In_{0.52}Al_{0.48}As$ heterostructure. *Phys. Rev. Lett.* **78**, 1335–1338 (1997).

[13] Koga, T., Nitta, J., Akazaki, T. & Takayanagi, H. Rashba spin-orbit coupling probed by the weak antilocalization analysis in InAlAs/InGaAs/InAlAs quantum wells as a function of quantum well asymmetry. *Phys. Rev. Lett.* **89**, 046801 (2002).

[14] Nitta, J., Bergsten, T., Kunihashi, Y. & Kohda, M. Electrical manipulation of spins in the Rashba two dimensional electron gas systems. *J. Appl. Phys.* **105**, 122402 (2009).

[15] Koo, H. C., Kwon, J. H., Eom, J., Chang, J., Han, S. H. & Johnson, M. Control of spin precession in a spin-injected field effect transistor. *Science* **325**, 1515–1518 (2009).

[16] Chuang, P. *et al.* All-electric all-semiconductor spin field-effect transistors. *Nat. Nanotechnol.* **10**, 35–39 (2015).

[17] Debray, P., Rahman, S. M. S., Wan, J., Newrock, R. S., Cahay, M., Ngo, A. T., Ulloa, S. E., Herbert, S. T., Muhammad, M. & Johnson, M. All-electric quantum point contact spin-polarizer. *Nat. Nanotechnol.* **4**, 759–764 (2009).

[18] Kohda, M., Nakamura, S., Nishihara, Y., Kobayashi, K., Ono, T., Ohe, J., Tokura, Y., Mineno, T. & Nitta, J. Spin–orbit induced electronic spin separation in semiconductor nanostructures. *Nat. Commun.* **3**, 1–8 (2012).

[19] Korn, T., Kugler, M., Griesbeck, M., Schulz, R., Wagner, A., Hirmer, M., Gerl, C., Schuh, D., Wegscheider, W. & Schüller, C. Engineering ultralong spin coherence in two-dimensional hole systems at low temperatures. *New J. Phys.* **12**, 043003 (2010).

[20] Korn, T. & Schüller, C. Hole spin dynamics and valence-band spin excitations in two-dimensional hole systems. *Phys. Status Solidi B* **251**, 1881–1891 (2014).

[21] Schliemann, J., Egues, J. C. & Loss, D. Nonballistic spin-field-effect transistor. *Phys. Rev. Lett.* **90**, 146801 (2003).

[22] Koralek, J. D., Weber, C. P., Orenstein, J., Bernevig, B. A., Zhang, S.-C., Mack, S. & Awschalom, D. D. Emergence of the persistent spin helix in semiconductor quantum wells. *Nature* **458**, 610–613 (2009).

[23] Kohda, M. *et al.* Gate-controlled persistent spin helix state in (In,Ga)As quantum wells. *Phys. Rev. B* **86**, 081306 (2012).

[24] Sasaki, A., Nonaka, S., Kunihashi, Y., Kohda, M., Bauernfeind, T., Dollinger, T., Richter, K. & Nitta, J. Direct determination of spin–orbit interaction coefficients and realization of the persistent spin helix symmetry. *Nat. Nanotechnol.* **9**, 703–709 (2014).

[25] Dollinger, T., Kammermeier, M., Scholz, A., Wenk, P., Schliemann, J., Richter, K. & Winkler, R. Signatures of spin-preserving symmetries in two-dimensional hole gases. *Phys. Rev. B* **90**, 115306 (2014).

[26] Schönhuber, C., Walser, M. P., Salis, G., Reichl, C., Wegscheider, W., Korn, T. & Schüller, C. Inelastic light-scattering from spin-density excitations in the regime of the persistent spin helix in a GaAs-AlGaAs quantum well. *Phys. Rev. B* **89**, 085406 (2014).

[27] Weiss, D. Halbleiterphysik (2011). Lecture notes.

[28] Klitzing, K. v., Dorda, G. & Pepper, M. New method for high-accuracy determination of the fine-structure constant based on quantized Hall resistance. *Phys. Rev. Lett.* **45**, 494–497 (1980).

[29] Ando, T. Theory of quantum transport in a two-dimensional electron system under magnetic fields. IV. Oscillatory conductivity. *J. Phys. Soc. Jpn.* **37**, 1233–1237 (1974).

[30] Ando, T., Fowler, A. B. & Stern, F. Electronic properties of two-dimensional systems. *Rev. Mod. Phys.* **54**, 437–672 (1982).

[31] Colerdige, P. T., Stoner, R. & Fletcher, R. Low-field transport coefficients in GaAs/$Ga_{1-x}Al_xAs$ heterostructures. *Phys. Rev. B* **39**, 1120–1124 (1989).

[32] Elhamri, S., Newrock, R. S., Mast, D. B., Ahoujja, M., Mitchel, W. C., Redwing, J. M., Tischler, M. A. & Flynn, J. S. $Al_{0.15}Ga_{0.85}N$/GaN heterostructures: Effective mass and scattering times. *Phys. Rev. B* **57**, 1374–1377 (1998).

[33] Coleridge, P. T., Hayne, M., Zawadzki, P. & Sachrajda, A. S. Effective masses in high-mobility 2D electron gas structures. *Surf. Sci.* **361–362**, 560–563 (1996).

[34] Knap, W. Weak antilocalization and spin precession in quantum wells. *Phys. Rev. B* **53**, 3912–3924 (1996).

[35] Bergmann, G. Weak anti-localization - an experimental proof for the destructive interference of rotated spin $^1/_2$. *Solid State Commun.* **42**, 815–817 (1982).

[36] Cohen, M. L. & Chelikowski, J. *Electronic structure and optical properties of semiconductors* (Springer-Verlag, Berlin, 1989).

[37] Vurgaftman, I., Meyer, J. R. & Ram-Mohan, L. R. Band parameters for III-V compound semiconductors and their alloys. *J. Appl. Phys.* **89**, 5815 (2001).

[38] Winkler, R., Culcer, D., Papadakis, S. J., Habib, B. & Shayegan, M. Spin orientation of holes in quantum wells. *Semicond. Sci. Technol.* **23**, 114017 (2008).

[39] Winkler, R., Noh, H., Tutuc, E. & Shayegan, M. Anomalous Rashba spin splitting in two-dimensional hole systems. *Phys. Rev. B* **65**, 155303 (2002).

[40] Madelung, O. (ed.). *Data in Science and Technology*, chap. Semiconductors - Group IV Elements and III-V Compounds (Springer-Verlag, Berlin, 1991).

[41] Nakwaski, W. Effective masses of electrons and heavy holes in GaAs, InAs, AlAs and their ternary compounds. *Physica B* **210**, 1–25 (1995).

[42] Yu, P. Y. & Cardona, M. *Fundamentals of Semiconductors - Physics and Materials Properties* (Springer-Verlag, Berlin, 1995).

[43] Winkler, R. Rashba spin splitting in two-dimensional electron and hole systems. *Phys. Rev. B* **62**, 4245–4248 (2000).

[44] Dresselhaus, G. Spin-orbit coupling effects in zinc blende structures. *Phys. Rev.* **100**, 580–586 (1955).

[45] Gerchikov, L. G. & Subashiev, A. V. Spin splitting of size-quantization subbands in asymmetric heterostructures. *Sov. Phys. Semicond.* **26**, 73–78 (1992).

[46] Dollinger, T. *Spin transport in two-dimensional electron and hole gases.* Ph.D. thesis, Universität Regensburg (2014).

[47] Wong, A. & Mireles, F. Spin Hall and longitudinal conductivity of a conserved spin current in two dimensional heavy-hole gases. *Phys. Rev. B* **81**, 085304 (2010).

[48] Fabian, J., Matos-Abiague, A., Ertler, C., Stano, P. & Žutić, I. Seminconductor spintronics. *Acta Phys. Slovaca* **57**, 565–907 (2007).

[49] Miller, J. B., Zumbühl, D. M., Marcus, C. M., Lyanda-Geller, Y. B., Goldhaber-Gordon, D., Campman, K. & Gossard, A. C. Gate-controlled spin-orbit quantum interference effects in lateral transport. *Phys. Rev. Lett.* **90**, 076807 (2003).

[50] Moser, J., Matos-Abiague, A., Schuh, D., Wegscheider, W., Fabian, J. & Weiss, D. Tunneling anisotropic magnetoresistance and spin-orbit coupling in Fe/GaAs/Au tunnel junctions. *Phys. Rev. Lett.* **99**, 056601 (2007).

[51] Schliemann, J. & Loss, D. Spin-Hall transport of heavy holes in III-V semiconductor quantum wells. *Phys. Rev. B* **71**, 085308 (2005).

[52] Voisin, P., Delalande, C., Voos, M., Chang, L. L., Segmuller, A., Chang, C. A. & Esaki, L. Light and heavy valence subband reversal in GaSb-AlSb superlattices. *Phys. Rev. B* **30**, 2276–2278 (1984).

[53] Kammermeier, M. *Strained Hole Systems with Rashba and Dresselhaus Spin-Orbit Coupling.* Master's thesis, Universität Regensburg (2014).

[54] Sun, Y., Thompson, S. E. & Nishida, T. *Strain Effect in Semiconductors - Theory and Device Applications* (Springer, New York, 2010).

[55] D'yakonov, M. I. & Perel', V. I. Spin orientation of electrons associated with the interband absorption of light in semiconductors. *Sov. Phys. JETP* **33**, 1053–1059 (1971).

[56] Culcer, D. & Winkler, R. Spin polarization decay in spin-$\frac{1}{2}$ and spin-$\frac{3}{2}$ systems. *Phys. Rev. B* **76**, 195204 (2007).

[57] Glazov, M. M. & Ivchenko, E. L. Precession spin relaxation mechanism caused by frequent electron-electron collisions. *JETP Letters* **75**, 403–405 (2002).

[58] Leyland, W. J. H., John, G. H., Harley, R. T., Glazov, M. M., Ivchenko, E. L., Ritchie, D. A., Farrer, I., Shields, A. J. & Henini, M. Enhanced spin-relaxation time due to electron-electron scattering in semiconductor quantum wells. *Phys. Rev. B* **75**, 165309 (2007).

[59] Elliott, R. J. Theory of the effect of spin-orbit coupling on magnetic resonance in some semiconductors. *Phys. Rev.* **96**, 266–279 (1954).

[60] Yafet, Y. *Solid State Physics*, vol. 14, chap. *g* Factors and Spin-Lattice Relaxation of Conduction Electrons, 1–98 (Academic Press, New York and London, 1963).

[61] Ehehalt, J. *Optimierung und optische Eigenschaften von Quantenstrukturen hergestellt durch Überwachsen von Spaltflächen.* Ph.D. thesis, Universität Regensburg (2009).

[62] Gerl, C. *Hochbewegliche zweidimensionale Lochsysteme in GaAs/AlGaAs Heterostrukturen.* Ph.D. thesis, Universität Regensburg (2009).

[63] Utz, M. *Epitaxie von (Ga,Mn)As.* Ph.D. thesis, Universität Regensburg (2012).

[64] Arzberger, M. *Wachstum, Eigenschaften und Anwendungen selbstorganisierter InAs-Quantenpunkte.* Ph.D. thesis, Technische Universität München, WSI (2001).

[65] Wu, J. & Jin, P. Self-assembly of InAs quantum dots on GaAs(001) by molecular beam epitaxy. *Front. Phys.* **10**, 7–58 (2015).

[66] Aumeier, F. *Strukturelle Untersuchungen an Graded-Buffer-Systemen mit dem Transmissionselektronenmikroskop.* Master's thesis, Universität Regensburg (2015).

[67] van der Pauw, L. J. A method of measuring specific resisitivity and Hall effect of discs of arbitrary shape. *Philips Res. Rep.* **13**, 1–9 (1958).

[68] Nitta, J., Lin, Y., Akazaki, T. & Koga, T. Gate-controlled electron g factor in an InAs-inserted-channel $In_{0.53}Ga_{0.47}As/In_{0.52}Al_{0.48}As$ heterostructure. *Appl. Phys. Lett.* **83**, 4565–4567 (2003).

[69] Lin, Y., Koga, T. & Nitta, J. Effect of an $InP/In_{0.53}Ga_{0.47}As$ interface on spin-orbit interaction in $In_{0.52}Al_{0.48}As/In_{0.53}Ga_{0.47}As$ heterostructures. *Phys. Rev. B* **71**, 045328 (2005).

[70] Gozu, S., Hong, C. & Yamada, S. Low temperature high electron mobility in $In_{0.75}Ga_{0.25}As/In_{0.75}Al_{0.25}As$ modulation-doped hetrostructures grown on GaAs substrate. *Jpn. J. Appl. Phys.* **37**, L1501–L1503 (1998).

[71] Romanato, F., Napolitani, E., Carnera, A., Drigo, A. V., Lazzarini, L., Salviati, G., Ferrari, C., Bosacchi, A. & Franchi, S. Strain relaxation in graded composition $In_xGa_{1-x}As/GaAs$ buffer layers. *J. Appl. Phys.* **86**, 4748–4755 (1999).

[72] Inoue, K., Harmand, J. C. & Matsuno, T. High-quality $In_xGa_{1-x}As/InAlAs$ modulation-doped heterostructures grown lattice-mismatched on GaAs substrates. *J. Cryst. Growth* **111**, 313–317 (1991).

[73] Ercolani, D., Biasiol, G., Cancellieri, E., Rosini, M., Jacoboni, C., Carillo, F., Heun, S., Sorba, L. & Nolting, F. Transport anisotropy in $In_{0.75}Ga_{0.25}As$ two-dimensional electron gases induced by indium concentration modulation. *Phys. Rev. B* **77**, 235307 (2008).

[74] Capotondi, F. *Structural and transport studies of InAlAs/InGaAs quantum wells.* Ph.D. thesis, University of Modena and Reggio Emilia (2005).

[75] Ercolani, D. *Transport properties of InGaAs based devices.* Ph.D. thesis, University of Modena and Reggio Emilia (2007).

[76] Mendach, S., Hu, C. M., Heyn, C., Schnüll, S., Oepen, H. P., Anton, R. & Hansen, W. Strain relaxation in high-mobility InAs inserted-channel heterostructures with metamorphic buffer. *Physica E* **13**, 1204–1207 (2002).

[77] Heyn, C., Mendach, S., Löhr, S., Beyer, S., Schnüll, S. & Hansen, W. Growth of shallow InAs HEMTs with metamorphic buffer. *J. Cryst. Growth* **251**, 832–836 (2003).

[78] Capotondi, F., Biasiol, G., Vobornik, I., Sorba, L., Giazotto, F., Cavallini, A. & Fraboni, B. Two-dimensional electron gas formation in undoped $In_{0.75}Ga_{0.25}As/In_{0.75}Al_{0.25}As$ quantum wells. *J. Vac. Sci. Technol. B* **22**, 702–706 (2004).

[79] Cordier, Y., Chauveau, J.-M., Ferre, D. & Dipersio, J. Comparison of $In_{0.33}Al_{0.67}As/In_{0.34}Ga_{0.66}As$ on GaAs metamorphic high electron mobility transistors grown by molecular beam epitaxy with normal and inverse step on linear graded buffer layers. *J. Vac. Sci. Technol. B* **18**, 2513–2517 (2000).

[80] Capotondi, F., Biasiol, G., Ercolani, D., Grillo, V., Carlino, E., Romanato, F. & Sorba, L. Strain induced effects on the transport properties of metamorphic InAlAs/InGaAs quantum wells. *Thin Solid Films* **484**, 400–407 (2005).

[81] González, M. U., González, Y. & González, L. Study of the relaxation process during InGaAs/GaAs (001) growth from in situ real-time stress measurements. *Appl. Phys. Lett.* **81**, 4162–4164 (2002).

[82] Andrews, A. M., Romanov, A. E., Speck, J. S., Bobeth, M. & Pompe, W. Development of cross-hatch morphology during growth of lattice mismatched layers. *Appl. Phys. Lett.* **77**, 3740–3742 (2000).

[83] Lavoie, C., Pinnington, T., Nodwell, E., Tiedje, T., Goldman, R. S., Kavanagh, K. L. & Hutter, J. L. Relationship between surface morphology and strain relaxation during growth of InGaAs strained layers. *Appl. Phys. Lett.* **67**, 3744–3746 (1995).

[84] Fitzgerald, E. A., Xie, Y.-H., Monroe, D., Silverman, P. J., Kuo, J. M., Kortan, A. R., Thiel, F. A. & Weir, B. E. Relaxed Ge_xSi_{1-x} structures for III-V integration with Si and high mobility two-dimensional electron gases in Si. *J. Vac. Sci. Technol. B* **10**, 1807–1819 (1992).

[85] Beanland, R., Aindow, M., Joyce, T. B., Kidd, P., Lourenço, M. & Goodhew, P. J. A study of surface cross-hatch and misfit dislocation structure in $In_{0.15}Ga_{0.85}As/GaAs$ grown by chemical beam epitaxy. *J. Cryst. Growth* **149**, 1–11 (1995).

[86] Akazaki, T., Nitta, J., Takayanagi, H., Enoki, T. & Arai, K. Improving the mobility of an $In_{0.52}Al_{0.48}As/In_{0.53}Ga_{0.47}As$ inverted modulation-doped structure by inserting a strained InAs quantum well. *Appl. Phys. Lett.* **65**, 1263–1265 (1994).

[87] Richter, A., Koch, M., Matsuyama, T., Heyn, C. & Merkt, U. Transport properties of modulation-doped InAs-inserted-channel $In_{0.75}Al_{0.25}As/In_{0.75}Ga_{0.25}As$ structures grown on GaAs substrates. *Appl. Phys. Lett.* **77**, 3227–3229 (2000).

[88] Capotondi, F., Biasiol, G., Ercolani, D. & Sorba, L. Scattering mechanisms in undoped $In_{0.75}Ga_{0.25}As/In_{0.75}Al_{0.25}As$ two-dimensional electron gases. *J. Cryst. Growth* **278**, 538–543 (2005).

[89] Zaremba, E. Transverse magnetoresistance in quantum wells with multiple subband occupancy. *Phys. Rev. B* **45**, 14143–14149 (1992).

[90] Grbić, B., Leturcq, R., Ihn, T., Ensslin, K., Reuter, D. & Wieck, A. D. Strong spin-orbit interactions and weak antilocalization in carbon-doped *p*-type $GaAs/Al_xGa_{1-x}As$ heterostructures. *Phys. Rev. B* **77**, 125312 (2008).

[91] Grayson, M. & Fischer, F. Measuring carrier density in parallel conduction layers of quantum Hall systems. *J. Appl. Phys.* **98**, 013709 (2005).

[92] Hirmer, M., Schuh, D. & Wegscheider, W. Carbon doped InAlAs/InGaAs/-InAs heterostructures: Tuning from n- to p-doping. *Appl. Phys. Lett.* **98**, 082103 (2011).

[93] Wurstbauer, U., Soda, M., Jakiela, R., Schuh, D., Weiss, D., Zweck, J. & Wegscheider, W. Coexistence of ferromagnetism and quantum Hall effect in Mn modulation-doped two-dimensional hole systems. *J. Cryst. Growth* **311**, 2160–2162 (2009).

[94] Ohno, H., Munekata, H., Penney, T., von Molnár, S. & Chang, L. L. Magnetotransport properties of *p*-type (In,Mn)As diluted magnetic III-V semiconductors. *Phys. Rev. Lett.* **68**, 2664–2667 (1992).

[95] Wurstbauer, U. *Herstellung und Charakterisierung von Mangan dotierten III-V Halbleiterheterostrukturen.* Ph.D. thesis, Universität Regensburg (2008).

[96] Wurstbauer, U., Śliwa, C., Weiss, D., Dietl, T. & Wegscheider, W. Hysteretic magnetoresistance and thermal bistability in a magnetic two-dimensional hole system. *Nature Phys.* **6**, 955–959 (2010).

[97] Gold, A. Scattering time and single-particle relaxation time in a disordered two-dimensional electron gas. *Phys. Rev. B* **38**, 10798–10811 (1988).

[98] Knott, S., Hirschmann, T. C., Wurstbauer, U., Hansen, W. & Wegscheider, W. Magnetoresistance effects and phase coherent transport phenomena in a magnetic nonplanar two-dimensional hole system. *Phys. Rev. B* **84**, 205302 (2011).

[99] Ramvall, P., Carlsson, N., Omling, P., Samuelson, L., Seifert, W., Stolze, M. & Wang, Q. $Ga_{0.25}In_{0.75}As$/InP quantum wells with extremely high and anisotropic two-dimensional electron gas mobilities. *Appl. Phys. Lett.* **68**, 1111–1113 (1996).

[100] Löhr, S., Mendach, S., Vonau, T., Heyn, C. & Hansen, W. Highly anisotropic electron transport in shallow InGaAs heterostructures. *Phys. Rev. B* **67**, 045309 (2003).

[101] Chang, J. C. P., Chen, J., Fernandez, J. M., Wieder, H. H. & Kavanagh, K. L. Strain relaxation of compositionally graded $In_xGa_{1-x}As$ buffer layers for modulation-doped $In_{0.3}Ga_{0.7}As/In_{0.29}Al_{0.71}As$ heterostructures. *Appl. Phys. Lett.* **60**, 1129–1131 (1992).

[102] Goldman, R. S., Wieder, H. H., Kavanagh, K. L., Rammohan, K. & Rich, D. H. Anisotropic structural, electronic, and optical properties of InGaAs grown by molecular beam epitaxy on misoriented substrates. *Appl. Phys. Lett.* **65**, 1424–1426 (1994).

[103] Rammohan, K., Rich, D. H., Goldman, R. S., Chen, J., Wieder, H. H. & Kavanagh, K. L. Study of μm-scale spatial variations in strain of a compositionally step-graded $In_xGa_{1-x}As$/GaAs(001) heterostructure. *Appl. Phys. Lett.* **66**, 869–871 (1995).

[104] Gozu, S., Kita, T., Sato, Y., Yamada, S. & Tomizawa, M. Characterization of high indium content metamorphic InGaAs/InAlAs modulation-doped heterostructures. *J. Cryst. Growth* **227-228**, 155–160 (2001).

[105] Quang, D. N., Tuoc, V. N. & Huan, T. D. Roughness-induced piezoelectric scattering in lattice-mismatched semiconductor quantum wells. *Phys. Rev. B* **68**, 195316 (2003).

[106] Rosini, M., Cancellieri, E., Ercolani, D., Biasiol, G., Jacoboni, C. & Sorba, L. Transport anisotropy in InGaAs 2D electron gases. *Physica E* **40**, 1392–1394 (2008).

[107] Hirmer, M. *High-mobility two-dimensional hole gases in III-V semiconductor heterostructures: growth and transport properties.* Ph.D. thesis, Universität Regensburg (2012).

[108] Kanda, Y. & Yasukawa, A. Hall-effect devices as strain and pressure sensors. *Sensors and Actuators* **2**, 283–296 (1982).

[109] Bockhorn, L., Barthold, P., Schuh, D., Wegscheider, W. & Haug, R. J. Magnetoresistance in a high-mobility two-dimensional electron gas. *Phys. Rev. B* **83**, 113301 (2011).

[110] Markus, Y., Meirav, U., Shtrikman, H. & Laikhtman, B. Anisotropic mobility and roughness scattering in a 2D electron gas. *Semicond. Sci. Technol.* **9**, 1297–1304 (1994).

[111] Saku, T., Horikoshi, Y. & Tokura, Y. Limit of electron mobility in AlGaAs/GaAs modulation-doped heterostructures. *Jpn. J. Appl. Phys.* **35**, 34–38 (1996).

[112] Umansky, V., de Picciotto, R. & Heiblum, M. Extremely high-mobility two dimensional electron gas: Evaluation of scattering mechanisms. *Appl. Phys. Lett.* **71**, 683–685 (1997).

[113] Dmitriev, I. A., Mirlin, A. D., Polyakov, D. G. & Zudov, M. A. Nonequilibrium phenomena in high Landau levels. *Rev. Mod. Phys.* **84**, 1709–1763 (2012).

[114] Tokura, Y., Saku, T., Tarucha, S. & Horikoshi, Y. Anisotropic roughness scattering at a heterostructure interface. *Phys. Rev. B* **46**, 15558–15561 (1992).

[115] Komiyama, S., Nii, H., Ohsaw, M., Fukatsu, S., Shiraki, Y., Itoh, R. & Toyoshima, H. Resistance and resistivity of two dimensional electron gas at high magnetic fields. *Solid State Commun.* **80**, 157–163 (1991).

[116] Richter, C. A., Wheeler, R. G. & Sacks, R. N. Overshoot of quantum Hall plateaus. *Surf. Sci.* **263**, 270–274 (1992).

[117] Ramvall, P., Carlsson, N., Omling, P., Samuelson, L., Seifert, W., Wang, Q., Ishibashi, K. & Aoyagi, Y. Quantum transport in high mobility modulation doped $Ga_{0.25}In_{0.75}As$/InP quantume wells. *J. Appl. Phys.* **84**, 2112–2122 (1998).

[118] Kendirlik, E. M., Sirt, S., Kalkan, S. B., Dietsche, W., Wegscheider, W., Ludwig, S. & Siddiki, A. Anomalous resistance overshoot in the integer quantum Hall effect. *Sci. Rep.* **3**, 1–6 (2013).

[119] Sailer, J., Wild, A., Lang, V., Siddiki, A. & Bougeard, D. Quantum Hall resistance overshoot in two-dimensional (2D) electron gases: theory and experiment. *New J. Phys.* **12**, 113033–113051 (2010).

[120] Sailer, J. *Materials and devices for quantum information processing in Si/SiGe.* Ph.D. thesis, Technische Universität München, WSI (2010).

[121] Nitta, J. Spin-orbitronics in semiconductor heterostructures (2015). Workshop: Emergent Relativitstic Effects in Condensed Matter, Regensburg.

[122] Zawadzki, W. & Pfeffer, P. Spin splitting of subband energies due to inversion asymmetry in semiconductor heterostructures. *Semicond. Sci. Technol.* **19**, R1–R17 (2004).

[123] Störmer, H. L., Schlesinger, Z., Chang, A., Tsui, D. C., Gossard, A. C. & Wiegmann, W. Energy structure and quantized Hall effect of two-dimensional holes. *Phys. Rev. Lett.* **51**, 126–129 (1983).

[124] Eisenstein, J. P., Störmer, H. L., Narayanamurti, V., Gossard, A. C. & Wiegmann, W. Effect of inversion symmetry on the band structure of semiconductor heterostructures. *Phys. Rev. Lett.* **53**, 2579–2582 (1984).

[125] Luo, J., Munekata, H., Fang, F. F. & Stiles, P. J. Observation of the zero-field spin splitting of the ground electron subband in GaSb-InAs-GaSb quantum wells. *Phys. Rev. B* **38**, 10142–10145 (1988).

[126] Das, B., Miller, D. C., Datta, S., Reifenberger, R., Hong, W. P., Bhattacharya, P. K., Singh, J. & Jaffe, M. Evidence for spin splitting in $In_xGa_{1-x}As/In_{0.52}Al_{0.48}As$ heterostructures as $B \to 0$. *Phys. Rev. B* **39**, 1411–1414 (1989).

[127] Dresselhaus, P. D., Papavassiliou, C. M. A., Wheeler, R. G. & Sacks, R. N. Observation of spin precession in GaAs inversion layers using antilocalization. *Phys. Rev. Lett.* **68**, 106–109 (1992).

[128] Jusserand, B., Richards, D., Allan, G., Priester, C. & Etienne, B. Spin orientation at semiconductor heterointerfaces. *Phys. Rev. B* **51**, 4707–4710 (1995).

[129] Ganichev, S. D. *et al.* Experimental separation of Rashba and Dresselhaus spin splittings in semiconductor quantum wells. *Phys. Rev. Lett.* **92**, 256601 (2004).

[130] Engels, G., Lange, J., Schäpers, T. & Lüth, H. Experimental and theoretical approach to spin splitting in modulation-doped $In_xGa_{1-x}As/InP$ quantum wells for B→0. *Phys. Rev. B* **55**, R1958–R1961 (1997).

[131] Grundler, D. Large Rashba splitting in InAs quantum wells due to electron wave function penetration into the barrier layers. *Phys. Rev. Lett.* **84**, 6074–6077 (2000).

[132] Donner, A. *Gating of hybrid semiconductor nanostructures.* Master's thesis, Universität Regensburg (2012).

[133] Wild, A. *Development of a robust platform for spin qubits in SiGe heterostructures.* Ph.D. thesis, Technische Universität München, WSI (2013).

[134] Schmalzbauer, M. *Heterostructure design of Si/SiGe two-dimensional electron systems for field-effect devices.* Ph.D. thesis, Universität Regensburg (2014).

[135] Polyakov, D. G., Evers, F., Mirlin, A. D. & Wölfle, P. Quasiclassical magnetotransport in a random array of antidots. *Phys. Rev. B* **64**, 205306 (2001).

[136] Al'tshuler, B. L. & Aronov, A. G. *Modern Problems in Condensed Matter Sciences*, vol. 10, chap. 1 - Electron-Electron Interaction In Disordered Conductors (Elsevier, Amsterdam, 1985).

[137] Gornyi, I. V. & Mirlin, A. D. Interaction-induced magnetoresistance: From the diffusive to the ballistic regime. *Phys. Rev. Lett.* **90**, 076801 (2003).

[138] Paalanen, M. A., Tsui, D. C. & Hwang, J. C. M. Parabolic magnetoresistance from the interaction effect in a two-dimensional electron gas. *Phys. Rev. Lett.* **51**, 2226–2229 (1983).

[139] Choi, K. K., Tsui, D. C. & Palmateer, S. C. Electron-electron interactions in GaAs-$Al_xGa_{1-x}As$ heterostructures. *Phys. Rev. B* **33**, 8216–8227 (1986).

[140] Li, L., Proskuryakov, Y. Y., Savchenko, A. K., Linfield, E. H. & Ritchie, D. A. Magnetoresistance of a 2D electron gas caused by electron interactions in the transition from the diffusive to the ballistic regime. *Phys. Rev. Lett.* **90**, 076802 (2003).

[141] Simmons, M. Y., Hamilton, A. R., Pepper, M., Linfield, E. H., Rose, P. D. & Ritchie, D. A. Weak localization, hole-hole interactions, and the "metal"-insulator transition in two dimensions. *Phys. Rev. Lett.* **84**, 2489–2492 (2000).

[142] Proskuryakov, Y. Y., Savchenko, A. K., Safonov, S. S., Pepper, M., Simmons, M. Y. & Ritchie, D. A. Hole-hole interaction effect in the conductance of the two-dimensional hole gas in the ballistic regime. *Phys. Rev. Lett.* **89**, 076406 (2002).

[143] Braña, A. F., Diaz-Paniagua, C., Batallan, F., Garrido, J. A., Muñoz, E. & Omnes, F. Scattering times in AlGaN/GaN two-dimensional electron gas from magnetoresistance measurements. *J. Appl. Phys.* **88**, 932–937 (2000).

[144] Wurstbauer, U. & Wegscheider, W. Magnetic ordering effects in a Mn-modulation-doped high mobility two-dimensional hole system. *Phys. Rev. B* **79**, 155444 (2009).

[145] Das Sarma, S. & Hwang, E. H. The so-called two dimensional metal-insulator transition. *Solid State Comm.* **135**, 579–590 (2005).

[146] Watson, J. D., Mondal, S., Csáthy, G. A., Manfra, M. J., Hwang, E. H., Das Sarma, S., Pfeiffer, L. N. & West, K. W. Scattering mechanisms in a high-mobility low-density carbon-doped (100) GaAs two-dimensional hole system. *Phys. Rev. B* **83**, 241305 (2011).

[147] Senz, V., Ihn, T., Heinzel, T., Ensslin, K., Dehlinger, G., Grützmacher, D. & Gennser, U. Analysis of the metallic phase of two-dimensional holes in SiGe

in terms of temperature dependent screening. *Phys. Rev. Lett.* **85**, 4357–4360 (2000).

[148] Habib, B., Tutuc, E., Melinte, S., Shayegan, M., Wasserman, D., Lyon, S. A. & Winkler, R. Spin splitting in GaAs (100) two-dimensional holes. *Phys. Rev. B* **69**, 113311 (2004).

[149] Bockhorn, L., Gornyi, I. V., Schuh, D., Reichl, C., Wegscheider, W. & Haug, R. J. Magnetoresistance induced by rare strong scatterers in a high-mobility two-dimensional electron gas. *Phys. Rev. B* **90**, 165434 (2014).

[150] Hikami, S., Larkin, A. I. & Nagaoka, Y. Spin-orbit interaction and magnetoresistance in the two dimensional random system. *Prog. Theor. Phys.* **63**, 707–710 (1980).

[151] Bergman, G. Influence of spin-orbit coupling on weak localization. *Phys. Rev. Lett.* **48**, 1046–1049 (1982).

[152] Poole, D. A., Pepper, M. & Hughes, A. Spin-orbit coupling and weak localisation in the 2D inversion layer of indium phosphide. *J. Phys. C: Solid State Phys.* **15**, L1137–L1145 (1982).

[153] Kawaguchi, Y., Takayanagi, I. & Kawaji, S. Spin-orbit interaction in two dimensional systems in InAs n-inversion layers. *J. Phys. Soc. Jpn.* **56**, 1293–1296 (1987).

[154] Chen, G. L., Han, J., Huang, T. T., Datta, S. & Janes, D. B. Observation of the interfacial-field-induced weak antilocalization in InAs quantum structures. *Phys. Rev. B* **47**, 4084–4087 (1993).

[155] Minkov, G. M., Sherstobitov, A. A., Germanenko, A. V., Rut, O. E., Larionova, V. A. & Zvonkov, B. N. Antilocalization and spin-orbit coupling in the hole gas in strained GaAs/$In_xGa_{1-x}As$/GaAs quantum well heterostructures. *Phys. Rev. B* **71**, 165312 (2005).

[156] Al'tshuler, B. L., Aronov, A. G., Larkin, A. I. & Khmel'nitskii, D. E. Anomalous magnetoresistance in semiconductors. *Sov. Phys. JETP* **54**, 411–419 (1981).

[157] Pikus, F. G. & Pikus, G. E. Conduction-band spin splitting and negative magnetoresistance in A_3B_5 heterostructures. *Phys. Rev. B* **51**, 16928–16935 (1995).

[158] Iordanskii, S. V., Lyanda-Geller, Y. B. & Pikus, G. E. Weak localization in quantum wells with spin-orbit interaction. *JETP Lett.* **60**, 206 (1994).

[159] Golub, L. E. Weak antilocalization in high-mobility two-dimensional systems. *Phys. Rev. B* **71**, 235310 (2005).

[160] Wind, S., Rooks, M. J., Chandrasekhar, V. & Prober, D. E. One-dimensional electron-electron scattering with small energy transfers. *Phys. Rev. Lett.* **57**, 633–636 (1986).

[161] Lin, J. J. & Bird, J. P. Recent experimental studies of electron dephasing in metal and semiconductor mesoscopic structures. *J. Phys.: Condens. Matter* **14**, R501 (2002).

[162] Al'tshuler, B. L., Aronov, A. G. & Khmel'nitskii, D. E. Effects of electron-electron collisions with small energy transfers on quantum localisation. *J. Phys. C: Solid State Phys.* **15**, 7367 (1982).

[163] Choi, K. K., Tsui, D. C. & Alavi, K. Dephasing time and one-dimensional localization of two-dimensional electrons in GaAs/$Al_xGa_{1-x}As$ heterostructures. *Phys. Rev. B* **36**, 7751–7754 (1987).

[164] Chakravarty, S. & Schmid, A. Weak localization: The quasiclassical theory of electrons in a random potential. *Phys. Rep.* **140**, 193–236 (1986).

[165] Studenikin, S. A., Coleridge, P. T., Ahmed, N., Poole, P. J. & Sachrajda, A. Experimental study of weak antilocalization effects in a high-mobility $In_xGa_{1-x}As$/InP quantum well. *Phys. Rev. B* **68**, 035317 (2003).

[166] Sun, L., Zhou, W., Yu, G., Shang, L., Gao, K., Zhou, Y., Lin, T., Cui, L., Zeng, Y. & Chu, J. Strong spin–orbit interactions in an InAlAs/InGaAs/InAlAs two-dimensional electron gas by weak antilocalization analysis. *Jpn. J. Appl. Phys.* **48**, 063004 (2009).

[167] Niimi, Y., Baines, Y., Capron, T., Mailly, D., Lo, F., Wieck, A. D., Meunier, T., Saminadayar, L. & Bäuerle, C. Quantum coherence at low temperatures in mesoscopic systems: Effect of disorder. *Phys. Rev. B* **81**, 245306 (2010).

[168] Kohda, M., Nihei, T. & Nitta, J. Quantum well thickness dependence of spin orbit interaction in gated InP/$In_{0.8}Ga_{0.2}As$/$In_{0.52}Al_{0.48}As$ asymmetric quantum wells. *Physica E* **40**, 1194–1196 (2008).

[169] Faniel, S., Matsuura, T., Mineshige, S., Sekine, Y. & Koga, T. Determination of spin-orbit coefficients in semiconductor quantum wells. *Phys. Rev. B* **83**, 115309 (2011).

[170] Moriya, R. *et al.* Cubic Rashba spin-orbit interaction of a two-dimensional hole gas in a strained-Ge/SiGe quantum well. *Phys. Rev. Lett.* **113**, 086601 (2014).

[171] Hansen, A. E., Björk, M. T., Fasth, C., Thelander, C. & Samuelson, L. Spin relaxation in InAs nanowires studied by tunable weak antilocalization. *Phys. Rev. B* **71**, 205328 (2005).

[172] Kunihashi, Y., Kohda, M. & Nitta, J. Enhancement of spin lifetime in gate-fitted InGaAs narrow wires. *Phys. Rev. Lett.* **102**, 226601 (2009).

[173] Roulleau, P., Choi, T., Riedi, S., Heinzel, T., Shorubalko, I., Ihn, T. & Ensslin, K. Suppression of weak antilocalization in InAs nanowires. *Phys. Rev. B* **81**, 155449 (2010).

[174] Dong, L. & Xuan, G. Strong tuning of Rashba spin-orbit interaction in single InAs nanowires. *Nano Lett.* **12**, 3263–3267 (2012).

[175] Ohkawa, F. J. & Uemura, Y. Quantized surface states of a narrow-gap semiconductor. *J. Phys. Soc. Jpn.* **37**, 1325–1333 (1974).

[176] Dietl, T. Interplay between carrier localization and magnetism in diluted magnetic and ferromagnetic semiconductors. *J. Phys. Soc. Jpn.* **77**, 031005 (2008).

[177] Efros, A. L. Metal-non-metal transition in heterostructures with thick spacer layers. *Solid State Commun.* **70**, 253–256 (1989).

[178] Nixon, J. A. & Davies, J. H. Potential fluctuations in heterostructure devices. *Phys. Rev. B* **41**, 7929–7932 (1990).

[179] Ilani, S., Yacoby, A., Mahalu, D. & Shtrikman, H. Microscopic structure of the metal-insulator transition in two dimensions. *Science* **292**, 1354–1357 (2001).

[180] Das Sarma, S., Hwang, E. H. & Li, Q. Two-dimensional metal-insulator transition as a potential fluctuation driven semiclassical transport phenomenon. *Phys. Rev. B* **88**, 155310 (2013).

[181] Abrahams, E., Anderson, P. W., Licciardello, D. C. & Ramakrishnan, T. V. Scaling theory of localization: Absence of quantum diffusion in two dimensions. *Phys. Rev. Lett.* **42**, 673–676 (1979).

[182] Anderson, P. W. Absence of diffusion in certain random lattices. *Phys. Rev.* **109**, 1492–1505 (1958).

[183] Smet, J. H. Metal–insulator transition: A plane mystery. *Nature Phys.* **3**, 370–372 (2007).

[184] Das Sarma, S. & Hwang, E. H. Two-dimensional metal-insulator transition as a strong localization induced crossover phenomenon. *Phys. Rev. B* **89**, 235423 (2014).

[185] Abrahams, E., Kravchenko, S. V. & Sarachik, M. P. Metallic behavior and related phenomena in two dimensions. *Rev. Mod. Phys.* **73**, 251–266 (2001).

[186] Kravchenko, S. V., Kravchenko, G. V., Furneaux, J. E., Pudalov, V. M. & D'Iorio, M. Possible metal-insulator transition at $B = 0$ in two dimensions. *Phys. Rev. B* **50**, 8039–8042 (1994).

[187] Senz, V., Heinzel, T., Ihn, T., Ensslin, K., Dehlinger, G., Grützmacher, D. & Gennser, U. Coexistence of weak localization and a metallic phase in Si/SiGe quantum wells. *Phys. Rev. B* **61**, R5082–R5085 (2000).

[188] Hanein, Y., Shahar, D., Yoon, J., Li, C. C., Tsui, D. C. & Shtrikman, H. Observation of the metal-insulator transition in two-dimensional n-type GaAs. *Phys. Rev. B* **58**, R13338–R13340 (1998).

[189] Ribeiro, E., Jäggi, R. D., Heinzel, T., Ensslin, K., Medeiros-Ribeiro, G. & Petroff, P. M. Metal-insulator transition in a disordered two-dimensional electron gas in GaAs-AlGaAs at zero magnetic field. *Phys. Rev. Lett.* **82**, 996–999 (1999).

[190] Hanein, Y., Nenadovic, N., Shahar, D., Shtrikman, H., Yoon, J., Li, C. C. & Tsu, D. C. Linking insulator-to-metal transitions at zero and finite magnetic fields. *Nature* **400**, 735–737 (1999).

[191] Coleridge, P. T., Williams, R. L., Feng, Y. & Zawadzki, P. Metal-insulator transition at $B = 0$ in p-type SiGe. *Phys. Rev. B* **56**, R12764–R12767 (1997).

[192] Shabani, J., Das Sarma, S. & Palmstrøm, C. J. An apparent metal-insulator transition in high-mobility two-dimensional InAs heterostructures. *Phys. Rev. B* **90**, 161303 (2014).

[193] Efros, A. L., Pikus, F. G. & Burnett, V. G. Density of states of a two-dimensional electron gas in a long-range random potential. *Phys. Rev. B* **47**, 2233–2243 (1993).

[194] Zala, G., Narozhny, B. N. & Aleiner, I. L. Interaction corrections at intermediate temperatures: Longitudinal conductivity and kinetic equation. *Phys. Rev. B* **64**, 214204 (2001).

[195] Wurstbauer, U., Knott, S., Westarp, C. G. v., Mecking, N., Rachor, K., Heitmann, D., Wegscheider, W. & Hansen, W. Anomalous magnetotransport and cyclotron resonance of high mobility magnetic 2DHGs in the quantum Hall regime. *Physica E* **42**, 1022–1025 (2010).

[196] Knobel, R., Samarth, N., Harris, J. G. E. & Awschalom, D. D. Measurements of Landau-level crossings and extended states in magnetic two-dimensional electron gases. *Phys. Rev. B* **65**, 235327 (2002).

[197] Nagaosa, N., Sinova, J., Onoda, S., MacDonald, A. H. & Ong, N. P. Anomalous Hall effect. *Rev. Mod. Phys.* **82**, 1539–1592 (2010).

[198] Wensauer, C. *Anomaler Hall-Effekt in zweidimensionalen InAs:Mn-Lochsystemen.* Master's thesis, Universität Regensburg (2011).

[199] Vogel, D. *Anomaler Hall-Effekt und Metall-Isolator-Übergang in zweidimensionalen InAs:Mn-Lochsystemen.* Ph.D. thesis, Universität Regensburg (2015).

[200] Wurstbauer, U., Knott, S., Zolotaryov, A., Schuh, D., Hansen, W. & Wegscheider, W. Strong localization effect in magnetic two-dimensional hole systems. *Appl. Phys. Lett.* **96**, 022103 (2010).

[201] Wurstbauer, U., Gronwald, I., Stöberl, U., Vogl, A., Schuh, D., Weiss, D. & Wegscheider, W. Ferromagnetic Mn modulation-doped two-dimensional hole systems. *Physica E* **40**, 1563–1565 (2008).

[202] Wurstbauer, U., Schuh, D., Weiss, D. & Wegscheider, W. From weak to strong localization in a ferromagnetic high mobility 2DHG. *Physica E* **42**, 1145–1147 (2010).

Publications

Material grown during this work has contributed to the following publications:

- **Magnetooptical study of Zeeman effect in Mn modulation-doped InAs/InGaAs/InAlAs quantum well structures**
  Ya. V. Terent'ev, S. N. Danilov, H. Plank, **J. Loher**, D. Schuh, D. Bougeard, D. Weiss, M. V. Durnev, S. A. Tarasenko, I. V. Rozhansky, S. V. Ivanov, D. R. Yakovlev, and S. D. Ganichev, *J. Appl. Phys.* **118**, 113906 (2015)

- **Emergence of spin-orbit fields in magnetotransport of quasi-two-dimensional iron on gallium arsenide**
  T. Hupfauer, A. Matos-Abiague, M. Gmitra, F. Schiller, **J. Loher**, D. Bougeard, C. H. Back, J. Fabian, and D. Weiss, *Nat. Commun.* **6**, 7374 (2015)

- **Magneto-photoluminescence of InAs/InGaAs/InAlAs quantum well structures**
  Ya. V. Terent'ev, S. N. Danilov, **J. Loher**, D. Schuh, D. Bougeard, D. Weiss, M. V. Durnev, S. A. Tarasenko, M. S. Mukhin, S. V. Ivanov, and S. D. Ganichev, *Appl. Phys. Lett.* **104**, 101111 (2014)

Acknowledgements

I would like to express my personal gratitude for the support experienced during the time of my studies and name those who essentially contributed to my PhD project.

I could not have been more fortunate as for **Dominique Bougeard** accepting me to his team on the research of epitaxial semiconductor nanostructure devices, revealing the wide, fascinating spectrum of the field in an inspiring communicative environment of scientific exchange. As an excellent doctoral advisor, he guided the progress of my project by his uniquely patient, clear and constructive way of mentoring. I personally learned from his example of enthusiastically making the best of any challenge, appreciating his profound advice on any matter and had the greatest pleasure in our conversations on topics of diverse mutual interests.

As the co-examiner of this thesis, I thank **Christian Schüller** for his kind interest in my work on the spin-orbit interaction of 2D hole gas systems as well as for his time granted in helpful discussions on this subject.

My deepest gratitude is expressed towards **Paul Wenk** for his great effort in kindly providing a theorist's perspective on various scientific problems that crossed our paths within the valence energy band structure, and in particular for his contributions to the theoretical framework of the anisotropic Hall offset phenomenon. Special thanks are given to **Jonathan Eroms** for pointing us in the right direction on this puzzling issue.

The global expertise of **Dieter Schuh** on the III-V spintronic MBE system, its maintenance and on the growth processes, as well as on every thinkable electronics problem at our setups, was vital for the realization of this project. Thank you, Didi, for sharing your great experimental experience in scientific discussions and also for the non-scientific conversations.

The great number of MBE-grown samples for this thesis and other projects would not have been doable without the invaluable pre-growth preparations by **Imke Gronwald**, maintaining an overview of the holder situation, loading the wafers into the MBE system daily and carefully managing the wafer database. Also, she performed all AFM imaging for this work. Our conversations on arts and life have been a great pleasure to me.

Martin Utz I like to thank for his patience in my training of mastering the MBE process technology and particularly for introducing me to the growth of high-T_C (Ga,Mn)As layers, and also **Marika Hirmer** and **Andreas Rudolph** for advising me at the beginning of my research on MBE.

I am grateful to **Dieter Weiss** and his staff members for generously granting the measurement periods in the ^{3}He/^{4}He dilution refrigeration system and for the instruction in its operation, as well as for the authorization to the processing machinery in the cleanroom ambience.

Thanks to the preparation and interpretation of numerous high-resolution TEM images by **Florian Aumeier** of the Group of **Josef Zweck**, we could gain valuable insights in our buffered indium heterocrystals.

I am very thankful for **Yakov Terent'ev**'s and **Sergey Ganichev**'s interest in collaborating on publications on the magneto-photoluminescence of my InAs-based QW material system as for stimulating discussions on these experiments.

Also, I enjoyed the meetings with **Martin Oltscher** and **Mariusz Ciorga** on our continuous cooperation on III-V heterostructures for exciting electrical spin injection experiments.

Benedikt Bauer and **Peter Olbrich** are acknowledged within the shared supervision of the Pockels effect experimental setup as part of the advanced physics laboratories module.

Our technician **Andi Schützenmeier** is highly appreciated for his uncomplicated and expert assistance in all mechanical jobs and for keeping the magnet sample rods in shape and functioning.

Also from the staff of our Chair, I feel grateful towards **Ulla Franzke** for her kind help in faculty issues and administerial paperwork, as well as towards **Martin Furthmeier** and **Peter Müller** for technical support and for profound conversations on the most various topics.

To my long-time friend **Mario Bamesreiter**, who accompanied me during every facet of our studies in physics, I am sincerely thankful. I could benefit tremendously from his skills and inherently deep comprehension of technology and physics, amongst miscellaneous other non-physical questions in all these years together.

I am most glad to have met a true friend in **Michael Schmalzbauer**, having established the greatest genuinely unique connection starting from day one.

Christian Neumann ever provided helpful thoughts when asked on any topic of my work, yet also was the best partner in any of our spontaneous off-topic endeavours. Thanks to his pleasant being, we could create the most amusing and trusting atmosphere in our office.

I am fortunate to have spent my time with fellow doctoral researchers and friends **Juliane Laurer**, **Joachim Hubmann**, **Stephan Furthmeier**, **Andreas Bayer**, **Michaela Trottmann**, **Florian Dirnberger** and **Johannes Kierig**, as well as every current and former Master and Bachelor candidate in our Group, creating the finest productive everyday working atmosphere and collegiality.

My sister **Marlene Loher** dearly assisted me with her qualified eye for the peculiarities of the English language within this thesis.

I deeply wish to thank my family and my fiancée Johanna for their essential support, understanding and encouragement throughout these years.

Financial support of this project was granted by the **DFG** within the collaborative research center SFB 689: *Spin phenomena in reduced dimensions.*